Ministère de l'Enseignement Supérieur et de la Recherche Scientifique
Ecole Nationale Polytechnique

Département d'Electronique
Laboratoire des Dispositifs de Communication et de Conversion Photovoltaïque
Centre de Développement des Energies Renouvelables

DOCTORAL THESIS

ELECTRONICS

Presented by: **TAGHEZOUIT Bilal**

_____

Contribution to Monitoring and Performance Analysis of Photovoltaic Systems

_____

Publicly defended on **10/23/2022** in front of the jury composed of:

President	Prof. Mourad Haddadi	Professor (ENP)
Supervisor	DR. Amar Hadj Arab	Research Director (CDER)
Supervisor	Prof. Cherif Larbes	Professor (ENP)
Examiner	DR. Abdelhamid Kaabeche	Research Director (CDER)
Examiner	Prof. Farid Bouchafa	Professor (USTHB)
Examiner	Prof. Mourad Adnane	Professeur (ENP)

ENP 2022

DOCTORAL THESIS

ELECTRONICS

Presented by: **TAGHEZOUIT Bilal**

_____

Contribution to Monitoring and Performance Analysis of Photovoltaic Systems

_____

Publicly defended on 10/23/2022 in front of the jury composed of:

President	Prof. Mourad Haddadi	Professor (ENP)
Supervisor	DR. Amar Hadj Arab	Research Director (CDER)
Supervisor	Prof. Cherif Larbes	Professor (ENP)
Examiner	DR. Abdelhamid Kaabeche	Research Director (CDER)
Examiner	Prof. Farid Bouchafa	Professor (USTHB)
Examiner	Prof. Mourad Adnane	Professeur (ENP)

ENP 2022

Ministère de l'Enseignement Supérieur et de la Recherche Scientifique
Ecole Nationale Polytechnique
Département d'Electronique
Laboratoire des Dispositifs de Communication et de Conversion Photovoltaïque
Centre de Développement des Energies Renouvelables

Thèse de Doctorat

Electronique

Présenté par : **TAGHEZOUIT Bilal**

_____

Contribution au Monitoring et à l'Analyse des Performances des Systèmes Photovoltaïques

_____

Présentée et soutenue publiquement le 23 /10/ 2022 devant le jury composé de:

Président	Prof. Mourad Haddadi	Professeur (ENP)
Directeur de thèse	DR. Amar Hadj Arab	Directeur de recherche (CDER)
Co-Directeur de thèse	Prof. Cherif Larbes	Professeur (ENP)
Examinateur	DR. Abdelhamid Kaabeche	Directeur de recherche (CDER)
Examinateur	Prof. Farid Bouchafa	Professeur (USTHB)
Examinateur	Prof. Mourad Adnane	Professeur (ENP)

ENP 2022

<div dir="rtl">

ملخص

تعتبر المراقبة الفعالة والموثوقة لمحطات الطاقة الشمسية الكهروضوئية (PV) ضرورية للحفاظ على الطاقة المولدة بالمواصفات المرغوبة. في هذه الرسالة، نقترح طريقة تعتمد على الأجهزة الافتراضية (VI) لتصميم نظام مراقبة لمحطة كهروضوئية بقوة 9.54 كيلو واط باستخدام جهاز الحصول على البيانات (DAQ) وبرنامج LabVIEW. نظام المراقبة المصمم قادر على قياس وعرض وتحليل وتسجيل جميع البيانات الإعلامية للنظام الكهروضوئي المتصل بالشبكة (GCPVS) عبر واجهة بديهية وسهلة الاستخدام في الوقت الفعلي. تمت معايرة القياسات جيدًا باستخدام أجهزة مرجعية. يتعلق الجزء الثاني من هذه الأطروحة بالنمذجة الاعتبارية للمولد الكهروضوئي والعاكس من أجل تقدير إنتاج الكهرباء وتحليل أداء النظام الكهروضوئي، وقد تم التحقق من صحة النتائج التي تم الحصول عليها من النماذج التجريبية ومعايرتها من خلال البيانات المقاسة. تم تصميم واجهة مستخدم لنمذجة وتحليل أداء نظام الكهروضوئية باستعمال LabVIEW.

الجزء الأخير من هذه الرسالة كان مخصصا لتصميم أداة تشخيصية بسيطة وفعالة من أجل اكتشاف وتحديد الأعطال التي تحدث في نظام الطاقة الكهروضوئية. تم حساب القيم المتبقية باستخدام النماذج البارامترية واللامعلمية. بينما يتم إجراء تحليل الزوائد باستخدام طريقتين لاكتشاف الأعطال، يتم تنفيذ التقنية الأولى من خلال تحليل معدلات فقدان الأداء (PLR) لأربعة مؤشرات كهربائية، بينما يتم تحقيق التقنية الثانية باستخدام مخطط المتوسط المتحرك الأسي المزدوج (DEWMA). لتقييم التقنيات المقترحة، تم أخذ عدة عينات من التغيرات المحيطية والأعطال الكهربائية التي تحدث في النظام الكهروضوئي المتصل بالشبكة. أظهرت النتائج التي تم الحصول عليها أن عملية الكشف والتعريف للأعطال قد تم تحقيقها بنجاح.

الكلمات الدالة: الأنظمة الشمسية الكهروضوئية، القياس، المراقبة، النمذجة، تحليل الأداء، كشف الأعطال، الذكاء الاصطناعي.

</div>

Résumé

Un monitoring efficace et fiable d'un système photovoltaïque (PV) est indispensable pour maintenir la puissance générée aux spécifications souhaitées. Dans cette thèse, nous proposons une méthode basée sur l'instrumentation virtuelle (VI) permettant de réaliser un système de monitoring pour une installation PV de 9,54 kWc en utilisant à la fois un instrument d'acquisition de données (DAQ) et le logiciel LabVIEW. Le système de monitoring réalisé est capable de mesurer, afficher, analyser et enregistrer toutes les données informatives d'un système PV connecté au réseau (SPVCR) via une interface intuitive et conviviale en temps réel. Les mesures ont été bien calibrées avec des instruments de référence. La deuxième partie de cette thèse porte sur la modélisation comportementale du générateur PV et de l'onduleur afin d'estimer la production électrique et d'analyser les performances du SPVCR. Les résultats obtenus à partir des modèles empiriques ont été validés et calibrés utilisant des données expérimentales. Une interface utilisateur de modélisation et d'analyse de performance d'un système PV sous LabVIEW a été conçue.

La dernière partie de cette thèse est consacrée à la conception d'un outil de diagnostic simple et efficace afin de détecter et d'identifier les défauts survenant dans le système PV. Les résidus ont été calculés avec des modèles paramétriques et non paramétriques. Alors que l'examen des résidus est effectué à l'aide de deux techniques de détection de défauts. La première technique est effectuée par l'analyse du taux de pertes de performance (PLR) des quatre indicateurs électriques, tandis que la seconde technique est réalisée à l'aide d'un schéma à double moyenne mobile pondérée exponentiellement (DEWMA). Afin d'évaluer les techniques proposées, différents défauts électriques et anomalies environnementales survenant dans le SPVCR ont été pris en compte. Les résultats obtenus montrent que la détection et l'identification des défauts ont été réalisées avec succès.

Mots clés : Systèmes photovoltaïques, mesure, monitoring, modélisation, analyse de performance, détection de défauts, intelligence artificielle.

Abstract

Efficient and reliable monitoring of a photovoltaic (PV) plant is essential to maintain the power generated at the desired specifications. In this thesis, we propose a method based on Virtual Instrumentation (VI) to realize a monitoring system for a 9.54 kWp PV system using both a Data Acquisition (DAQ) device and LabVIEW software. The implemented monitoring system is able to measure, display, analyze and record all the informative data of the Grid Connected PV System (GCPVS) via an intuitive and user-friendly interface in real-time. The measurements were well-calibrated with reference instruments. The second part of this thesis concerns the behavioral modeling of the PV generator and the inverter in order to estimate the electricity production and analyze the performance of the GCPVS. The results obtained from the empirical models were validated and calibrated by experimental data. A user interface for modeling and analyzing the performance of a PV system under LabVIEW has been designed.

The last part of this thesis is dedicated to the design of a simple and efficient diagnostic tool in order to detect and identify faults occurring in the PV system. The residuals were calculated with parametric and nonparametric models. While the analysis of the residual is performed using two fault detection techniques. The first technique is carried out by analyzing the Performance Loss Rates (PLR) of four electrical indicators, whereas the second technique is achieved using the Double Exponentially Weighted Moving Average (DEWMA) scheme. In order to evaluate the proposed techniques, different electrical faults and environmental anomalies occurring in the GCPVS were taken into account. The obtained results show that the detection and the identification of faults were successfully achieved.

Keywords: Photovoltaic systems, Measurement, Monitoring, Modelling, Performance analysis, Fault detection, Artificial intelligence.

Acknowledgments

Table of Contents

List of Tables

List of Figures

List of acronyms

AC	Alternating Current
AFCI	Arc-Fault Circuit Interrupter
AI	Artificial Intelligence
AM	Air Mass
ANN	Artificial Neural Network
AOI	Angle Of Incidence
a-Si	Amorphous Silicon
ATB	Annual Technology Baseline
AUC	Area Under the Curve
B/T	Bottom/Top
BDI	Bi-Directional Inverter
BIPV	Building Integrated PV
BNEF	Bloombergnef
BOS	Balance Of System
C/L	Closed-Loop
CAPEX	Capital Expenditure
CDER	Centre De Développement Des Energies Renouvelables
CdTe	Cadmium Telluride
CIGS	Copper Indium Gallium Selenide Cell
CIS	Copper Indium Selenide
CNN	Convolutional Neural Networks
COVID-19	Coronavirus Disease of 2019
CPV	Cumulative Percentage Variance
c-Si	Crystalline Silicon
CSP	Concentrating Solar Power
CSV	Comma-Separated Values
CT	Current Transformers
DAQ	Data Acquisition
DAS	Data Acquisition System
DC	Direct Current
DEWMA	Double Exponential Weighted Moving Average
DHI	Diffuse Horizontal Irradiance
DNI	Direct Normal Irradiance
DT	Decision Tree
DZD	Algerian Dinar
E/W	East/West
ECM	Earth Capacitance Measurement
EER	Equal Error Rate
EL	Electroluminescence
ETSG	Electrical Time Series Graph
EWMA	Exponentially Weighted Moving Average
FDD	Fault Detection and Diagnosis
FDe	Fault Detection
FDI	Fault Detection and Identification
FDi	Fault Diagnosis
FER	Fixed Electrical Reconfiguration
FFT	Fast Fourier Transform
FL	Fuzzy Logic
FPGA	Field Programmable Gate Array
FPR	False-Positive Rate
GaAs	Gallium Arsenide
GBSSL	Graph-Based Semi-Supervised Learning
GCI	Grid-Connected Inverter
GCPV	Grid Connected Photovoltaic
GCPVS	Grid Connected Photovoltaic System
GFDI	Ground Fault Detection Interrupter
GHI	Global Horizontal Irradiance
GISTEL	Gisement Solaire par télédétection (Solar Radiation by Teledectection)
GLRT	Generalized Likelihood Ratio Test
GPIB	General Purpose Interface Bus
GPR	Gaussian Process Regression

HJT	Hetero-Junction Solar Cells
IAM	Incidence Angle Modifier
IBC	Interdigitated Back Contact
ICs	Integrated Circuits
IEA	International Energy Agency
IEC	International Electrotechnical Commission
IFC	International Finance Corporation
INES	Institut National De l'Énergie Solaire
IoT	Internet of Things
IP	Internet Protocol
IR	Infrared
IRENA	International Renewable Energy Agency
ISO	International Organization for Standardization
I-V	Current -Voltage
I-VCA	I-V Curve Analysis
KAUST	King Abdullah University of Science and Technology
KDE	Kernel Density Estimation
KELM	Kernel Extreme Learning Machine
kNN	K-Nearest Neighbors
L/H	Low/High
Lab	Laboratory
LAN	Local Area Network
LAPART	Laterally Primed Adaptive Resonance Theory
LCL	Lower Control Limits
LCOE	Levelized Cost Of Electricity
LED	Light Emitting Diode
LFM	Loss Factors Model
LID	Light-Induced Degradation
MAE	Mean Absolute Error
MBB	Multi-Busbar
MCB	Miniature Circuit Breaker
ML	Machine Learning
MLT	Machine Learning Techniques
MPP	Maximum Power Point
MPPT	Maximum Power Point Tracking
MRSD	Multi-Resolution Signal Decomposition
NOCT	Nominal Operating Cell Temperature
NREL	National Renewable Energy Laboratory
O&M	Operation And Maintenance
OCPD	Overcurrent Protection Device
ODM	One Diode Model
OPA	Open Platform Communications
OPV	Organic Photovoltaic
P2P	Peer-To-Peer
PC	Personal Computer
PCA	Principal Component Analysis
PCC	Point Of Common Coupling
PCE	Power Conditioning Equipment
PCs	Principal Components
PERC	Passivated Emitter and Rear Contact
PID	Potential Induced Degradation
PLA	Power Losses Analysis
PLC	Power Line Communication
PLR	Performance Loss Rates
PNN	Probabilistic Neural Network
POA	Plane Of Array
Ppk	Peak Power
PSM	Physical Solar Model
PV	Photovoltaic
P-V	Power -Voltage
PVFS	PV Failure Sheets
PVG	PV Generator
PVM	PV Module
PVPMC	Photovoltaic Performance Modeling Collaborative

PVPS	Photovoltaic Power Systems Programme
PVS	PV Systems
RCCB	Residual Current Circuit Breaker
RCD	Residual Current Detector
RDM	Real-Time Difference Measurement
RHI	Reflected Horizontal Radiation
RMSE	Root Mean Square Error
RNE	Renewable Energy
ROC	Reference Operating Condition
RS 232	Recommended Standard 232 (Computer Serial Interface)
RS 485	Recommended Standard 485
RTD	Resistance Temperature Detectors
S/N	South/North
SA	Statistical Approach
SAPM	Sandia Array Performance Model
S-C	Short Circuited
SCADA	Supervisory Control And Data Acquisition
SNL	Sandia National Laboratories
SPE	Squared Prediction Error
SSTDR	Spread Spectrum Time Domain Reflectometry
STC	Standard Test Conditions
SVM	Support Vector Machine
TDR	Time Domain Reflectometry
THD	Total Harmonic Distortion
TMY	Typical Meteorological Year
TOPCon	Tunnel Oxide Passivated Contact
TPR	True Positive Rate
UAV	Unmanned Aerial Vehicle
UCL	Upper Control Limits
USB	Universal Serial Bus
VI	Virtual Instrumentation
VT	Voltage Transformer
WMS	Weather Monitoring Stations

Symbols

a	Aging factor for DC current of the PV array
b	Aging factor for DC voltage of the PV array
b_{id}	Daily Initialization Bit
Ci	Current indicator
CO_2	Carbon dioxide
C_1, C_2, C_3	Empirical coefficient allowing respectively P_{DC0}, P_{S0} and C_0 to vary linearly with DC-voltage (1/V).
$c0, c1$	Empirically determined coefficients relating Imp to effective irradiance. $c0 + c1 = 1$, (dimensionless)
Cve	Additional Empirically determined coefficients relating Vmp to effective irradiance.
$c2, c3$	Empirically determined coefficients relating Vmp to effective irradiance (c2 is dimensionless, and c3 has units of 1/V)
cti	Normalized temperature coefficient for MPP current.
ctv	Normalized temperature coefficient for MPP voltage.
C_0	Parameter defining the curvature of the relationship between AC power and DC power (1/W).
E_r	Daily received irradiation
E_e	Effective irradiance
$f1$	Constant heat transfer component $(W/m^2 K)$
$f2$	Convective heat transfer component $(W/m^2 K)$
G, E	Irradiance
G_0, E_0	Reference global irradiance at STC=1000W/m².
G_i, G_{POA}	Tilted irradiance or plane of array irradiance
I_{mp_STC}	Current at the maximum-power point at STC (A)
I_{MPP}	DC Current at MPP
$IdcR$	DC current indicator
I_{DCs}	Estimated DC current at MPP
I_{SC}	Short Circuit Current
Idc_{Sim}	Simulated DC current
Idc_{Meas}	Measured DC Current
k	Boltzmann's constant, 1.38066E-23 (J/K)
N_s	Number of cells in series in a module's cell-string
N_p	Number of cell-strings in parallel in module
n	Number of measurements
N_{sp}	Number of samples during the day
$PacR$	AC power indicator
$PdcR$	DC power indicator
P_{S0}	DC power required to start the inversion process, (W).
P_{DC0}	DC-power level at which the AC-power rating is achieved at the ROC, (W).
P_{ACo}	Maximum AC-power rating for inverter at reference operating condition (ROC), (W).
P_{MPP}	Maximum DC power
Pac_{Meas}	Measured AC Power
Pdc_{Meas}	Measured DC Power
$p0$	NOCT coefficient of PV module temperature
p	Number of parallel PV string
$p1$	Parameter takes into account the relationship between estimated T_c and G_i
$p2$	Parameter takes into account the relationship between estimated T_c and W_v
PR	Performance Ratio
Pr	Power ration
P_{ACs}	Predicted AC-power output from inverter based on predicted DC power and voltage, (W).
P_{DCs}	Predicted DC-power input to inverter, equal to the PV array maximum power, (W).
Pac_{Sim}	Simulated AC power
Pdc_{Sim}	Simulated DC power
p	String in parallel
q	Elementary charge, 1.60218E-19 (coulomb)
R^2 or $R2$	Coefficient of determination
Rp	Parallel Resistor
Rs	Series Resistor
s	Number of PV module in series.

$s2$	Empirically-determined coefficient establishing the rate at which module temperature drops as wind speed increases.
$s1$	Empirically-determined coefficient establishing the upper limit for module temperature at low wind speeds and high solar irradiance.
Sf	Soiling factor (=1 when clean)
T^2	Hotelling Control Charts
T_a , T_{amb}	Ambient temperature
T_{av}	Average temperature
T_0	Nominal or reference temperature at STC = 25°C
T_c	Cell temperature inside module (°C)
T_e	Effective temperature
T_{NOCT}	Temperature of PV cell at NOCT
T_{cs}	Estimated PV cell temperature
T_{ms}	Estimated temperature of PV module
$\delta(T_c)$	Thermal voltage per cell at temperature Tc. For diode factor of unity (n=1) and a cell temperature of 25ºC, the thermal voltage is about 26 mV per cell
ΔT	Parameter that depends on the module construction and materials as well as on the mounting configuration of the module. In our PV array ΔT is estimated at 2°C.
Δ_t	Sampling time in hours
V_{MPP}	DC Voltage at MPP
$VdcR$	DC Voltage indicator
V_{DC0}	DC-Voltage level at which the AC-power rating is achieved at the ROC, (V).
V_{DCs}	Estimated DC voltage at MPP
Vdc_{Meas}	Measured DC Voltage
V_{OC}	Open Circuit Voltage
V_{ocx}	Open circuit voltage at 25°C and more than 1200W/m².
Vdc_{Sim}	Simulated DC voltage
V_x	Vacuum voltage at all given T_{ms} and G_{ip}
V_{mp_STC}	Voltage at maximum-power point at STC (V)
Vi	Voltage indicator
Vr	Voltage ratio
W_v or W_s	Wind velocity or speed
Y_a	Array Yield
Y_f	Final Yield
Y_r	Reference Yield

Introduction

Global renewable energy capacity additions in 2020 and 2021 reflect unprecedented momentum for the energy transition. Despite the COVID-19-induced economic slowdown, the world added more than 265 gigawatts (GW) of renewable energy in 2020, and over 256 GW in 2021 reaching a total installed capacity of 3064 GW [1]. In most countries, generating electricity from solar photovoltaic (PV) is now more cost-effective than generating it from coal and gas-fired power plants. These cost reductions have led to record bids in the bidding processes [2].

The solar PV market in recent years has seen strong expansion with at least 175 GWdc added in 2021, reaching a total installed capacity of 942 GWdc [3]. This growth is due to innovations and competitiveness in the solar PV market, electricity demand, low maintenance costs and rapid return on investment [4].

A PV system comprises one or several PV modules connected to either an electricity network (Grid-connected PV) or to a series of loads (Off-Grid). It comprises various electric devices aiming at adapting the electricity output of the modules to the standards of the grid or to the load: inverters, charge controllers and batteries. The inverter is essential for grid-connected systems and is required for most off-grid systems. The storage battery and charge controller are necessary for off-grid systems but also are increasingly needed for grid-connected PV systems [3]. According to IRENA the total installed capacity of solar PV in the world at the end of 2021 is estimated at 849 GW including 844 GW (+ 99%) for Grid-connected PV, while off-grid system represents only 4.9 GW of total installed capacity (+0.57) [1].

New PV system designs are being developed in order to increase the added benefit of the energy produced by either lowering the installation costs, increasing the efficiency, or adding functions to the system. Some of these innovations include advanced power electronics to optimize the performance ratio of PV systems. Some new PV systems have additional functions, such as coupling PV energy with storage and power grid, including storage for electromobility, agricultural PV and floating PV systems [5].

As the share of solar PV in terms of its contribution to overall electricity generation is strongly increasing, the reliability of PV electricity generation is becoming more important. National grid managers require high availability and a high level of predictability from PV energy suppliers [6]. However, Solar PV systems like all power generation systems can be prone to various failures during operation affecting PV system components (i.e., modules, inverters, batteries, cables or protections) [7]. The most general effect of faults is the loss of produced energy, caused by one or more independent faults. Knowing that the performance of PV installations depends on many parameters, including environmental conditions, and the efficiency of each component of the PV system. In the absence of a reliable monitoring system, the PV system can operate with poor performance for several months before the detection and identification of anomalies. This can lead to a significant loss of income [8]. Therefore, reliable and accurate monitoring of the PV system is highly recommended.

According to IEC 61724 standard [9], a reliable monitoring system allows for measuring all environmental and electrical parameters that influence system performance. The sensors and data acquisition (DAQ) instruments must be selected according to the standard recommendations. IEC 61724 Standard gives a description of terminology, equipments and methods for performance monitoring and analysis of PV systems. In the IEC 61724 standard, version 2017 there are three classes (A, B and C) regarding the precision. In the 2021version, there are only two classes, class A (high accuracy) and class B (Medium accuracy), knowing that calibration of the measures is crucial for accurate monitoring.

Great recommendations and guidelines about procedures measurement and monitoring in PV systems are well reported by reputable institutions [8], [10]–[13]. Furthermore, the integration of the PV system behavior models allows creating reference thresholds for the monitoring system, which makes it possible to quantify power losses and analyze performance in order to ensure a reliable operation of any PV system and to send alerts in the event of a drop in performance.

Power losses can be minimized by sending real-time alarms to the operator at the location of the fault in order to take maintenance action.

Many important reports were published by IEA-PVPS Task 13 [14], which gives constructive guidelines, methods and models designed for analytical monitoring and performance of PV systems.

Numerous fault detection techniques have been proposed in recent years, making it possible to monitor performance, detect malfunctions and identify the type of fault present on the DC or AC side of the PV system [15]–[18].

The integration of intelligent fault diagnosis techniques in monitoring software allows the detection and identification of the various faults affecting the PV system in order to improve the reliability and safety of PV systems.

The main aim of this thesis is to present a research work on the design and development of a PV monitoring interface under LabVIEW enhanced by adding accurate empirical models, advanced performance analysis and integration of an intelligent fault diagnostic algorithm in order to detect multiple faults occurring in grid-connected PV systems (GCPVS).

There are three principal objectives of this research which are:

1) Design of an accurate and robust monitoring system based on data logger and LabVIEW software in order to monitor and to analyze the measured parameters of the PV system installed at the CDER.

2) Modeling the energy output of the grid-connected PV system (GCPVS) with performance analysis.

3) Developing PV fault detection and identification techniques based on empirical models and statistical analysis techniques.

In this thesis, we have proposed a complete supervision solution of a 9.54 kWp GCPVS using a user-friendly monitoring interface under LabVIEW. The monitoring interface includes:

1) Measurements and calibration of all necessary parameters according to IEC 61724.

2) Development of the real-time monitoring interface which allows the recovery, visualization, and recording of measurements.

3) Simulation of the electrical behavior of the GCPVS with validation of PV array and inverter models, as well as performance analysis.

4) Diagnosis of some real faults and anomalies using two fault detection techniques.

The thesis is organized into four chapters and a conclusion:

Chapter 1 presents a literature review of PV systems. This chapter contains four sections: 1) Trend and generalities of PV systems, 2) measurement and data monitoring techniques in PV systems, 3) overview of the existing model for a PV system from irradiance to AC power, and 4) the possible faults occurring PV system with detection and diagnosis techniques.

Chapter 2 describes the design and the development of the monitoring system installed in the GCPVS. The proposed monitoring interface is based on the Virtual Instrumentation (VI) under LabVIEW software in order to monitor and analyze the measured parameters of the PV system by the DAQ device. It is worth noting that all installed sensors are well calibrated with reference sensors and instruments.

In addition, some case studies carried out at the CDER concerning measurement and monitoring were presented as follows:
- ✓ Case 1: LabVIEW-based monitoring for an off-grid PV system.
- ✓ Case 2: Monitoring & control of a PV water pumping test bench using LabVIEW.
- ✓ Case 3: I-V characterization and test of PV modules using PVPM 2540C device.
- ✓ Case 4: Advanced electrical measurement of the grid-connected PV system using a three-phase network analyzer.

The principal goal of **Chapter 3** is to model and analyze the performance of the 9.54 kWp Grid Connected PV System. Accurate parametric performance models were proposed in order to simulate the electrical behavior of GCPVS. The parameters of behavioral models were identified using MATLAB curve fitting toolbox. Additionally, a non-parametric model based on Principal Component Analysis was proposed. Furthermore, several models were selected and compared to choose the best models. These models were well calibrated with experimental data in order to minimize errors as much as possible. Finally, a user interface for modeling and performance analysis of the PV system under LabVIEW was designed.

Finally, in **Chapter 4,** we present two fault diagnostic techniques. The first technique is based on an accurate parametric behavioral model to calculate the residuals. The residual analysis of four electrical indicators (i.e., DC current, DC voltage, DC Power and AC power) is carried out by the assessment of performance loss rates (PLR), allowing the detection and the identification of the fault type occurring in the PV system. Six types of faults and nine cases were considered in this section: 1) Open circuit Fault 2) PV string Fault, 3) partial shading of pylons, 4) soiling on the PV array, 5) short circuit fault with four cases (i.e., 2, 3, 4 and 6 PV Modules short-circuited) and 6) DC -AC efficiency faults. Finally, these faults were detected and identified under a friendly user interface with other additional features. The second technique consists of developing a simple and efficient diagnostic method based on parametric models and the double exponentially weighted moving average (DEWMA) scheme. The residuals were calculated with parametric and nonparametric models. Whereas the residuals quantification is performed using the DEWMA technique in order to detect and identify faults occurring in the PV system. Six environmental and electrical faults in the 9.54 kWp grid-connected PV system were considered to evaluate the feasibility of the designed detection methods. These faults were successfully identified.

A **conclusion** completes this research with a summary of the achievements of this thesis and the recommendations for further work.

Chapter 1

Review on PV Systems: Monitoring, Modeling and Fault Diagnosis

Chapter 1 : Review on PV Systems: Monitoring, Modeling and Fault Diagnosis

This chapter contains 1) a literature review on PV systems, 2) measurement and data monitoring techniques in PV systems, 3) an overview of the existing model for a PV system from irradiance to AC power and 4) a review of possible faults occurring in a PV system with detection and diagnosis techniques.

1.1 PV Systems; trend and generalities.

1.1.1 Solar PV trend

Before we turn to Solar Photovoltaics (PV), we would allocate it into the family of renewable energies. The term renewable (or regenerative) means that the supply of energy is not used up. The Sun rises every day, the wind blows every year, and plants grow again after the harvest.

As Figure 1.1 shows, the actual primary energies of renewable energies are the movements of the planets, the heat of the Earth, and solar radiation.

Solar radiation is the basis for a surprising range of energies. Thus, the use of hydropower is only possible by the condensation of water and subsequent precipitation onto land.

The atmospheric movement originates mostly due to solar radiation, which is also the basis for the use of wind power. In the case of biomass products, it is again sunlight that causes photosynthesis, and thus the growth of biomass is conditioned by it. Solar radiation can also be used directly for the generation of heat, for instance in a thermal collector for domestic water. Thermal solar power stations generate and process heat from concentrated sunlight in order to drive generators for the production of electricity.

Thanks to the photovoltaic effect, irradiance is directly converted into electrical energy without complicated intermediate processes and the use of mechanical converters [19].
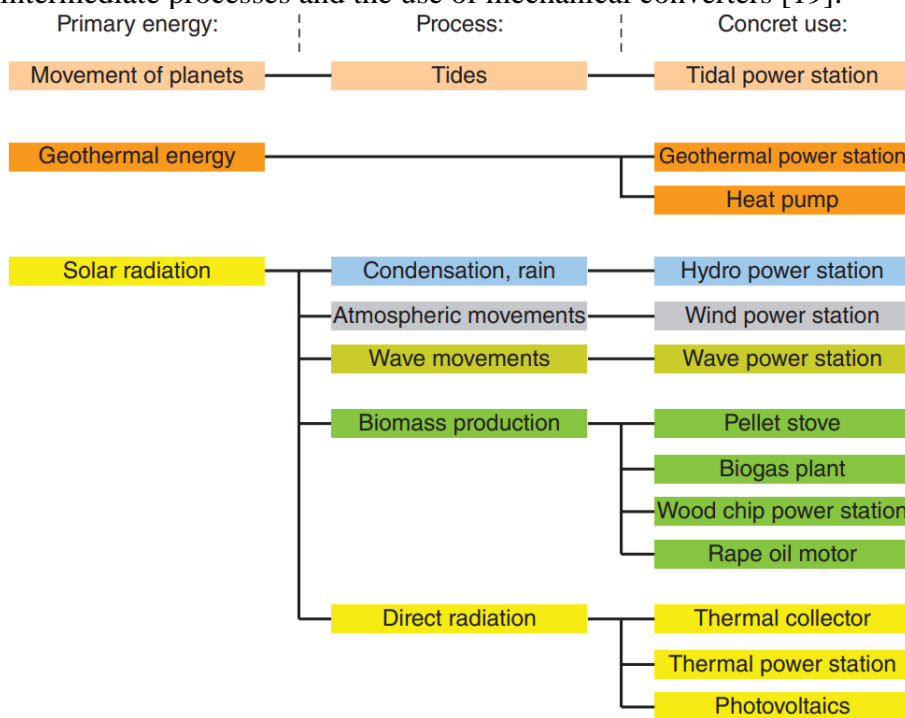
Figure 1.1 Various possibilities for the use of renewable energies [19]

Despite the economic downturn caused by COVID-19 in 2020 and 2021, the capacity of renewable energies has increased much more than in recent years. Most of the expansion has taken place in China. Most other countries continued to increase their renewable energy capacity at a rate similar to the preceding years. At the end of 2021, the global renewable energy production capacity stood at 3064 GW. Renewable generation capacity increased by 257 GW (+9.1%) in 2021, China was the biggest contributor, adding 121 GW to the continent's new capacity.

Solar power continued to dominate capacity expansion, with an increase of 133 GW (+15.6%), followed closely by wind power with 93 GW (+11.3%). Renewable Hydropower capacities increased by 19 GW (+1.54%) and bioenergy by 10 GW (+7.2%). Geothermal energy increased by 1.6 GW (+10%). Solar and wind power continued to dominate the expansion of renewable energy capacity, together accounting for 88% of all net renewable energy additions in 2021 [1]. In most countries, producing electricity from solar PV and wind is now more cost-effective than generating, it from coal and gas power plants. These cost declines have led to record-low bids in tendering processes [2]. Figure 1.2 illustrates trends in installed renewable energy capacity around the world through the end of 2021.

According to Lazard's latest LCOE report- version 15, the cost of onshore wind and utility-scale solar continues to be competitive with the marginal cost of coal, nuclear and combined cycle gas generation. The former values average $27/MWh for utility-scale solar and $25/MWh for utility-scale wind, while the latter values average $42/MWh for coal, $29/MWh for nuclear and $24/MWh for combined cycle gas generation [20].

In [21], National Renewable Energy Laboratory (NREL) Annual Technology Baseline (ATB) provides a consistent set of technology cost and performance data for energy analysis. ATB metrics include capital expenditure (CAPEX), operation and maintenance (O&M) expenditure, capacity factors, and levelized cost of energy (LCOE) [22]. The ATB includes current and projected estimates based on technology innovation for land-based wind, offshore wind, utility-scale PV, commercial PV, residential PV, concentrating solar power, geothermal, hydropower, utility-scale PV-plus-battery, fossil energy technologies and other technologies.
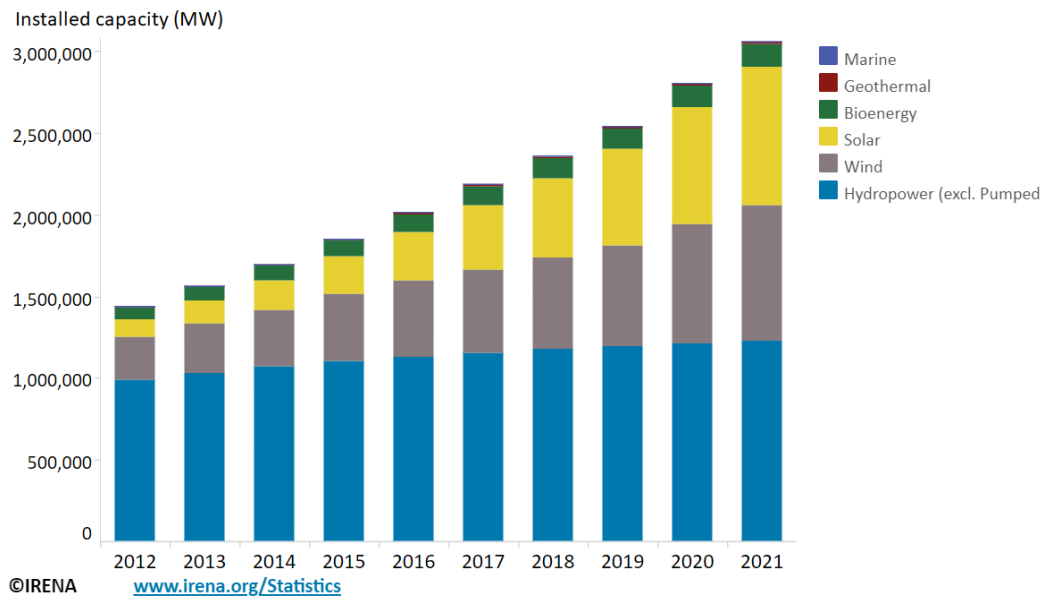
Figure 1.2 Installed renewable energy capacity trends in the world (2012-2021)

Faced with this major energy transition in the world, Algeria has revised its ambitious program which was launched in 2011, with the aim of installing a power of renewable origin with a capacity of 22 GW over the period 2015-2030. Solar PV took a part with a power integration of 13.5 GW [23]. According to the International Renewable Energy Agency (IRENA), the total capacity of solar PV installed in Algeria until the end of 2021 remains fixed at 423MWp, and the wind capacity is only 10MWp [24].

Solar PV technology has shown an ever-increasing market growth thanks to technology and price development. Solar PV will play a key role in the energy transition. This trend is already visible when looking at the evolution of renewable energy technologies as shown in Figure 1.3.
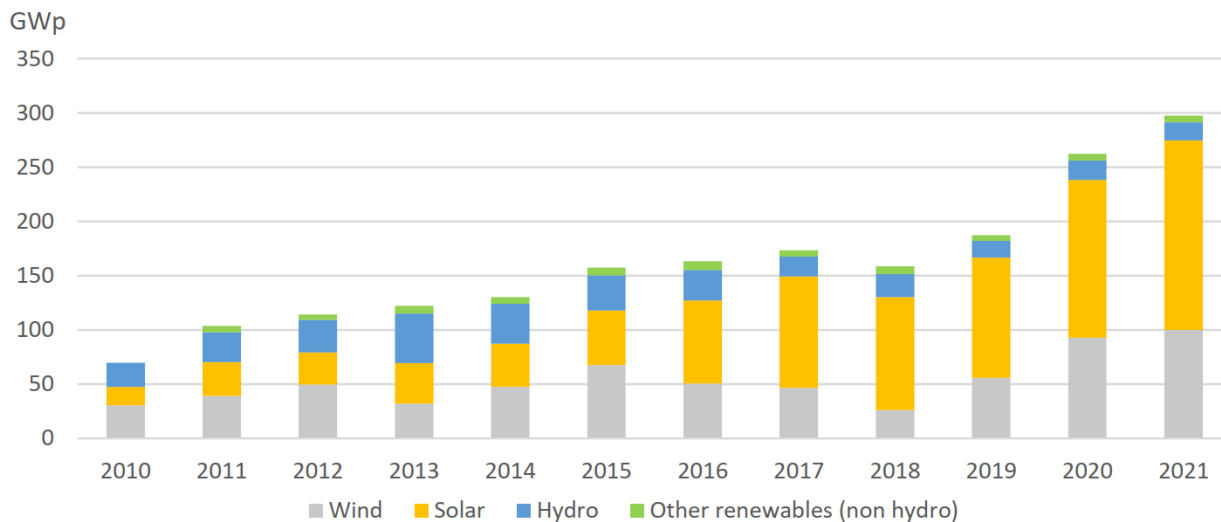
Figure 1.3 Evolution of Renewable Energy Annual Installations (2010-2021).

Despite the second year of the COVID-19 pandemic, preliminary reported market data shows that the global solar PV market again grew significantly in 2021. At least 175 GW of PV systems have been installed and commissioned in the world, reaching a total electricity capacity of 942 GWdc at the end of 2021. The CO_2 savings resulting from existing PV installations reached 1100 million tons of CO_2 [25].

According to Lazard's LCOE report [20], version 15 noted that the LCOE of unsubsidized large-scale PV based on crystalline silicon was estimated at a range of \$30–\$42 per MWh, while thin-film solar plants were estimated at \$28–\$37 per kWh, in China the lastest LCOE is \$22 per MWh. The report included statistics for the LCOE for residential PV as well, which were \$147–\$221 per MWh. Commercial and industrial rooftop solar was a bit better, \$67–\$180 per MWh, and community solar was even better, \$59–\$91 per MWh [26], [27].

Solar PV manufacturing capacity will continue to grow, with new technologies joining the mix, significant factories for new cell technologies such as tunnel oxide passivated contact (TOPCon) and heterojunction will be built in 2022 [28]. Photovoltaic cells represent the smallest unit in a PV power producing device. Wafer sizes, and thus cell sizes have progressively increased, Nowadays, cell sizes range from 156,75 x 156,75 mm^2 (named M2) up to 210 x 210 mm^2 (named M12). In general, cells can be classified as either wafer-based crystalline silicon c-Si (Monocrystalline and Multicrystalline), compound semiconductor (thin-film), or organic.

PV modules are typically rated from 290 W to 800 W, depending on the technology and the size. Specialized products for building integrated PV (BIPV) systems exist, sometimes with higher nominal power due to their larger sizes. Crystalline silicon modules consist of individual PV cells connected and encapsulated between a transparent front, usually glass, and backing material, usually plastic or glass. Thin-film modules encapsulate PV cells formed into a single substrate, in a flexible or fixed module, with transparent plastic or glass as the front material. Their efficiency ranges between 9% (OPV), 10% (a-Si), 17% (CIGS and CIS), 19% (CdTe), 25% GaAs (non-concentrated) and above 40% for some CPV modules [3]. The price of the PV module depends on the efficiency, reliability and technology chosen, according to the Energy Trend website the low price is \$0.23/Wp for 280/335W Multi-Module and \$0.26/Wp for 365/440W Mono PERC Module and \$0.29/Wp for M12 Mono PERC Module [29].

In Figure 1.4 NREL presents a chart of the highest confirmed conversion efficiencies for champion modules for a range of PV technologies, plotted from 1988 to 2020.

Champion Module Efficiencies
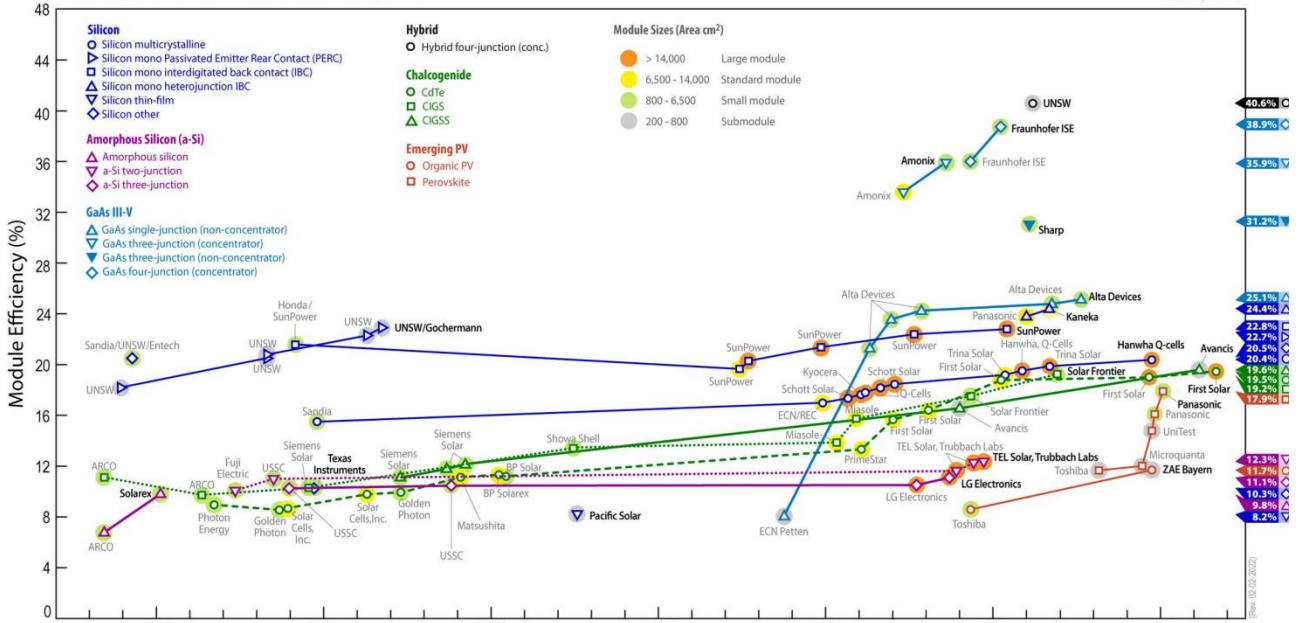
Figure 1.4 chart of the highest confirmed conversion efficiencies for champion modules for a range of PV technologies, plotted from 1988 to 2020.

The last year has seen a surge in manufacturers releasing more efficient solar PV modules based on high-performance N-type heterojunction or HJT cells. For the first time, the efficiency of the recent modules is now above 21%. SunPower and LG modules using IBC cells still lead the pack, but only just, as the new Panasonic EverVolt H and REC Alpha Pure modules featuring N-type HJT cells are very close to the level of the leading IBC cells. Next-generation modules featuring multi-busbar (MBB) half-cut P-type cells from Trina Solar, JinkoSolar, and the new shingled cells from Hyundai have helped increase modules efficiency above 21% [30]. Figure 1.5 shows the Solar cell type and most efficient solar PV modules in 2020.

| Poly PERC | Mono PERC | Shingled mono cells | Half-cut mono PERC |
| 16 - 17% | 17 - 19% | 18 - 20% | 18 - 20% |

| Half-cut mono PERC MBB | Shingled mono PERC | Half-cut MBB heterojunction | N-type IBC |
| 19 - 20.5% | 19 - 20.5% | 20 - 22% | 20 - 23% |
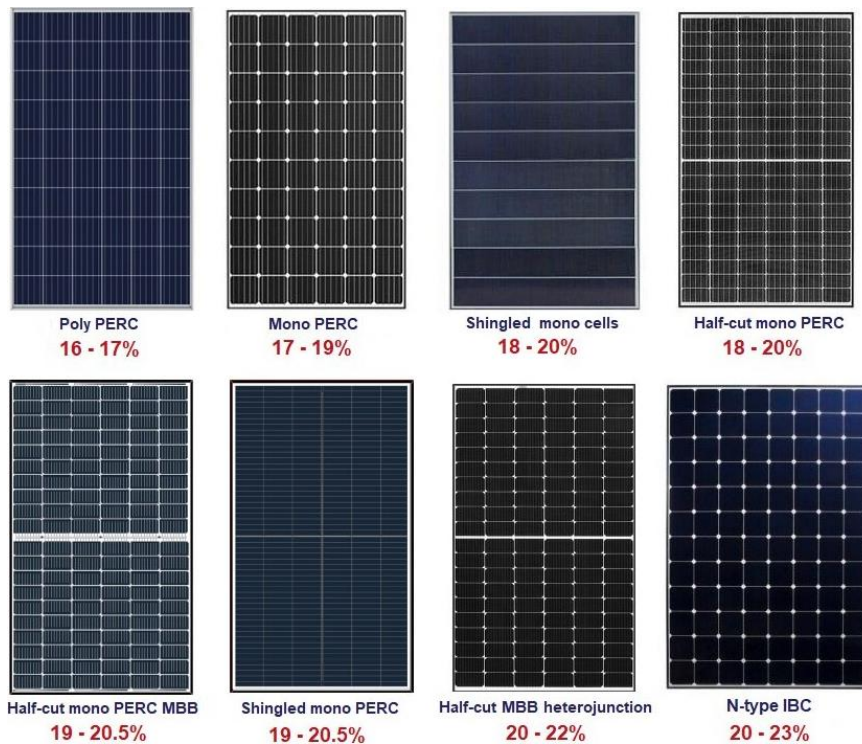
Figure 1.5 Solar cell type and most efficient solar PV modules in 2020.

More efficient modules using N-type cells also benefit from a lower rate of light-induced degradation or LID, which is as low as 0.25% of power loss per year. The industry standard is 80-84% retained power output after 25 years. However, some high-end manufacturers, such as Sunpower, LG, Panasonic and REC guarantee as much as 88% to 92% remaining power output on most modules after 25 years of use [31].

A PV system consists of one or several PV modules connected to either an electricity network (Grid-connected PV) or to a series of loads (Off-Grid). It comprises various electric devices aiming at adapting the electricity output of the modules to the standards of the grid or the load: inverters, charge controllers or batteries. A wide range of mounting structures has been developed especially for **BIPV**; including PV facades, sloped and flat roof mountings, integrated (opaque or semi-transparent) glass-glass modules and PV tiles. Single or two-axis tracking systems have recently become more and more attractive for ground-mounted systems, particularly for PV utilization in countries with a high share of direct irradiation. By using such systems, the energy yield can typically be increased by 10-20% for **single-axis trackers** and 20-30% for **double-axis trackers** compared with fixed systems [3].

Bifacial modules have a growing competitive advantage despite higher overall installation costs. Indeed, recent competitive projects in desert areas boosted the market confidence in bifacial PV performance and production lines are increasingly moving towards bifacial modules.

Balance of system (BOS) component manufacturers and suppliers represent an important part of the PV value chain and BOS components are accounting for an increasing portion of the system cost as the PV module price is falling. Accordingly, the production of BOS products has become an important sector of the overall PV industry. The **inverter** technology has become the focus since it is increasingly considered as the core of the PV system, supporting grid stability with new grid codes. Since these new grid codes require the active contribution of PV inverters to ensure grid management and grid protection. Furthermore, new inverters are now being developed with sophisticated control and interactive communications features [32]. With these functions, the PV power plants can actively support the grid management, for instance, by providing reactive power and other ancillary services [33]. In the case of distributed PV systems, advanced inverters play a key role in storage battery management, communication, monitoring, controlling home appliances, as well as charging EVs [3].

Solar PV inverter manufacturers strive for continuous technological developments, including optimized product operations, flexibility, and efficiency. This factor is expected to create immense opportunities for the solar PV inverter market in the near future. According to the latest reports, the companies Huawei, Sungrow, SMA, Power Electronics, and ABB hold more than 50% of the market [34]. Today grid-connected inverters have achieved excellent efficiencies (e.g., SolarEdge HD Wave "99.2%", Huawei Smart String Inverter "99.0%", SMA Sunny Tripower CORE2 "98.6%"… etc.)

Some inverter manufacturers started using digital technology such as the Internet of Things (IoT) and Artificial intelligence (AI) techniques. Most recent grid-connected inverters are equipped with sophisticated and smart monitoring, this monitoring generally includes 1) accurate measurement of electrical quantities, 2) performance analysis, 3) fault detection and diagnosis (i.e., string fault, arc fault, ground fault, partial shading, dust accumulation, potential induced degradation (PID) and other faults) and 4) sending alarms and reports. The application of machine learning for failure detection or optimization of electricity generation contributed to the lowering the cost of O&M. String inverters with multiple MPPT inputs allow 1) combining multiple configurations of installed modules/strings, 2) managing different module technologies, tilt, orientation, mismatch and shading and 3) detecting faults in an inverter for performance efficiency and optimal. Moreover, other inverters even incorporate an I-V curve measurement with an online diagnostic [35] [36]. Despite this progress, many challenges remain to be solved before solar PV can become a major source of power generation worldwide, this leads to a sustainable energy future [37].

1.1.2 PV System Types

In this section, we have briefly presented the general information on PV systems. PVEducation Website [38] gives general notions on solar photovoltaics with brief explanations, equations, and even interactive graphs. A Photovoltaic reference book on system design and practice that contains a detailed description of PV plants system technology was published in [39]. In [19] the author has written a book on the photovoltaics fundamentals, technology and practice, this book contains well-organized technical information and concepts, as well as very user-friendly diagrams about design, on-site measurement and performance in PV systems. Recently Yaman and Eklas have published in [40] a guide to provide a hands-on approach to learning about solar PV systems fundamental for students and professionals. A project developer's guide of utility-scale solar PV power plants was reported in [8], this guidebook focuses on aspects of project development that are specific to solar. From this perspective it covers all aspects of the overall project development process including site identification, plant design, energy yield, permits/licenses, contractual arrangements, and financing. In [41] authors have explained step-by-step the design of large-scale PV power plants with a brief definition and simple schematic.

PV modules are the key components for every PV power plant from tiny roof-top systems of a few kilowatts to plants in the gigawatt range which may demand millions of modules. [42] describes the entire solar PV supply chain, starting in the early chapters with detailed discussions of the basic ingredients and the manufacturing processes of silicon-based PV systems, and concluding with chapters that discuss the multitude of applications of PV systems being used today. PV Modules are required to efficiently, safely, and sustainably convert solar irradiance into electric power over a service life of decades. For such long operational times, reliability is the dominating property of a product [43]. An overview of the technological development of PV Module in the last year was reported in [44].

Most solar modules are made up of many silicon-based PV cells which generate direct current (DC) electricity from sun irradiance using what is known as the **photovoltaic effect**. It is sunlight or irradiance, not heat, which produces electricity in PV cells. The PV cells are linked together within the solar module. PV modules are generally connected together in 'strings or panels' to create a PV array.

Plane of array (POA) irradiance is a well-known term used to quantify the incident irradiance on a PV module. It is the parameter most directly related to the power output and is used extensively in PV performance analysis and modeling of PV arrays [45]. POA irradiance is defined as the sum of the direct normal (DNI) and diffuse (DHI) irradiance components incident on a surface with a given tilt and angle of incidence (AOI) [46]. Note that GReflected is often called reflected horizontal radiation (RHI) [47] (see Figure 1.6). PV module can generate energy during cloudy and overcast weather, but the amount of energy depends on the 'thickness' and height of the clouds, which determines how much irradiance can pass through.
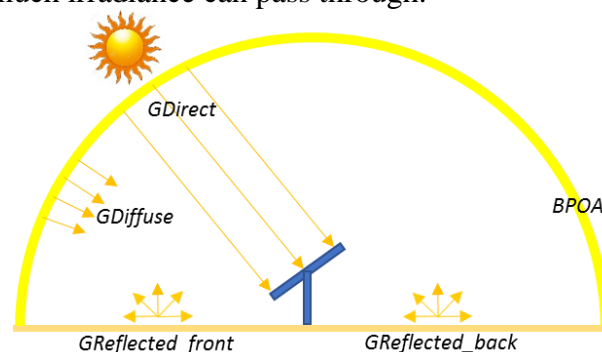
Figure 1.6 Irradiance component, Including Albedo, on a Bifacial PV Module [47].

Bifacial PV modules collect irradiance on both sides of the modules with monofacial PV, calculating and measuring RHI component is important when using bifacial PV modules. When mounted on a surface which albedo reflects enough light, the energy production increase is estimated to a maximum of 15% with structure, and possibly up to 30% with a single-axis system. Among the advantages of bifacial PV modules are: 1) high efficiency 2) less space & modules

required, 3) high durability, 4) energy production during bad weather, and 5) angle of installation. While the disadvantages are: 1) the high cost associated and 2) heavyweight. Figure 1.7 (a-d) illustrates the installations possibilities of bifacial modules and (e) a comparison of power generation curves for monofacial and bifacial modules for four configurations; Slanted South/North (S/N), Horizontal Bottom/Top (B/T), Vertical East/West (E/W) and tracked E/W [48].
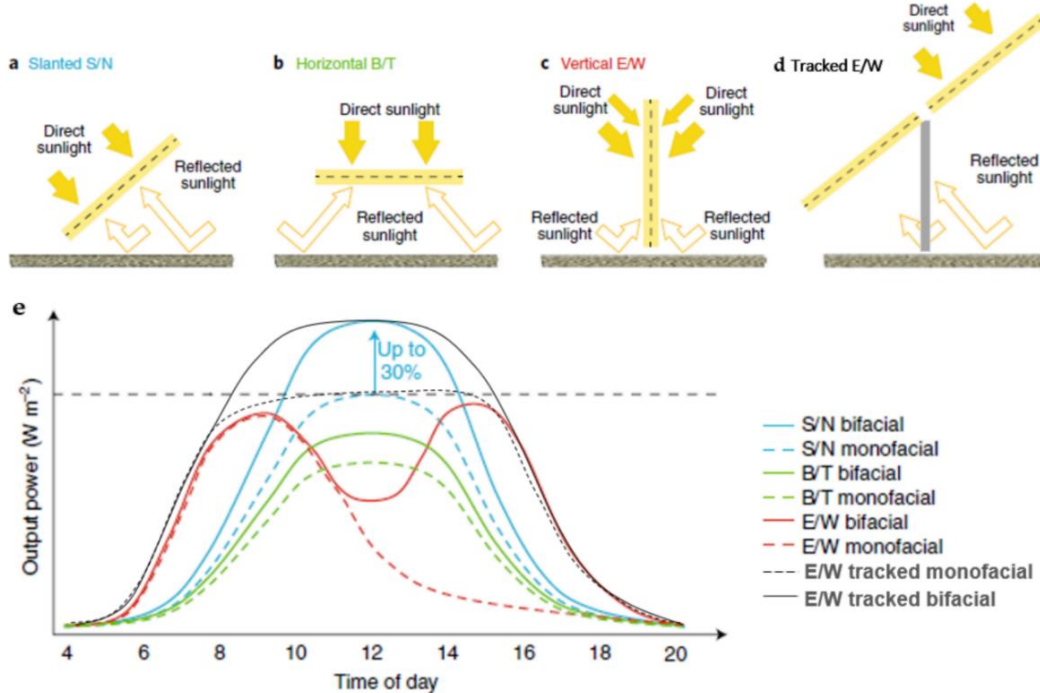
Figure 1.7 (a–d) possibilities for installations of bifacial modules and (e) a comparison of power generation curves for monofacial and bifacial modules [49].

The energy generation from the PV module depends on the environmental conditions to which it is exposed during its lifetime. Usually, PV modules are tested at Standard Test Conditions (STC) where the electrical efficiency is often perceived as a conclusive indicator of their quality. STC rating is useful to compare the performance of different technologies in conditions that can be easily recreated in a laboratory environment, however it fails in giving accurate information on how much energy it can generate for long-term operations. The energy rating allows the customer to compare not only similar products from different manufacturers but also completely different technologies. It should also provide a realistic estimated energy value for the region of installation and should be simple, accurate, repeatable, and agreed in terms of methodology for its calculation. The solar modules operating efficiency is dependent on many external factors. Depending on the local environmental conditions these various factors can reduce module efficiency and overall system performance. The main factors which affect solar modules efficiency are 1) in-plane irradiance, 2) operating cell temperature, 2) shading, 3) soiling, 4) tilt & orientation, 5) location and 6) time of year and another factor. To include all the parameters affecting the performance of a PV module in terms of energy generation, the International Electrotechnical Commission (IEC) has designed a standard IEC 61853 divided into four different parts. [50].
Figure 1.8 illustrates the I-V curve of 670W Trina-solar bifacial module (a) at various irradiances with fixed module temperature of 25℃ and (b) at various module temperatures with constant irradiance of 1000 W/m^2. we can see clearly the impact of the irradiance and cell temperature on the PV modules power rating.
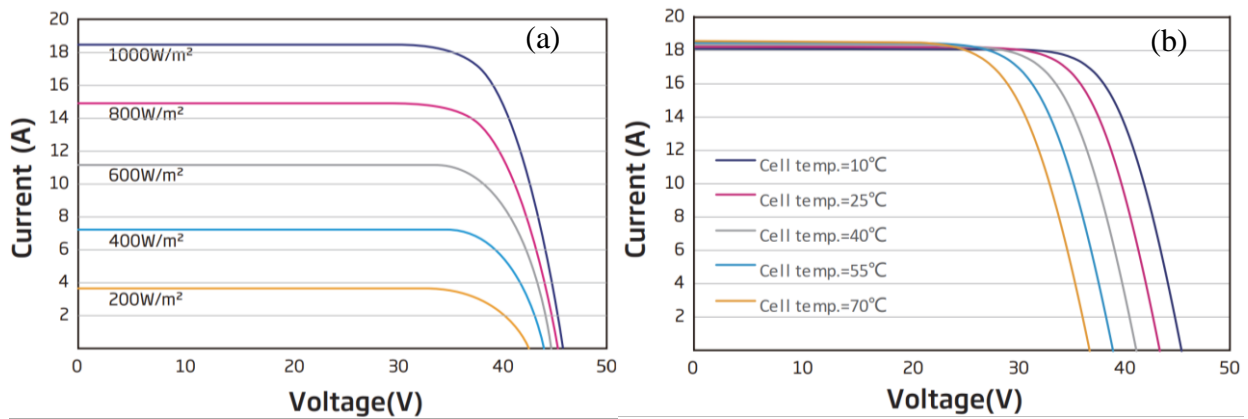
Figure 1.8 I-V curve of 670W Trinasolar bifacial module (a) at various irradiances with fixed module temperature of 25 ∘C and (b) at various module temperatures with constant irradiance of 1000 W/m^2.

PV systems are mainly classified according to their application. The main classifications are stand-alone systems and grid connected PV systems. PV systems can be designed to supply DC and AC loads. These systems can also be connected with energy storage systems and other energy sources. Figure 1.9 gives a brief classification of PV system configuration. Depending on the configuration, PV systems are divided into three categories as briefly explained below.
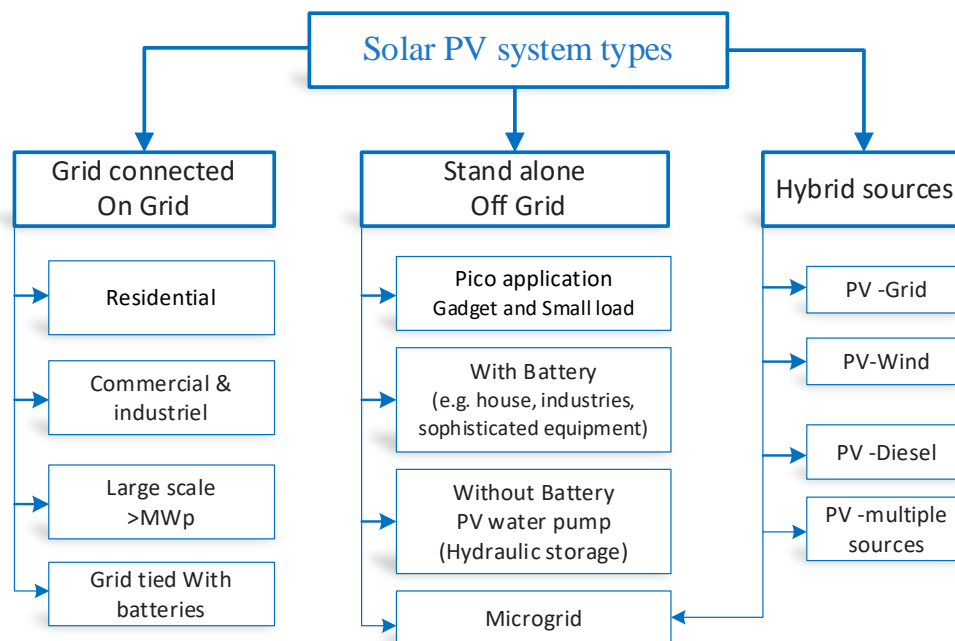
Figure 1.9 Classification of PV system categories.

Grid-connected PV system

Grid-connected PV system (GCPVS) are usually connected to the power network. The schematic diagram of a GCPVS is shown in Figure 1.10. The GCPVS can be installed almost anywhere. Based on the installation location, the GCPVS are divided into three main categories: 1) residential, 2) commercial and industrial and 3) utility-scale. For a GCPVS, the grid acts as an energy storage system [41].
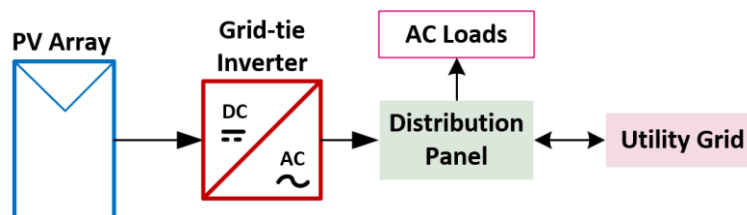
Figure 1.10 Schematic diagram of a grid-connected PV system.

Inverters are the most critical part of a solar system, in grid-connected PV systems, an inverter is used to convert electricity from direct current (DC) as produced by the PV array to alternating current (AC) that is then supplied to the electricity network. The typical weighted conversion efficiency is in the range of 95% to 99%. Grid connected inverters have special functions adapted for use with PV arrays, including MPPT , anti-islanding protection , low voltage ride through, active power limiting and other features [32]. In the GCPVS, there are three main types of inverters ; 1) central inverter, 2) string inverter, and 3) micro inverter [33] [19].

Central inverter can be used for the whole PV array using DC combiner (500kVA-5MVA), this type of inverter is used only for utility-scale power plant. String inverter with rated power from 1kVA to 250KVA can used for residential, commercial, industrial and utility PV installations. The new string inverters are equipped with several MPPT inputs with a voltage up to 1500 VDC; the MPPT number increases according to the inverter power. Residential inverters are usually equipped with 1 to 2 MPPT inputs (e.g., Fronius primo and SMA sunny boy...etc.). The string inventers intended for commercial and utility installations contains up to 12 MPPT inputs (e.g., SMA Sunny Tripower CORE2 and Sungrow SG250HX). Ingeteam Enterprise recommends string inverters for projects <10MW, and central inverters for even larger projects >10MW [51].

PV modules with integrated inverters, usually referred to as "AC modules", can be directly connected to the electricity grid with the permission of the grid operator, they offer better partial shading management, installation flexibility and accurate monitoring for each module. Similarly, micro-inverters, connected to one (1) module up to four (4) also exist, despite their higher initial cost, they present some advantages where array sizes are small and maximal performance is to be achieved.

In the residential, commercial and industrial PV system, the generated electricity is either consumed immediately by local loads or is sold to electricity supply companies. While for the utility-scale PV plant all produced power is injected into the electrical grid, this is called a grid-connected centralized PV system.

When the GCPVS produces insufficient power or it is unable to produce electricity, the solar PV can be compensated by another source of electricity according to the demand in the smart grid.

The commercial, industrial, and utility-scale PV plants can be installed as: 1) ground-mounted, 2) floating on a water surface, building-integrated, rooftop mounted, and agrivoltaics [41].

A ground-mounted PV plant is installed on a land, whereas a floating PV plant is installed on a water lake. In a building-integrated PV (BIPV) system, solar modules are placed in the facade of a building. BIPV products can take various shapes, colors and be manufactured using various materials, although a vast majority use glass on both sides. They can be assembled in way that they fill multiple functions usually devoted to conventional building envelope solutions. An agrivoltaics or agrophotovoltaics plant is installed in a greenhouse or agricultural farm and a rooftop mounted PV system is installed on roof of a house, building, or factory.

New utility-scale PV plants are increasingly using trackers to maximize production and in parallel, the use of bifacial PV modules increases relatively fast as well. The addition of storage systems also becomes a trend in some countries [3].

The new utility-scale PV-plus-battery configuration represents a DC-coupled system in which one-axis tracking PV and 4-hour lithium-ion battery storage shares a single bidirectional inverter (Figure 1.11). For example the PV-plus-battery technology is represented as having a 130-MW_{DC} PV array, a 50-MW_{AC} battery, and a shared 100-MW_{AC} inverter [52].
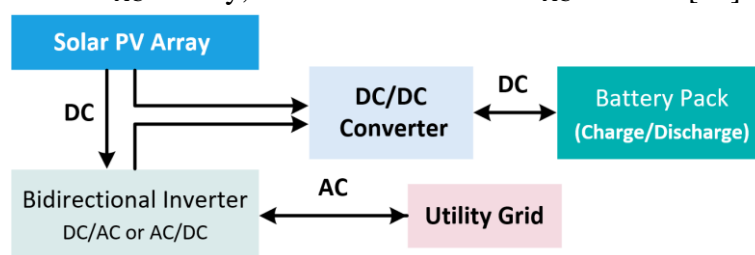
Figure 1.11 Schematic diagram of a grid-connected PV system plus battery.

Stand-alone PV systems

The stand-alone or off-grid PV systems are used in the remote areas (households and villages) and other applications that have no access to the power grid. A stand-alone PV system operates independently of the grid, with part of the produced energy stored in energy storage systems such as batteries. A schematic diagram of a stand-alone PV system is shown in Figure 1.12. A stand-alone PV system includes PV modules, charge controller, batteries and inverter [53].

Batteries used for solar energy storage are available in two main types, lead-acid (AGM & Gel) and lithium-Ion. There are several other types available such as redox flow batteries and sodium-ion. Battery capacity is generally measured is either Amp hours (Ah) for lead-acid, or kilowatt hours (kWh) for lithium-ion. The lifetime of a battery varies, depending on operating regime and conditions battery technology and cycle life, but is typically between 5 and 10 years Most modern energy storage systems use rechargeable lithium-ion batteries and are available in many shapes and sizes which can be configured in several ways, most lithium batteries come with a 10-year warranty [54].

A charge controller (or regulator) is used to maintain the battery at the highest possible state of charge (SOC) and provide the user with the required quantity of electricity while protecting the battery from deep discharge or overcharging. Some charge controllers also have integrated MPP trackers to maximize the PV electricity generated [55].

If there is a requirement for AC electricity, a "stand-alone inverter" can supply conventional AC appliances. The inverter converts the DC power generated by the PV modules to the AC power for AC loads. In recent off-grid inverter two main functions are taken into consideration, the management of the battery discharge and the charging of the battery via the electrical network or other AC source, this product is called Inverter/chargers (e.g., Victron Energy MultiPlus and Quattro). Some all-in-one product combines an MPPT Solar Charge Controller and inverter/charger for easy installation and minimum of wiring (e.g., Victron Energy EasySolar) [56].
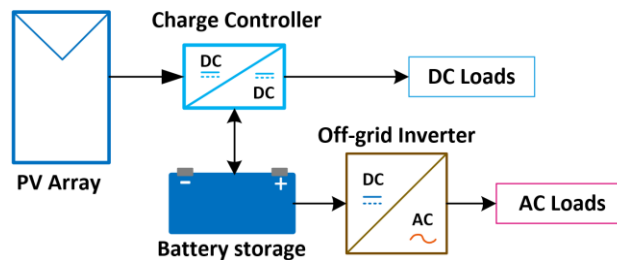
Figure 1.12 Schematic diagram of a stand-alone PV system.

Stand-alone PV system provides electricity for lighting, refrigeration and other low-power loads such as smartphones and PCs to meet the energy needs of off-grid communities.

There are several other non-domestic applications such as satellite, military equipment, telecommunications, vehicle integrating PV, etc. Among the most profitable and reliable application the water pumping, where the PV array is directly connected to the pump controller (e.g., GRUNDFOS [57], Lorentz [58]) .The pump can only operate in the presence of irradiation, the water flow is proportionally related to the amount of sunshine received by the PV array, and instead of storing energy electric, the water is usually stored in a tank.

Hybrid PV systems

In the hybrid PV system, more than one type of generator is exploited. In this type of system, solar PV array is the main generator. The other generators can be wind turbine, diesel engine generator, or the utility grid. The schematic diagram of a hybrid-connected PV plant is shown in Figure 1.13. The system can provide electricity for both DC and AC loads [41].

PV-diesel hybrid systems combine the advantages of PV and diesel generator in micro grids. They allow mitigating fuel price increases, deliver operating cost reductions, and offer higher service quality than traditional single-source generation systems.

The combining of technologies provides new possibilities to provide a reliable and cost-effective power source in remote places such as for telecom base stations for instance.

In PV-grid hybrid system, the DC power can be stored in a battery or converted by a solar inverter into AC power which can be used to run home appliances. Depending on the type of system, excess solar energy can either be fed into the electricity grid for credits, or stored in a variety of different battery storage systems. The hybrid inverters operate in bidirectional mode DC to AC and AC to DC [59]. Recently, various hybrid inverter topologies have been developed, manufacturers offer several features and configurations depending on the type of hybrid system (e.g., SMA Sunny Tripower Smart Energy, Fronius Primo GEN24 Plus…etc.). Large-scale hybrids system can be used for decentralized microgrids in villages powered today by diesel generators, for example in Central Africa. The large-scale hybrid system can combine several renewable sources with lithium-ion battery storage.
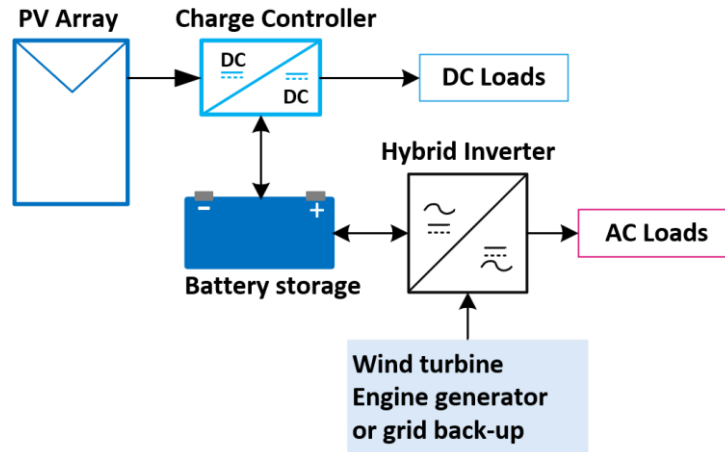
Figure 1.13 Schematic diagram of a hybrid PV system.

1.2 Data acquisition and monitoring in PV system

1.2.1 Introduction

Data acquisition (DAQ) is the measurement, recording, analyzing, and presentation of real-world phenomena. It includes electrical measurements such as voltage, current, power as well as measurements through sensors and transducers including irradiance, temperature, humidity, wind speed, precipitation, pressure, flow, level, strain, acceleration, and more parameters [60]. DAQ systems are used to collect and store data for performance evaluation. Data acquisition systems differ according to following parameters: 1) channels number, 2) measured signals from sensors, 3) sampling rate, 4) control option, 5) data transfer protocol, and 6) program development software. The DAQ systems are currently used in PV systems for monitoring performances and controlling operations, indeed an accurate and reliable assessment of the PV systems is essential for a sustainable development. For manufacturers, performance evaluation is a key criterion for the quality of their products. On the other hand, for research surveys, it is a crucial indicator for identifying future challenges. For end customers, a reliable performance assessment can simplify the monitoring of its installation and better generate energy [61].

In large scale PV power plant, an effective Operation and Maintenance (O&M) service allows the PV system production to reach its expected level of efficiency; which therefore increases the confidence of end users, while the O&M costs are significant [62]. In [63] a solution to reduce these costs was proposed. The O&M contract generally includes the following core services; 1) Continuous monitoring of the plant operation and periodic reporting, 2) Preventive maintenance and 3) Corrective maintenance [7], [64]. Figure 1.14 present an overview of O&M aspects and services for PV power plants during their technical life cycle.

Monitoring of PV systems is mandatory to provide information that allows 1) maintaining, operating and controlling PV installations, 2) reducing costs 3) and avoiding undesirable power outages. The main characteristics of any monitoring systems are categorized into following types: (i) monitored parameters and sensors, (ii) data acquisition and control device, (iii) data transfer mechanism, (iv) program development software, (v) and monitoring method [65].

According to [66], plant size, system criticality and O&M costs determine the adequate monitoring system. On the other hand, plant size is important for monitoring system design. Adopting wired sensors in small plants is economic and less complex. While, wireless networks are more convenient for medium and big sized plants.

Basic monitoring PV system consists in measuring of essential quantities of the PV installation and providing reports to end users. For advanced monitoring system it mainly composed by 1) sensors (environmental and electrical), 2) accurate data acquisition system with reliable communication protocols, 3) metrics for data analysis 4) algorithms for fault diagnosis and 5) forecasting models for prevision of future energy.

The three main areas of best practices for system monitoring are the following: 1) data presentation, 2) quality of monitoring equipment, and 3) transparency of measurement protocols and procedures. The monitoring approach and associated cost depends on the revenue linked with the performance of the asset. IEC 61724 classifies monitoring systems (A, B, C); the O&M service related to monitoring depends on the system class (Table 1.1).

The objective of monitoring is to provide enough information in order to accomplish an "energy balance" accounting for the amount of solar resource available, and the losses in each energy conversion process up to delivery at the point of interconnection. A monitoring system should account for clipping of output due to high DC-to-AC ratio, interconnect limits, and called-for curtailment or any other reason.

With the increased interest in monitoring PV system, more and more papers related to these systems are emerging. Most of them deal with one part of the monitoring system such as: sensors, data acquisition, performance analysis, fault detection…etc.

Several important reports were published by IEA- Photovoltaic Power Systems (PVPS) in Task 13 (i.e., Performance, Operation and Reliability of Photovoltaic Systems) [14], this report give a constructive guidelines, methods and models that may be designed for analytical monitoring of PV systems. Numerous recommendations and standards for measurement and monitoring in PV system are reported by renowned institutions [8], [10]–[13].

A good review on the state of the art of data acquisition and monitoring of PV systems have been reported in the literature [61], [65], [67], [68]. In [67], [69] authors presented an overview of remote monitoring solutions for PV system along with the main proposals, commercial products and international experiences. Data acquisition system, and data storage are overviewed in [65], [67] as well as monitored parameters with sensors used and data transmission methods in [65]. Data transfer mechanisms, wired, wireless, and power line communication systems are introduced in [70]. Moreover, data analysis methods for PV systems are presented in [65], and dedicated software for monitoring systems in [67].

Over the past decade, various aspects of PV monitoring systems have been reported in a wide range of publications. The modern architecture of remote monitoring system consists of three levels: 1) measurement and acquisition, 2) pretreatment and recording and 3) Storage and Web services. In the literature several authors have conducted studies on the design and development of data acquisition (DAQ) and monitoring systems for PV installations [71]–[74]. Recently , In [75] a wide comparison of commercial PV monitoring software around the world presented in a compact overview containing all the features with a cost analysis.
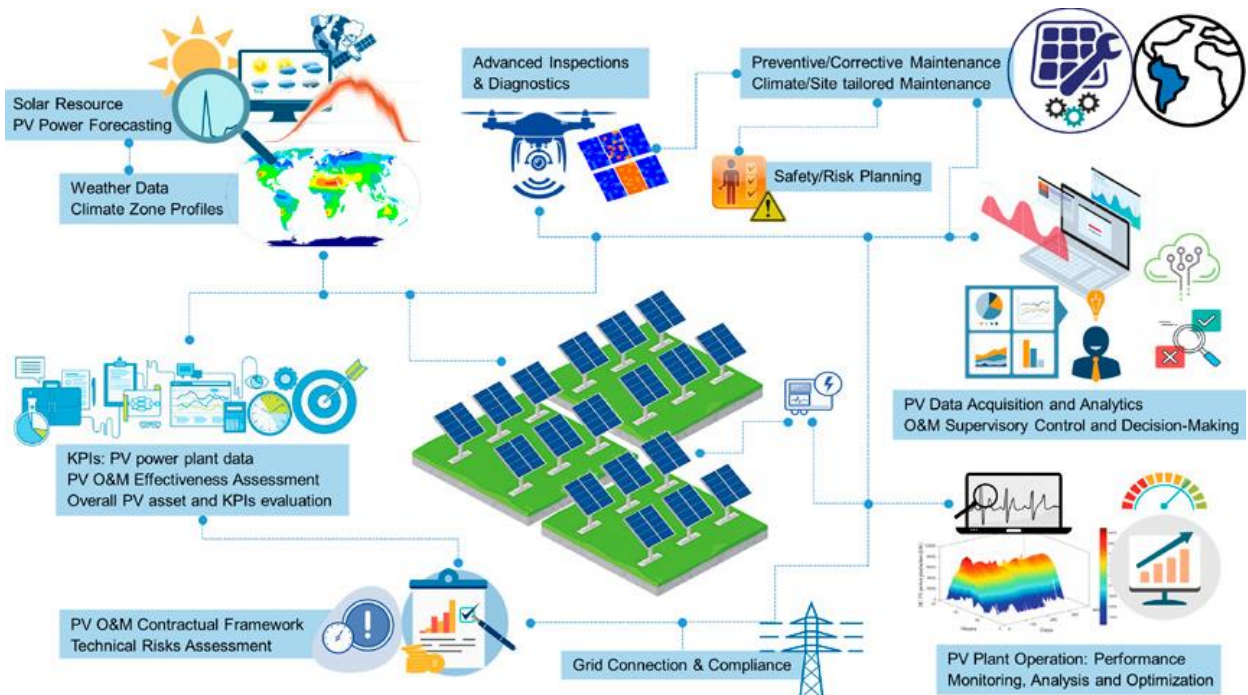
Figure 1.14 Overview of operations and maintenance (O&M) aspects and services for PV power plants during their technical life cycle (source: CEA-INES).

Table 1.1 Monitoring System Classifications.

Features	Class A	Class B	Class C
Precision	Greatest	Medium-level	Basic
Typically, targeted PV system size	Utility-scale	Commercial& Industrial	Residential and small commercial
Suitable applications			
System performance assessment	●	●	●
Documentation of a performance guarantee	●	●	
Forecasting performance	●	●	
Electricity network interaction assessment	●	●	
Monitoring integration of distributed generation, storage, & loads	●	●	
System losses analysis	●		
PV technology assessment	●		
PV system degradation measurement	●		

1.2.2 Analytical monitoring solution for PV systems

The monitoring of a PV installation makes it possible to evaluate the performance of PV systems. A monitoring system is usually composed of sensors, data acquisition and software. There are various solutions to monitor the electrical production and performance of PV systems, [76]. The main criteria for classification and selection of the monitoring system according to the standard IEC 61724-1 [77] :

- The parameters to be measured according to the size and application of the PV system.
- Sample measurement, accuracy of measure, presentation and analysis of data.
- The quality and cost of the DAQ system.
- The transparency of protocols and measurement procedures.

It is possible also to classify the different monitoring systems according to the information dependence that comes from the components constituting the PV system.

1.2.2.1 Full Turnkey PV monitoring systems.

This monitoring technique is used to monitor and collect data from solar PV system. the PV monitoring manufacturers offer a full turnkey system, equipped with (DAQ hardware, software, web interface and optional meteorological sensors), the electrical sensors are integrated in the power converter or measured by power meter.

This kind of monitoring system gives reliable and continuous data with low maintenance, but is limited in terms of configuration, calibration, and personalization of the DAQ system. There are two types of turnkey PV monitoring system; monitoring designed by inverter manufacturers and Multi brand monitoring.

1) Monitoring PV designed by inverter manufacturers.

Monitoring and control systems from inverter manufacturers are usually the cheapest solution to evaluate performances of solar systems. Most of inverter's manufacturers provide free portals and softwares that allow to monitor PV system (e.g., SMA Sunny Portal, Fronius Solar Web, Huawei Fusion Smart PV…etc.) [78], [79]. PV inverter manufacturers also provides sophisticated monitoring products, which makes it possible to measure meteorological quantities with the connection of several inverters and other products of inverter manufacturers using RS 485 or Ethernet protocol as shown in Figure 1.15 [80].

Figure 1.15 Monitoring & control from SMA inverter manufacturer.

2) Multi brand solar monitoring (non-inverter dependent).

The multi-brand solar datalogger gathers all the indicators of the inverters, the electricity meters, the environmental sensors (i.e., irradiance, temperature, wind speed, etc.) and other devices using RS485 protocol. This solution is an inverter-independent energy management system where datalogger can monitor solar power plants with up to 100 inverters and also offers many other useful functions (e.g., Solar-Log dataloggers are compatible with over 2,300 inverter models and with over 130 different component manufacturers [81]). Figure 1.16 illustrate the multi brand monitoring & control system proposed by Solar-Log company.

Figure 1.16 Multi brand monitoring & control system (Solar-log).

1.2.2.2 Custom monitoring system

However, for more accuracy, flexibility and, customization, it is recommended for Education, Research and metrology to use a custom monitoring system, where the user can select sensors, data acquisition hardware and application software. Indeed, this PV monitoring system is based on the parameters measurement influencing on the performance of the PV system, mainly the meteorological and electrical parameters. In this type of monitoring, the electrical parameters are measured by external voltage and current sensors in DC/AC side, The hardware and software data acquisition and control are flexible and customizable. Using this solution, an additional sensors or actuators can be added, as presented by the Figure 1.17.
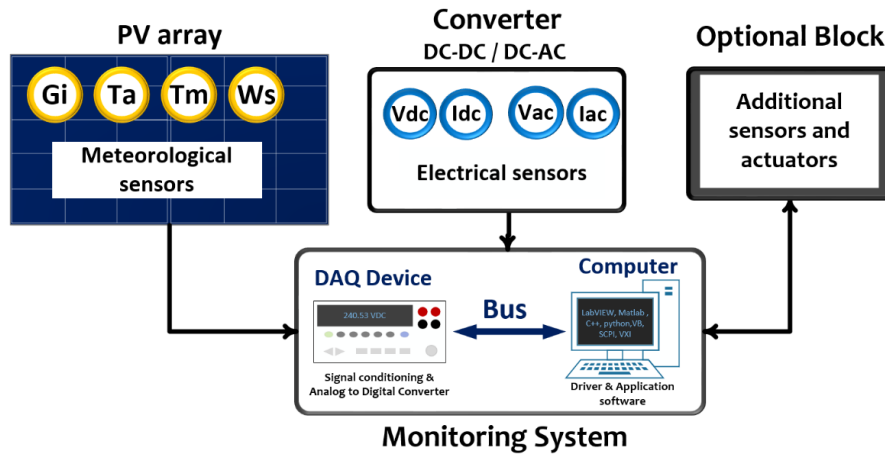
Figure 1.17 Synoptic scheme of the external PV monitoring using DAQ and software.

Solar irradiance, temperature, voltage and current is the important parameters to monitor PV systems. Then, it depends on whether the PV system is grid connected or not. Selecting the ideal data acquisition depends on the application. Typical factors include sample rates, channel scalability, signal conditioning, sensor types, analysis capability, mobility, and environmental conditions [60]. Table 1.2 describe different types of data acquisition and control instrument. Figure 1.18 illustrates some type of DAQ device (a) Arduino DUE,(b) PC-based DAQ Keithley 6510 and (c) Real-time DAQ (NI- CompactRIO).

Table 1.2 Type of data acquisition and control instruments.

DAQ Type	Description
Microcontroller kit	Can acquire voltage signal from 0-5V, the signal from sensors, must be conditioned before being measured.
PC-based	provide electrical and physical measurement capabilities for engineers who need a customizable, accurate, yet cost-effective way of conducting benchtop measurements.
Embedded Real-Time	provide real-time processing capabilities and sensor-specific conditioned I/O, which is ideal for stand-alone data logging, industrial monitoring, and control applications.
High Speed	combine the advantages of an oscilloscope with a DAQ system. can measure signal from kS and MS with triggers, signal conditioning, and simultaneous sampling,
Portable	fully integrated, data acquisition and display stations with secure, built-in data storage and network connectivity.
Wireless	allows to collect data from entire site without the high cost of wiring points to remote or unpowered locations.

(a) Open devlopement kit based Microcontroller (Arduino DUE) (b) PC-based DAQ (Keithley 6510) (c) Real-time DAQ (NI - CompactRIO)

Figure 1.18 some type of DAQ instrument

Various sampling intervals were proposed from seconds up to one hour. Nevertheless, basing on the IEC 61724 standard, this interval should be selected based on parameter types. For example, for parameters that depend on irradiance, sampling period should be 1 min or less, and for parameters with high time sample, it should be between 1 and 5 min. The DAQ instrument can control actuators based on decisions using 0-5V digital signals or 0-12V relay board.

Offred Software by DAQ manufacturers allow to acquire, report, and analyze data from data acquisition and controller with a range of easy to use and cost-effective software tools. Turnkey software offered by DAQ manufacturers are limited by an executable interface with fixed and non-modifiable functionality. For a test bench, several instruments of different brands are used.

So, it is highly recommended to use a single data acquisition and control environment. For programming microcontroller, C language is commonly used, LABVIEW software is usually used as data acquisition and system design and it provides comprehensive measurement and control tools. For calculation and analysis, generally MATLAB is the most popular choice. Data analysis is a powerful tool for understanding PV system performance, but it is fundamentally limited by the quality of sensors and models being used, in addition to the condition of the array.

1.2.3 Parameters description for analytical monitoring.

Usually, the performance of a PV module is measured at the factory under Standard Test Conditions (STC), according to IEC 60904. However, the indoor measurement of the STC PV performance reveals the power production of the module at only one particular measurement condition. The labeled STC performance values do not automatically reveal the real PV power production at the site-specific meteorological and environmental conditions (e.g., lower irradiance, high temperatures, dust and snow…etc.), in these conditions the module label values might overestimate the PV power production at this location. To avoid unpleasant surprises, the measurement of meteorological and electrical parameters makes it possible to evaluate the performance of the installation under outdoor conditions in a specific location.

Furthermore, the data acquisition of essential parameters is the key for predicting the prospective energy yields and the operation and maintenance costs incurred by environmental conditions that might impair the operation of large-scale solar power plant.

International standards set the parameters for PV systems measurements and monitoring. The IEC 61724 presents guidelines for analysis and monitoring PV systems performances [82]. Figure 1.19 illustrates major elements comprising different PV system types, especially for grid-connected systems without local loads, energy storage, or auxiliary sources, as shown by the bold lines, and presents an example for IEC standard application on PV system and illustrates the electrical and environmental data to measure [9].
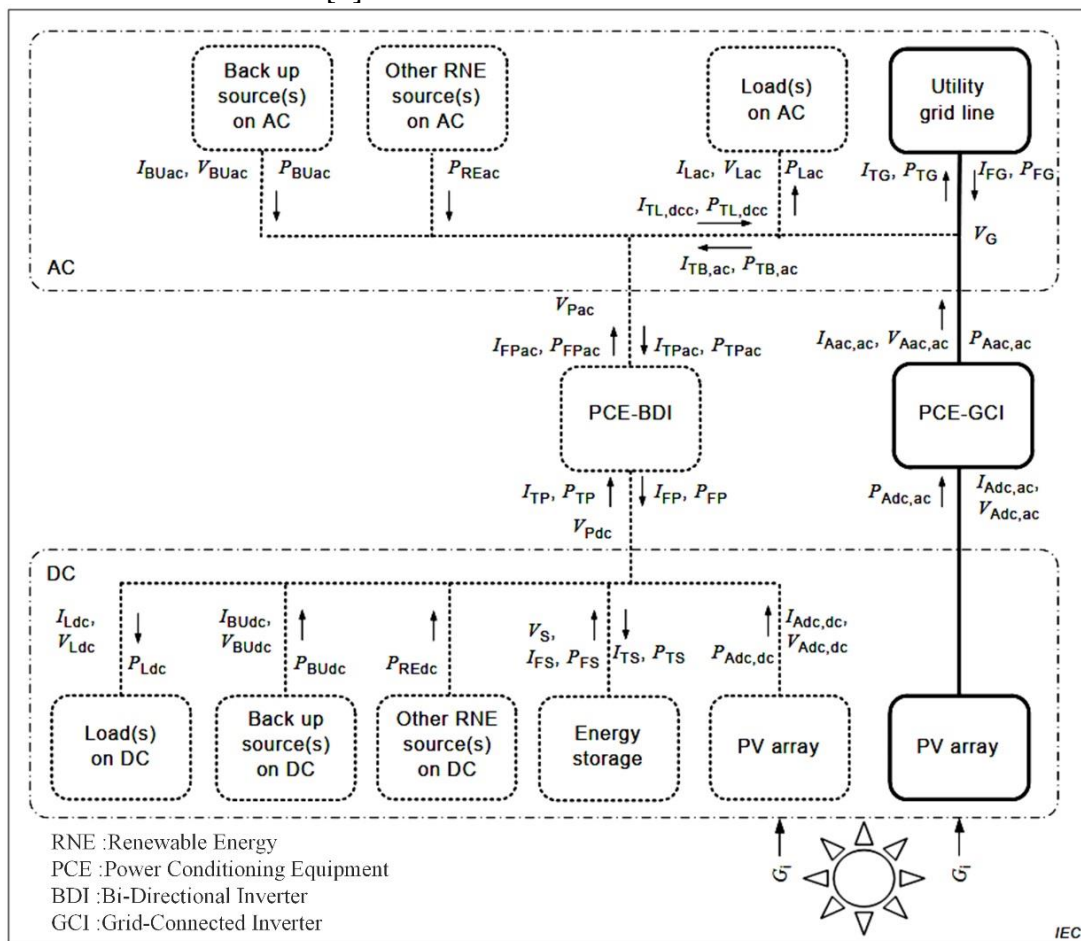
Figure 1.19 Possible elements of PV systems. (source: IEC 61724 standard)

Table 1.3 illustrates the principal parameters to measure according to IEC 61724 standard for Performance Monitoring of both grid-connected and stand-alone PV system.

Table 1.3 Principal parameter according to IEC 61724 standard for PV System Performance Monitoring

Meteorology – Total irradiance, in the plane of the array – Ambient air temperature – Wind speed	Photovoltaic array – Output voltage – Output current – Output power – Module temperature – Mounting / tracker
characteristics Load – Load voltage – Load current – Load power	Energy storage – Operating voltage – Current to/from storage – Power to/from storage
Utility grid – Utility voltage – Each phase - Current to/from utility grid – Power to/from utility grid	Back-up sources – Output voltage – Output current – Output power

As monitoring budgets increase, measurement data sources can be expanded allowing for additional analysis options and backups. Table 1.4 gives recommended parameters to measure in the PV system depending on the selected monitoring class.

Table 1.4 Recommended Measured Parameters in PV system.

Category	Parameter	Symbol	Units	Required parameters for		
				Class A	Class B	Class C
Irradiance	In-plane irradiance	G_i	W/m^2	●	●	●
	In-plane direct beam irradiance	$G_{i,b}$		For concentrator systems		
	In-plane diffuse irradiance	$G_{i,d}$		For concentrator systems		
	Global horizontal irradiance	G_G		●	○	
	Diffuse horizontal irradiance	G_d		●		
Environmental Factors	Ambient air temperature	T_{amb}	°C	●	●	●
	PV module temperature	T_{mod}		●	●	
	Soiling ratio	SR		●		
	Wind speed	WS	m/s	●	●	
	Wind direction	WD	degrees	●		
Tracker system	Tracker tilt angle	φ_T	Degrees	●		
	Tracker azimuth angle	φ_A		●		
PV array output	voltage (DC)	V_A	V	●		
	current (DC)	I_A	A	●		
	power (DC)	P_A	kW	●	●	
Inverter output	voltage (AC)	V_{inv}	V	●		
	current (AC)	I_{inv}	A	●		
	power (AC)	P_{inv}	kVA	●	●	●
	power factor	λ_{inv}		●		
System output	Output voltage (AC)	V_{out}	V	●		
	Output current (AC)	I_{out}	A	●		
	Output power (AC)	P_{out}	kVAr	●	●	●
	System power factor			●		

However, sensor manufacturers are constantly improving their products and designing innovative sensors to keep pace with new standards with better reliability and performance.

1.2.4 Environmental measurement

1.2.4.1 Irradiance measurement

Good quality, reliable radiation data is extremely important for all activities in the solar energy sector. Photovoltaic (PV) and concentrating solar power (CSP) thermal systems may have slightly differing requirements, but they need accurate solar radiation information for the same reasons.

For outdoor PV performance measurements, a reference cell and pyranometer can be used to measure the POA irradiance [83] .

Pyranometers

Pyranometers are always used if as accurate as possible global radiation measurement data are required. For this purpose, various classes of accuracy are defined in the ISO Standard 9060 (see Table 1.5). A pyranometer costs between 600€ and 2000€, depending on the class. In the market there are two types of pyranometers: thermopile pyranometers and silicon cell pyranometers. thermopile pyranometers are more accurate where manufacturers offer models for all three classes, however for silicon cell pyranometer it is offered only for class C with a low cost [19].

Table 1.5 pyranometers classes according to ISO 9060 [19].

Property	Secondary standard (A)	First class (B)	Second class (C)
Quality	Excellent	Good	Fair
Cost	High	Medium	low
Accuracy (daily sum) (%)	±2	±5	±10
Resolution (W m-2)	±1	±5	±10
Long-term stability (%)	±0.8	±1.5	±3
Response time (s)	<15	<30	<60

Thermopile Pyranometer

For thermopile pyranometers (Figure 1.20), a thermopile is used within the instrument as the sensor, and the thermal gradients are measured across hot and cold areas (black and white). The radiation intensity is proportional to the temperature differences between the two sensing areas. Accuracy depends upon the sensitivity of the material used in the sensors, the response time, and the distortion characteristics of the material constituting the dome covering the sensors.

The voltage signal output by the thermopile is very small, typically around 10 *mV* with full Sun irradiance (1000 W/m^2).

In plane irradiance, recorded at the same plane as the PV array, which is measured using pyranometers or calibrated reference device. Horizontal irradiance data may be measured, in order to compare with standard meteorological information from other locations. If reference cells or modules are used, they should be calibrated and maintained following IEC 60904-2 or IEC 60904-6 standard. According to IEC 61724-1:2017 standard for PV monitoring systems [82], The class is not only determined by the hardware that is used, but also by quality checks and measurement procedures. The standard contains detailed specifications at monitoring system component level.

IEC 61724-1:2017 standard specifies for each class of monitoring system the pyranometer class that must be used, including required instrument heating, azimuth and tilt angle accuracy. It also defines cleaning and calibration intervals for pyranometers. The standard also defines requirements for measurement of module- and air temperature, wind speed and direction, soiling ratio, and (AC and DC) current and voltage. In the report IEA-PVPS T13-03:2014 "Analytical Monitoring of Grid-connected Photovoltaic Systems" an interval of 1 to 2 weeks is recommended for pyranometers cleaning. A recalibration is recommended at least every 3 years.

Silicon-cell Pyranometer

Silicon-cell pyranometer (Figure 1.21) is compact and cost-effective designed for routine measurement of solar radiation, it is especially designed for photovoltaic system monitoring. It can be used under all weather conditions. For silicon photocell pyranometers, electric current is generated by a photo-sensitive diode in proportion to solar intensity. Ordinarily, silicon photocell pyranometers are not fully sensitive to the full spectrum of visible light, and they cannot "see" a certain portion of the electromagnetic spectrum such as under cloudy conditions or vegetative canopies. The class of most of Si- pyranometers is C. however, In full sunlight conditions they are calibrated to properly output solar radiation measurements [84].

| Figure 1.20 Thermopile Pyranometer SR20 (Class A). (Source : Hukseflux) | Figure 1.21 Silicon-cell Pyranometer rt1 (Class C). (source: kipp & zonen) |

PV Reference cells

Measuring the radiation from PV reference cells sensors is an economical alternative. For a price range between 100€ and 500€, with accuracy from ±5% to ±10%. Especially designed for the monitoring of PV systems. To measure the irradiance, the solar cell is short-circuited with a low-ohmed shunt resistor, and the voltage drop at the shunt is measured. As the short-circuit current of a solar cell is proportional to the irradiance, a simple arrangement is possible. The temperature dependency of ISC can be compensated for by building in a temperature sensor together with a downstream temperature-dependent voltage amplifier. Therefore, solar cell sensors are mainly used for continuous monitoring of a PV system. For this, they are mounted on the module plane so that they receive the exact radiation available for the PV installation. indeed, it is highly recommended that the reference cell be of the same technology (E.g., c-Si, a-Si, CdTe ... etc.) as the modules installed. In this case, the limited spectral sensitivity of the sensors is an advantage as they correspond exactly to that of the monitored modules [19]. Figure 1.22 illustrates some commercial PV reference cells for PV installation and research application.
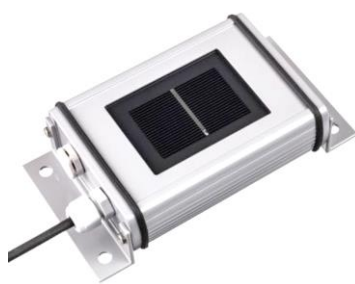
PV Reference Cell with cell temperature measurement from IMT solar   Bifacial Reference Cell (rear face) from ReRa Systems   Very accurate Outdoor Reference Cells for calibration from Fraunhofer ISE
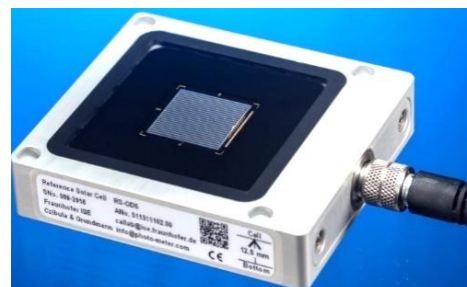
Figure 1.22 PV Reference cell sensors.

Table 1.6 summarizes the advantages and disadvantages of both types of sensors. In [85], [86] a comparison between Pyranometers and PV reference cells for outdoor PV system performance monitoring are reported.

Table 1.6 Comparison of pyranometers and PV reference cell sensors [19].

Pyranometer	PV reference cell
- Expensive	+ Economical
+ High accuracy	- Low accuracy
+ Sensitivity independent of λ	- Strong spectral dependency
- Sluggish	+ Small response time (<1 s)
+ Hardly direction dependent	- Strong directional dependency
	+ Behaves as a solar module
Use: Measurement of global radiation for comparing various sites	Use: Measurement of radiation in module level for plant monitoring

Measuring direct and diffuse radiation: For an accurate yield estimate, the separation of the global radiation into direct and diffuse radiation is necessary. The direct radiation, is measured using a pyrheliometer, it must continuously track the Sun (Figure 1.23).

In the case of diffuse radiation, one uses a normal pyranometer in which the direct radiation is carried out by a tracker shade ball (Figure 1.24).

A solar monitoring station includes a set of instruments to measure the different components of solar radiation that are of importance to solar energy production; global horizontal irradiance (GHI), direct normal irradiance (DNI) and diffuse horizontal irradiance (DHI) (Figure 1.25).

Albedo measurement: Bifacial PV modules generate power using both the global solar radiation and the reflected solar radiation. The measurement of albedo, or ground surface reflectance, is performed using an albedometer kit that measures both global and reflected solar radiation. As illustrated in Figure 1.26 the Albedometer is composed of two pyranometers, both installed horizontally, the downfacing one measuring reflected solar radiation.

Figure 1.23 Pyrheliometer measurement comparison 2018. (Source: NREL)

Figure 1.24 Sensor for measuring diffuse radiation.

(a)   (b)
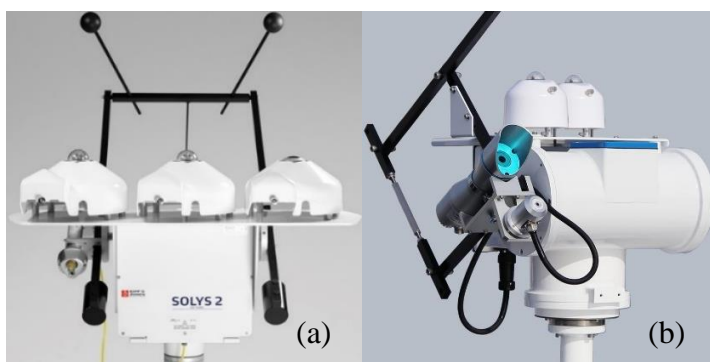
Figure 1.25 Solar monitoring station (a) Kipp & Zonen SOLYS2 Sun Tracker and (b) EKO STR-21G-S2.

Figure 1.26 Albedometer Kipp & Zonen CMP11.

Satellite-based irradiance measurement

Services are available that take data from satellites and process them with models to create an estimate of ground-level irradiance at a site. Although less accurate than a well maintained and calibrated on-site pyranometer, satellite measurements can be more accurate than an on-site pyranometer that is dirty, out of calibration, or installed incorrectly.

1.2.4.2 Temperature measurement

Electrical temperature measurement is used in a wide variety of industries. From melting steel to baking cookies, the environment, required measurement resolution and accuracy, and temperature ranges can vary greatly and the type of sensor used to measure these temperatures must be chosen accordingly. This application note discusses the fundamentals of selecting and interfacing to temperature sensors [87].

In a PV system the ambient air temperature and back-of-module temperature measurements are taken outdoors. For this, different types of temperature sensors are used, the most used sensors are 1) Thermistors 2) Resistance Temperature Detectors (RTD) and 3) Thermocouples. Note that the semiconductor-based temperature sensor is usually incorporated into integrated circuits (ICs). Thermistors are the best option for measurements below 150°C and for more information you can see [88].

Ambient air temperature

The ambient temperature sensor should be mounted in a location representing the conditions of the PV array. Ambient temperature sensors are mounted in the solar radiation protection shield, the uncertainty, including instrumentation, should be less than 1°C. Figure 1.27 shows the ambient temperature Pt 1000 probe and the radiation shield. Generally, in the weather station the radiation shield is offered with air temperature and relative humidity sensors inside.

(a) Ambient Temperature Sensor with Analog Output (10 V / 20 mA / Pt1000)

(b) Weather and Radiation Protection Shield for Ambient Temperature Sensors
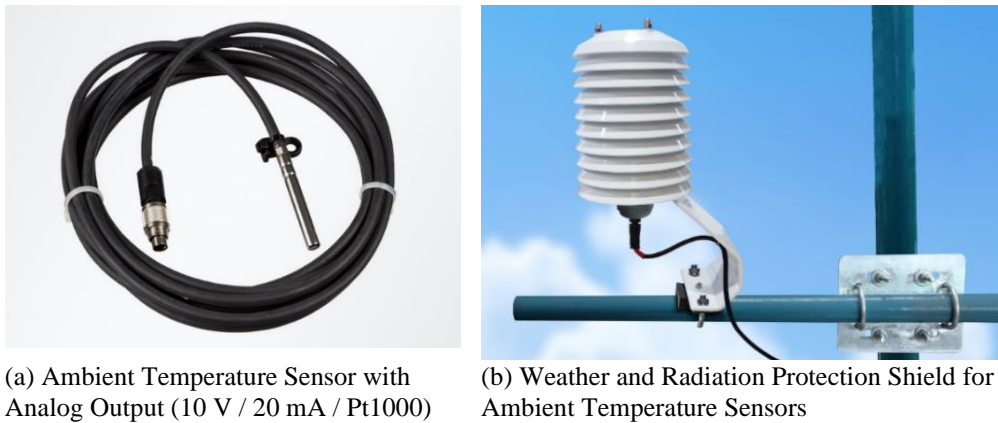
Figure 1.27 Ambient temperature probe with radiation shield.

Module Temperature measurement

In general, the module temperature does not exceed 70°C, so a 100°C sensor does the trick. The most used sensors for measuring the temperature of PV modules are RTD and thermistors, thanks to their higher accuracy. it is strongly recommended to use Class A sensors (±0.2°C) especially in large-scale installations and research applications, in order to have an uncertainty including instrumentation less than 1°C [82].

The surface shape of the sensors used must be flat so that it is well attached to the back sheet of the module. The location of sensor on module are given in IEC 61829 method A (center of back surface of module in center of PV array). the difference of temperature between operating modules is between 2°C to 5°C, so it is better to measure the temperature of several modules in PV array.

To determine the temperature of the PV cell/module without temperature sensor, the equivalent cell/module temperature can be obtained by measuring of V_{OC} using potential divider sensor at a level of accuracy below than 0.5% according to IEC60904-5.

Figure 1.28 shows a Pt 100 surface temperature sensor with analog output, specially proposed to measure the temperature of PV modules. Figure 1.29 illustrates the mounting of Pt 1000 surface temperature sensor (Apogee CS240) in the back sheet of PV module using Kapton tape.

Figure 1.28 Surface PV Module Temperature Sensor
with box connection from IMT Solar company.
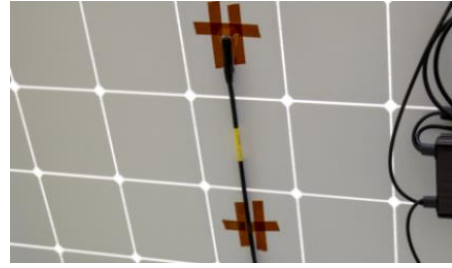
Figure 1.29 Pt 1000 sensor (Apogee CS240)
mounted in back of a PV module.

1.2.4.3 Wind sensors

In a PV system, it is recommended to measure the wind speed, because its influence on the cooling of the temperature of the PV modules during production, which slightly increases the efficiency, while measuring the wind direction is not really important. Wind speed should be measured at height (10 meter) and at the same array conditions. [82]. Wind speed sensors accuracy should be higher than 0,5 m/s for values measured for less than 5 m/s. And should be higher than 10% of reading for wind speed values greater than 5 m/s. Two main types of wind sensors exist on the market, the traditional models based on the mechanical rotation of the miniaervane (Figure 1.30 a-b), and recent models based on ultrasonic probes (Figure 1.30-c).

Wind speed sensor anemo   (a)   Wind speed and direct   (b)   wind speed and direction Ultrasonic   (c)
from MB-Control   from YOUNG   sensor from Campbell Scientific
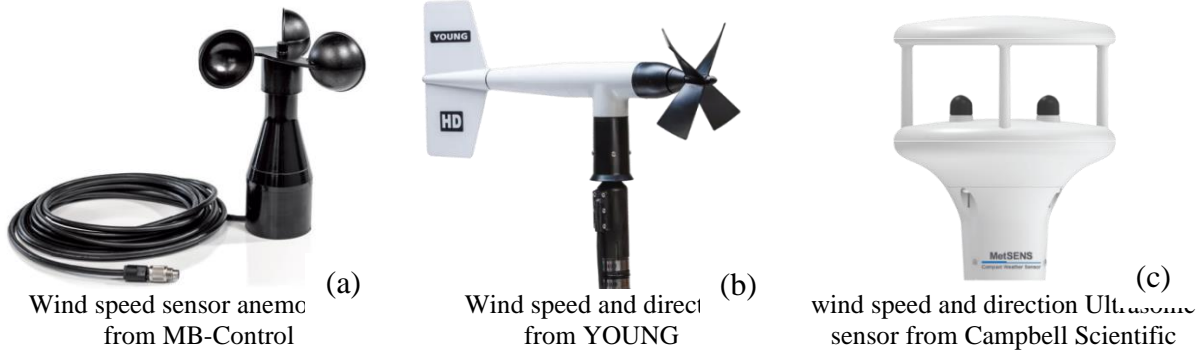
Figure 1.30 Wind speed & direction sensors.

1.2.4.4 Dust and snow sensors

Monitoring of the light transmission loss caused by dust on PV modules using sensor provides the information for solar energy plant management systems which helps to plan exactly when and where to perform the cleaning. This solution is maintenance-free, water-free, easy to install. The alarms can be set in system software to indicate when a certain soiling ratio has been reached and cleaning is needed [89] [90]. the use of soiling sensors allows to determine and monitor soiling rates for performance analysis in order to optimize washing schedules for best return-on-investment. Figures 1.31 display a commercial soiling sensors (a) DustIQ Soiling monitoring system Offred by Kipp & Zonen and (b) Mars optical soiling sensor From Atonometrics.

(a) DustIQ Soiling Monitoring System   (b) Mars Optical Soiling Sensor
from Kipp & Zonen   From Atonometrics

Figure 1.31 Commercial Soiling Sensors.

1.2.4.5 Weather monitoring station.

Solar resource assessment refers to the analysis of a prospective solar energy production site with the end goal being an accurate estimate of that facility's annual energy production.

Weather Monitoring Stations (WMS) is a modular platform that contain multiple high end pyranometers and weather sensors combined as a turnkey solution for PV monitoring applications. Standard measurement parameters (POA Irradiance, Horizontal Irradiance, PV back-panel temperature, Relative humidity, Barometric pressure, Ambient temperature, Wind speed and direction, Rain Gauge). This station is compact and simple to install and to connect to any inverter or SCADA system using RS-485 Modbus interface or other interfaces. However, The WMS offers a complete set of instruments for the rooftop and utility-scale photovoltaic project developer. However, Apogee instruments company offers a selection of accurate sensors specially dedicated for the monitoring of a PV system [91]. In [92] "NRG Systems provider" groups comprehensive line of different environmental sensors from different manufactures for resource assessment and site monitoring station.

Besides, other sensor manufacturers provide a turnkey weather monitoring station with hardware and software DAQ designed specifically to measure critical environmental parameters of the PV plant to better analyze performance (e.g., 1) Kipp & Zonen RT1 Smart Rooftop Monitoring System [93], [94] 3) EKO PVmet stations [95]). For utility scale PV system and research test system, an advanced performance analysis is very recommended, this analysis requires the use of Class A sensors and instrument as well as the measure of additional parameters such as dust accumulation, albedo and other (e.g., SunScout Class A Solar Resource Assessment System [96] and SOLAR1000 Solar Monitoring Station [97] proposed by Campbell Scientific company). Figure 1.32 displays some commercial weather monitoring stations.

| METSENS600 6 parameters from Campbell Scientific | Weather station for PV system from SMA | SOLAR1000 up to 18 parameters for utility scale PV from Campbell Scientific |
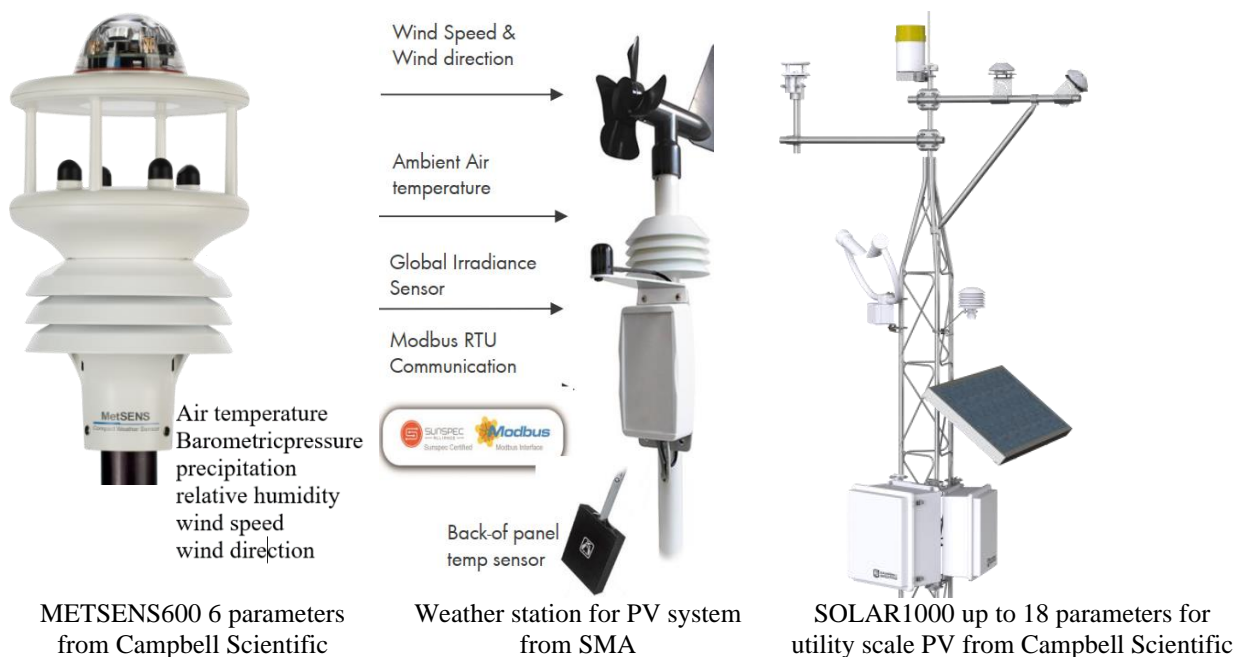
Figure 1.32 Commercial Weather monitoring stations.

1.2.5 Electrical measurement

1.2.5.1 Voltage and current measurement:

Voltage and current values may be measured either on DC side (i.e., PV module, string or PV array, DC/DC controller and battery bank) or AC side (i.e., AC module, inverter, transformers, loads). Voltage and current sensors accuracy, including signal conditioning, should be higher than 1% of the reading [82]. The voltage and current can be measured by sensors or transducers [98]. In [99] authors present an overview of different principle techniques to measures current and voltage signals.

In [100] LEM company offers a variety of voltage and current transducers technologies (e.g., Hall Effect, Fluxgate and Air-Core and other technology), each technology was presented with main feature and principle of measure. Fluxgate technologies offer a higher accuracy, high performance with a larger bandwidth, while closed-loop (C/L) Hall Effect and air-core are cost-effective and versatile solutions for measuring voltage and current.

Voltage sensors

Depending on the type of configuration and size of the PV system, voltage sensors are used to measure various voltage levels (i.e., low, medium and high) at various points, for reliable and efficient operation. The typical range of voltage measurement in the PV system is 0-1500V in DC side and 0-690V in AC side.

A resistive potential divider based on resistor is typically used for DC voltage measurement. Voltage Transformer (VT) based on electromagnetic induction principle are used to measure the AC voltage, this type of sensors does not require power supply VT present a low-cost solution to measure the AC Voltage (Figure 1.33-a).

Voltage can be measured using current transducer to measure the small current flowing due to the voltage applied to a circuit with a large resistance. This current can be measured by an optimized Hall Effect or fluxgate sensor or an air-core transducer based on digital technology. So. The use of voltage transducers to allow isolated measurement.

The figure 1.33-b display transducer for sensing voltage in single-phase installations. This transducer is applicable on circuits of 120V, 208V, 240V, 277V, and 480V, and provide a fully isolated, 4-20 mA output proportional to rated voltage in both sinusoidal and non-sinusoidal signals, compact, easy-to-install DIN rail mounted enclosure.

Figure 1.33-c shows the famous voltage transducer LV 25-P based on closed loop Hall effect, the range measurement is from 10V to 500V. Figure 1.33-d displays CV 3-2000 transducer for medium voltage measurement with very high accuracy (±0.2%), the voltage output is 10 V for 2000V. These two sensors are designed by LEM company for the electronic measurement of voltages: DC, AC, pulsed, with galvanic separation between the primary circuit and the secondary circuit. Voltage hall effect transducers have excellent accuracy, low thermal drift, low common mode disturbance, good linearity and good immunity to external interferences.

(a) AC voltage transformer 230V-6V   (b) AC voltage rail mounting In 500V out 4-20mA   (c) DC/AC Voltage Hall effect sensors LEM LV-25P   (d) DC/AC Voltage CV 3-2000
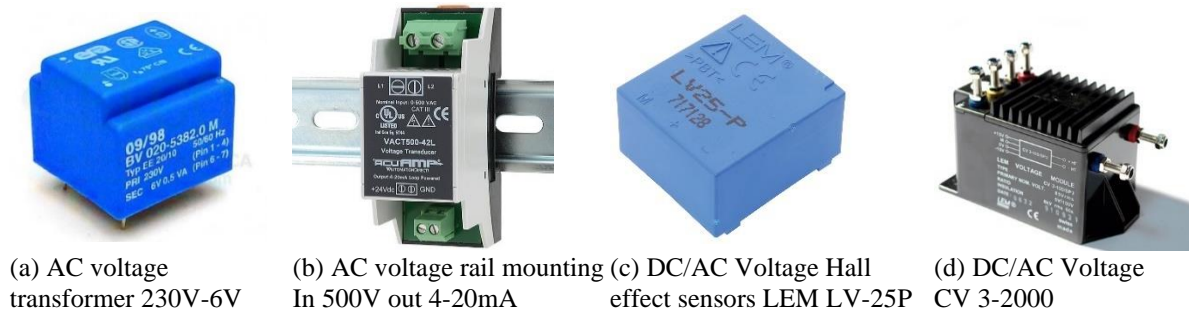
Figure 1.33 Different voltage sensors for DC /AC measurement.

Current sensors

The information of current flow is essential for health monitoring system, in order to improve its stability. Many current measuring techniques are available depending on the type of application and its requirements in terms of precision, cost, size, and bandwidth. So, it is important to understand the working principles and technical limitations of various current measuring techniques. To measure DC current there are two main methods using shunts resistor or current transducers. The price for both methods depends on their accuracy and range, which requires an in-depth study to determine the price for each case. Using shunts resistor (Figure 1.34-a) is quietly simple and does not require an extra power supply unlike current transducers. The AC current can be measured using current transformers (CT), this type of AC sensor produces an output in proportion to the current flowing through the primary winding.

The AC current is also measured using Rogowski Coil current sensor. Figure 1.34-b displays LEM split-core AC Rogowski Coil current sensor, the measuring range is from 10 to 10000 A with a Class accuracy of 0.5 according to IEC 61869. The current transformers and Rogowski Coil do not require a power supply, it's self-powered.

The use of current transducers requires a power supply and can measure both DC and AC current. Current transducers have excellent accuracy, low-temperature drift, good linearity, optimized response time, good immunity to external interference, no insertion loss and current overload loss [70]. Figure 1.34-c displays the LEM LA100P current sensor based on the C/L Hall effect, the measuring range is 0 to ±150 A for DC and AC, and the accuracy is around 0.45%.

Figure 1.34-d shows a LEM LESR sensor based on the C/L Hall effect performing at the level of Fluxgate technology without the added cost, the accuracy is $\pm$ 0.5 %, and the operating temperature is from -40°C to + 105°C, this type of sensor is specially designed to be integrated into electronic cards (e.g., solar inverter, meter, battery management system… etc.). in LESR series four sensor models are proposed with the nominal current ranges 6, 15, 25 and 50A, the price is around $20.

Figure 1.34-e illustrates a split-core current transducer offered by ACUAMP company for DC or AC signals, it is combined Hall effect sensor and signal conditioner with an industrial output of 4 to 20 mA or ±10 V, this type of sensor is reliable but expensive, approximately $200.

| (a) Shunt DC sensor from Victron | (b) split-core Rogowski Coil AC sensor | (c) DC/AC C/L Hall effect sensor | (d) DC/AC C/L hall effect Fluxgate level | (e) DC/AC Hall effect split core sensor |
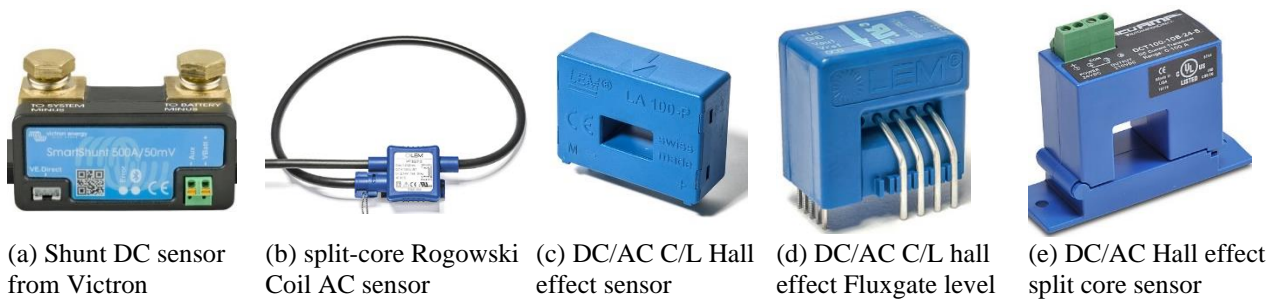
Figure 1.34 some commercial current sensors for DC /AC measurement.

1.2.5.2 Power measurement

Power data can be on DC or AC side or both sides. It can be measured directly using power sensors or calculated in real-time as sampled voltage and current values [82] [98].

The power meters on the AC side take into consideration the power factor and harmonic distortion. Power meter's accuracy including signal conditioning should be greater than 2% of the reading. Figures 1.35 illustrate some power meters models existing on the market from standard to high accurate power analyzers. For more information and feature check the manufacturer's datasheet. The high-performance benchtop power analyzer is used in the test and certification labs of PV inverters and other accurate application measurements thanks to their precision and high speed in measurement.

| (a) Low-cost standard power meter (Schneider PM3200) | (b) smart meter For PV system (Fronius) | (c) Power Quality Meters (Siemens 9810) | (d) High-Performance benchtop Power Analyzer (Yokogawa WT1800E) |

Figure 1.35 Some power meters devices exist on the market from standard to high performance.

1.2.6 On-site measurement techniques for PV array

Because of the inherent inaccuracies of data monitoring alone, it is common to implement a secondary check of the DC array to detect string- and module-level faults through periodic inspection and testing [19]. Uncertainties such as weather variability, soiling or shading, the causes can also lie in wiring issues in the PV array or underperforming PV modules.

In addition to real-time monitoring, an on-site performance assessment may be required to identify and correct potential problems. Such measures contribute to a good understanding of the operating conditions and enable more accurate production forecasts. On-site measurements are used for 1) fault detection of PV arrays and 2) identifying degraded or defective PV modules. Various on-site inspection techniques based on portable test equipment are used, ranging from PV output power characterization to imaging techniques for localizing cell cracks or open-circuit failures, to spectroscopic methods for materials analysis. Two groups of methods can be differentiated: a) inspection methods for PV strings and b) inspection methods for single PV modules.

In [101], ten on-site inspection methods were reported :
1. Drone-mounted electroluminescence & thermal infrared imaging of PV arrays
2. Daylight I-V measurement of PV strings and PV modules
3. PV module characterization with mobile PV test centers
4. Dark I-V measurement of PV strings and PV modules
5. PV plant testing vehicle for PV strings
6. Electrical impedance spectroscopy of PV strings
7. Daylight electroluminescence imaging
8. Ultraviolet fluorescence imaging
9. Outdoor photoluminescence imaging of field-deployed PV modules
10. Spectroscopic methods for polymeric materials.

Figure 1.36-a illustrates an I-V curve tracer (PVA-1500T PV Analyzer from Solmetric) for PV modules, strings and arrays, up to 1500Vdc and 30Adc. Figure 1.36-b displays an unmanned aerial vehicle (drone) that carries a thermal camera, this drone can also carry an electroluminescence camera, in order to make an inspection on the PV arrays as soon as possible. Figure 1.36-c shows a mobile quality inspection for PV module (Mobile PV-Testcenter), which 1) takes power measurements of PV modules according to EN60891, 2) conducts electroluminescence inspections to highlight possible problems - cracks on the module cells, and 3) uses thermal imaging of the modules to identify hotspots.

- Power measurement
- Electroluminescence
- Thermal imaging

| (a) IV-curve tracer for PV modules / strings / arrays, up to 1500V / 30A PV Analyzer Solmetric | (b) Drone-mounted electroluminescence & thermal infrared imaging of PV arrays | (c) Mobile quality inspection in PV plant |

Figure 1.36 Some PV on-site inspection & performance assessment methods.

Figure 1.37 represents the methodology for quality control in a PV plant with a mobile PV testing Lab. The process of quality control initiates with identifying the modules to be tested. Identification of the least-performing PV string is done with the help of real-time monitoring

system. Depending on the performance of the string least and medium performing strings are selected for testing.

Visual Inspection of 10% modules from each plant has been performed. Furthermore, 20 sample modules from each type were selected from these inspected modules and were gone through Flash Testing. IR image of the PV module and string is taken to check the hotspot, faulty string, bypass diode failure affected module. After IR thermography inspection, the sample PV modules are tested in STC using on-site PV mobile. The I-V measurements are taken in Sun Simulator and compared with reference Module characteristics to evaluate the degradation of the PV module. EL image of the module is taken in the mobile lab which is used to detect defects in PV cells. A correlation between the results of the I-V curve, IR image, EL & visual inspection of the PV module is obtained in order to identify the problems in field and proof to claim replacement of the modules if warranty conditions are not satisfied [102].
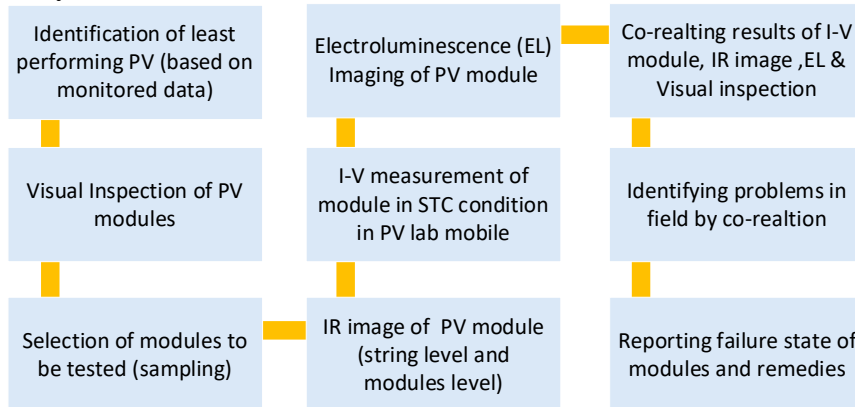
Figure 1.37 Methodology for Quality control in PV plant with mobile PV testing Lab [102].

1.3 Modeling and performance in PV systems.

1.3.1 Introduction

PV performance models are used to predict or estimate the output power of a PV system, which typically includes PV modules, DC/DC converter, DC/AC converter, and other Balance of System (BOS) components.

The energy output of PV models depends on the geographic location of the PV installation, in order to determine the amount of solar irradiance received on the Plane of Array (POA). The weather data for a given location will vary depending on latitude, season and climate change; being able to accurately determine the production profile due to these changing variables allows a better match of the system load with the expected production [103].

Some models make general assumptions about system components and ratings. While other more complex models take into account the manufacturer's parameters given in the datasheet, the physical parameters (i.e., electrical, thermal and optical) [104] and the empirically derived data.

In this section, we cannot describe all the PV performance models, but we will just give some references. In the literature, many authors carried out studies dealing with the behavioral modelization of the PV system [45], [105]–[111].

[45] report the various PV performance models and software developed and utilized by researchers at Sandia National Laboratories (SNL), in addition to PV performance models, hybrid system and battery storage models are discussed.

In the PV modeling field, two main techniques are used to predict solar PV power, namely, techniques based on parametric models and nonparametric models [112], [113].

The parametric model designs the PV system as a white box where each subsystem can be modeled using a set of parameters. This method requires detailed information about the characteristics and the behavior of each relevant component of the PV system.

The non-parametric or data-driven models design the PV system like a black box. These models are based on statistical and machine learning techniques [114]–[118], they do not assume any knowledge of the internal characteristics and processes of the PV system.

47

Indeed, these models estimate the behavior of the PV system from a historical time series of inputs and outputs. the accuracy of a nonparametric model depends mainly on the quality of the data. Both PV modeling techniques may share the same inputs (irradiation, ambient temperature, wind speed etc.) and the same output (AC power generated by the PV system). [119] proposes an analytical model to investigate the effects of solar irradiance, cell temperature and wind speed on the performance of a PV system.

Using parametric and non-parametric PV models, we distinguish three main applications:

1) **Design and sizing**: This step is carried out before the installation of the PV system, according to the desired power consumption demands**,** the sizing and design tools help to size your adequate power for each component of the system and to make a techno-economic study [45], [120]. The core of the energy yield estimation process is the PV yield modeling tools. PV yield modelling tools are used by developers and independent consulting engineers during the design phase of the PV project to estimate the expected energy yield of the system. A variety of tools and software programs are available on the website (e.g., PVGIS, SAM, RETScreen, PVsyst and PVSol ...etc.) [121], [122]. The output of any PV modeling software strongly depends on the underlying model algorithms and the chosen input parameters. These parameters include the 1) solar resource and weather related parameters, 2) system design configuration, 3) technical characteristics of the components and 4) several additional inputs that are often based on user estimates or assumptions. Soiling, mismatch, cabling and other field related losses or derating factors are examples of the many user estimates required during the PV energy yield modelling process.

2) **Performance monitoring and fault diagnosis**: The PV models are used to 1) assess performance, 2) detect anomalies, 3) identify faults and 4) send alarms. The PV models provide a baseline against which to compare with real-time measurements of the PV system, from small residential rooftop to large utility-scale systems [123]. In general, these models are incorporated in the power converter unit or in the monitoring software [75], [124].

3) **Forecasting of future energy**: in this application, the models are used to forecast the irradiance, weather data and PV power, to manage and control the flow of production by renewable and fossil sources in the smart grid. Forecast resolutions are available at 5-to-60-minute time frames, extending up to 7 days in advance [116], [125]. This forecast is shared with 1) grid operators, 2) owners of renewable power plants (who are required to notify grid operators in advance of the amount of energy their system will produce) and 3) energy traders. In addition, future peer-to-peer (P2P) PV markets will require PV energy prediction forecasts for efficient energy trading [6]. However, the performance of PV systems depends on static metadata (i.e., tilt, azimuth) and dynamic weather data. [50] shows that, rather than finding annual performance data, a better approach is to obtain PV system metadata (module tilt and azimuth, installed capacity), and use representative, regionally resolved distributions to calculate specific annual performance distributions based on annually varying weather information.

1.3.2 Modeling steps

The parametric modeling approach relies on a set of sub-models to predict AC power injected into the electrical grid [105] (Figure 1.38).
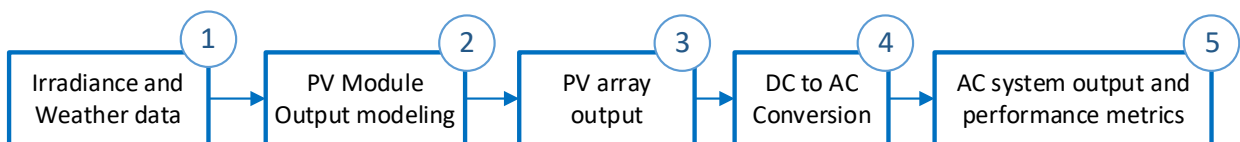
Figure 1.38 Main steps of PV performance modeling.

1) Irradiance and Weather data

Obtaining irradiance and weather data is typically the first step in setting up and running a PV performance model. Historical data is typically used to estimate the output of PV systems, while real-time measurement data is used to model the output expected from an operating system to validate that it is functioning properly.

Historical irradiance and weather data – This step consists in selecting a data source to define the irradiance and the meteorological conditions expected for a chosen site. Typical sources include 1) Typical Meteorological Years (TMY), 2) data derived from satellites, 3) on-site measurements, etc. There are many possible approaches to choosing meteorological data for performance modeling studies.

Incident Irradiance – This step aims to translate horizontal measured irradiance to beam and diffuse components on the plane of the PV array. There are numerous algorithms available to make these translations.

Shading, Soiling, and Reflection Losses – If the PV array is partially shaded or the modules are soiled then the amount of the incident irradiance that is available for conversion to electrical energy is reduced. Various algorithms exist to calculate shading and its effect on the system. Fewer methods exist to predict the amount of soiling on the PV array with time. usually, this step is treated with a constant derate factor. So, effective irradiance is the total plane of array (POA) irradiance adjusted for the angle of incidence losses, soiling, and spectral mismatch.

2) PV Module Output modeling

This part describes the models of the PV module, including methods for measuring and estimating model parameters. The PV module model depends on many electrical and meteorological parameters [50]. In general, all models of the PV module using as input tilted irradiation and cell temperature.

PV modules models: In the literature, several models were developed to reproduce the electrical behavior of PV modules [45]. The PV models make it possible to predict in different weather conditions either: 1) DC voltage and DC current in detail using several parameters (E.g., Sandia PV Array Performance Model (SAPM) [126], one diode model with 5 parameters [127]..etc.) or, 2) directly estimate the DC power using a simple model like (PVWatts by NREL [128]).

Indeed, there are different types of models that have been applied either in the sizing tools or in the monitoring and diagnostic techniques citing, for example, the physical model [129] semi-empirical [126], empirical [130], statistical and machine Learning [114], [118], [131].

The estimation of the model's parameters is strongly required to validate the model and to calibrate it so that it approximates better to the real measurements under the conditions without faults [132]. [133] present a detailed procedures for determining model coefficients using outdoor electrical and meteorological measurements, which contributes to uncertainty in the resulting models. Recently the parameters estimation is carried out using several artificial intelligence techniques to improve the accuracy of the models [115], [134], [135].

Cell/module Temperature – The PV cell/module temperature is influenced by a number of factors, including 1) module materials and construction, 2) mounting and racking configurations, 3) the incident irradiance (modified by shading and soiling), 4) the wind speed, 5) and ambient temperature.

Note that the operating temperature of PV cells / modules is obtained using several measurement techniques [136] or models, generally either:

a. Measured using a temperature sensor (e.g., RTD, thermocouple etc.…) mounted on the back sheet of the module [77].
b. Measured using infrared instruments [136].
c. Obtained from open circuit voltage (V_{OC}) measurements of the module [137].
d. Estimated using behavioral models [138], [139].

3) PV array output

Mismatch Losses

When mismatch is present, either due to inherent performance differences between series modules and parallel strings, heterogeneous irradiance or temperature on the PV array, or even differential wiring losses across the PV array. This fact means that any combined value of current and voltage may not equal the maximum power point (MPP) for all modules in the array.

This step aims to calculate the magnitude of this loss. Few performance modeling applications include this loss explicitly, except by means of a scalar derate factor. Treating this part of the performance modeling problem is especially important in order to accurately represent performance of PV array technologies designed to reduce such mismatch losses

DC to DC Maximum Power Point Tracking

The performance of an PV array is characterized by the system's I-V curve. To harvest power from the system, the voltage must be adjusted in order to maximize the power. This function is called Maximum Power Point Tracking (MPPT).

Most if not all performance modeling applications of the PV system assume that the DC voltage can be held at the MPP at all times. While there are differences between MPPT algorithms that are implemented in inverters and DC/DC converter components. A control system is used to find the MPP, which changes with varying irradiance and cell temperature.

Few of current performance models can distinguish between the effectiveness of different MPPT algorithms or represent performance under non-maximum power-point conditions. As PV systems become more prevalent, utilities will begin to require inverters to operate the arrays off the MPP in order to help support grid operations. Current performance models cannot represent performance under such conditions.

4) DC to AC Conversion

Power Conversion from DC to AC allows injecting the PV power to the AC grid. This step accounts for the conversion efficiency of the inverter. This efficiency can vary with environmental parameters such as temperature and well as electrical conditions, such as DC voltage and DC power level. There are a number of inverter models that are used to estimate this conversion efficiency [140], [141]. As more PV systems are added to the electrical grid, the requirements for interconnection are changing. New PV inverters are needed to offer advanced functions to help support the robust operation. These functions include [142]:

- Volt-VAr (voltage regulation)
- Commanded Power Factor (voltage regulation)
- Frequency-watt (frequency regulation)
- Commanded Maximum Power (frequency regulation)
- L/H Voltage Ride-Through
- L/H Frequency Ride-Through

5) AC system output and performance metrics

AC Losses – Once the power has been converted to AC, it must be transmitted to a point of interconnection. The value of energy produced by the PV system needs to include all losses before the utility meter. Any losses along this transmission path (wire losses, transformer losses, etc.) are accounted. For a residential PV system, these losses can likely be neglected, but for utility-scale plants these losses can be significant and should be included in a performance model. Few existing models represent this process in any detail [143].

System Performance Over Time – Monitoring of PV system output can help to identify anomalies (e.g., degradation, electrical faults in DC and AC side, etc.). There are a number of metrics used to evaluate performance of PV system (e.g., performance ratio, yield metrics, etc.) as defined in IEC 61724 [77] [82].

However , the PVPMC web site gives more than one model for each step modeling and provide PV-lib toolbox for MATLAB and python platforms [105]. In many cases, existing PV performance models neglect one or more of these steps by making an assumption or adding a derating factor. As PV system design options become more and more complicated with new components.

1.3.3 Performance analysis

Continuous monitoring of the PV system is essential during the operational phase, while a good monitoring solution makes it possible to acquire and analyze a number of parameters and to compare them with the simulation results in order to ensure the reliable and stable operation of any PV system and to send alarms in the event of a drop in performance.

The performance of the PV system depends on many parameters, including 1) environmental condition (i.e., effective irradiance on the plane of array, ambient temperature and wind speed), 2) efficient of the PV system components (PV modules, inverters and cables) and 3) O&M services. To include all the parameters affecting on the performance of a PV module in terms of energy generation, the International Electrotechnical Commission (IEC) has designed a standard IEC 61853 divided into four different parts [50]. Several works have been published on the performance analysis of grid connected PV system with different characteristics in different locations using different techniques [111], [144]–[152].

Recently in [153] a performance evaluation of an MW-Size grid-connected PV power plant considering the tilt angle impact using PVsyst was reported , in [154] a detailed performance analysis of a 19 MWp commercial solar PV power plant installed in India with three different configurations of fixed-tilt, adjustable-tilt and horizontal single-axis tracker at a single location, is carried out. A performance assessment of 28 kWp rooftop grid-connected PV system under desertic weather conditions in Adrar has been presented in [155].

The calculation of the expected energy yield is typically provided by a cascade of specific models, each solving a particular question regarding energy conversion. The energy rating allows to compare not only similar products from different manufacturers, but also completely different technologies. It should also provide a realistic estimated energy value for the region of installation and should be simple, accurate, repeatable, and agreed in terms of methodology for its calculation. Figure 1.39 illustrates the energy flow from sunlight to the consumer of electrical power for a typical grid-connected PV system highlighting the different sub-models and the related uncertainties in the different steps. The character of each sub-model and the freedom to select input parameters varies considerably depending on the simulation tool in use and the experience of the user. The performance analysis are based on the evaluation of metrics performance of PV systems defined in standard IEC 61724-1:2021 RLV Photovoltaic system performance - Part 1: Monitoring [77]. In general, the expected energy production or final system yield (Y_f), is reported together with the performance ratio (PR), which quantifies the overall efficiency of energy conversion of the PV system. The PR represents the ratio between the system yield (Y_f) and the solar energy input or reference yield (Y_r), and should be accompanied by an uncertainty [7]. Table 1.7 displays the suggested calculated parameters with symbols and units.
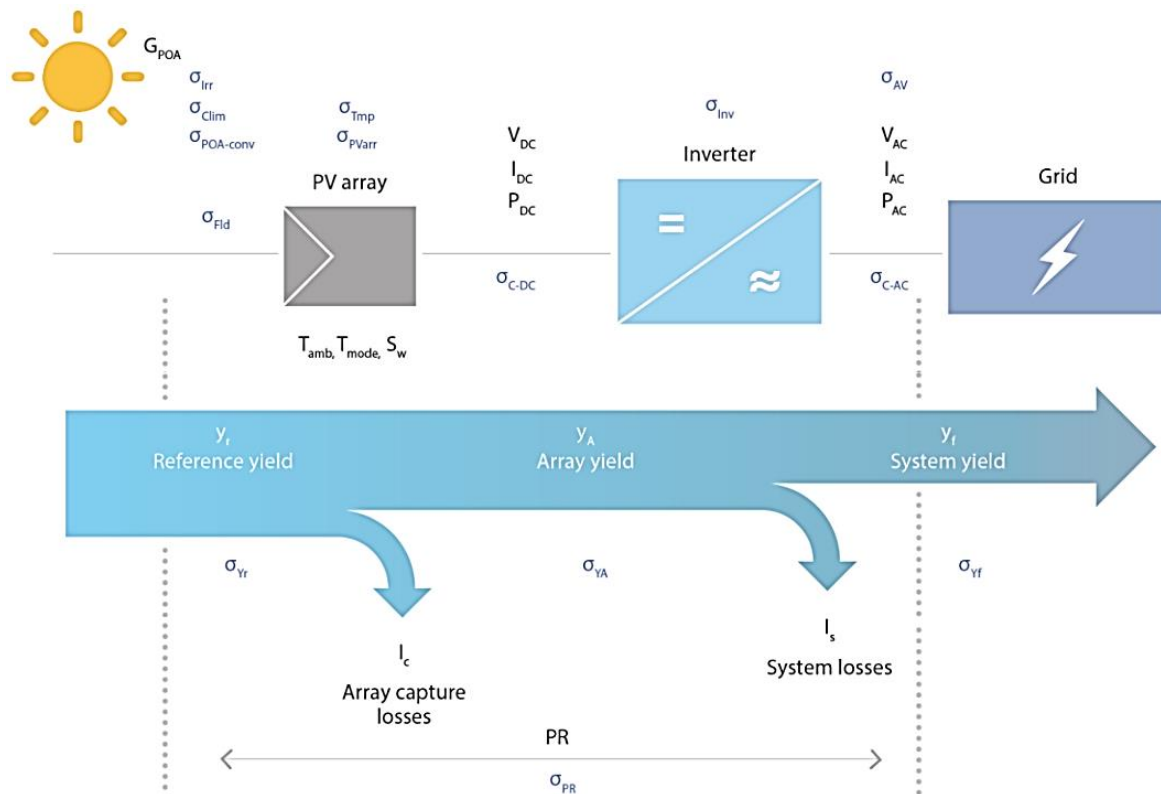
Figure 1.39 Energy flow diagram in a grid-connected photovoltaic system. In black the calculated parameters and in blue the related uncertainties [7].

Table 1.7   Suggested calculated parameters with symbols and units.

Parameter	Symbol	Unit
Irradiation		
In-plane irradiation	G_{POA}	kWh·m–2
Electrical energy		
PV array output energy	E_A	
Inverter output energy	E_{inv}	kWh
Energy output from PV system	E_{out}	
Array power rating		
Array power rating (DC)	P_0	kWp
Yields and yield losses		
PV array energy yield	Y_A	
Final system yield	Y_f	
Reference yield	Y_r	kWh·kWp–1
Array capture loss	L_C	
Balance of system (BOS) loss	L_{BOS}	
Efficiencies		
Array efficiency	η_A	
System efficiency	η_f	None
BOS efficiency	η_{BOS}	

Table 1.8 summarizes various anomalies that affect PV systems with the derating factors and estimated uncertainty, this table contain data values only, with no reference to the source of this information. The numbers and associated uncertainties are most likely chosen by the modelling engineer by 1) considering the energy yield 2) modelling tool used, 3) experience from previous modelling and model validation activity and 4) the availability of information for the specific project in question. It is therefore likely, that some input values may be selected based on 1) general assumptions, 2) modelling experience or 3) traditionally accepted convention. Some loss elements may be lumped together into a single generic loss due to lack of project specific information.

Table 1.8 Technical and system design data.

Loss	Expected loss rate and uncertainty
Soiling	Amount of soiling to be expected is often provided and ranges from 1.0% to 3.0% with most values between 1.0 and 1.5%. The uncertainty of this value is often provided and is given as ±1.0 percentage point with only one exception where a value of ±3.0 % is used.
Shading	Expected amount of shading is provided with typical values of 0.6%, 0.7%, 1.4%, 2.7%, 2.8%, 3.3% and 3.6%. However, most installations expect 0% shading loss. The uncertainty in this estimate is given as ±0.5% in most examples and as ±1.0% and ±2.0% in two specific projects.
Reflection	Expected amount of loss due to reflection from the module surface (also known as Incidence Angle Modifier (IAM) loss) is provided with typical values of 2.8%, 2.9%, 3.0%, 3.2%, 3.6% or alternative with a value of 0.0%. The uncertainty in this estimate is always given as ±0.5% when stated.
Thermal	Yearly loss as compared to operation under Standard Test Conditions (STC i.e., irradiance of 1000 W/m2, air mass (AM) of 1.5 and module temperature of 25 °C) has been calculated as 0.1%, 0.3%, 0.8%, 1%, 1.2%, 4.9%, 5.4%, 11.3% or 14.5 % with uncertainties stated as either ±0.2%, ±0.5% or ±1.0%.
String mismatch	Calculated to values of 0.4%, 0.7%, 0.8 %, 0.9%, 1.0%, 1.10% or 2.1% with uncertainty stated as ±0.5% (except for one example of ±1.0%).
DC/AC cable	Calculated as 0.1%, 0.2%, 0.6%, 0.7%, 0.9 %, 1%, 3.4%, 6.2% or 7.4 %, always with an estimated uncertainty stated as ±0.2%.
Inverter	Calculated as 1.1%, 1.6%, 1.7 %, 1.9%, 2.0 %, 2.2 %, and 3.2%, always with an estimated uncertainty stated as either ±1.0% or ±2.0%.
Transformer	Calculated as 1.0% and 1.3% with one value at 2.0% and always given with an un certainty of ±0.5%.
Grid access	For all systems where the information is provided, the full production is expected to be delivered to the grid with no other loss (Power Factor = 1). The combined overall uncertainty in the calculated energy yield is then provided as ±3.2%, ±4.5%, ±5.1%, ±5.9%, ±6.1%, ±6.8% or ±7.3%.

1.4 Fault detection and identification.

Fault detection is defined as "the indication that something is wrong with the monitored system". In addition to fault detection, fault classification or identification can automatically identify and recognize the type of fault. To further assist maintenance personnel in fault finding, fault location can estimate the exact location of the fault in (module, cable, junction box, etc.) to speed up system recovery in the its safe state after a fault and exploit the maximum performance of the PV plant. So, fault detection, identification, and localization are essential to monitor and identify unexpected anomalies in PV systems [156].

1.4.1 Faults affecting the PV systems

Solar PV systems like all electricity production systems can be subject during exploitation to a miscellaneous faults that affect the components of the PV system such as PV modules, cables, protections or inverters [7]. In recent years, several researchers have focused on the Fault Detection and Diagnosis (FDD) of PV systems; this has allowed to create a large publication database with diverse representations (I.e., texts, tables and diagrams) on the definition and classification of the different faults that falling the electricity production yield and lifetime of the PV systems [157], [158]. However, The faults occurring in the PV system can be classified according to diverse considerations [157], although the classification according to the DC or AC side of the fault occurring in the PV installation is the most used. In the DC side of the PV system, most faults are located in PV array (e.g., temporary and permanent mismatch, short circuit, open circuit, line-line and line-ground faults …etc.), other faults are due to Balance of System (BOS) components (e.g., cable, fuses, switches and DC/DC converter). Whereas, in the AC side, two types of faults can be noted: total blackout and grid abnormalities mainly due to unbalanced voltage and lightning [16]. Figure 1.40 displays common faults with distribution in different sides of a grid-connected or stand-alone PV system. While Figure 1.41 shows the tree classification of the various faults that can occur in a typical PV system. Another detailed faults classification was given in Figure 1-A. A statistical study with power loss evaluation and clustering of faults affecting the installed PV systems in different climate zones in the world, allows to reduce the number of faults in new systems to be installed [159]. A short description for each loss power, anomaly or fault are given

in Table 1 Appendix A. Recently IEA PVPS published a new report about quantification of technical risks in PV power systems [160], They presented PV Failure Sheets (PVFS) which contain photos and severity level of many risks and faults in the operation and installation of modules and inverters (Figure 2- Appendix A).
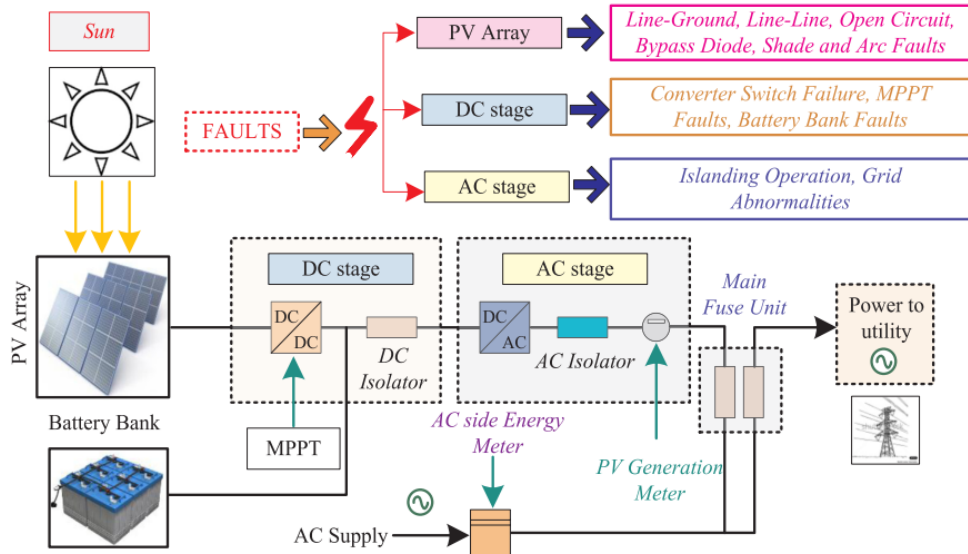
Figure 1.40 Typical PV schematic to show fault occurrences [157].
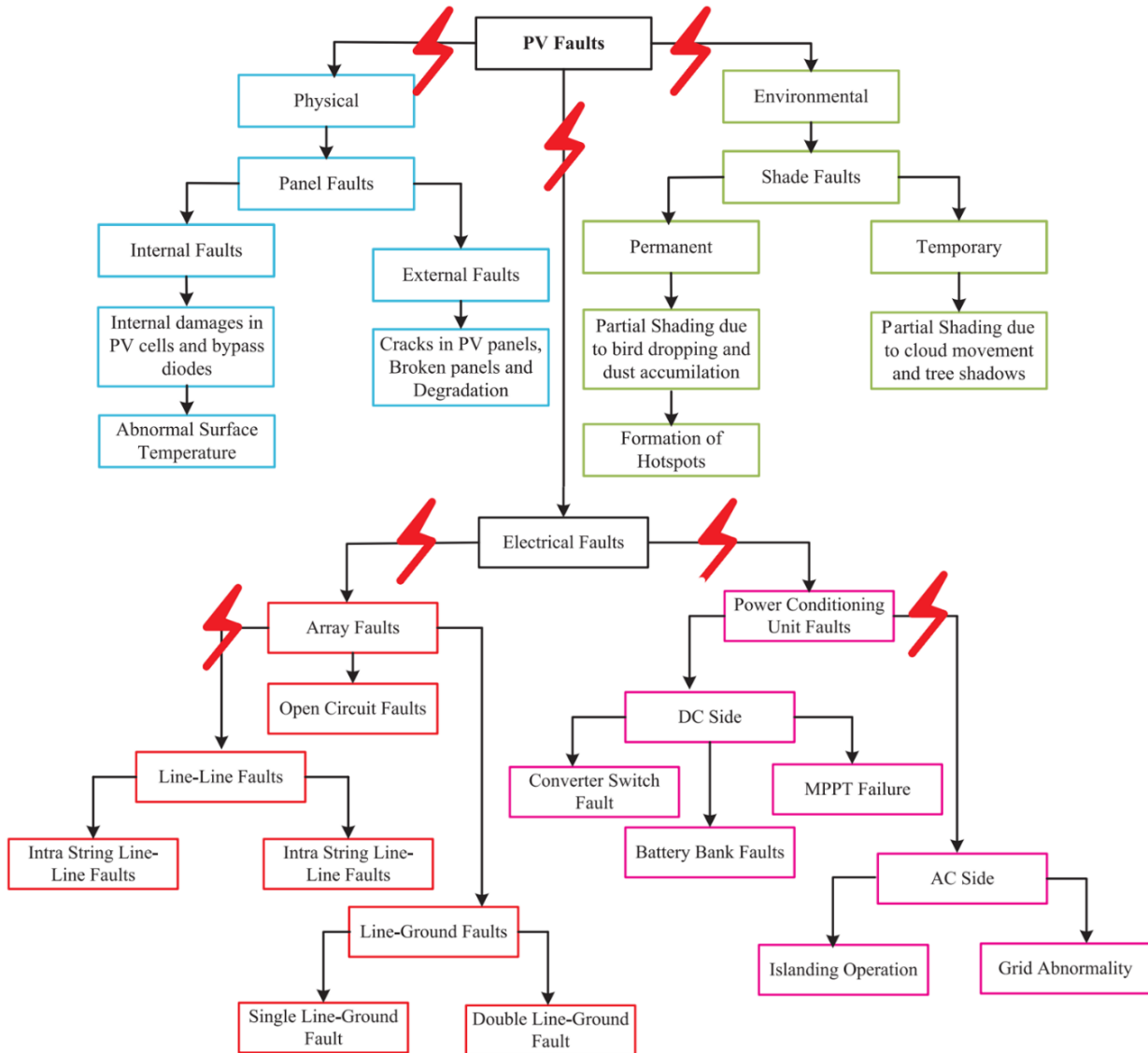
Figure 1.41 Classification of faults in PV Systems [157].

54

1.4.2 Faults Detection Techniques

In order to diagnose the anomalies and failures in the PV system, many FDD techniques have been proposed in recent years, allowing to monitor performances, detect the malfunctions and identify the type of fault present in the DC or AC side of the PV system, [15]–[18], these techniques help to increase the system reliability and lifetime of the PV installations. Recently, IEA PVPS Task 13 [6] has published new report that provides an easy introduction to those in the field who are not trained in new diagnosis techniques and are just starting to learn PV performance monitoring, as well as the report provides a handy reference guide for experts that summarizes in detail Twenty-two (22) research papers studied on the use of advanced algorithms in PV failure monitoring. A variety of fault detection methods are used by different researchers to identify and classify faults, including; 1) Identifying electrical signatures, 2) Comparing historical data to current PV system behavior, 3) Comparing a simulated PV system to actual measured performance and 4) Comparing performance of different components or subsystems. In implementing the methods listed above, a number of approaches are used: 1) Applying statistical tests to infer faults, 2) Applying machine learning algorithms to detect and identify faults, 3) Specification of instructions and rules to be programmed into a fault detection system when data suggests a fault occurrence and 4) Simulating electrical behavior of the PV system using empirical models. Furthermore, in some cases, a combination of two or more methods or approaches are used by a fault diagnosis system.

More than one approach can also be used for implementing the method such as by the use of machine learning algorithms and statistical tests [6]. Figure 1.42 illustrates the Faults Detection and Identification techniques investigated in this sub-section.
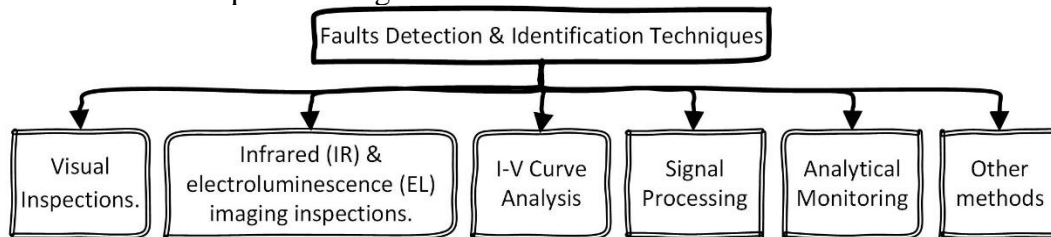
Figure 1.42 Faults Detection & Identification techniques investigated in this section.

During operation of PV system, the PV modules may develop defects and failures (E.g., soiling, hot spot, breaking, browning, discoloration and delamination) [161], which can be repaired if they are detected in time. To ensure the safe operation of PV modules without power losses, reliable and fast diagnostic methods to assess the performance of PV modules are required during the production process [162]. In first time a visual inspection is recommended, because is the most effective and quickest method. Indeed, there are several techniques that allow an advanced inspection with localization and assessment of specific failure modes affecting the PV modules. [101] report ten (10) on-site inspection techniques using mobile test equipment ranging from PV output power characterization, to imaging techniques for localizing cell cracks or open-circuit failures to spectroscopic methods for materials analysis.

1) Infrared (IR) and electroluminescence (EL) imaging inspections.

Most O&M companies offer regular Infrared (IR) and Electroluminescence (EL) imaging inspections of PV plants to ensure the best performance and safety of the PV array [163]. The IR and EL imaging are non-destructive measurement techniques which can provide in real-time high-resolution images of PV modules. However, not all defects of PV modules lead to a temperature increase, for this limitation a combination of IR and EL measurement techniques are necessary in order to identify the most common defects in the PV modules with high accuracy [164]. In recent years, several Machine Learning (ML) techniques are used to automatically process the sequence of images acquired by IR and EL cameras attached on board of an Unmanned Aerial Vehicle (UAV) [165]–[168], in order to greatly minimize inspection times and to accurately analyze various forms of defects and failures in PV array. Figure 1.43 shows the imaging inspection process using IR camera attached to the drone board to detect and locate anomalies and failures occurring in the PV array.

The IR and EL imaging are complementary techniques, and each have their own strengths and weaknesses, [163]. While these techniques require sophisticated equipment's.
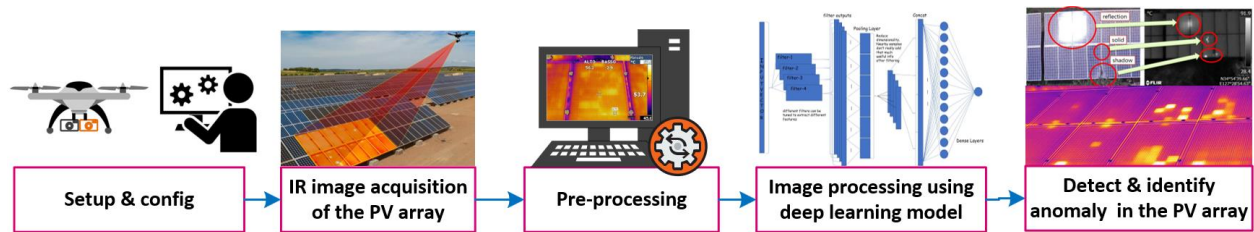
Figure 1.43 imaging inspection process using IR cameras attached on UAV for PV fault localization.

2) I-V Curve Analysis (I-VCA)

However, a robust and reliable FDD tools should be as simple in structure, flexible and economic and must incorporate an intelligent algorithms that can detect, distinguish and localize the majority of faults that occur the PV system accurately in real-time [169]. Indeed, the FDD methods based on electrical measurements unlike to IR and EL imaging techniques seem more appropriate to integrate inside the power converter. Among the old [170] and most methods used to diagnose faults appearing in the PV module, string or array [161], the static analysis of current and voltage (I-V) characteristics by the comparison between experimental I-V curve measured by an I-V curve tracer device and the excepted one based on models of the PV module [126], [171], and this under diverse measured values of in plane irradiance and PV module temperature. This type of FDD methods is based on mathematical models with accurate parameters identification using advanced techniques.

Chen et al. [172] presents an accurate modeling of PV modules using a one-dimensional deep residual network based on large datasets of measured I-V characteristic. A new analytical method based on the one-diode model are proposed in [173] to extract five-parameter of PV module under multi-peak conditions and other conditions. In [174] authors have extracted the parameters of PV array model using reinforcement learning approach. Das et al. [175] have used a metaheuristic optimization approach to detect and identify differentiate among the open and short circuited PV modules in solar PV array under non-uniform distribution of irradiance and temperature. An intelligent Fault Diagnosis (FDi) of PV arrays based on optimized kernel extreme learning machine (KELM) and parameters extraction from I-V characteristic curves have been realized in [176], in order to detect and classify accurately short and open circuit faults, degradation fault and partial shading condition.

Based on I-V characteristic and climatic data, a deep residual network FDD approach are proposed in [177] to detect different types and levels of most common faults of PV array, including partial shading, open circuit fault, short circuit fault and degradation. In [178] a novel degradation diagnosis method for PV modules that employing a xenon flash lighting system and a capacitor were proposed, the obtained results confirm the performance and practicability of proposed method for commercial PV modules. Chine et al. [179] have implemented a FDi technique into a Field Programmable Gate Array (FPGA) circuit based on combination of signal threshold approach and Artificial Neural Network (ANN) approach, using both simulated and measured current voltage of I-V characteristics of a number of PV strings. A fault detection (FDe) algorithm for PV systems based on Multi-Resolution Signal Decomposition (MRSD) for feature extraction, and two-stage Support Vector Machine (SVM) classifiers for decision making, is proposed in [180] to improve the detection accuracy for Line-Line fault scenarios. In [181] a Principal Component Analysis (PCA) method have used to train PV model based on I-V experimental data, in order to detect and classify the shading fault. The technological development of PV inverters in recent years has made it possible to integrate the online measurement of I-V curves of the PV strings connected to the inverter input, what makes these methods flexible to be functional in inverters with a low integration cost [182].

A low-cost I-V curve tracer dedicated to tracing I-V characteristics and to diagnose the faults of PV modules under real operating conditions is implemented in [183]. A recent commercial solution based on smart I-V Curve diagnosis was proposed in [184], this solution is able to carry out online I-V curve analysis every 5 minutes using advanced diagnosis algorithm, in order to automatically identify different failure types in PV the strings, while the sampling time for 128 point is very fast lower than 1 second (see Figure 1.44) . In [101] IEA-PVPS gave an interpretation of the deviations between the measured I-V curve and the predicted I-V curve, the deviation represents the faults in PV array or degradation of PV modules.
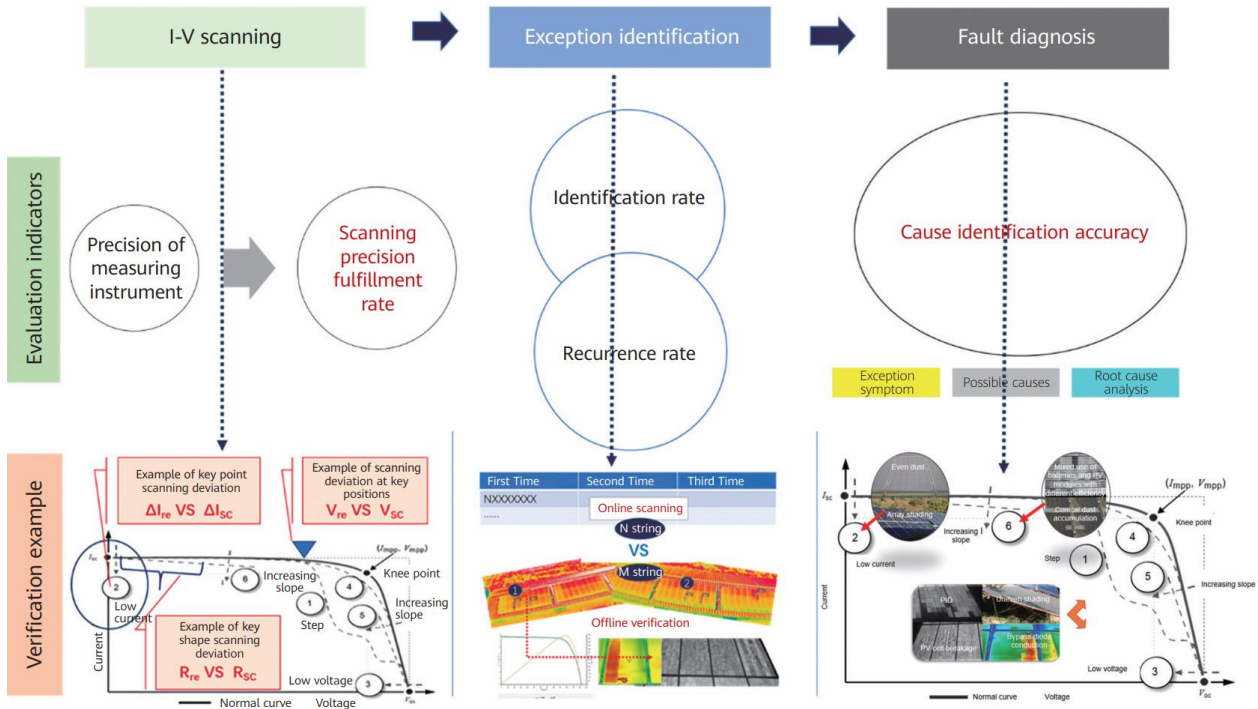
Figure 1.44 Smart I-V Curve diagnosis proposed by Huawei [184].

3) Signal processing methods

In [185] an Earth Capacitance Measurement (ECM) method was applied in order to estimate the disconnection location in PV strings by comparing the earth capacitance measures of the failed string with that of the good string, knowing that this method could be applied to locate the disconnection position in the string without the irradiance presence. Another FDD techniques using the Spread Spectrum Time Domain Reflectometry (SSTDR) technique has been presented by [186] for detecting ground faults in PV arrays. In [187] a detection method for series DC arc faults in a PV system based on time and frequency characteristics of a parallel capacitor current has been proposed. Wang et al [188] have studied the performance of the Fast Fourier Transform (FFT) arc detection method compared to the wavelet method by using synthetic waveforms, from the test results, wavelet analysis is more efficient than the traditional Fourier transform approach. In [189] three-year research program at Sandia National Laboratories (SNL) are summarized to improve PV ground faults, the authors have presents the suggested changes to ground fault standards and gave a good recommendations for array safety and operation.

However, ECM and SSTDR approaches do not require irradiance and meteorological data, but for their implementation, external signal hardware is required, which increase significantly the installation cost. In the solar PV market, various electronic devices have been proposed for FDD, especially for line-line faults, arc faults and ground faults, but most of them cannot detect and locate other faults occurring in PV systems. Figure 1.45 illustrates the fault detection diagram based on the analysis of the output signal to detect anomalies and classify the faults occurring in the PV system.
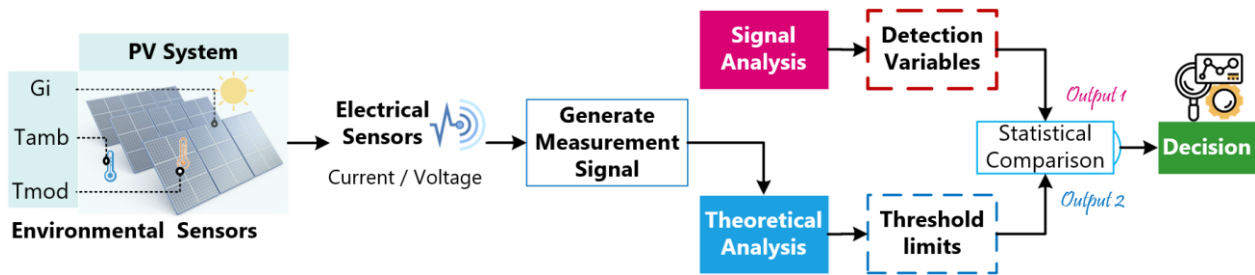
Figure 1.45 Signal processing technique for fault detection.

4) Analytical Monitoring approaches

However, continuous monitoring of the PV system is essential during the operational phase to ensure rapid detection of faults, reduce downtime, maintain long-term profitability and exploit its full power. According to IEC 61724 standard a better monitoring system is split into three important areas: 1) measurement, 2) data exchange and 3) performance analysis.

With technological development in recent years, the use of the Internet of Things (IoT) technique, is recommended to check the performance and the system evolution in real-time [18], [190] while, the integration of intelligent FDD techniques in the monitoring software allow to increase reliability and safety of PV systems.

A monitoring system allows to measure the PV system yield and to compared it with simulation results in order to raise warnings daily if there is a performance shortfall. The key to a reliable monitoring and FDD strategy is to have good simultaneous and accurate measurements of the both meteorological and electrical parameters of the PV system. Without a reliable monitoring system, the PV system can operate with poor performance for several months before the fault is detected and identified. This can result in a major loss of income [8] . So, the power losses can be minimized by sending real-time alarms to the operator about the location of failure allowing them to take maintenance actions.

Several FFD techniques have been studied in the last ten years to accurately detect and identify faults in grid connected PV systems [16]. These techniques are generally based on the processing and analysis of data measured from PV system, where the experimental data are measured and recovered using data acquisition system (DAS) essentially composed by sensors, data acquisition and software application [65]. The FDi process is determined by comparison between both normal and faulty data for each type of failure. while, the classification of failure is the most important step of the failure routine process. Many authors have used the comparison technique between the simulation and experimental data based on diverse algorithm, where the simulation data of the PV array are given using parametric models [134], [191] or non-parametric models [114] [192]. Generally, FDD techniques that exploit the analytical monitoring data are based on one of the following methods: 1) Real-time difference measurement, 2) Statistical analysis and Signal processing, and 3) Machine learning, although the combination of these methods offers quicker and very accurate detection. Indeed, each data analytic technique used for the FDD in monitored PV systems, has its own advantages and limitations. Hence, the decision for the most cost effective and more appropriate FDD solution depends on numerous factors [16], [193].

Recently IEA PVPS Task 13 [194] reports on a benchmarking study of the various approaches for calculating the Performance Loss Rates (PLR) of commercial and research PV power plants in diverse climatic zones. PLRs are calculated with weather and power data from the PV systems. The PLR is used by power plant owners, operators, and investors to determine the expected power output of a PV system over its installed life. Therefore, discrepancies in various calculation methods can have a significant impact on the finances of a PV installation. The benchmarking study is necessary due to the inconsistency in reported PLR results based on the many different approaches currently used to calculate the PLR of PV systems. This comparative study is focused on identifying which of the various approaches produce similar results and what causes inconsistencies between these different methods. The findings of the study lead to a PLR framework which defines the basic four steps common to PLR determination.

After initial exploratory data analysis and data quality grading, the four steps are 1) input data cleaning and filtering, 2) performance metric selection, corrections, and aggregation, 3) time series feature corrections, and 4) application of a statistical modeling method to determine the PLR value.

Real-time difference measurement (RDM)

Many large PV systems use analytical monitoring and performance analysis to avoid economic losses due to malfunctions problems [11]. Chouder and Silvestre [195] have presented an automatic supervision and Fault Detection procedure in DC side of the PV systems, analyzing both power losses and deviation of the DC current and DC voltage under MATLAB & Simulink environment. An evaluation of Current indicator (Ci) and Voltage indicator (Vi) at MPP for automatic detection of main faults occurring the PV systems were performed in [196], this method is simple and can be integrated in the inverter, for a real-time supervision of the PV system. In [197], a level online FFD technique based on Power Losses Analysis (PLA) for solar PV systems was proposed. [198] presents a remote supervision and FDi of Grid Connected PV (GCPV) systems using PLA method by means of the Open Platform Communications (OPC) technology-based monitoring. Madeti and Singh [199] proposes an online monitoring FDe technique based on Vi analysis allow to reduces the sensors number using power line communication (PLC), with an economic analysis of GCPV systems. In [200] two indicators named power ration (Pr) and voltage ratio (Vr) are defined, in order to determine the fault type, time and the location of failure. A review of main strategies for automatic FDD based on PLA at the AC side, and both Ci and Vi at the DC output of the PV array is reported in [201]. Chaibi et al. [202] presents a simple and efficient approach to detect and to identify most common faults in PV systems as well as short and open circuit faults , partial shading condition and inverter disconnection, three indicators are used to give information on the state of the PV system regarding normal and faulty operation. In the literature few studies that exploit satellite data instead of on-site data measurements in order to estimate the PV energy production, Drews et al [203] have used the satellite-derived solar irradiance data analyzed by PLA method to remotely detect failure in a PV system. The main advantage of automatic FDD method based on Real-time Difference Measurement (RDM) that they can practically identify the common faults that occurring in the PV array.

The implementation is easy with minimal required components, detection time is improved and the FDe accuracy depend on the fixed threshold limits from behavior PV model. Despite the fairly low degree of complexity of RDM techniques, the data measurements acquired during faulty operation of the PV system were really necessary for better validation. Moreover, the empirical models are specific to the considered site, therefore, the model parameters must be adjusted for other installations using more advanced techniques. Figure 1.46 displays the diagram of FDD process based on real-time difference measurement used to detect and identify faults in both DC and AC sides of PV system.
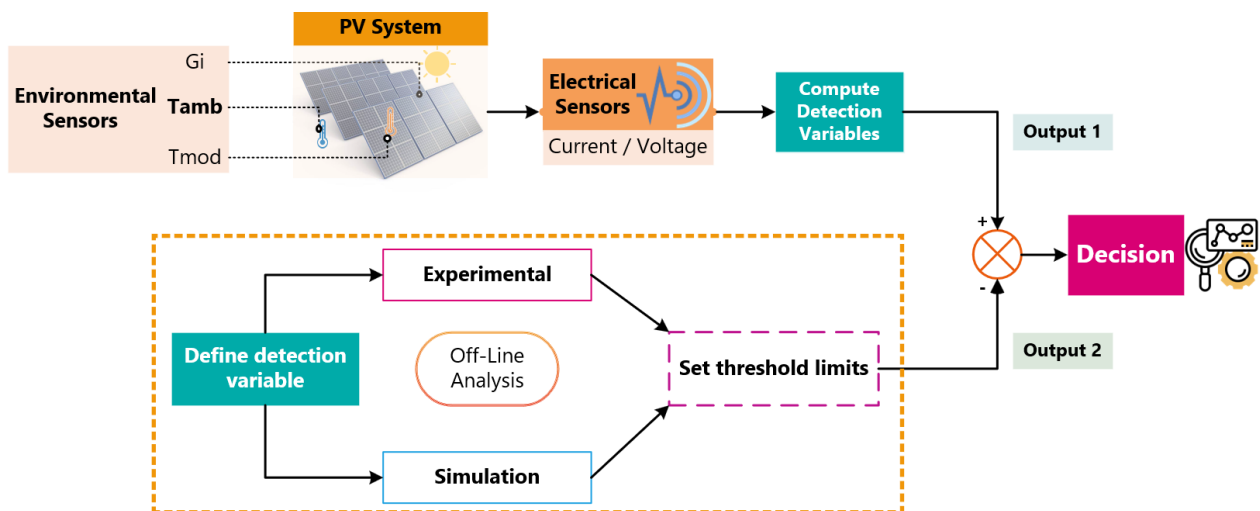
Figure 1.46 RDM technique process for fault detection and identification

Statistical Approach (SA)

Recently, several statistical techniques were developed for performance monitoring and FDe mainly in the DC side of the PV system. The most implementations of statistical techniques, define thresholds for each monitored parameter and compare the measured value to the lower and upper limits in order to get a decision on normal or faulty operation [6], [112]. In [204], authors published a report which present four methods based on advanced statistical analysis used to improve efficiency and to offer quicker and exact alarms, particularly for the residential PV system. Garoudja et al [205] have used statistical method combining between the one-diode model to predict power produced from the PV array and the Exponentially Weighted Moving Average (EWMA) control chart based on residuals of output DC power to detect in real-time the presence of anomalies, a continuity of this work was published in [206] introducing the multivariate EWMA chart for fast detection fault combining with univariate EWMA to identify fault. Data from PV systems are measured in a noisy environment, which confuse the important features in the data and decrease the faults detection capability. In [207] a statistical robust FDe strategy is designed to monitor the DC side of a PV system, with ability to treat the measurement noise problem in the data by using multiscale representation. A PV FDe algorithm based on t-test statistical approach is proposed in [208], to identify DC side failures of 1.98 kWp GCPV system under LabVIEW in real-time. A data-based statistical approach for detecting anomalies and partial shading occurring in PV system is proposed in [209], this method exploits the ability and flexibility of the PCA model to extract relevant features from multivariate time series data, and the aptitude for detection of multivariate charts (T^2 and SPE) to monitor the DC and AC parts of a PV system. In addition [210] are used a modified local outlier factor method to evaluate fault degree and to identify the failure of PV array under MATLAB/Simulink, this method present several advantage : higher accuracy in all-scale PV system, economic and simple architecture .Mansouri et al [211] have developed a technique combining the advantages of Principal Component Analysis (PCA) and Wavelet optimized EWMA, to monitor fault in PV systems. An unsupervised approach based on functional PCA and modeling parameters, for autodetecting outliers of identical sets of PV solar arrays was proposed in [212]. A multi-level decomposition wavelet transformation method have used in [213] to detect the fault location and components of the inverter, this method are fast and accurate with a simple structure and low cost realization.

[214] have proposed an online technique to identify the faults under low irradiance and partial shading from the faulty conditions based on the mean of wavelet packets, using Simulink and is experimentally tested on a 1.6 kW PV array. Indeed, the statistical techniques can detect quickly most faults in the PV array including e.g. (open-circuit, line-line, partial shading and degradation faults), but cannot detect the level of one faulty module from the PV array. the Statistical techniques are simple and easy to implement with minimum sensors (no requirement of meteorological data) and do not require any training process. While the noise in sampling signal affects the detection capability. Figure 1.47 illustrates the flowchart of the faults detection process using a statistical approach to detect and classify faults affecting the PV system.
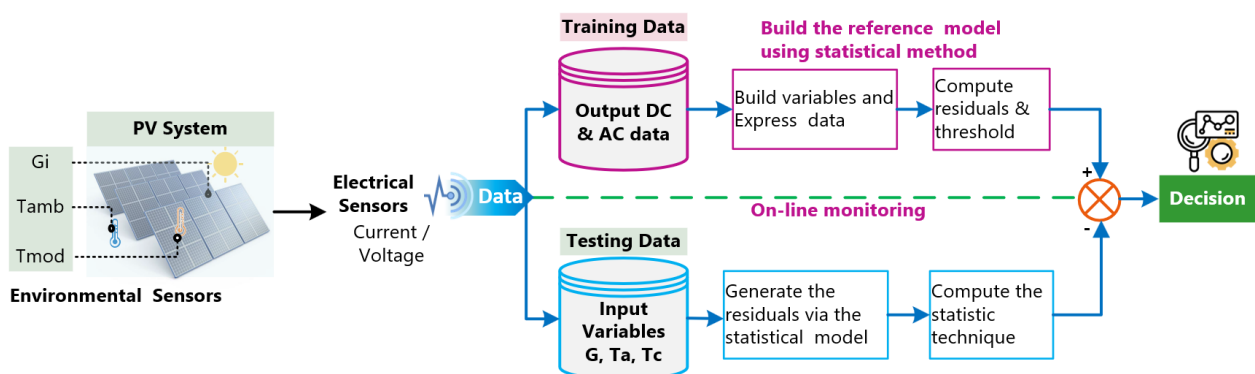
Figure 1.47 Fault detection and identification process using statistical apporach.

Machine learning Techniques (MLT)

Machine learning is a multidisciplinary field, it can be classified into two classes supervised and unsupervised supervised learning techniques are used for regression and classification which trains a model using input and output data, and predicts future responses. While unsupervised methods are mainly used for clustering data and it's can group and interpret data based only on input data. These methods could be implemented for FDD in PV systems, thanks to their rapid detection response times and high accuracy. Recently a review on FDi of PV systems using Artificial Intelligence techniques (from 2003 to 2019) including machine learning and deep learning are reported in [18]. Garoudja et al [215] have proposed an enhanced machine learning method based on probabilistic neural network (PNN) classifier to detect and diagnose DC side anomalies that occurs in the PV systems, the parameters extraction of the one diode model (ODM) and simulation of healthy operations of the grid-tie PV system are performed using a PSIM™/Matlab™ co-simulation, three faulty operating cases were tested: three modules short-circuited, ten modules short-circuited, and a string fault, the efficiency of this approach is guaranteed from two short-circuited PV modules. In [216] a learning algorithm based on ANN Laterally Primed Adaptive Resonance Theory (LAPART) was used to detect module level faults with minimal error, the results showed that the LAPART algorithm can quickly learn PV performance data (only 4 days of one minute data) and provide an accurate multi-level FDe. The k-nearest neighbors algorithm (kNN) is a non-parametric method used for classification and regression.

In [217] four approaches based on kNN algorithm are designed to detect faults, kNN-based Shewhart and EWMA schemes (parametric and nonparametric), the results showed a high capability for detecting open circuit faults, short-circuit faults, and temporary shading, whereas this algorithm cannot distinguish the partial shading among faults occurring in the DC side of the PV array. Another Real-time detection and classification technique based on clustering kNN rule has been proposed in [218], the proposed learning technique does not require any predefined threshold values for FDe, which are difficult to choose for PV systems, where the output power is highly dependent on climatic conditions. In [219] , a C4.5 decision tree (DT) approach is proposed to detect and diagnose the faults in a GCPV system using a non-parametric model by learning the task. In this work, SNL models were used to predict the power produced from PV array under normal operation condition (i.e., fault free). Then, the supervised decision tree algorithm is employed to classify four cases: 1) fault free, 2) string fault, 3) short-circuit fault, and 4) line–line fault. The results showed a high accuracy with 99.86% and 99.80% for the detection and diagnosis model respectively. Hence, as a supervised learning technique, this method needs data, and a set of training examples to build a good classifier able to distinguish between faults.

A PV FDe approach which combines both the statistical and numerical methods are proposed in [220], where the least squares method is used for comparison between measured data and simulated data from Bishop model, and the fault level classification was established by Fuzzy Logic (FL) technique. Moreover, Tadj et al. [221] have used GISTEL model, based on the satellite image improved by FL technique to detect the faults of PV system. In [118], a machine learning technique (MLT) merged with statistical testing hypothesis to detect fault in PV systems. The MLT based on Gaussian process regression (GPR) method are used for modeling, while a generalized likelihood ratio test (GLRT) chart is applied to detect inverter disconnection and partial shading faults.

Authors in [222] present an PV FDe algorithm which includes both ANN technique and FL system interface. The proposed algorithm is tested to detect ten cases of faults either a combination between four cases of faulty PV modules (from 1 to 4) and two cases of low and high partial shading, the variations of the voltage and power of the studied PV system are used as input for both ANN and the FL system. Currently, most FDD methods for the PV arrays do not take advantage of the temporal-spatial distribution information contained in the operation data. Zhu et al [223] proposes a spatial-temporal composite function combined with fuzzy rules to diagnose array fault in large-scale PV power plant, the proposed method can identify effectively various faults just using the current data measurement of PV array.

In [224] authors present an FDD model for PV system using transformation of normalized sequential PV array current and voltage into Electrical Time Series Graph (ETSG), the fault features are automatically extracted by Convolutional Neural Networks (CNN). A graph-based semi-supervised learning (GBSSL) approach for fault detection and classification in solar PV arrays are proposed in [225] , the GBSSL model exploits the measurements available in existing PV systems, such as PV-array voltage and current, in plane irradiance and ambient temperature, so that no additional hardware installation is needed, only a few data points are necessary for self-learning, the proposed technique can suitably detect and identify the open circuit faults and line–line faults. An unsupervised monitoring procedure for detecting anomalies in PV systems using a one-class SVM technique are proposed in [226], the one-diode model is used under PSIM™ to simulate healthy operation of the monitored PV array, while the one-class SVM method is applied to residuals between measured and simulation data for FDe. The ML techniques have a rapid detection response, make it possible to distinguish faults which have the same signature and to classify faults with high accuracy, the setting threshold limits is not required. The FDD accuracy depends proportionally with trained PV model to estimate the expected energy yield. Hence, these techniques require more advanced skills for real-time hardware and software implementation, as well as obtaining training dataset of all possible faults' scenarios could be difficult. Figure 1.48 shows the process diagram of model training and fault classification based on machine learning techniques.
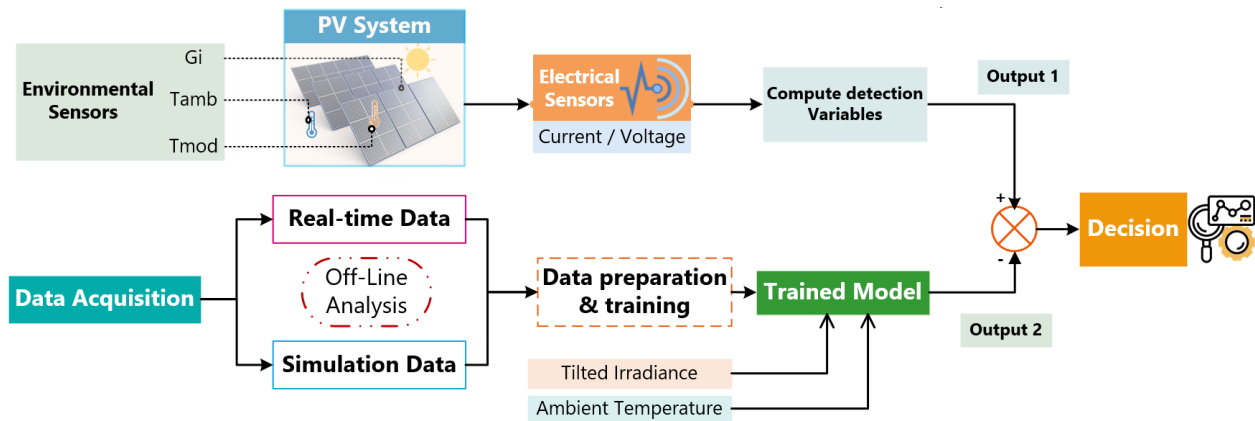
Figure 1.48 Regression model and fault classification using machine learning techniques.

5) Other methods

On the other hand, applying signal transmission method especially to the PV array, makes it possible to detect local disconnection of interconnect cables in PV modules and open-circuit failure of bypass diodes. the signal transmission device is small, lightweight, and inexpensive. It consists of two parts: a transmitter and a receiver [161]. The location of each faulty module in arrays help to identify the fault quickly, but this would involve a high investment cost due to the large number of sensors required. Pei et al. [227] proposes a fault-locating strategy to identify module blocks faults for large-scale arrays, using an improved voltage sensor placement method, that allow diminishing the number of voltage sensors, the investment cost and wiring complexity are significantly reduced, this method can accurately locate the single and multiple module blocks in the different sub-arrays under open circuit, short circuit, partial shading and degradation faults, unfortunately this technique cannot properly identify other types of faults such as temporary soiling. Generally, monitoring of electrical DC & AC is performed by the inverter in a large-scale PV power plant. Although monitoring by central inverter can detect its own failure or a reduction in power generation amount, but the monitoring of each PV string is not supported. In [228], a new effective failure detection method is proposed to detect faults in PV strings by the measure of the DC current value of each string. The data collection is performed using wireless communication method, realizing easy installation.

In [229] authors propose a fixed electrical reconfiguration (FER) technique for the modules of the PV array, that can reduce the mismatch and power losses caused by the non-uniform distribution

of the partial shading on the entire PV array. The technique proceeds with renumbering of the modules of the PV array according to the proposed algorithm followed by electrical rewiring.

Table 1.9 summarize and discuses briefly the ability to detect, identify and localize some electrical fault (i.e., 1) Ground Faults, 2) Line-line faults 3) Open circuit faults 4) Mismatch Faults 5) DC-arc faults) using existing solutions [156].

Table 1.9 Summary of existing PV fault detection, identification and location [156].

Fault Type	Method	Detection?	Identification?	Location?
Ground Faults (or line-line fault with ground point)	Ground Fault Detection Interrupter (GFDI)	✓	✗	✗
	Insulation resistance monitor	✓	✗	✗
	(Residual Current Detector) RCD	✓	✗	✗
	Time Domain Reflectometry (TDR)	✓	✓	✓
	Spread Spectrum TDR (SSTDR)	✓	✓	✓
	I-V curve analysis	✓	✓	✗
	Statistical method	✓	✗	✗
Line-line faults	Overcurrent Protection Device (OCPD)	✓	✗	✗
	RCD	✓	✗	✗
	TDR	✓	✓	✓
	I-V curve analysis	✓	✓	✗
	Statistical method	✓	✗	✗
	Performance comparison	✓	✗	✗
	Capture loss analysis	✓	✓	✗
	Performance ratio	✓	✗	✗
	Machine learning	✓	✓	✗
Open circuit faults	I-V curve analysis	✓	✓	✗
	Performance comparison	✓	✗	✗
	Capture loss analysis	✓	✓	✗
	Performance ratio	✓	✗	✗
	Machine learning	✓	✓	✗
Mismatch faults	I-V curve analysis	✓	✓	✗
	Performance comparison	✓	✗	✗
	Infrared (IR) thermography	✓	✗	✓
	Internal series resistance	✓	✗	✗
	Machine learning	✓	✓	✗
DC-arc faults	Arc-Fault Circuit Interrupter (AFCI)	✓	✗	✗
	Machine learning	✓	✗	✗

Chapter 2

Data Acquisition and Monitoring of PV Systems

Chapter 2 : Data Acquisition and Monitoring of PV Systems

2.1 Introduction

The data analysis from PV installed systems indicate that best Operation and Maintenance (O&M) could improve the average performance ratio from 88% to 94% [13]. Indeed, the O&M contract for PV plants generally includes the following basic services: 1) Continuous monitoring of the PV installation with performance reports and fault alerts, 2) Preventive maintenance, and 3) Corrective maintenance [7], [64].

However, PV power generation systems put into operation require continuous, reliable and accurate monitoring system to determine PV performance, in order to maintain the cost effectiveness of PV systems (PVS) over the long term and harnessing its full potential always.

The performance of PV system depends on many parameters such as the 1) geographical location and climatic parameters, 2) efficiency of each component of the PVS, 3) monitoring solution chosen and 4) O&M services.

The monitoring process should preferably cover the following areas:

1) Measurement of meteorological and electrical parameters with calibration.
2) Retrieval, recording and visualization of all relevant data.
3) Performance analysis and report generation.
4) providing alarms for faults and malfunctions using intelligent algorithms.
5) forecasting based on accurate models for large-scale PV plants.

On the other hand, the evaluation PV performances can be monitored according to various solutions, the main criteria for classification and selection of the monitoring system according to the standard IEC 61724 are: 1) parameters to be measured according to size and application of the PV system, 2) sampling rate and accuracy of measurement, 3) processing, visualization and analysis of data, 4) quality and cost of the DAQ system and 5) transparency of protocols and measurement procedures. So, monitoring is very important, it can acquire and analyze several parameters for performance evaluation, to ensure reliable and stable operation of the PV systems.

Several recommendations and standards have been reported by renowned institutions (e.g. NREL, SNL and IEA PVPS .etc.) [8], [10]–[13]. However a good review on the state of the art of monitoring PV systems have been reported in [61], [65], [67], [68].

Many performance monitoring applications under LabVIEW and other programming environments for of PV systems are developed in [71], [230]–[236].

In summary, the purpose of the monitoring is to provide sufficient information to achieve an "energy balance" representing the amount of available solar energy and losses in each component of the PV system until delivery to the grid connection point.

This chapter describes the design and development of the monitoring system installed in the GCPVS. The proposed monitoring interface are based the Virtual Instrumentation (VI) under LabVIEW software to monitor and analyses the measured parameters of the PV systems by DAQ. Additionally, all installed sensors are well calibrated with reference sensors and instruments.

In the second part we present some case studies carried out at CDER, it concerns the measurement and the monitoring applied to different types of PV systems. These case studies are as follows:

✓ Case 1: LabVIEW based monitoring for an off-grid PV System.
✓ Case 2: Monitoring & control of a PV water pumping test bench using LabVIEW
✓ Case 3: I-V characterization and test of PV modules using PVPM 2540C.
✓ Case 4: Advanced electrical measurement of the grid connected PV system using three phase electrical networks analyzer.

2.2 Description of GCPV System at CDER with its associated monitoring

The GCPV system at Centre de Développement des Energies Renouvelables (CDER), Algiers, consists of a PV array of 90 modules (ISOFOTON I106-12) monocrystalline- Si technology (Figure 2.1). The PV array is composed of three identical PV sub-array of 3.18 kWp, with an inclination of 27° and an orientation of +20° to the southwest (200°). Each PV sub-array is connected in a way to have the following configuration: two strings in parallel of fifteen PV modules connected in series. Thereafter the PV sub-array is cabled through an electrical protection cabinet to the PV inverter (SMA Sunny Boy 3000TL-21) (Figure 2.2). The single-phase PV sub-systems are assembled in three-phase and connected to the low-voltage electrical grid (Sonelgaz) [237].

Figure 2.1 Picture of PV Array of the GCPV system on the top-roof at CDER.

Figure 2.2 Picture of the GCPV plant laboratory at CDER

The main electrical characteristics of PV Sub-array and SMA SB-3000 inverter are given respectively in Tables 2.1 and 2.2.

Table 2.1 Electrical Characteristic of PV Module and PV Generator Isofoton I106-12.

Parameters	$V_{OC}(V)$	$I_{SC}(A)$	$V_{MPP}(V)$	$I_{MPP}(A)$	$P_{MPP}(W)$
PV Module	21.6	6.54	17.4	6.1	106
PV Sub-Array	324	13.08	261	12.2	3180

Table 2.2 Electrical characteristic of PV Inverter SMA Sunny Boy-3000TL-21.

Parameters	P_{AC} Nominal	V_{MPP} range	Efficiency max	V_{AC} range	Frequency range
Value	3000 VA	175-500 V	97%	180-280 V	49.5-50.5 Hz

2.2.1 Description of SMA monitoring system

All solar inverters come with some form of remote monitoring which and is an important tool needed to track system performance [79]. Without reliable and accurate monitoring, it's difficult to know if a PV system is operating correctly or requires some form of maintenance.

The monitoring of the GCPV system is ensured by SMA sunny Webbox data logger [238] via RS485 communication bus, allowing to communicate with an external sensor system SMA sunny sensorbox to measures the environmental data (in-plane irradiance, PV module Temperature, Ambient air temperature and wind speed).

The electrical data of the three PV sub-systems (such as DC and AC rated currents, voltages and power, daily efficiency, network frequency and other performance parameters) are also retrieved from the PV inverters using SMA webbox via RS485 bus as shown in Figure 2.3.

Figure 2.4 shows a Picture of SMA SUNNY WEBBOX with RS485-Power Injector.
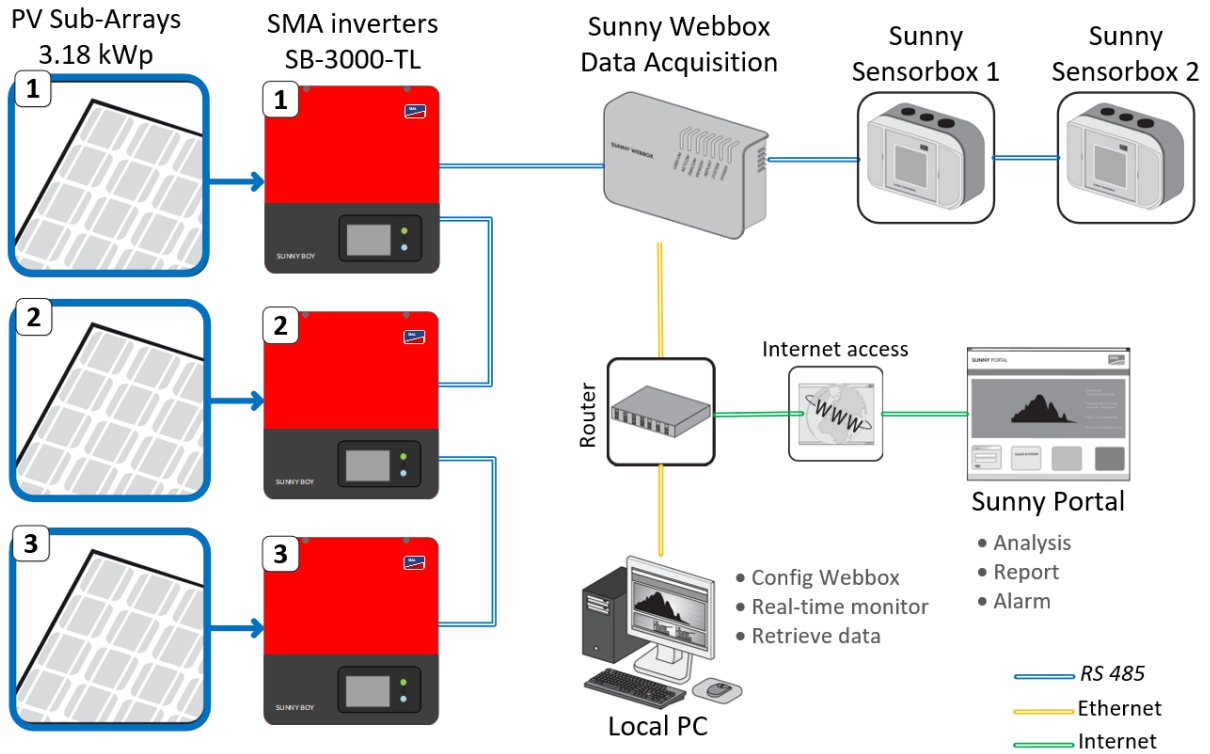
Figure 2.3 Synoptic diagram of the SMA monitoring system

Figure 2.4 Picture of SMA SUNNY WEBBOX with RS485-Power Injector

In the GCPV system we have use two SMA sunny sensorbox with additional sensors, in order to measure the following parameters:

- Tilted irradiances at 27° using 2 sensor (Figure 2.5)
- Ambient air temperature (Figure 2.6)
- Wind velocity Anemometer (Figure 2.7)
- Temperature of three different modules in the PV array, the temperature of modules is measured with pt100 surface temperature sensors, the sensors are mounted in the back of a solar PV modules (Figure 2.8)
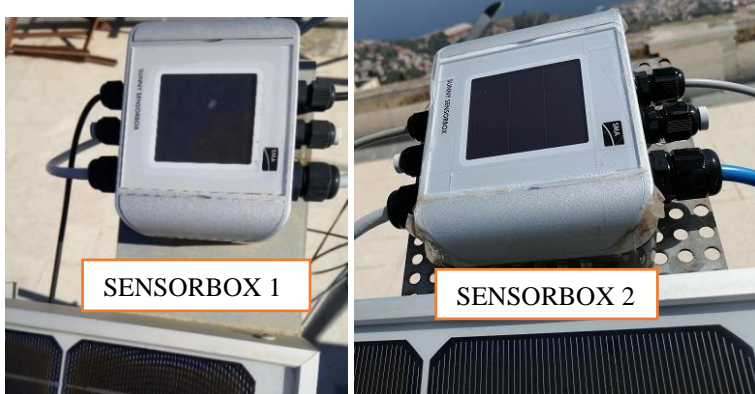
Figure 2.5 SMA SUNNY SENSORBOX

Figure 2.6 Ambient temperature box 4-wire.   Figure 2.7 Wind velocity Anemometer.

Figure 2.8 Three PT100 surface Sensors mounted to the back of modules.

The Sunny WebBox is operated via an integrated user interface with a local IP address . Also, the user interface allow to visualize all measured data for each device in real time (Figure 2.9), and alow to saving average data value for 5 min, 10 min or 15 min.
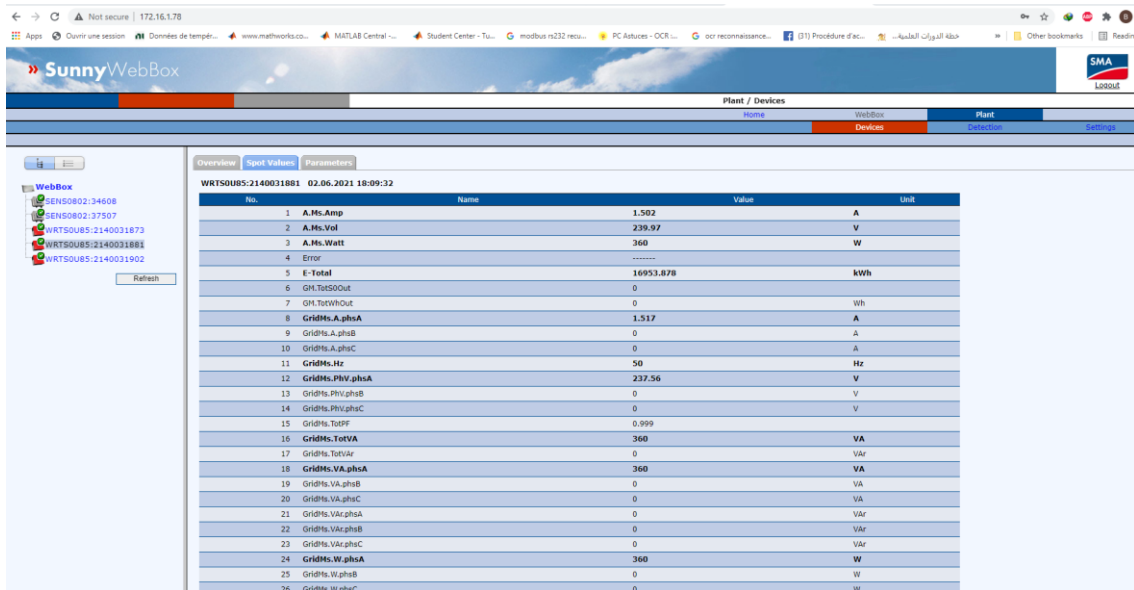
Figure 2.9 Detail real-time data for each installed devices.

Sunny portal interface: Sunny Portal is a simple and efficient Internet portal for monitoring the PV plant as well as visualizing and presenting plant data (Figure 2.10). where the data is collected via SMA Sunny Webbox. With Sunny Portal, PV system operators and installers can access key system data anytime, anywhere. The Sunny Portal features almost infinite options for analyzing data and visualizing yields, via a data table or a diagram (Figure 2.11). The yields of all inverters in a plant are compared automatically, allowing for the detection of even the smallest deviations. The powerful reporting functions also provide regular updates via e-mail to help ensure yields [239].

Figure 2.10 Sunny Portal overview interface.
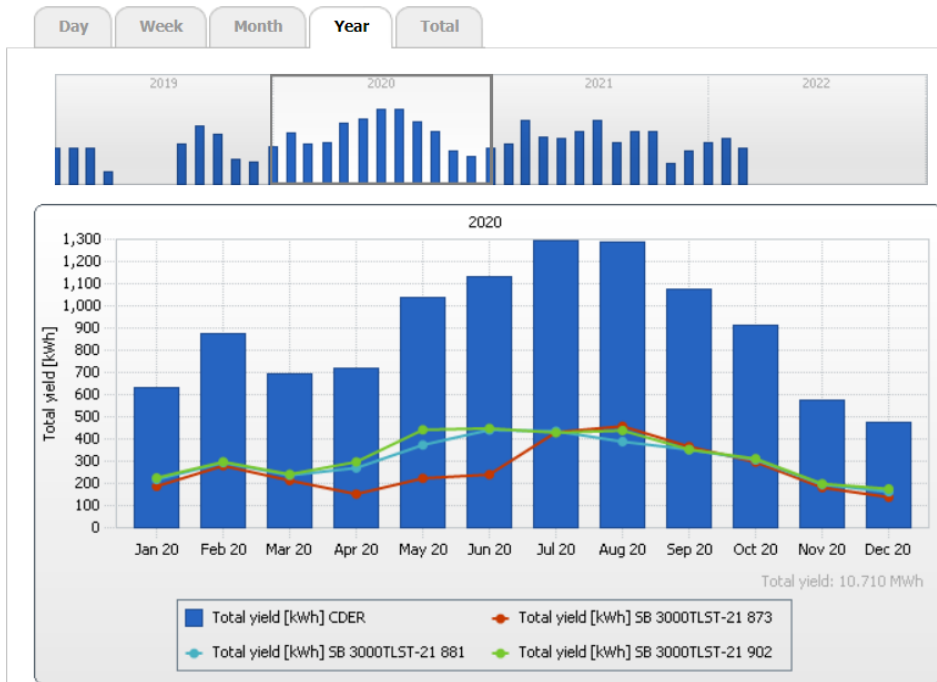
Figure 2.11 Sunny Portal Analysis Interface.

2.3 Monitoring of the GCPV mini-plant using external monitoring system

In this section we have implemented a monitoring system using PC-based data acquisition (DAQ) for a 9.54 KWp grid connected PV system (GCPVS).

PC-based DAQ is one of the most popular measurement and control techniques used to monitor industrial systems and to perform testing and characterization in research applications. This technique uses a combination of modular hardware and flexible software to turn the PC into a user-defined supervisory system. The requirements of IEC 61724 standard concerning performance monitoring of PV system can largely be achieved using PC-based DAQ.

2.3.1 Description

The PV Monitoring is applied for the three single phase PV sub-systems connected to the grid, it is based on the measurement of the quantities influencing the performance of the PV system, especially the environmental quantities (irradiance and temperature) and the DC/ AC electrical quantities (current and voltage).

The elements constituting the acquisition system are (Figure 2.12):
   • Irradiance sensors and temperature sensors installed on the PV array (Table 2.3).
   • Voltage and current sensors installed inside DC and AC electrical cabinets (Table 2.4).
   • Data acquisition device.
   • LabVIEW software under windows with the necessary drivers for each data acquisition unit.
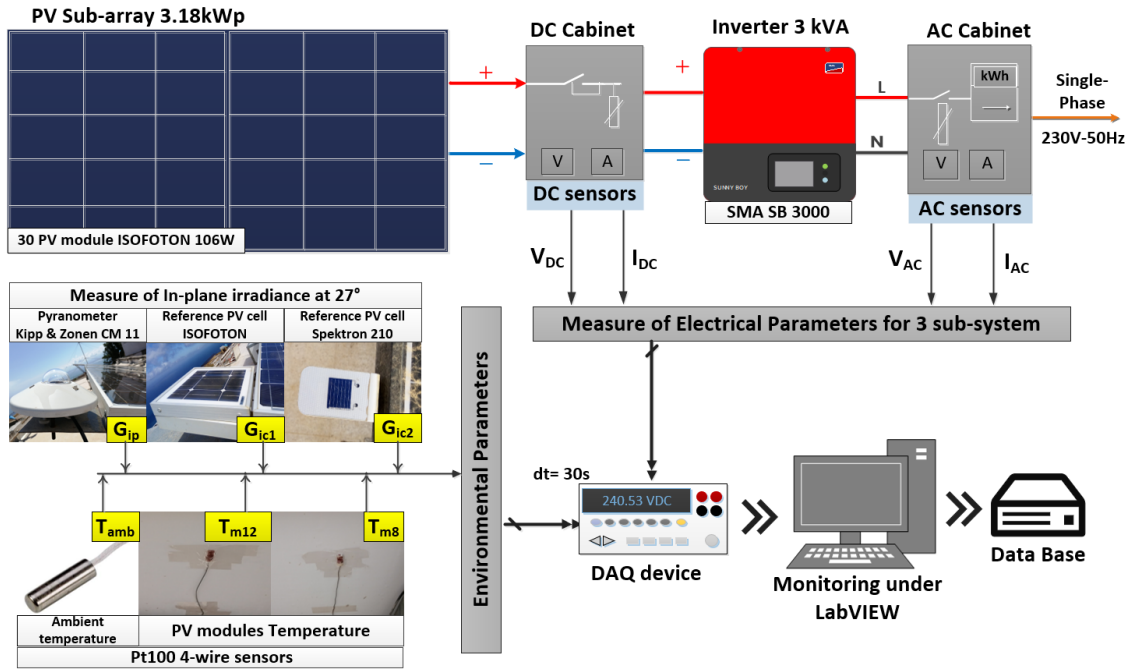
Figure 2.12 Synoptic diagram of the proposed PV monitoring system.

2.3.2 Sensor's specification and calibration

The specifications of the environmental and electrical sensors are summarized respectively in Tables 2.3 and 2.4. The calibration of the sensors was performed by comparison with other sensors and instruments used as a measurement reference.

Table 2.3 Environmental used sensors, and their characteristics.

Measured parameters	Sym.	Unit	Sensor type	Sensor Reference	Accuracy	Calibrating reference	Calibration factor
in-plane Irradiance _27°	$G_{i,iso}$	W/m^2	PV reference cell	Isofoton	5%	SMA Sensors Box	8550
	$G_{i,fr}$			Spektron 210			14900
	G_{ip}		Pyranometer	Kipp & zonen CM 11	2%	Pyranometer CMP21	201613
Ambien air Temperature	T_{amb}	°C	Pt100 probe 4-wire	WZP-Pt100	0.5 %	Thermometer & SMA Sensors Box	Direct Measure
PV module temperature PVM8/PVG1	T_{mod1}		Pt100 surface 4-wire	TC-direct	0.5 %		
PV module temperature PVM12/PVG1	T_{mod2}				0.5 %		

Table 2.4 Main characteristics of electrical sensors used for monitoring.

Measured parameters	Sym.	Unit	Sensor type	Sensor Reference	Accuracy	sub-system N°	Calibrating reference	Calibration factor
PV sub-array output DC voltage	V_{DC}	V	Voltage Divider	350V/5V	1%	1,2,3	Clamp-meter (Extech MA220), SMA PV inverter, and Datasheets	86.3
	V_{DC2}		Hall effect	LEM LV-25P	0.8 %	2		
PV sub-array output DC current	I_{DC}	A	Shunt Resistor	20A/0,5V	1%	1,2,3		200
	I_{DC2}		Hall effect	LEM LA-25P	0.95%	2		2.54
Inverter output AC voltage	V_{AC}	V	Voltage transformer	YHDC PE2818S (220V/9 V)	1%	1,2,3		18.3
	V_{AC2}		Hall effect	LEM LV-25P	0.8%	2		60.26
Inverter output AC current	I_{AC}	A	Current transformer	YHDC TA12-200 (5A/5mA)	1%	1,2,3		9.78
	I_{AC2}		Hall effect	LEM LA-25P	0.95%	2		2.53

Irradiance sensors

Figure 2.13 shows the irradiance sensors installed in the same plane on the array.

a) PV Reference Cell Isofoton   b) PV Reference Cell spektron 210   c) Pyranometer kipp&zonen CM11
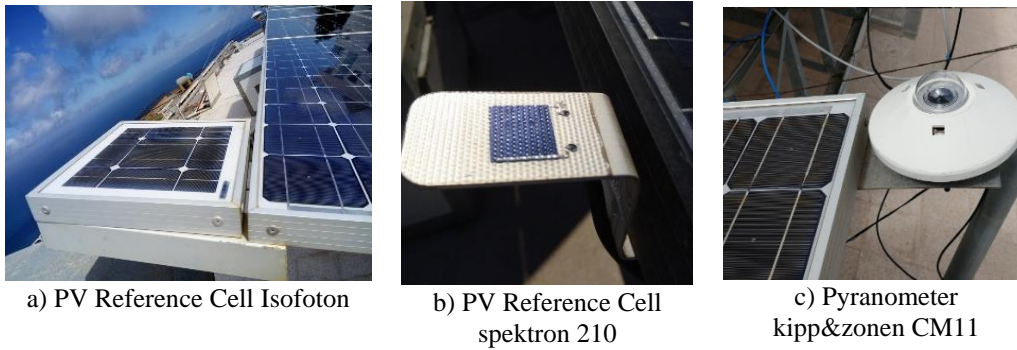
Figure 2.13 Irradiance sensors installed in the matching plane on the PV modules.

The pyranometer kipp&zonen (CM11) was calibrated by the CDER pyranometer calibration laboratory. This laboratory uses kipp&zonen CMP 21 as reference pyranometer with **CR6** measurement and control datalogger (Figure 2.14 & 3.15).
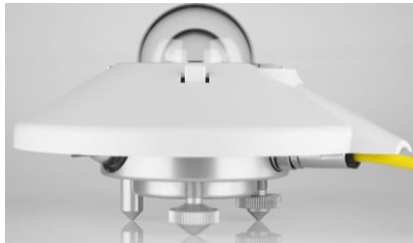
Figure 2.14 Pyranometer kipp&zonen CMP21.

Figure 2.15 Measurement and Control Datalogger Campbell Scientific CR6.

The CMP21 pyranometer is designed to measure irradiance on a plane surface. This is a high-performance research pyranometer and fully compliant with all Class A (ISO 9060 the highest possible pyranometer performance category).

Temperature sensors

Figure 2.16 (a) shows the measure of ambient temperature using PT 100 probe. The PV module Temperature is measured by PT100 surface sensors with 4-wire shielded output (Figure 2.16 b-c). The calibration of temperature measurement is carried out using a reference PT100 sensor with multimeter (Figure 2.17 a-b) or thermocouple with thermometer (Figure 2.17-c).

a) Ambient Temperature   b) PV module Temperature (PVM8/PVG1)   c) PV module Temperature (PVM12/PVG1)

2-wire PT100 probe   Surface pt100, 4-wire shielded output
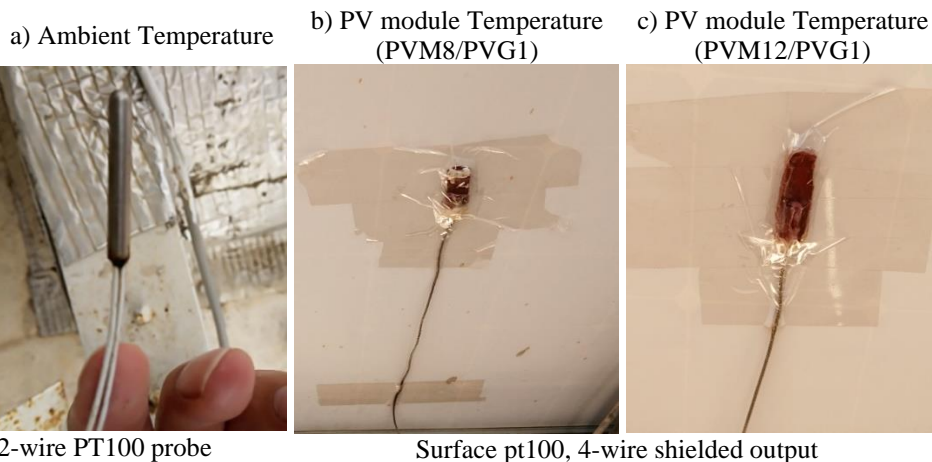
Figure 2.16 Ambient temperature and PV module sensors.

| a) Calibration with a reference PT100 sensor | b) Measure of PT100 resistance with multimeter | c) Calibration with thermometer |
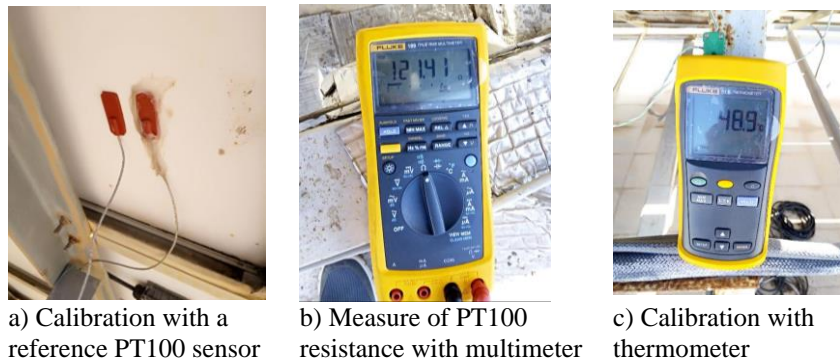
Figure 2.17 Calibration of PT100 sensors.

Voltage & Current sensors

The measurement of the electrical parameters at DC and AC sides of the PV system was carried out using two categories of sensors: 1) Low-cost sensors and 2) med-cost using Hall effect sensors (Figures 2.18 and 2.19). The low-cost sensors are mounted in all three sub-systems, they do not require a power supply. The Mid-cost hall effect sensors are just installed in subsystem 2, these sensors are isolated but require a $\pm$ 15-volt symmetrical power supply, and they can be used for DC&AC measurement.
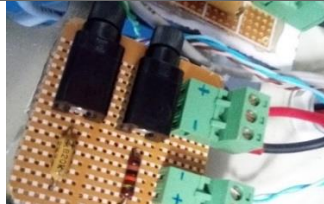
Measured parameters	Symbol	Low-cost voltage sensors	Hall effect voltage sensors
DC voltage	V_{DC}	Voltage divider with fuse 350V/5V	LEM (LV-25P) config for 390V
AC voltage	V_{AC}	Voltage transformer with fuse 220V/9 V	LEM (LV-25P) config for 270V

Figure 2.18 Voltage sensors realised for DC and AC side of the GCPV system.

Measured parameters	Symbol	Low-cost current sensors	Hall effect current sensors
DC current	I_{DC}	Shunt resistor 20A/0,5V	LEM (LA-25) & R=390Ω
AC Current	I_{AC}	Current transformer 5A/5mA	LEM (LA-25) & R=390Ω

Figure 2.19 Current sensors realised for DC and AC side of the GCPV system.

73

Considering the absence of a regenerative power supply with a DC Electronic Loads (400V / 20), the calibration of DC voltage and DC current sensors are realized after their installation in the PV system. Figure 2.20 illustrate the calibration of AC voltages transformers using two multimeters to measure the signal upstream and downstream of the sensor. Figure 2.21 shows the Calibration of AC current transformers with clamp meter EXTECH MA220 using a) rheostat load or b) Oil filled radiator laod. Figures 2.22 and 2.23 show the monted sensors in the DC and AC cabinets.

Figure 2.20 Calibration of AC voltage transformers with multimeter.
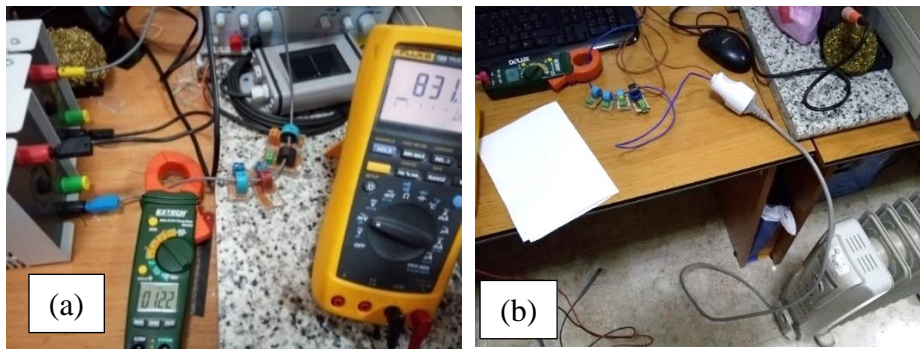
Figure 2.21 Calibration of AC current transformers with clamp meter EXTECH MA220 using a) rheostat load and b) Oil filled radiator laod.

Figure 2.22 mounted sensors on DC cabinet.   Figure 2.23 mounted sensors on AC cabinet.
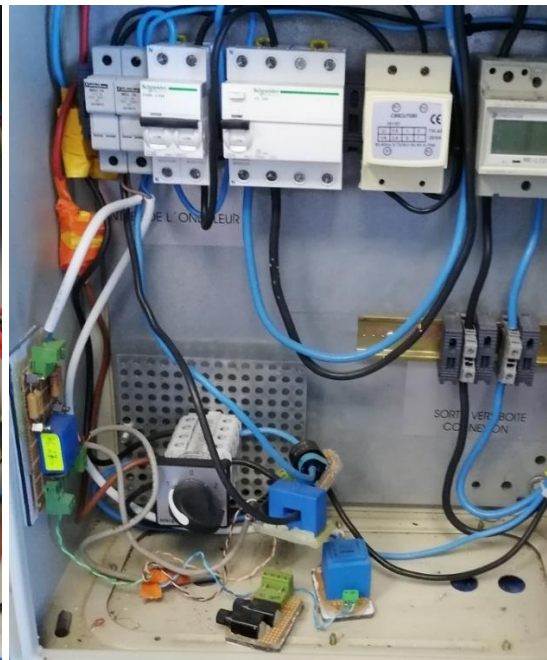
2.3.3 Monitoring of GCPV sub-system using Agilent 34970

Description of realized monitoring system

The monitoring is applied for one PV sub-system (N°2) of the GCPV system, it is carried out to require, display and analyze the measured data by the sensors, while these sensors have used to measure both meteorological and electrical parameters during the system operating.

The 34901A and 34902A channel multiplexer modules integrated in Agilent 34970A DAQ [240] board are used for measuring the signal at the output of sensors.

Using this DAQ 30sec. is chosen as the sampling time according to standard norm IEC 61724, which gives 2880 samples per day. The recovery of instantaneous measurements is performed by a graphical code developed under LabVIEW [241] environment using a user-friendly interface. Figure 2.24 shows the Monitoring system of the GCPVS based on sensors, Agilent 34970A DAQ and LabVIEW.
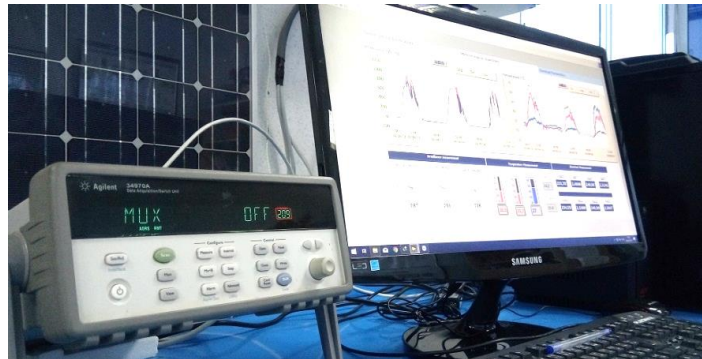
Figure 2.24 Monitoring of the GCPV system using Agilent 34970A DAQ and LabVIEW.

Figure 2.25 shows the graphical code can using Agilent LabVIEW driver to recover all measured data from Agilent 34970A.
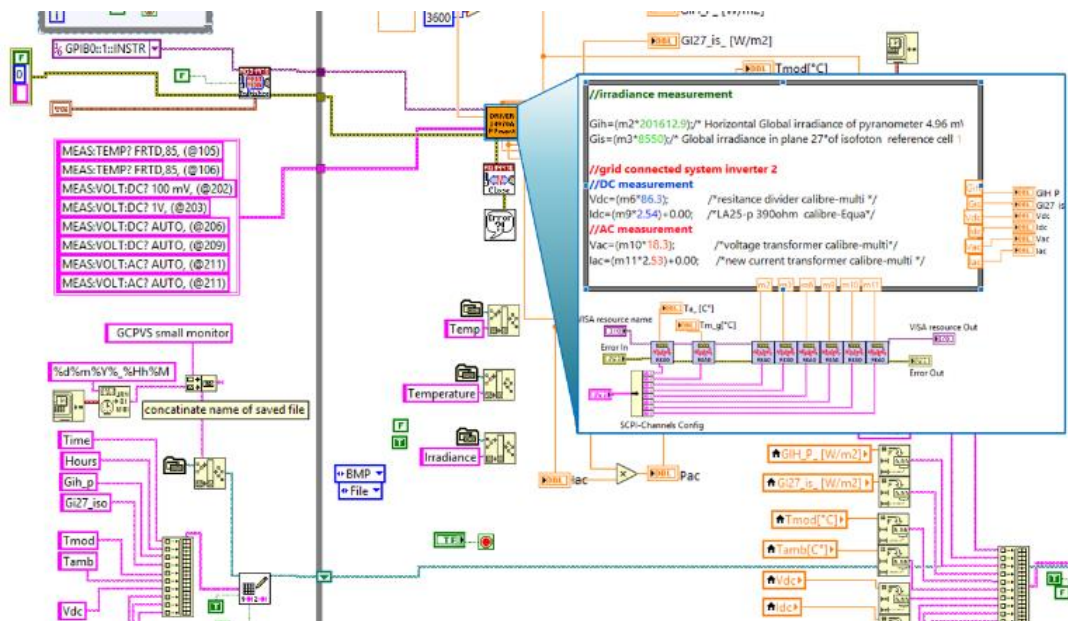
Figure 2.25 Sample of code diagram used to create PV monitoring interface.

After developing the graphical code for data acquisition and other additional programs, we have created a user-friendly and flexible interface (Figure 2.26) with the following features:

- Communication via GPIB or RS232 and Sampling frequency chosen by the user.
- Numerical indicators and Real time chart with time stamp for measured quantities.
- Record all data measurement in a CSV file.
- Remote and online monitoring using TeamViewer.
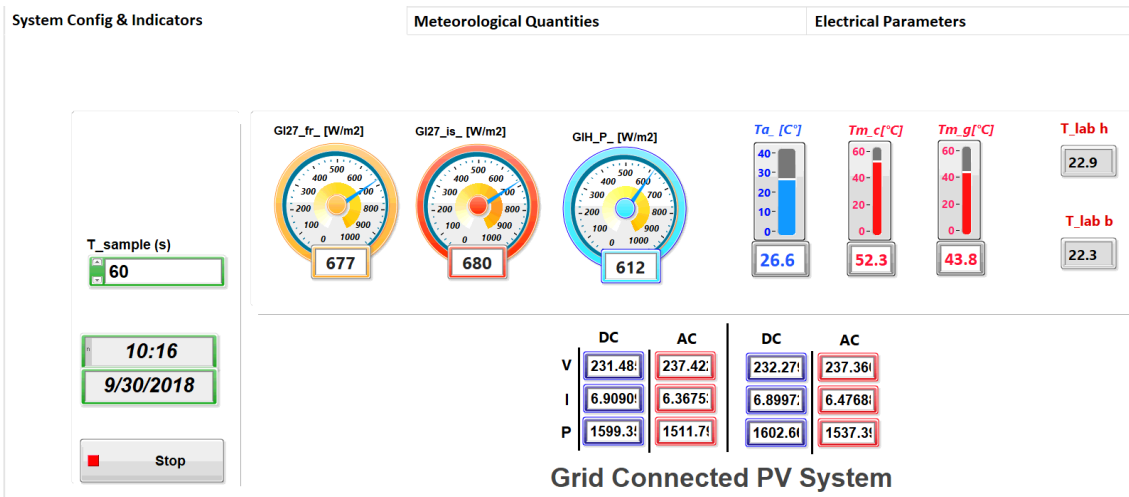
Figure 2.26 Designed monitoring interface under LabVIEW software and agilent 34970A.

Figure 2.27 illustrates the dynamic evolution of measured meteorological quantities with instantaneous indicators.
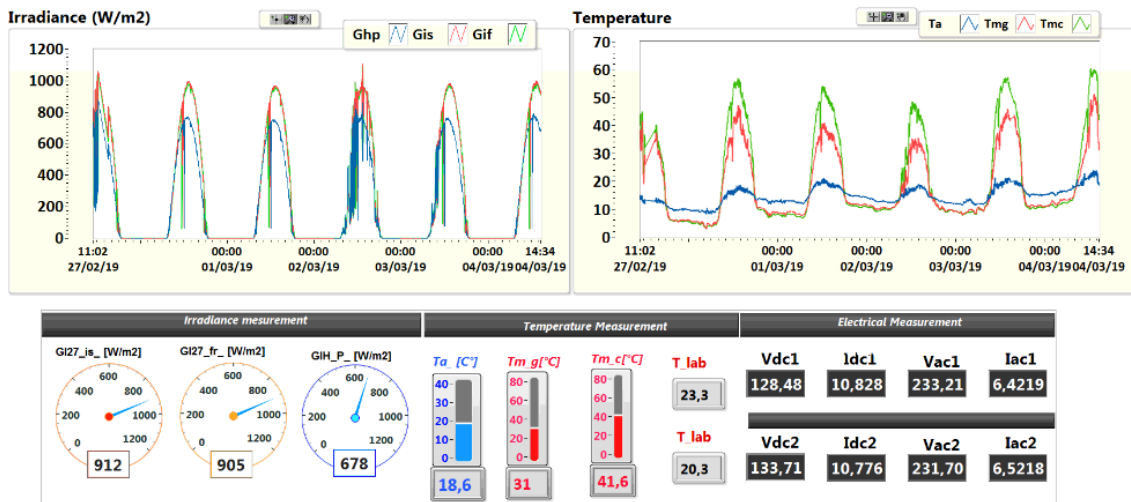
Figure 2.27 Tab_ dynamic evolution of measured meteorological quantities.

Figure 2.28 shows the dynamic evolution of measured electrical quantities in DC and AC side of PV sub-system.
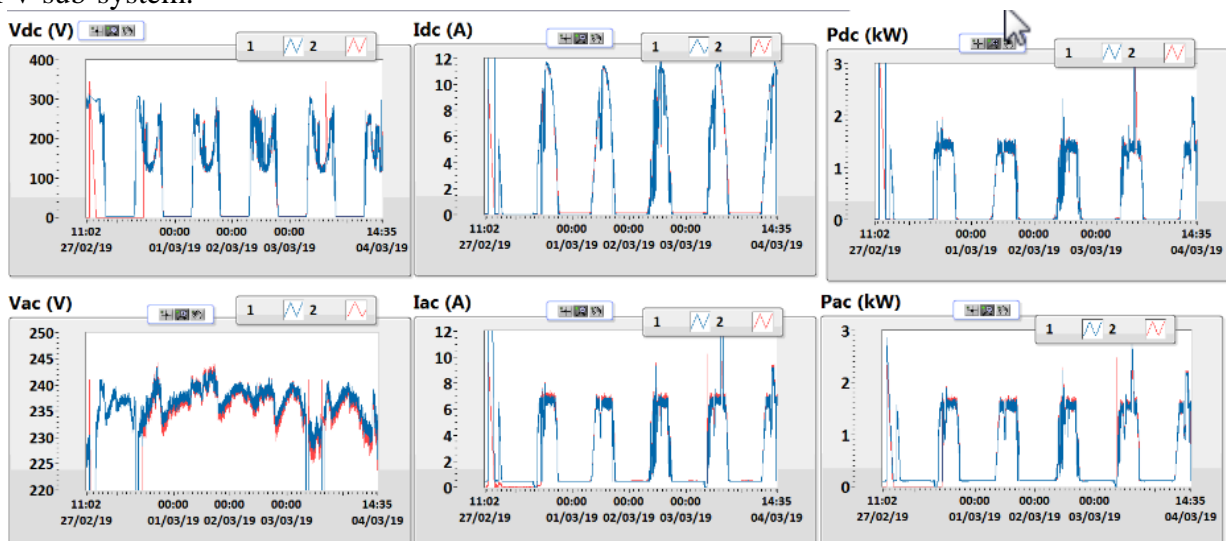
Figure 2.28 Tab_ dynamic evolution of PV sub-system measured electrical quantities.

Figure 2.29 shows the supervision interface shared using teamviewer software for on-line users.

76
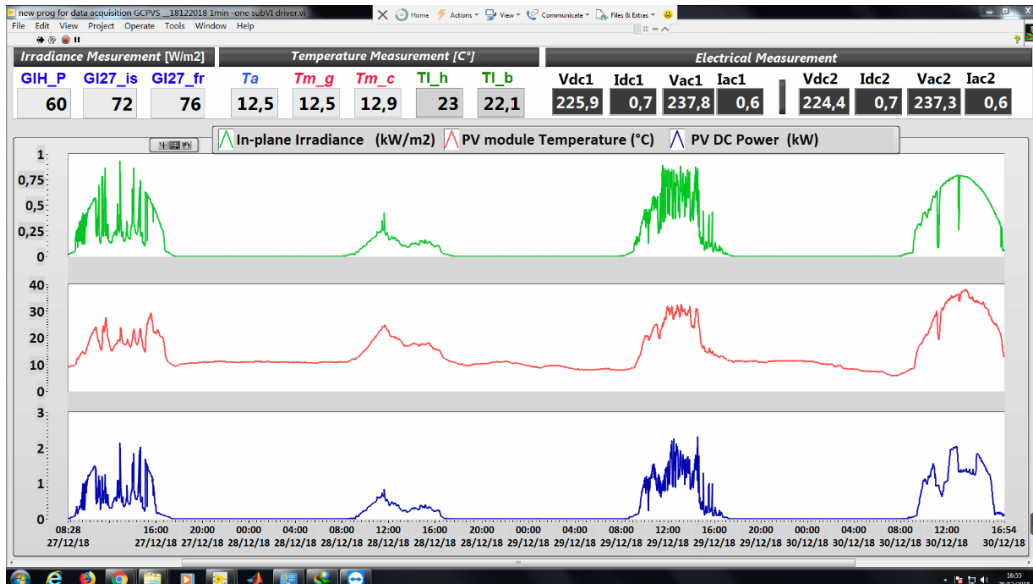
Figure 2.29 On-line monitoring using teamviewer software.

The results were very satisfactory (for data retrieval, display and recording). The measurement accuracy was acceptable, but for a performance monitoring and fault detection system, the sensors must be properly calibrated, for this a second calibration will be mandatory.

Second calibration using SMA monitoring system

The second calibration of the electrical sensors was performed using data from the SMA monitoring system based on inverter and sensor box measurements.

As an example we present the monitoring results of all PV system parameters during a typical day on 19/08/2018 using external sensors, agilent 34970A and LabVIEW.

SMA DAQ record data each five minutes, for this the measured data with agilent 34970A for t=30s, are averaged for t = 5 m, and then compared with the SMA data, and that to validate the measurements and optimize the calibration factor.

Figures 2.30 to 2.38 shown the measurement evolution for each parameter characterizing the GCPV system, where: The external measures with Agilent and LabVIEW are represented in the waveform in red color with acronym $(X_{\_Meas})$, and the SMA data are shown in blue color with acronym $(X_{\_SMA})$.
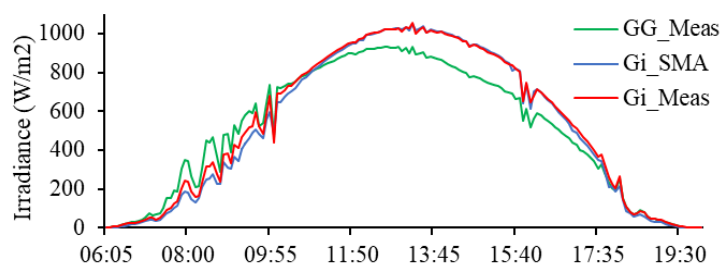
Figure 2.30 Global irradiance on the inclined and horizontal plane.
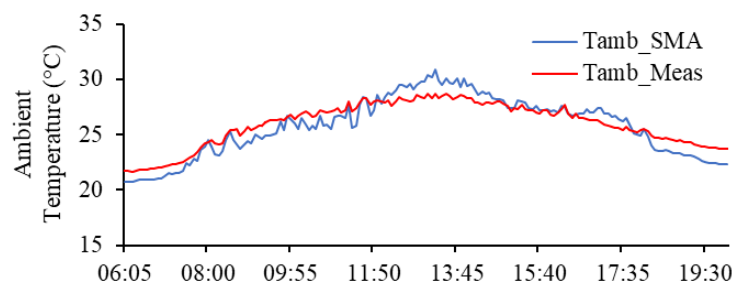
Figure 2.31 Ambient Air Temperature.

77
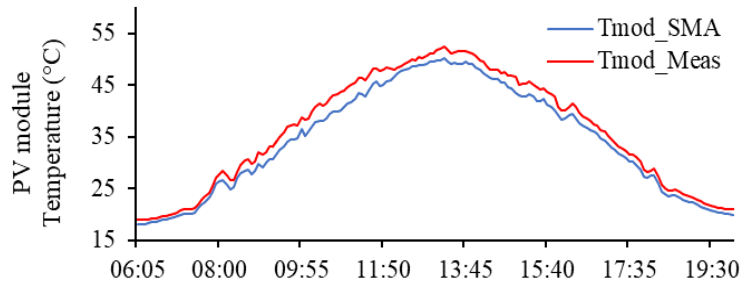
Figure 2.32 PV module Temperature.
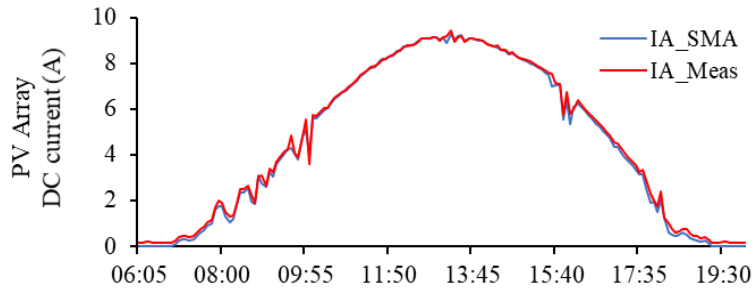
Figure 2.33 PV sub-array output DC current.
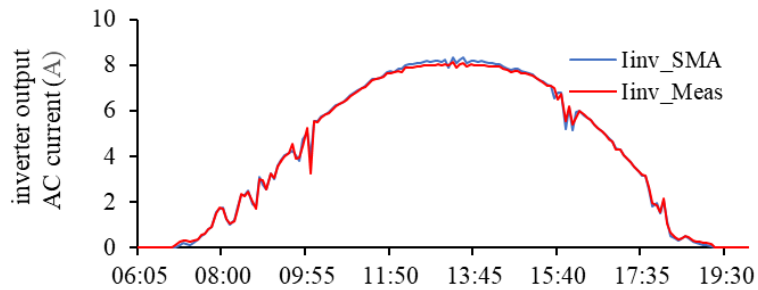
Figure 2.34 Inverter output AC current.
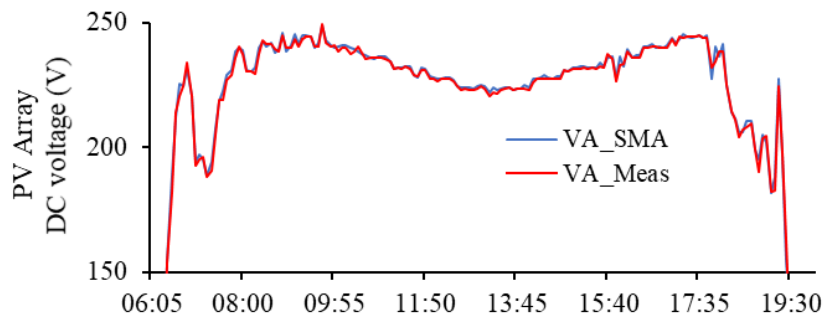
Figure 2.35 PV Sub-Array output DC voltage.
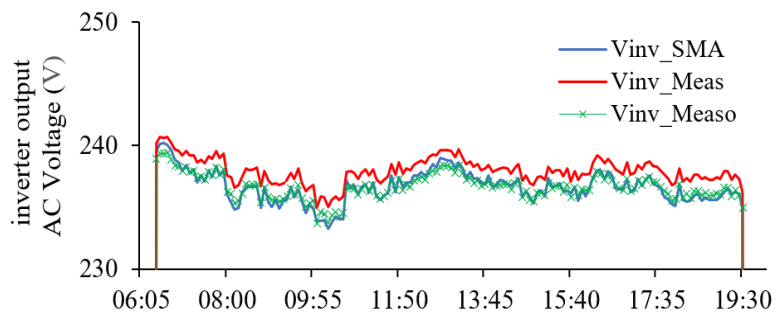
Figure 2.36 Inverter output AC voltage.
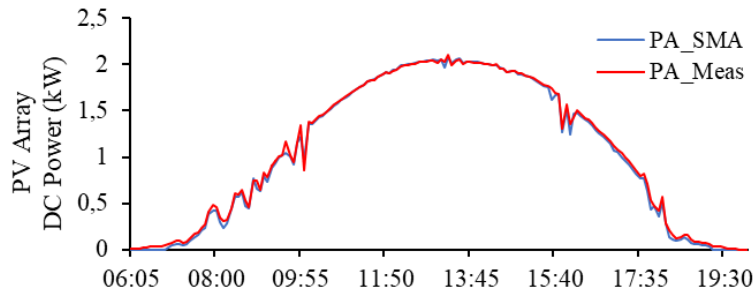
Figure 2.37 PV Sub-Array output DC Power.
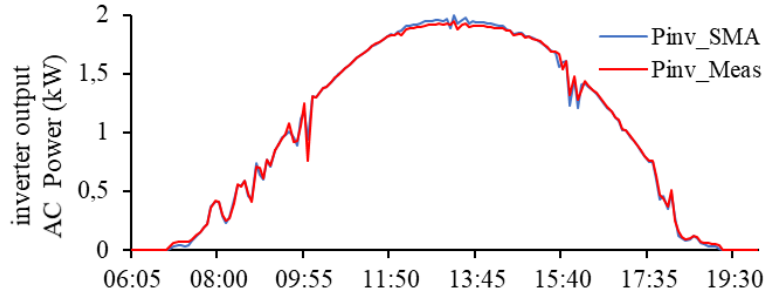
Figure 2.38 Inverter output AC power.

The MAE and RMSE error metrics were used to prove the accuracy and reliability of the sensors installed in front of the SMA monitoring sensors.

$$MAE = \frac{1}{n}\sum_{i=1}^{n}|X_{\_SMA} - X_{\_Meas}| \qquad (1) \qquad RMSE = \sqrt{\frac{1}{n}\sum_{i=1}^{n}(X_{\_SMA} - X_{\_Meas})^2} \qquad (2)$$

Table 2.5 give the calculation results of MAE and RMSE in percent and absolute values.

Table 2.5 Calculation the calculation results of MAE and RMSE in percent and absolute values.

Parameters	G_i	T_{amb}	T_{mod}	V_A	I_A	V_{inv}	V_{invo}	I_{inv}	P_A	P_{inv}
MAE	17.31	0.84	1.80	1.14	0.10	1.22	0.25	0.08	21.55	17.00
RMSE	25.27	0.96	1.95	1.84	0.15	1.30	0.32	0.12	33.84	28.04
MAE (%)	1.24	0.84	1.80	0.33	0.40	0.44	0.09	0.67	0.72	0.57
RMSE (%)	1.81	0.96	1.95	0.53	0.60	0.47	0.11	1.04	1.13	0.93

For the measure of the in-plane irradiance we notice that the error exceeds 1.2% and it comes back to the rapid variation of the irradiance at the beginning of the day because of the clouds. The PV module temperature measurement error exceeds 1.8%, because the two sensors are not installed on the same PV module and are exposed to same condition (ambient temperature, wind speed, shading, dust). The external electrical measurements are very close to the data measured by the SMA SB-3000TL-21 inverter, the error is less than 1%.

Globally From the obtained results, the measurements by the sensors installed in the GCPVS give the desired values with best accuracy and minimum error. As can be seen a good agreement is found with SMA reference measurement.

2.3.4 Monitoring of GCPV system using Keithley 2700

Due to data acquisition problems with unexpected bugs using the Agilent 34970A datalogger, we have used an older Keithley 2700 data acquisition with 40-multiplexer measurement module channels [242], this data logger is more reliable and ensures continuous monitoring.

In this section the monitoring will be carried out for the three PV subsystems, the used sensors are mentioned in Tables 3.3 and 3.4. Twenty (22) sensors were connected to 7702 40-channel acquisition modules, Pt 100 sensors (3) will be connected in 4-wire circuit for best accuracy.

Figure 2.39 shows a picture of Keithley 2700 DAQ with PC. To recover the data measured by Keithley 2700 in the LabVIEW environment, we have used the driver with a measurements configuration according to the signal type at the output of the sensors, namely: 1) DC voltage, 2) RTD 4 wire, 3) thermocouple, and 4) AC voltage (Figure 2.40).

Figure 2.39 Monitoring of GCPV system using Keithley 2700 DAQ under LabVIEW.
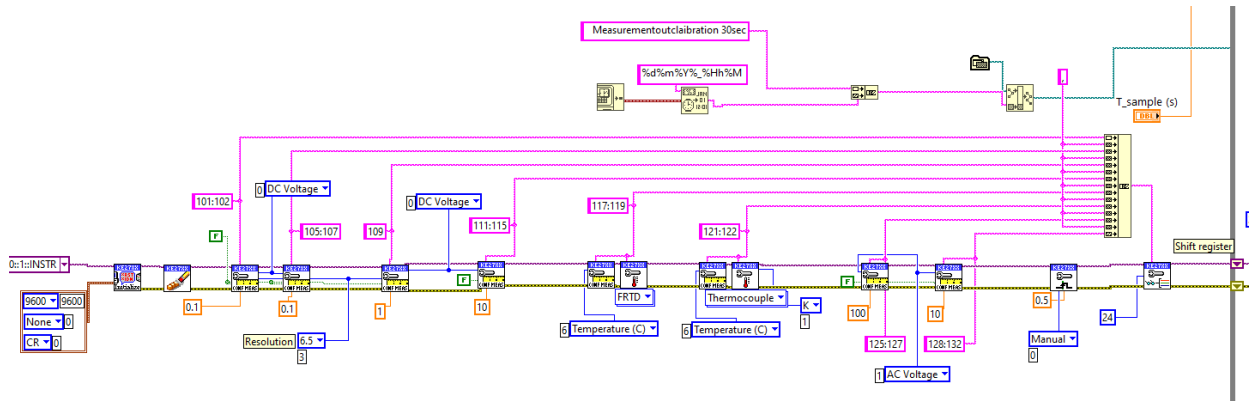
Figure 2.40 Code diagram_Config channel and recording for keithley 2700 DAQ.

After configuration, we have developed the graphical code for 1) scan channels, 2) calibrating and display measurement, and 3) recording data (Figure 2.41).
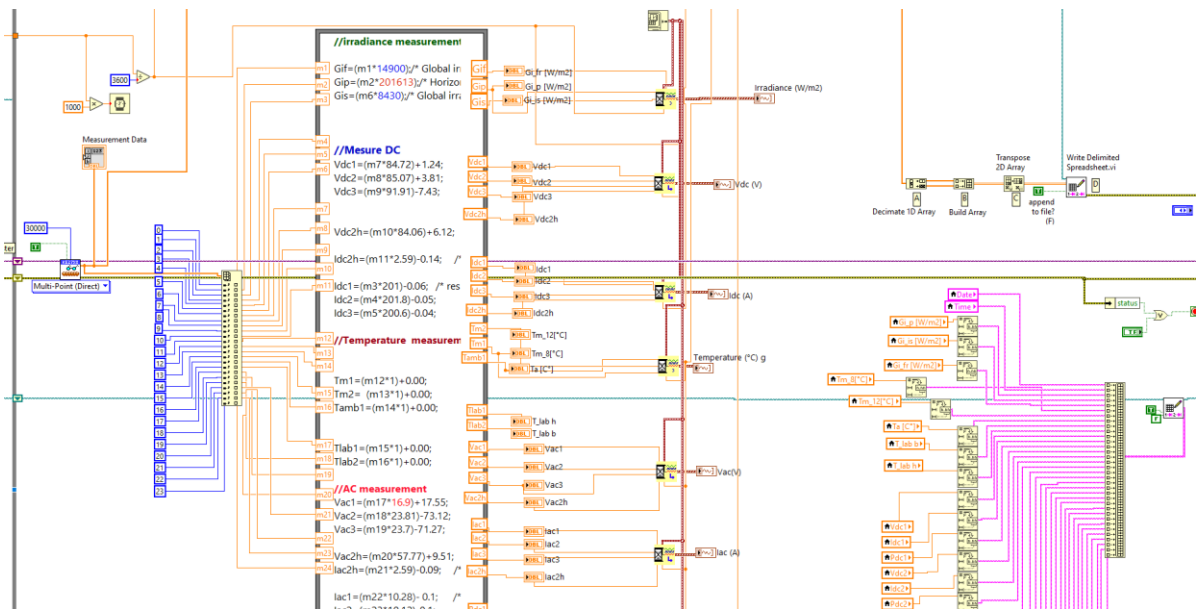
Figure 2.41 Code diagram for Channel Scan, calibration, display and recording data for keithley 2700 DAQ.

After developing and optimizing the graphical code for data acquisition and other additional programs, we have created a user-friendly and flexible interface with three main Tab namely: 1) system config and indicators (Figure 2.42), meteorological parameters (Figure 2.43), and electrical parameters (Figure 2.44).

80
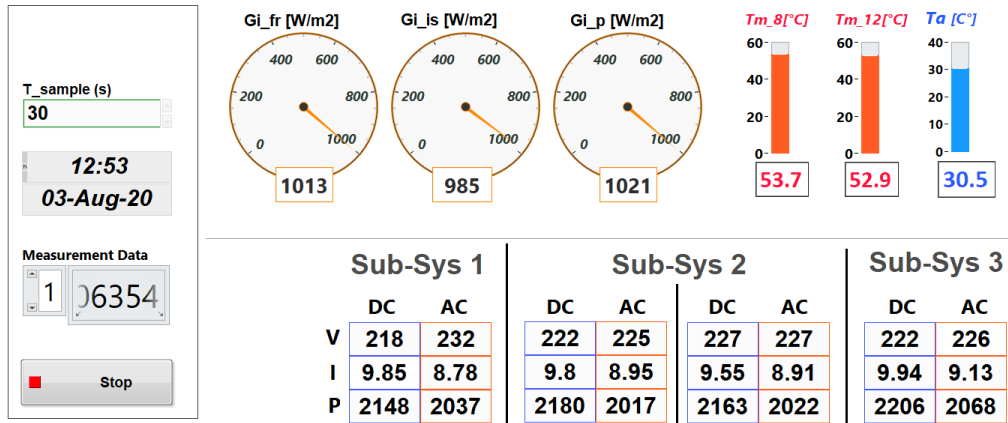
Figure 2.42 Designed monitoring interface using LabVIEW and keithley 2700 DAQ for three sub-system of the GCPVS.
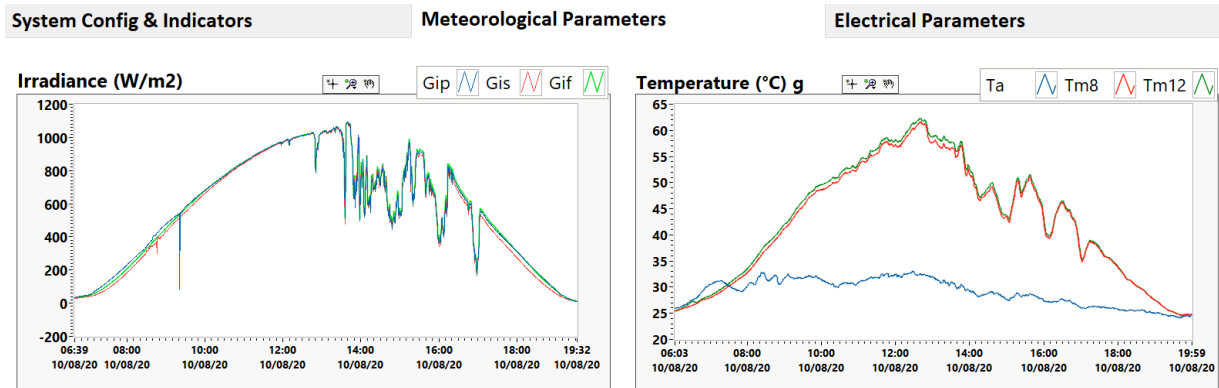
Figure 2.43 Tab_Real time meteorological measurement.
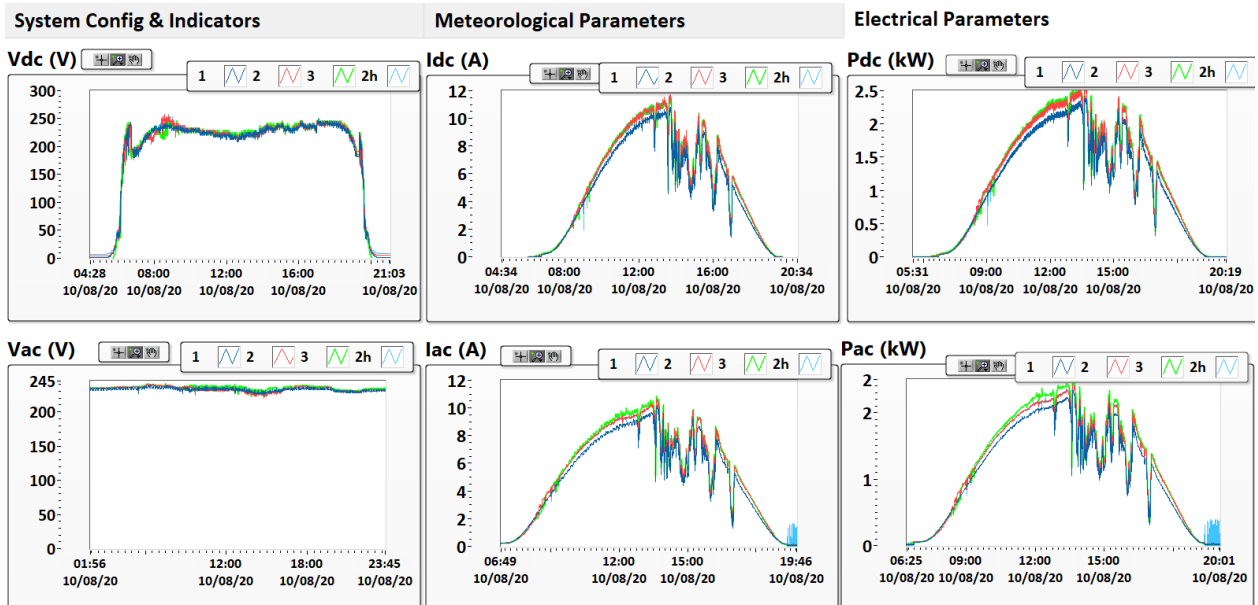
Figure 2.44 Tab_Real time electrical measurement for three PV sub-system.

The results were very satisfactory for retrieval and recording data. The accuracy of measurement are very suitable for three PV sub-system , the visualization of the first tab are designed using new NXG indicators. However, no error timeout encountered during data acquisition using keithely 2700, this device is very reliable under LabVIEW.

81

2.3.5 Monitoring of GCPV system using Fluke 2638A

In order to improve data acquisition as well as become familiar with other DAQ units, we installed Fluke 2638A (Figure 2.45). This device has the same features of the previous DAQ units, plus the following features [243]:

- Graphic color display with easy-to-use menus.
- Real-time plotting of data from up to four channels simultaneously with history recall.
- Built-in memory of 57,000 data records and configuration files, and a USB port allows collection and storage directly to a USB drive.
- USB and LAN connection interfaces are available.
- Complies with international category II security standards with two-level (administrator / authorized user).
- delivered with a factory calibration report.

Figure 2.45 Meteorological and electrical data monitoring measured using Fluke 2638A & LabVIEW.

To recover the data measured by Fluke 2638A in LabVIEW, we used the driver with a measurements configuration according to the signal type at the output of the sensors, namely: 1) DC voltage, 2) thermocouple K, 3) RTD 4-wire, and 4) AC voltage (Figure 2.46).
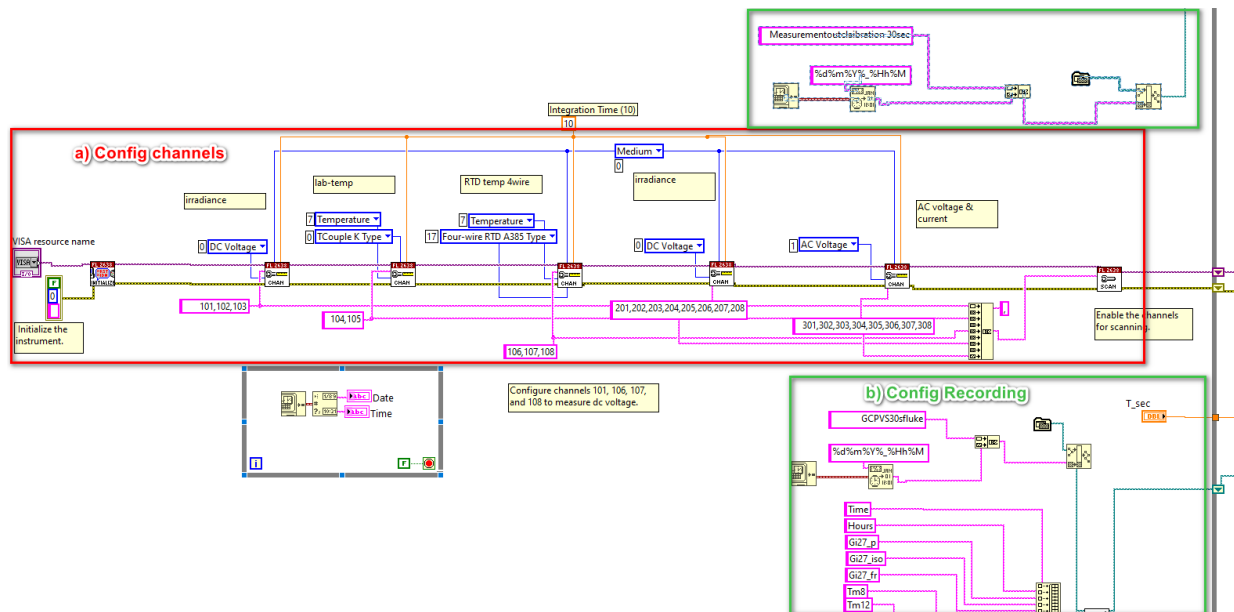
Figure 2.46 Code diagram_ a) config channel and b) config recording for Fluke 2638A DAQ.

After configuration, we have developed the graphical code for a) scan channels, c) measurement indexing and calibrating e) measurement visualization, and f) data recording (Figure 2.47).
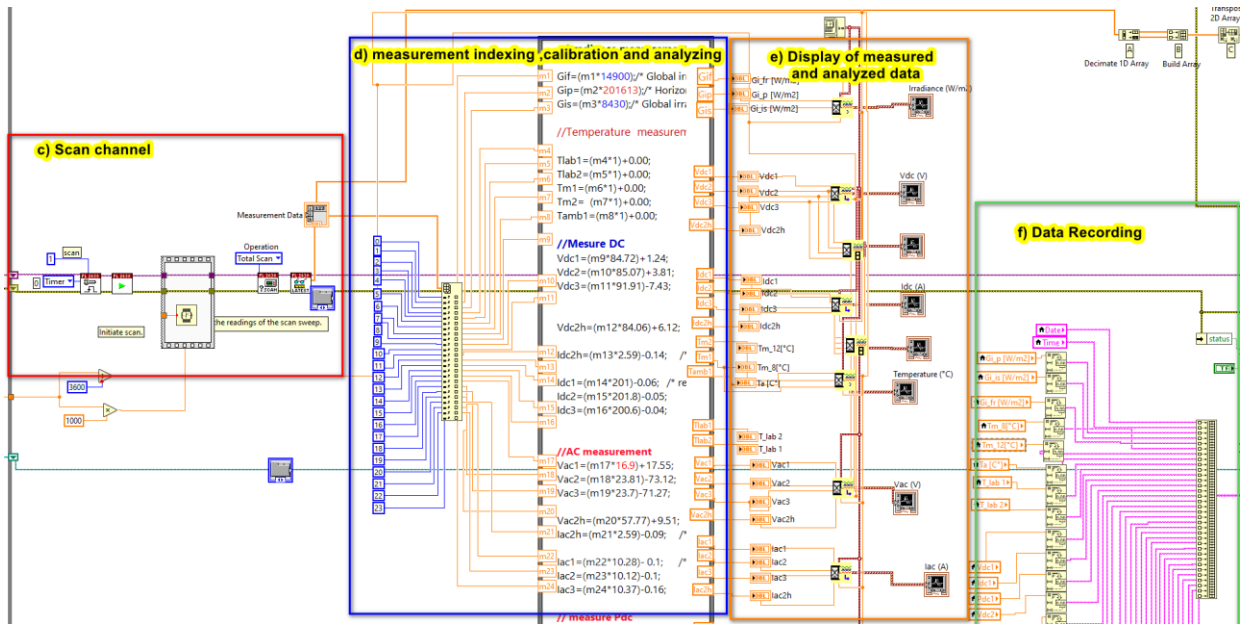
Figure 2.47 Code diagram for channel c) scan, d) calibration, e) display and f) data recording for Fluke 2638A DAQ.

After having developed and optimized for the third time the graphic code for the acquisition, visualization and recording of data, we have created a new version of the user interface based on NXG style with four main tabs namely:

1) System config and overview of instantaneous measured data (Figure 2.48).
2) Meteorological parameters and indicators clusters (Figure 2.49).
3) Waveform chart for DC & AC electrical parameters (Figure 2.50).
4) Real-Time analysis using ratio representation (Figure 2.51).
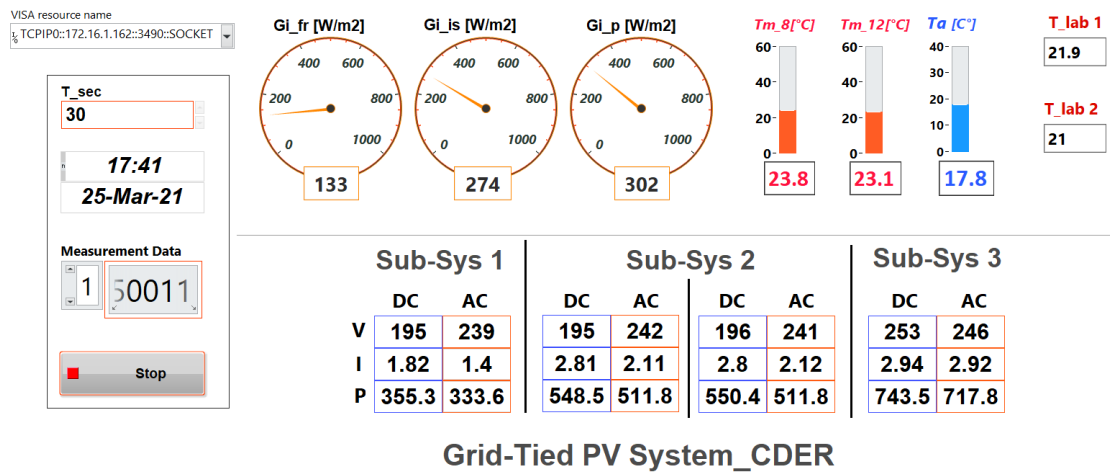
Figure 2.48 GCPVS Home user interface updated with additional sensors.
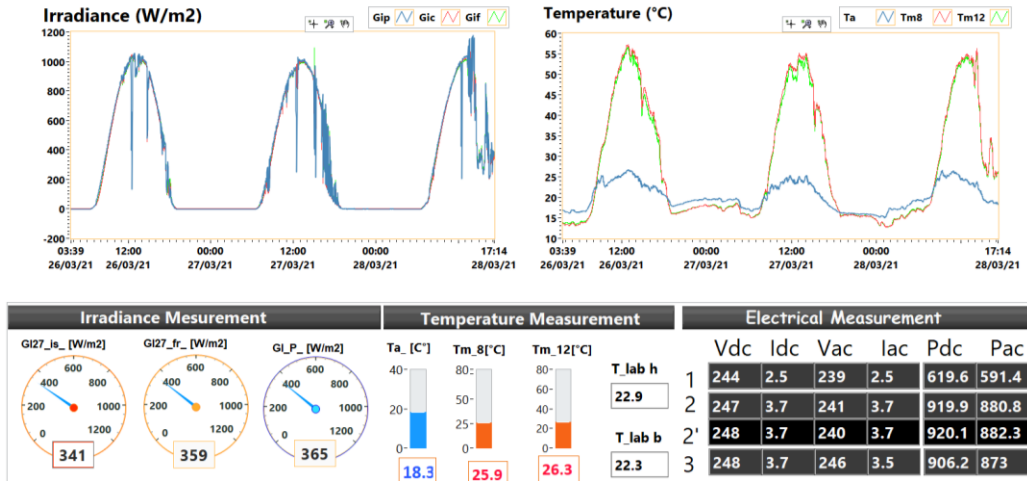
Figure 2.49 Tab_real time meteorological measurement and numerical measurement cluster.
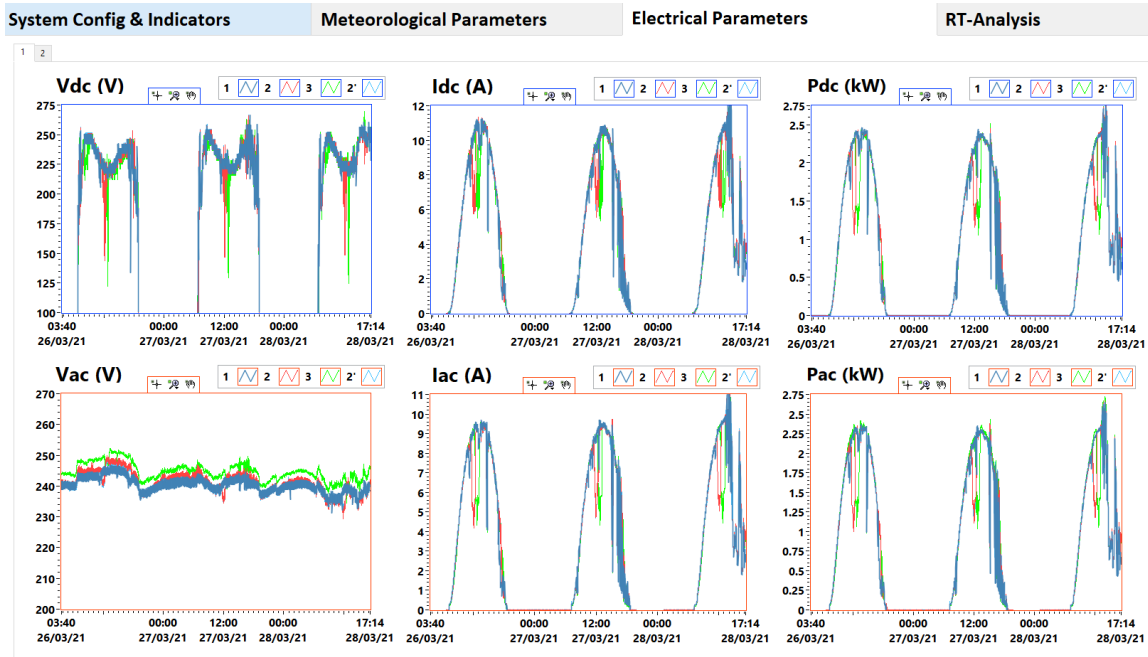
Figure 2.50 Tab_real time electrical measurement _page1_ separated DC & AC waveform.
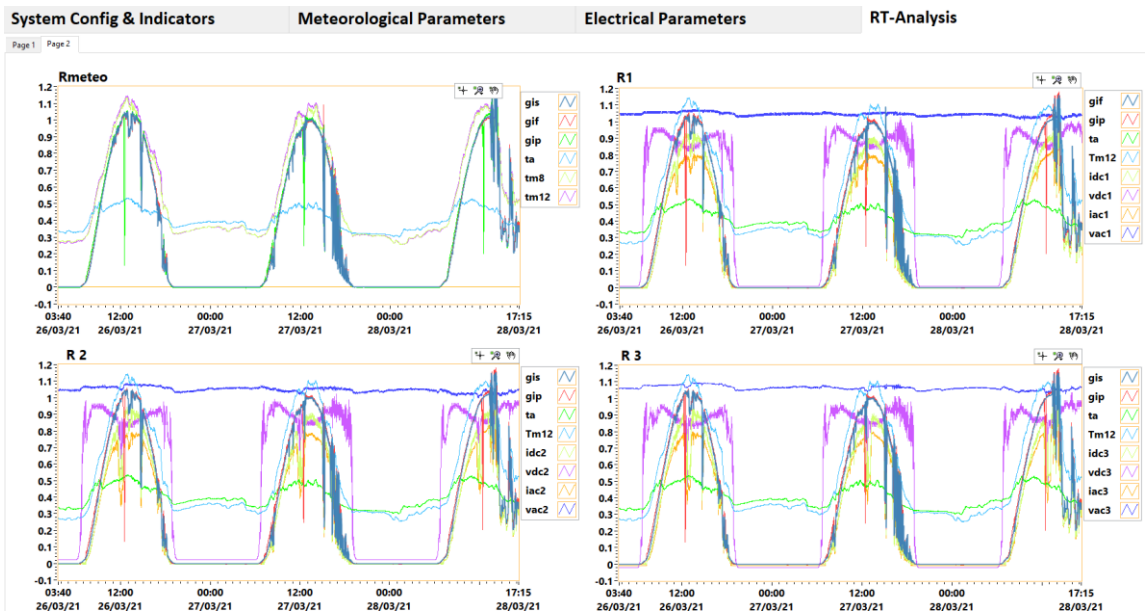
Figure 2.51 Tab_real time analysis _page2_ratio data presentation in the same waveform for each sub-system with meteorological data .

As shown in the figures 2.48 to 2.51, The results were very satisfactory for retrieval and recording data. The measurement are very accurate for three PV sub-system, the all tabs are designed using NXG indicators and chart. A fourth tab is added to display and analyze all measurement in the same time using ratio factor for each measure. Access to Fluke 2638A was very easy using the IP address. However, timeout error is encountered during data acquisition using Fluke 2638A with Ethernet communication, Maybe there is a driver programming problem, whatever the program needs to be revised and optimized especially if it will have problems on the communication network. In the other hand, no problem are noted using recording with USB drive.

2.4 Measurement and monitoring in PV systems: cases study

In this section, we present a data acquisition and monitoring case studies applied to different types of PV systems at CDER.

Case 1: LabVIEW based monitoring for an off-grid PV System.

In this case, we present a monitoring of an off-grid PV system. The PV system are composed of two symmetrical subsystems, connected in the parallel to an 48V-1000Ah batteries bank. The PV array composed of two PV generators (Table 2.6), can generates a total peak power of 3.66 KWp (Figure 2.54).

Table 2.6 Main features of PV generators.

	Module technology	Manufacturer	Connection	Total power
PV generator 1	monocrystalline 155W	condor	4 modules in series	1860Wp
PV generator 2	Polycrystalline 150W		3 strings in parallel	1800Wp
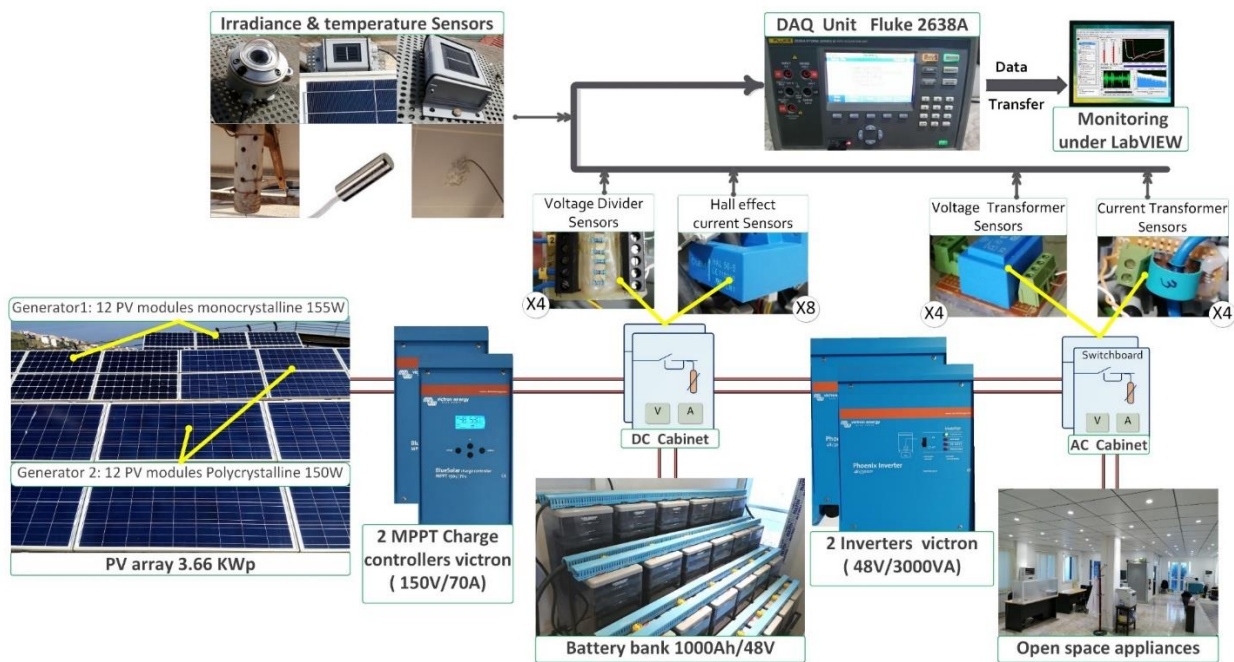
Figure 2.52 Synoptic diagram of the off grid PV system with monitoring.

Figure 2.53 shows the irradiance sensors using pyranometer for global horizontal irradiance and two PV reference cell to measure the tilted irradiance at 27° and 36°, the PV reference cell are equipped by an internal PT 100 sensor to measure the cell temperature. Figure 2.54 illustrates the temperature sensors using pt100 probe inserted in the radiation shield for air ambient measurement and pt100 surface sensor to measure the temperature of the module back sheet. Figure 2.55 shows the voltage and current sensors mounted in the DC cabinet. Voltage divider sensors are used to measure the DC voltage of PV generator and batteries. While the Open loop Hall effect sensors (LEM HAL-50) are used to measure the DC current of PV array, charge controller output, batteries and inverter input (load consumption).
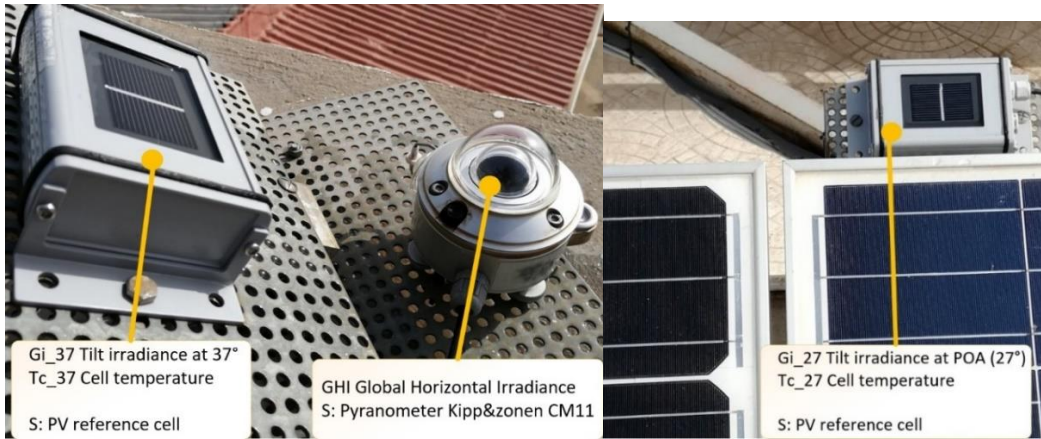
Figure 2.53 Irradiance sensors including temperature cell measurement.
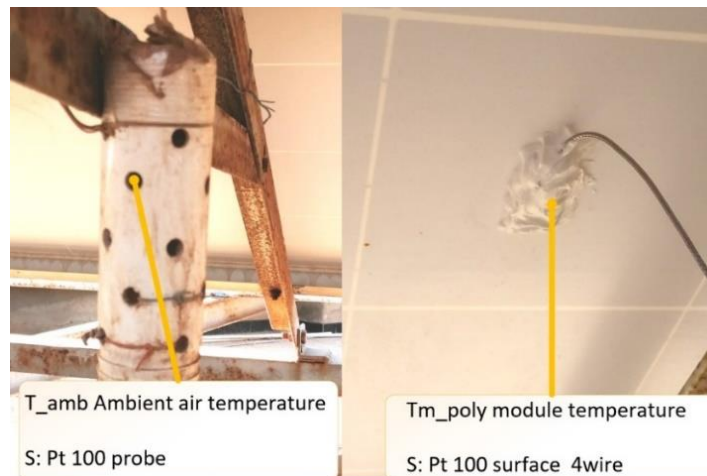
Figure 2.54 Sensors for air ambient and PV module Temperature.
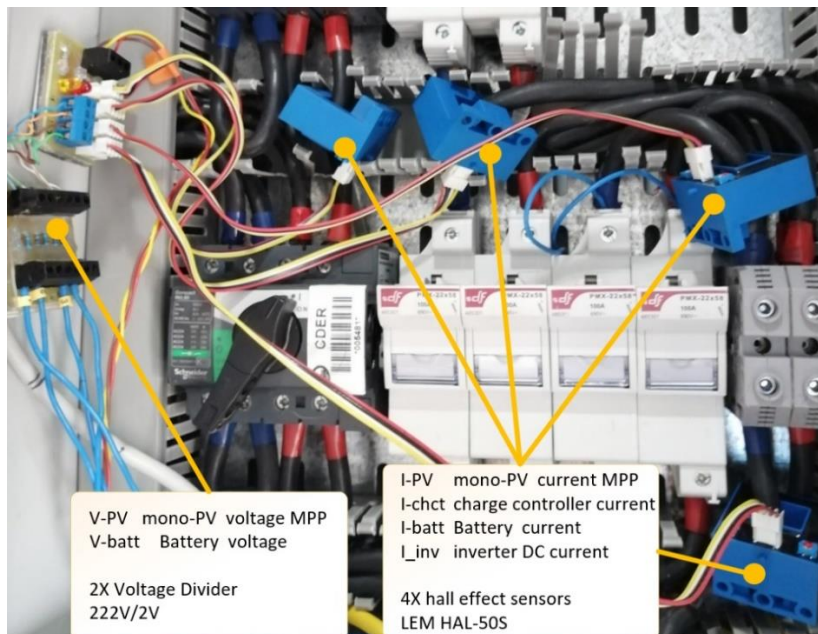
Figure 2.55 Voltage and current sensors mounted in the DC cabinet.

Figure 2.56 illustrates the voltage and current sensors mounted in the AC cabinet. Voltage transformer sensors are used to measure the AC voltage at the output of inverter and AC voltage from grid, while the current transformer sensors are used to measure AC current at the output of inverter and AC current from grid.
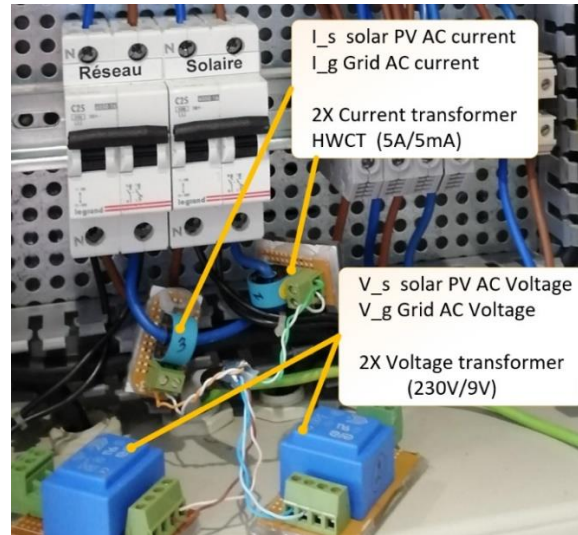
Figure 2.56 Voltage and current sensors mounted inside the AC cabinet.

The specifications of the environmental and electrical sensors are summarized respectively in Tables 2.7 and 2.8. The calibration of the sensors was performed by comparison with other sensors and instruments used as a measurement reference.

Table 2.7 Environmental sensors used, and their characteristics.

Measured parameters	Sym.	Unit	Sensor type	Sensor Reference	Accuracy	Calibrating reference	Calibration factor
Global horizontal irradiance	GHI	W/m^2	Pyranometer	Kipp & zonen CM 11	2%	Pyranometer CMP21	201613
in-plane Irradiance _27°	$G_{i,27}$		PV reference cell	imt-solar Si-mV-85-Pt100	Class A IEC61724-1	imt-solar datasheet multimeter	17352
in-plane Irradiance _37°	$G_{i,37}$						17902
PV cell temperature 27°	$T_{c,27}$	$°C$	Pt100 4-wire		Class A IEC 60751	Calibrated by imt-solar manufacturer RTD measured by fluke 2638	
PV cell temperature 37°	$T_{c,37}$						
Ambient air Temperature	T_{amb}	$°C$	Pt100 probe 4-wire	WZP-Pt100	0.5 %	Thermometer Multimeter	Direct Measurement
Temperature of the Polycrystalline module	T_{mp}		Pt100 surface 4-wire	TC-direct	0.5 %		

Table 2.8 Main characteristics of electrical sensors used for monitoring.

Measured parameters	Sym.	Unit	Sensor type	Sensor Reference	Accuracy	Cost (DZA)	Calibrating reference sensor	Calibration factor
PV generator voltage	V_{pv}	V	Voltage Divider	222V/2V	1%	50	multimeter	22.9
Battery voltage	V_{Bat}							
PV generator current	I_{pv}	A	Open loop Hall effect	LEM HAL-50 & HAS-50	0.8 %	5000	Clamp-meter (Extech MA220), Victron charge controller and Datasheets	12.5
Battery current	I_{Bat}							
Charge Controller current	I_{Chct}							
Inverter input current	$I_{inv,i}$							
Inverter output voltage	$V_{inv,o}$	V	Voltage transformer	230V/9V	1 %	450	multimeter	9.4
Grid voltage	V_g							
Inverter output current	$I_{inv,o}$	A	Current transformer	HWCT (5A/5mA)	1 %	380	Clamp-meter (Extech MA220), Victron charge controller and multimeter	10.63
Grid current	I_g							

Using fluke 2638A the chosen sampling time are 30 sec. for the whole of meteorological and electrical measurement according to standard norm IEC 61724, which gives 2880 samples per day. To recover the instantaneous data measured by fluke 2638A in the LabVIEW environment, we have used the driver with a measurements configuration according to the signal type at the output of the sensors, namely: 1) DC voltage, 2) RTD 4 wire, and 4) AC voltage (Figure 2.57). Figure 2.58 illustrates the code diagram for measure, calibration and visualization.
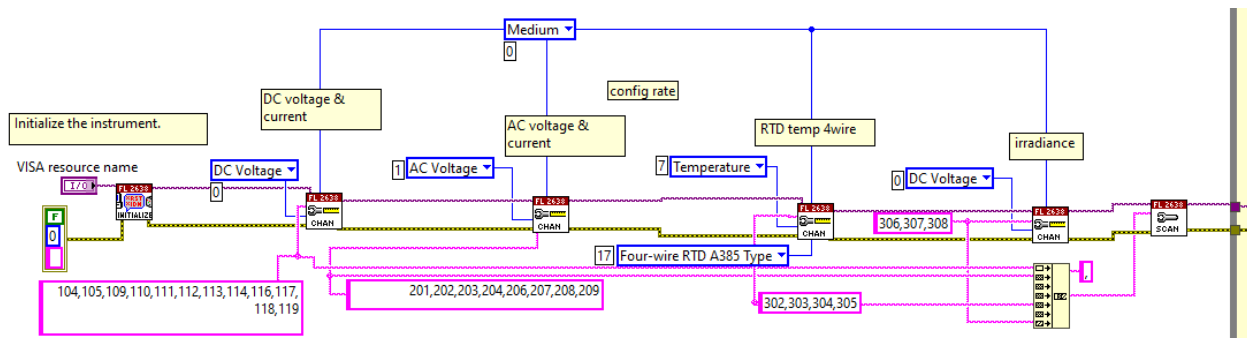
Figure 2.57 Code diagram for config measurement.
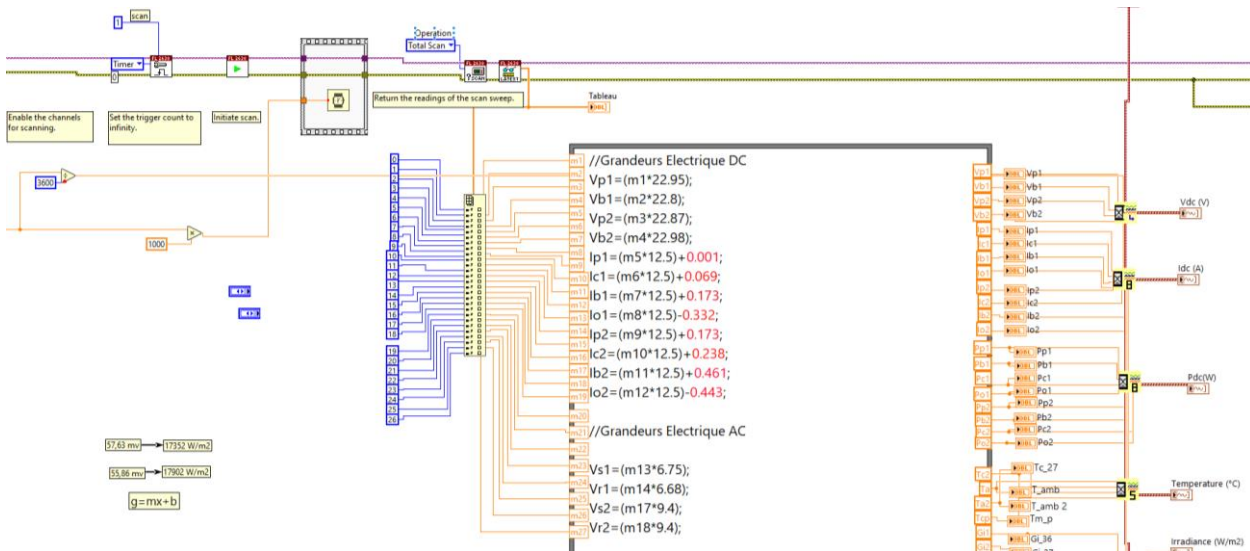
Figure 2.58 Code diagram for measure, calibration and display.

Following the graphical code development for data acquisition and other supplementary programs, we have designed the first version a user-friendly and flexible interface with three main Tab namely: indicators, config, and graphs (Figure 2.59).

The second version showed in Figure 2.60 was designed with NXG style to measure only the meteorological and environmental data with fast sampling for 5 sec or 10 sec.

The third version was designed by our colleagues at CDER, schematic monitoring represents all the components of the PV system with dynamic arrows showing the direction of the energy flow (Figure 2.61).
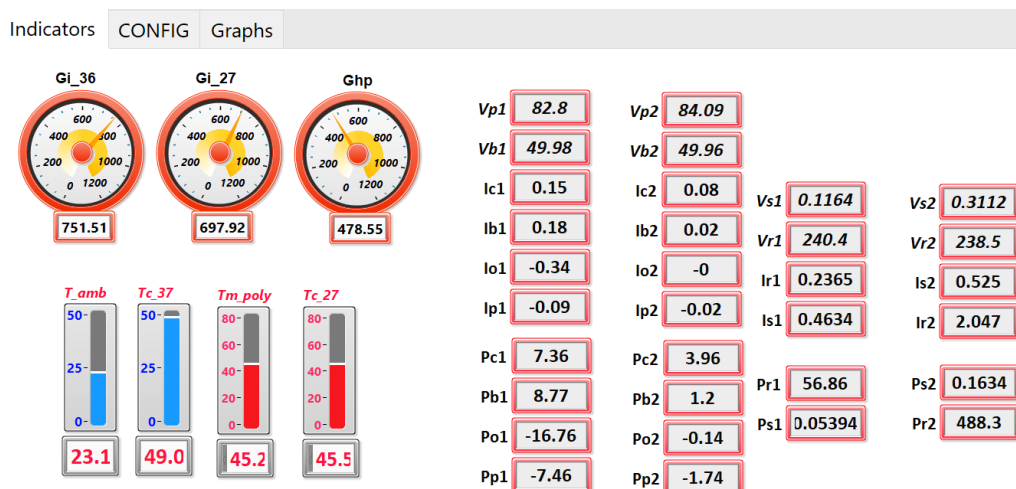
Figure 2.59 Version 1 of designed monitoring interface for the off-grid PV system under LabVIEW.
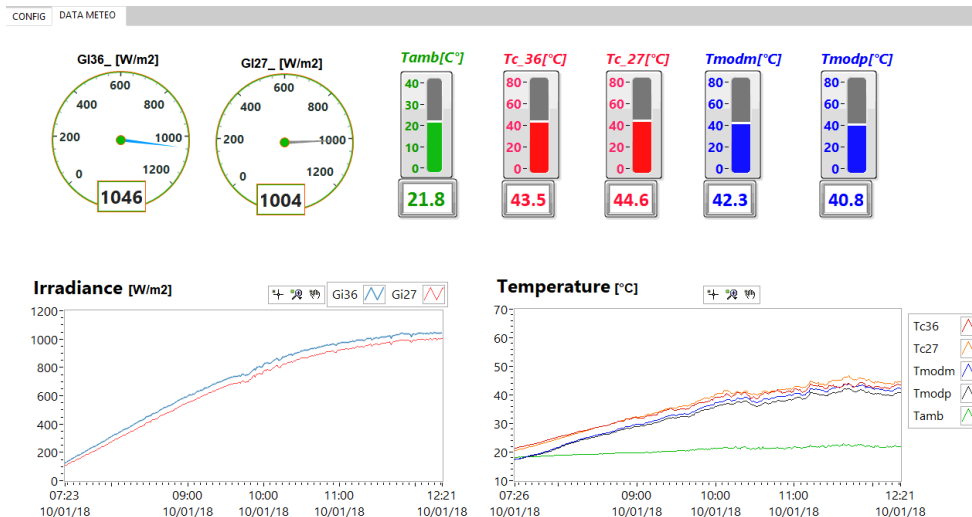
Figure 2.60 Version 2 of designed monitoring interface for the off-grid PV system under LabVIEW.
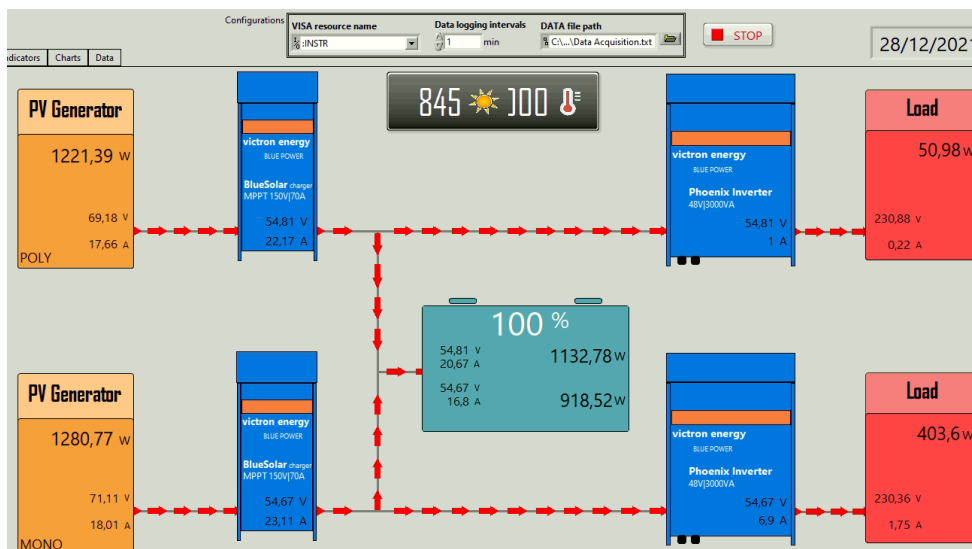
Figure 2.61 Version 3 of designed monitoring interface for the off-grid PV system under LabVIEW.

As an example we present the measurement of one PV sub-system during one day (13/20/2020) using external sensors, Fluke 2638A and LabVIEW.

Figures 2.62 to 2.67 shown the measurement evolution for each parameter characterizing the off grid sub system.

Figure 2.62 shows the irradiance measurement for global horizontal and tilted irradiance at 27° and 36°. Figure 2.63 illustrates the temperature measurement for air ambient, PV cell temperature at 27° and 36°, and PV module back sheet.

Figure 2.64 shows the DC voltage measurement of PV generator 2 and batteries. Figure 2.65 displays the DC current measurement of PV generator, charge controller output, batteries and inverter input. Figure 2.66 illustrates the AC voltage measurement at the output of inverter and from the electrical grid. Figure 2.67 shows the AC current measurement at the output of inverter and from the electrical grid.
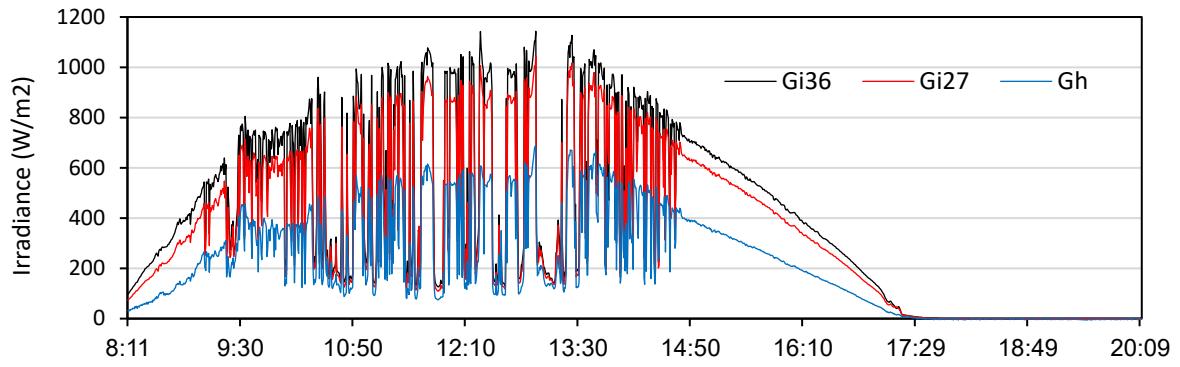
Figure 2.62 Global irradiance measurement on the inclined plane at 27° (Gi27) and 36° (Gi36) as well as on the horizontal plane (Gh).
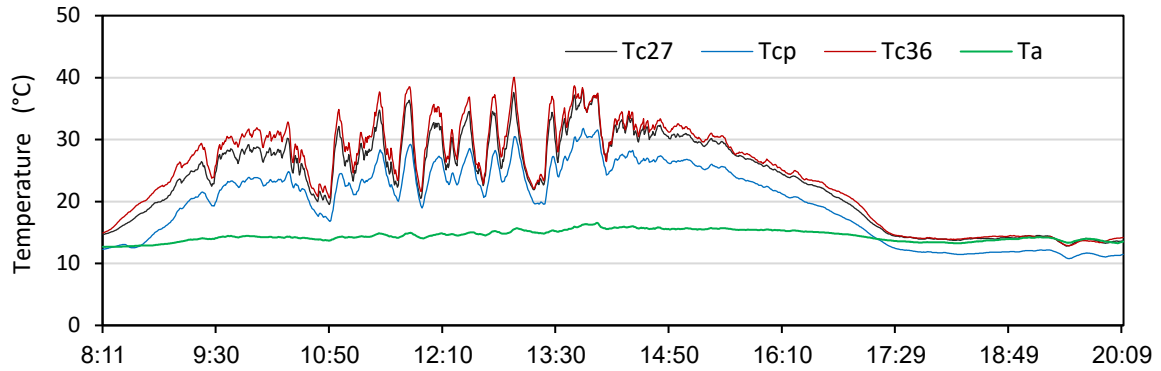
Figure 2.63 Temperature measurement of air ambient (Ta), PV cell at 27° (Tc27), PV cell at 36° (Tc36), and polycrystalline modules at 27° (Tcp).
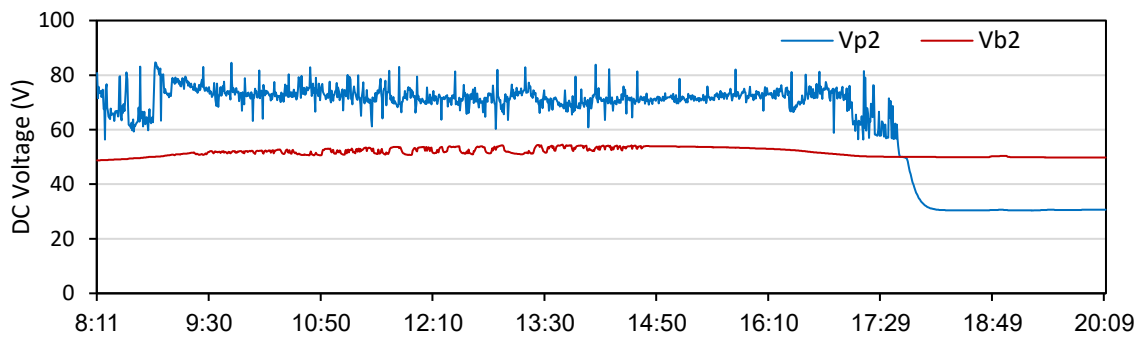
Figure 2.64 DC voltage measurement of PV generator 2 (Vp2) and batteries (Vb2).
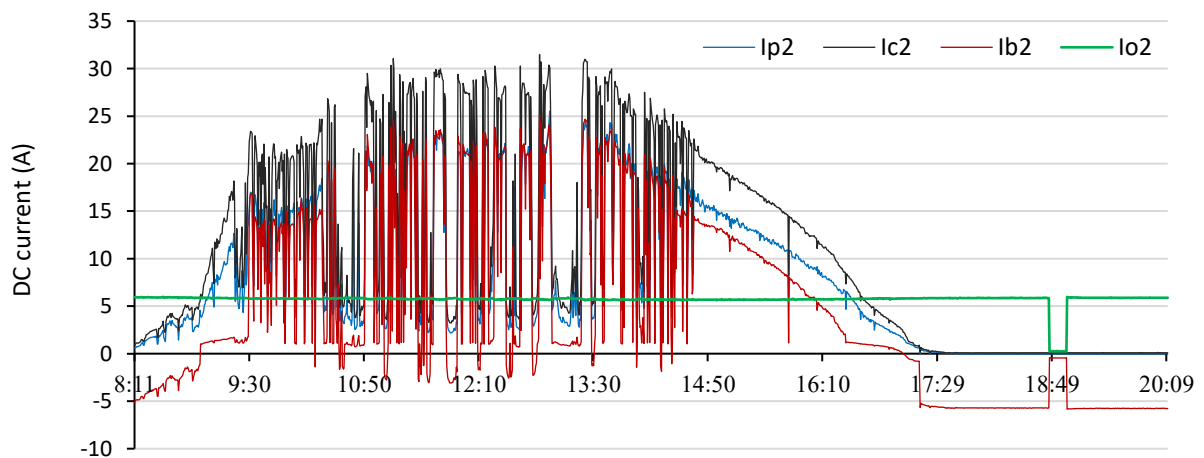
Figure 2.65 DC current measurement of PV generator 2 (Ip2), charge controller output (Ic2), batteries (Ib2) and inverter input (Io2).
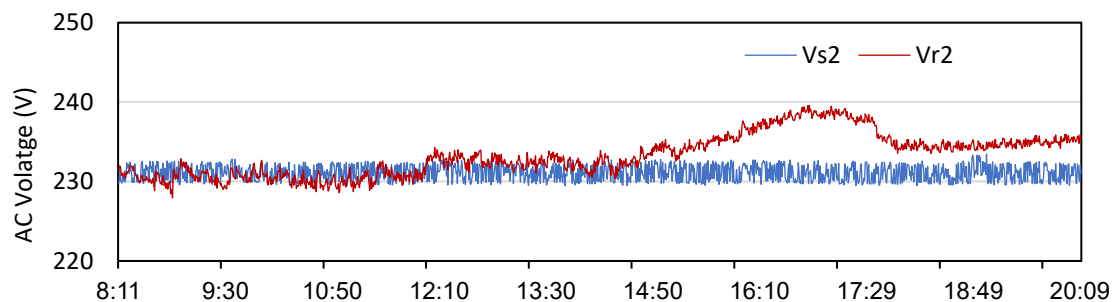
Figure 2.66 AC voltage measurement at the output of inverter (Vs2) and from the electrical grid (Vr2).
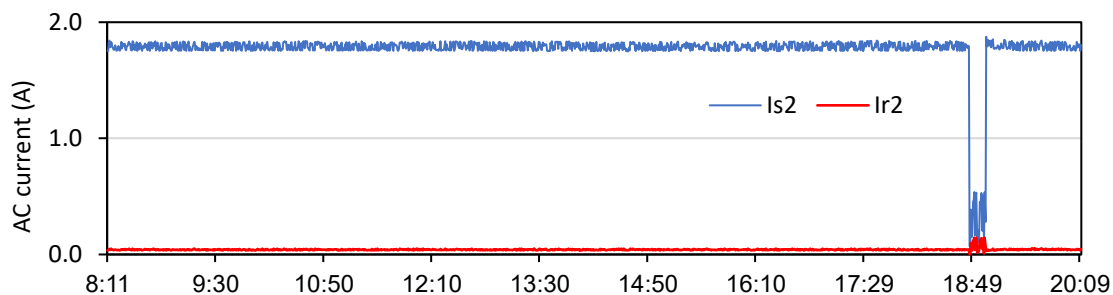
Figure 2.67 AC voltage measurement at the output of inverter (Is2) and from the electrical grid (Ir2).

As shown in the figures presented above, the designed interfaces are very user-friendly, the measurements of the environmental and electrical parameters were well calibrated. for measurements on the AC side, fluctuations are observed.

Case 2: Monitoring & control of a PV water pumping test bench using LabVIEW

In this case, we present data acquisition and control of a photovoltaic (PV) pumping system using LabVIEW.

We would present this system because it contains several additional features from the other system regarding the following items:

- Pressure level and flow rate sensors with 4-20 mA output
- Actuators (On/Off pump controller, Pneumatic valve, regulation air valve).
- Regulation of manometric pressure to simulate pump level by Control of valve.

The first phase in this section deals with the electronic instrumentation, which includes the wiring of sensors and actuators to the data logger Agilent 34970A, then the conditioning and the calibration ensured by the latter. However, the second phase is dedicated to the development of a program under LabVIEW environment and design a convivial graphical user-interface to retrieve data measured by different sensors and control pneumatic valves installed in the PV system in real time. The software platform designed has served as a system of monitoring and control of photovoltaic pumping system. All data obtained from the user-interface were recorded and archived in a database.

Description of PV Pumping System test bench
Test bench should be equipped with different sensors for each variable (such as irradiation, temperature, pressure, flow, water level, voltage and current) to better represent operating status and performances of PV pumping system in real time, it will:

- ✓ Test and evaluate PV pumping systems.
- ✓ Realize a database for the motor-pump system.
- ✓ Select the best pump for each application.
- ✓ Modeling photovoltaic pumping systems (PV module, inverter, pump-motor).

The Experimental test bench (Figures 2.68 & 2.69) was made of stainless steel and is easily removable. We distinguish the following parts:

- Water-Well
- Water-air tank
- Pump & inverter DC/AC
- Discharge branch between the well and the tank
- Discharge branch which includes the tank return to well
- Air compressor
- Sensors and transducers
- Actuators (Pneumatic valves)
- Control and display panel
- Connection cabinet for external measurements with additional instrumentation
- The PV array is composed of 30 modules A-75, for a total output 2.2 kWp
- Agilent 34970A Data Acquisition / Switch Unit (Data Logger) for measure and control.
- RS232 or GPIB cable

The management of the tank pressure applied to the pump, allows us to simulate the heights pumping in the water-well (2m) going from 0m to 120m, and 0-30 m^3/h   for the water flow pump. The pump inside water-well uses as power supply photovoltaic array 0 to 2.2 kW or programmable DC Power supply 0 to 3kW.

Figure 2.68 Solar pumps Test bench picture.
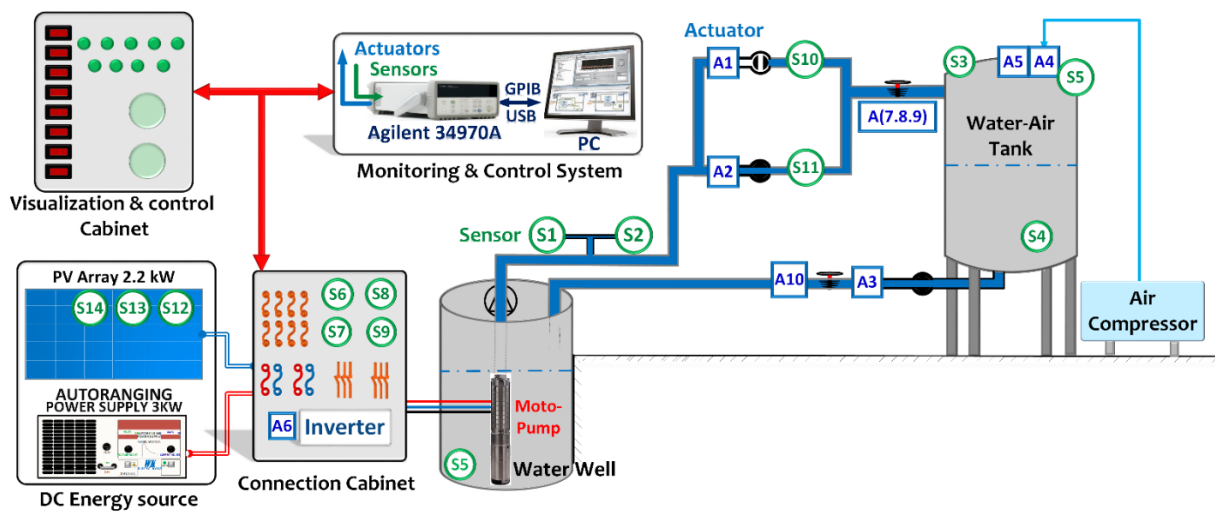
Figure 2.69 Solar pumps Test bench synoptic scheme with sensors and actuator's location.

Table 2.9 display List and Characteristics of Sensors and transducers used in the solar PV Pumping test bench.

Table 2.9 List and Characteristics of Sensors and transducers used in PV Pumping test bunch.

Sensors N°	Channel N° 34902	Measured quantities	Sensors type	Output Signal
S1	101	Pressure 0-10m	IMT industrie messtechnik 3276.69/76.001	4-20mA
S2	102	Préssion 0-160m		
S3	103	Tank pressure 0-160m		
S4	104	Tank height	TecfluidLE-70/TR420	
S5	105	well Height	Pressure sensors	
S6	106	DC Voltage	Voltage divider	0-5V
S8	108	AC Voltage		
S7	107	DC Current	Shunt 4A/150mV 25A/150mV	0-150mV
S9	109	DC Current		
S10	110	Water flow diameter Ø50mm	Contecesa TC50/TC32	4-20mA
S11	111	Water flow diameter Ø32mm		
S12	112	Irradiance on the inclined plane 36 °	reference cell (Atersa)	0-65mV
S13	113	PV module temperature	Termocouple (k)	(-1)- 5mV
S14	114	ambient temprerature		

Actuators in this system are pneumatic valves as illustrated in Table 2.10. While (A7 to A10) are manual valves not controllable.

Table 2.10 List and Description of Pneumatic valves used in PV Pumping System.

N° valves	N° Channel 34903	Description
A1	201	Pneumatic valve 50mm diameter for branch repression 50 mm
A2	202	Pneumatic valve 32mm diameter for branch repression 32 mm
A3	203	pneumatic valve 50 mm diameter of the discharge branch
A4	204	regulation valve air intake inside water-air tank
A5	205	regulation valve air exhaust inside water-air tank
A6	206	On-off pump controller

Measure and control With Agilent 34970A

The Agilent 34970A Data Acquisition / Switch Unit combines the advantages of measurement and control functions, with accuracy and multiple options for connecting signals for the systems testing and development. The measurement of different quantities characterizing our Test bench is performed by Agilent 34902A module 16 Channel Multiplexer, these measures require a good calibration using the information given by the manufacturer of each sensor or transducer, likewise, we can control the actuators installed in the system, using Agilent module 34903A 20 Channel Actuator.

User-Interface Under LabVIEW for pump test

This part is based on a LabVIEW software application that will allow us to recover the data measured by the sensors and control the actuators. After the development of a graphical code (Figure 2.70) for data acquisition, control and data recording, LabVIEW has allowed us to create a friendly and flexible user interface (Figure 2.71) with the following functionality:
- Communication through either GPIB or RS 232.
- Sampling frequency chosen by the user.
- Numerical indicators and Real-time chart for measured quantities.
- Remote control for actuators and regulation valves from the user interface.
- Data recording in an Excel file or other format.
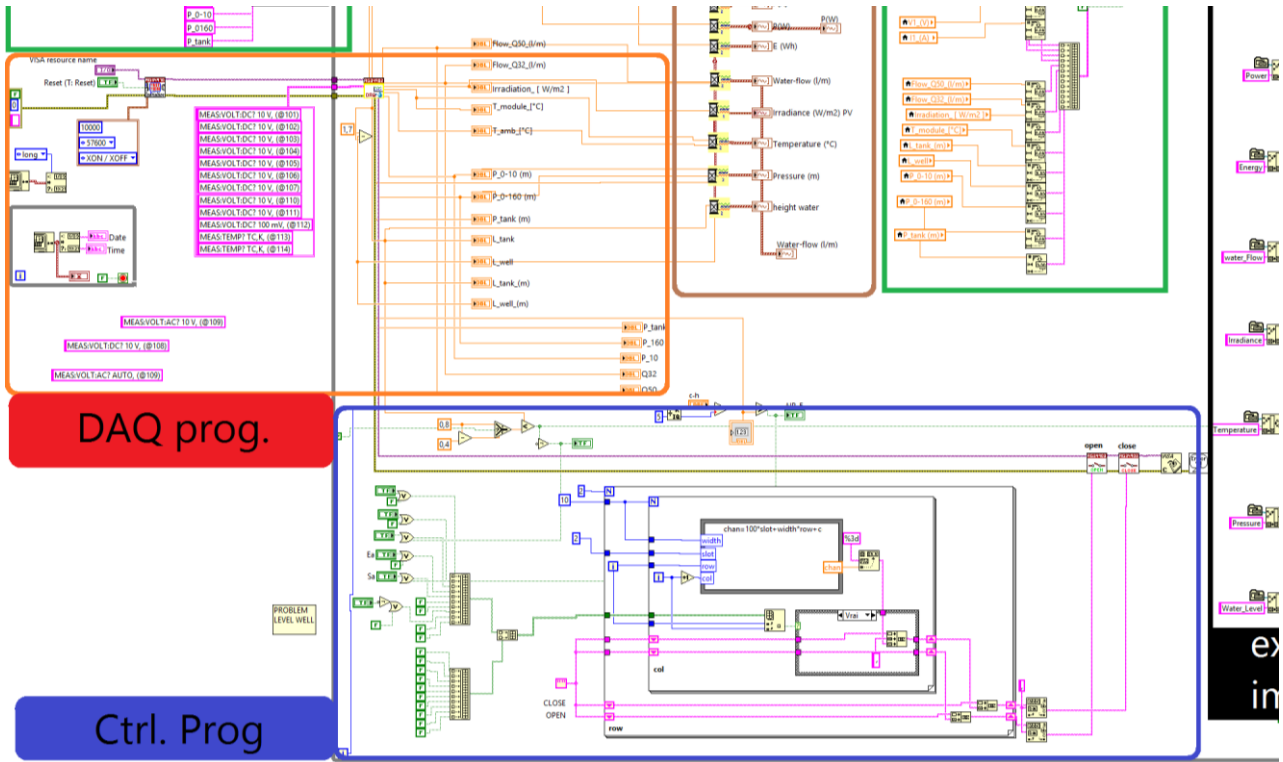
Figure 2.70 Sample of graphical code for monitoring and control of the PV test bench.
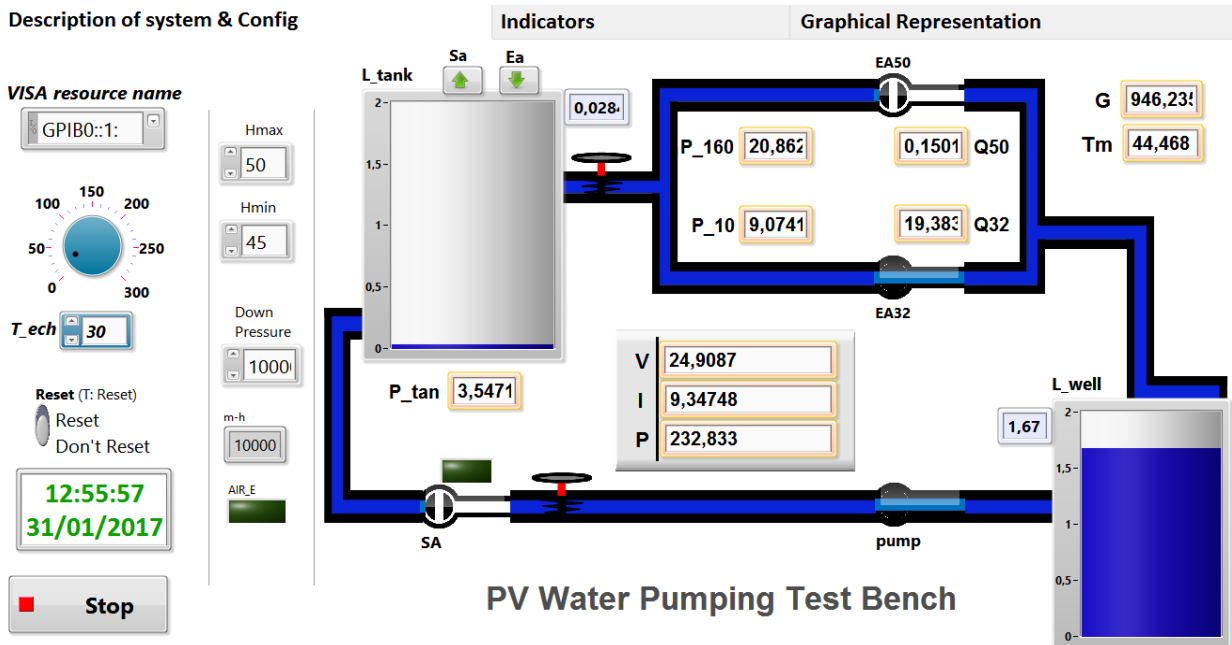
Figure 2.71 User interface_tab configuration & description of system.

The acquisition of measured data and remote control of pneumatic valves in real-time via the user interface under LabVIEW is friendly and reliable.

Case 3: I-V characterization and test of PV modules using PVPM 2540C.

I-V curve tracing is a performance verification method used in PV systems with traditional inverters. Performance verification is done by measuring current and voltage while varying an electrical load connected to a PV module string.

The peak measuring device tracer (PVPM 2540C) with the characteristics listed in Table 2.11 is used for the measurement, can provide both I-V and P-V curves of 101 samples every 0.05s.

The PVPM2540C device provide the I-V-curve measurement with 101 samples almost in 5 seconds for PV modules and small strings up to 250V and 40Adc, the device can also measure and calculate the peak power (Ppk), the series resistor (Rs) and the parallel resistor (Rp) from a single I-V-curve.

Table 2.11 PVPM 2540C Measuring Range.

Application	DC Voltage (V)	DC Current (A)	Temperature (°C)	Irradiance (W/m2)	Period for single measurement (s)	I-V curve samples
PV modules & small strings	25 / 50 / 100 / 250	2 / 5 / 10 / 40	-40 to +120 with Pt1000	0 to 1300 (Standard-Sensor)	0.02 – 2	101

Figure 2.72 illustrates a synoptic scheme for continuous I-V measurement for different PV module technology and power. Figure 2.73 display a picture of PV module (Sanyo 180Wp) in outdoor Tested condition.
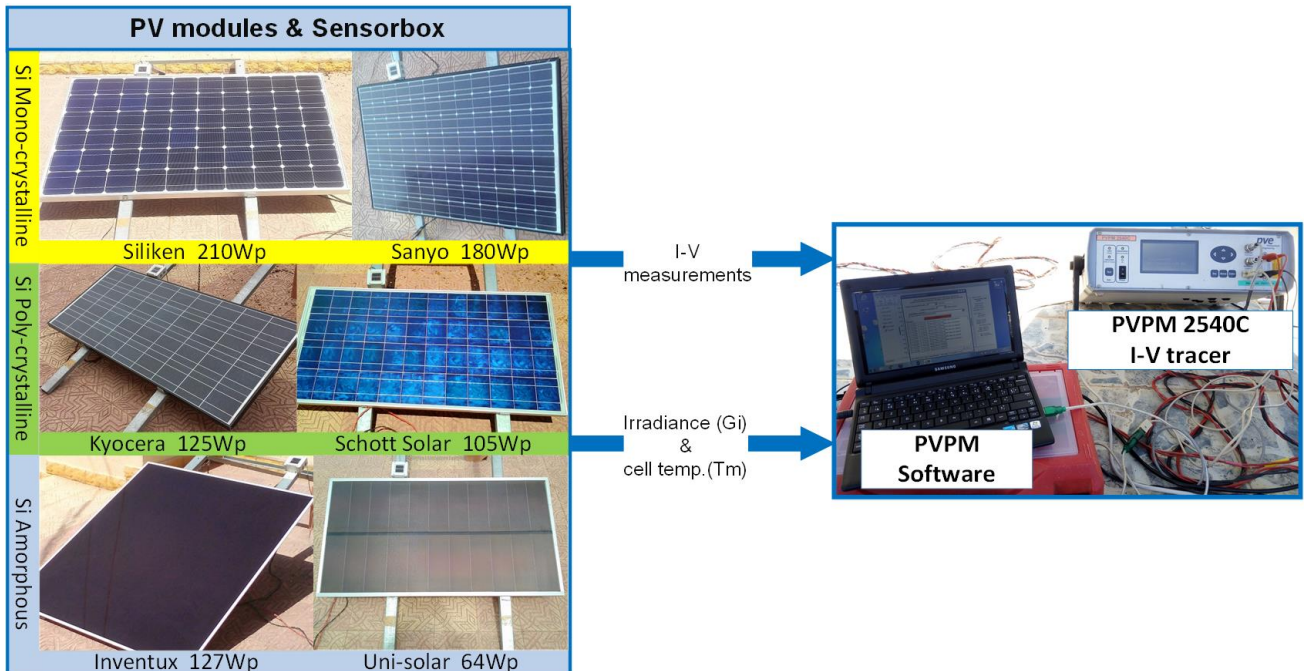
Figure 2.72 Synoptic scheme for continuous I-V measurement for different PV module technology and power.

Figure 2.73 Picture of Tested PV module (Sanyo 180Wp).

Figure 2.74 shows an Example of I-V characteristics measured for Sanyo 180 PV module at 13:21 under PVPM software.
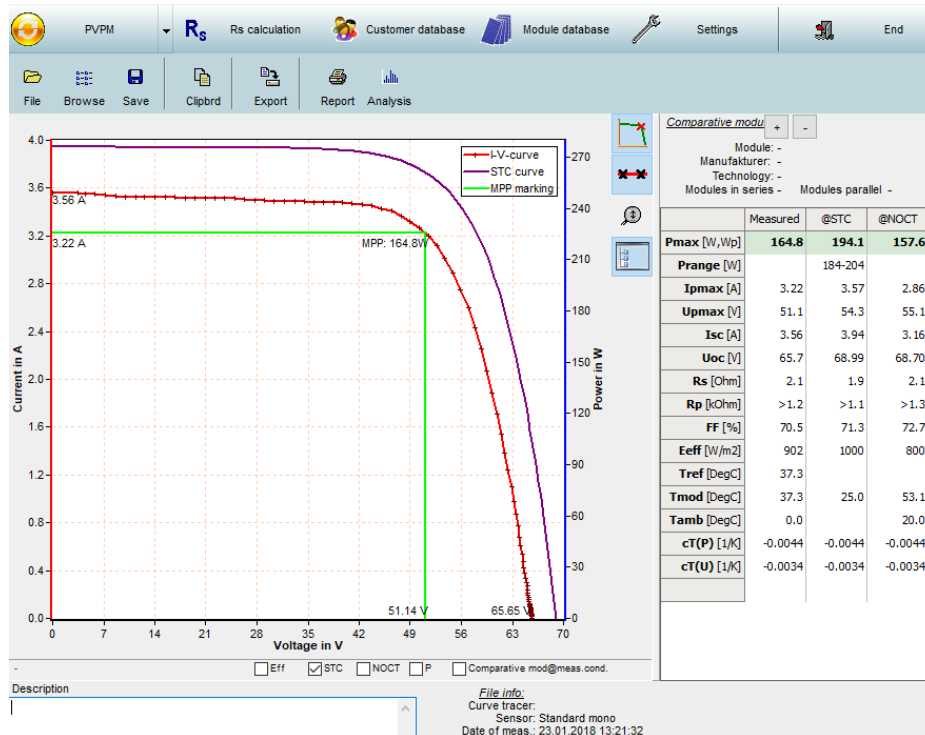
Figure 2.74 Example of I-V characteristics measured for Sanyo 180 PV module at 13:21.

This method has several limitations:

- **No real-time monitoring** - the procedure reports data from a single point in time. It is therefore heavily dependent on environmental conditions at the time of data capture and is not reproducible
- **Diagnostic information is not continuous** - defects or underperformance can go undetected for long periods of time (until the next I-V curve tracing). Data presented is partial and unrepresentative of the long-term health of the PV system.
- **No module-level analysis** - in PV systems with traditional inverters, modules are not analyzed individually, but are bundled with neighboring modules in the array. This lack of granularity leads to inaccuracies in error detection.
- **Requires costly labor & equipment** – if I-V curve tracing indicates a possible fault, without real-time and continuous diagnostic information, technicians are sent to the site to search for the problem with little direction or guidance. This search becomes more difficult and costly as installation size increases. Additionally, expensive thermal imaging (IR) cameras and portable electro-luminescence (EL) equipment will have to be deployed to detect the reduced output power of a single solar module.

Case 4: Advanced electrical measurement of the grid connected PV system using three-phase electrical networks analyzer.

In our GCPVS laboratory, we have used three-phase electrical network analyzer (Chauvin arnoux C.A 8336), in order to monitor the energy quality of PV production at the output of the three SMA inverters (Figure 2.75). On the other hand, the three-phase electrical network analyzer C.A 8335 was installed to measure load consumption in laboratory and inverters output for the phase 2 (Figure 2.76).

Two type of clamp meter were used namely:
1) E3N for DC & AC accurate current measurement (Figure 2.77).
2) MN93 for AC current measurement (Figure 2.78).

Furthermore, the electrical network analyzer allows the study of phenomena related to the PV system connection to the grid, namely: power quality, reactive power, current THD and voltage, …etc. [237].

In [244] electrical parameters at the point of common coupling (PCC) were studied, including the impact of the PV installation on the grid.

The C.A 8336 and C.A 8335 are equipped with 5 voltage measurement channels and 4 current measurement channels, the devices capture and records all parameters, transients, alarms and waveforms.

The measurement uncertainty of this device is better than 1%, is also very flexible, with a choice of sensors allowing measurements ranging from a few milliamperes to several kiloamperes.

It plays three roles and can be used to:

- Measure the RMS values, powers, and perturbations of electric distribution networks.
- Deliver a snapshot of the principal characteristics of a three-phase network
- Track the variations of various parameters over time.

Figure 2.75 C.A 8336 installed on PCC.   Figure 2.76 C.A 8335 installed on load-lab.

Figure 2.77 E3N DC/AC Current clamp.   Figure 2.78 MN93 AC Current clamp.

To retrieve data, we use Data*View* software, Data*View* is a tool for configuring and performing measurements, viewing data in real time, recovering recorded data and creating reports. As presented in Figure 2.79, All retreived mesurements in Data*View* software are reliable and very accurate. The use of a three-phase electrical network analyzer allows advanced monitoring of the energy quality of PV power plants connected to the grid.
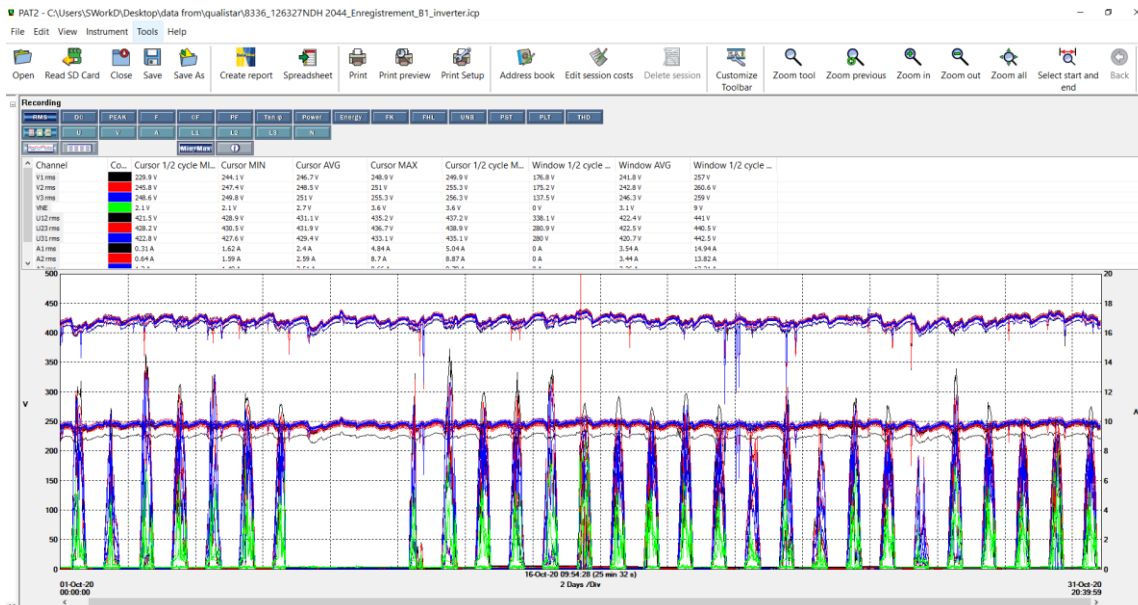
Figure 2.79 measured data by C.A 8336 viewed in DataView.

2.5 Conclusion

Comprehensive monitoring of all characteristic parameters adds value to the PV system allowing 1) extended system life, 2) low maintenance requirements and 3) low operating costs in order to have an optimum performance in a cost-effective and reliable way.

PC-Based measurement and control systems uses a combination with modular hardware and flexible software to turn computer into a supervisory system defined by the user. The external sensor realized and mounted in the GCPVS, are well calibrated with reference measurement and presents reliable and precise measurements. The use of sophisticated and accurate PC-based DAQ hardware (i.e., Agilent 34970A, Keithley 2700 and Fluke 2638A) with LabVIEW software creates a virtual instrumentation (VI) system useful for the acquisition, visualization, and analysis of measured data. A user-friendly interface under LabVIEW is designed, making it possible to retrieve, display and record the measured data of the climatic and electrical parameters which characterize the GCPVS. knowing that several versions were developed to design the final interface. Development using programming software is extensible for full functionality and application, The use and operation of the proposed monitoring platform is customizable, and can be applied to any size and type of the PV system, while the GCPVS presents one of the best applications for the monitoring system. The designed interface is thus extensible for modeling, performance analysis, and fault detection.

In the last section of this chapter, some case studies carried out at CDER are presented, it concerns the measurement and the monitoring applied to different types of PV systems. These case studies are as follows:
1) LabVIEW based monitoring for an off-grid PV System.
2) Monitoring & control of a PV water pumping test bench using LabVIEW.
3) I-V characterization and test of PV modules using PVPM 2540C.
4) Advanced electrical measurement of the grid connected PV system using three-phase electrical networks analyzer.

The results were very satisfactory, as we have already presented.

However, carrying out monitoring for different systems and PV test benches has enabled us to:

1) Know of new electrical and physical phenomena.
2) Become familiar with new conditioning and measurement techniques.
3) Handle multiple sensors, transducers, instruments, and software.

Chapter 3

Modeling and performance Analysis of Grid Connected PV System

Chapter 3 : Modeling and Performance Analysis of Grid Connected PV System

3.1 Introduction

The performance of PV installations depends on many parameters, including weather conditions, the performance of each component of the PV system and grid parameters. Solar PV systems can be subjected during operation to various faults that affect components of the PV system such as modules, cables, protections or inverters [7].

The simulation of the PV system connected to the grid makes it possible to create reference thresholds for the monitoring system carried out, which makes it possible to analyze the performance and power losses in order to detect and identify the various faults affecting the PV system.

The main goal of this chapter is to model and analyze the performance of the 9.54 kW Grid Connected PV System (GCPVS). Accurate parametric performance models were proposed in order to simulate the electrical behavior of GCPVS, the models' parameters were identified using MATLAB curve fitting toolbox. Additionally, a non-parametric model based on Principal Component Analysis was suggested. Furthermore, several models were selected and compared to choose the best model, this model are well calibrated with experimental data measurement in order to minimize errors as much as possible. Finally, a user-interface for modeling and performance analysis of the PV system under LabVIEW was designed.

3.2 Parametric modeling of Grid-connected PV system

The objective of the simulation of the GCPVS is to obtain the expected evolution of DC Power produced by the PV array as well as the AC power at the output of the PV inverter, considering real climatic conditions.

The simulation of the GCPVS is based on the parametric models implemented and evaluated under the MATLAB environment (Figure 3.1).

The modeling of some parts is optional in the performance monitoring and faults diagnosis applications. However, in this section, some modeling parts have not been established. As the irradiance on the plane of array was measured using pyranometer and PV cell reference sensors, the irradiance components were not modeled. Aging and mismatch losses were included in the models using derates factors. Shading and soiling are considered as fault for our system, so they are not modeled. The following figure illustrates the simulation diagram of the electrical generation behavior by the CGPVS from empirical models.
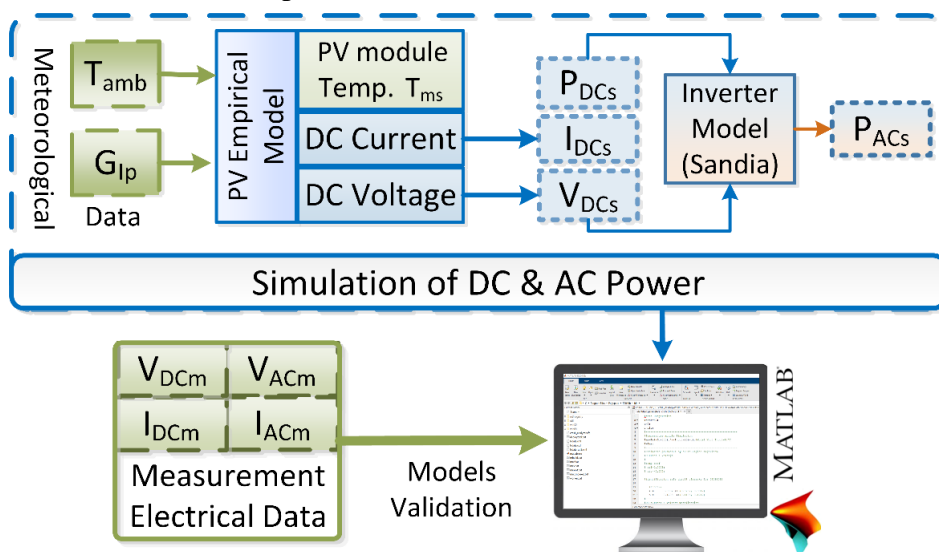
Figure 3.1 Simulation diagram of the PV system under MATLAB.

3.2.1 PV array Model

The behavioral model of a PV module depends on the many electrical and meteorological parameters. The PV cell or module temperature is usually obtained by prediction.

PV cell temperature model

The to estimate the temperature of the PV cell/module, numerous models have been introduced in the literature [138], [139], [171], [245], [246]. Among these models, eighth simple empirical models were selected; that are based on the Ross model, environmental parameters, or Nominal Operating Cell Temperature (NOCT) model. After comparing the simulation results of eight models with the measured PV module temperature data, the NOCT model appears the most suitable for our PV modules.

The NOCT is defined by the IEC 61215 standard for crystalline silicon modules, is the temperature that the module reaches in the following conditions: 45° south facing, 800 W/m^2 incident irradiance (G_i), ambient temperature (T_a) equal to 20 °C and wind speed (W_s) equal to 1 m/s. The NOCT is given in all PV module datasheets

Here, the estimated PV cell temperature (T_{cs}) is computed using Eq. (3.1) based on NOCT model [247], which is proportional to the evolution of ambient temperature (T_a) and tilted irradiance (G_i) in W/m^2.

$$T_{cs} = T_a + \frac{G_i}{800\ W/m^2} \cdot \big((p0.\,T_{NOCT}) - 20°C\big) \tag{3.1}$$

Where, $p0$ is the NOCT coefficient of PV module temperature.

DC current model at MPP

The dynamic model of the estimated DC current I_{DCs} at MPP is expressed by Equation 3.2 [248].

$$I_{DCs} = \big(a.\,p.\,I_{m0} + T_{Ci}.\,(T_{cs} - T_0)\big).\frac{G_i}{G_0} \tag{3.2}$$

Where:
a: Aging factor for DC current of the PV array.
p : Number of parallel PV string.
G_0: Reference global irradiance at STC=1000W/m^2.
T_0: Nominal temperature at STC = 25°C.

DC Voltage model at MPP

The dynamic model of the estimated DC voltage V_{DCs} at MPP which is introduced in by [249]. V_{DCs} is inversely proportional to the evolution of the PV cell temperature (T_{cs}), and slightly proportional to the evolution of tilted irradiance (G_{ip}) ,as is shown in the following equations (3.3-3.5).

$$V_{DCs} = V_x \left(1 + b.\ln\left(b - b.\exp\left(\frac{-1}{b}\right)\right)\right) \tag{3.3}$$

$$V_x = s.\frac{G_i}{G_0}.\,T_{Cv}.\,(T_{cs} - T_0) + s.\,V_{ocx} - s.\,(V_{ocx}).\exp\left(\frac{G_i}{G_0}.\ln\left(\frac{V_{ocx} - V_{oc0}}{V_{ocx}}\right)\right) \tag{3.4}$$

$$V_{ocx} = V_{oc0} + 1e^{-10} \tag{3.5}$$

Where;
b : Aging factor for DC voltage of the PV array $0.01 < b < 0.18$.
V_x : Vacuum voltage at all given T_{ms} and G_{ip}
s : Number of PV module in series.
V_{ocx} : Open circuit voltage at 25°C and more than 1200W/m².

3.2.2 PV Inverter model (Sandia)

The Conversion of DC power into AC power allows this power to be tied to the AC grid with high efficiencies. To estimate this conversion, a behavioral model developed by Sandia National Laboratories (SNL) [140] were used. The used model is defined by the following equations.

$$P_{ACs} = \{(P_{ACo}/(A-B)) - C.(A-B)\}(P_{DCs} - B) + C.(P_{DCs} - B)^2 \qquad (3.6)$$

$$A = P_{DC0}.\{1 + C_1.(V_{DCs} - V_{DC0})\} \qquad (3.7)$$

$$B = P_{S0}.\{1 + C_2.(V_{DCs} - V_{DC0})\} \qquad (3.8)$$

$$C = C_0.\{1 + C_3.(V_{DCs} - V_{DC0})\} \qquad (3.9)$$

The definition of the performance parameters is given below:

P_{ACs} : Predicted AC-power output from inverter based on predicted DC power and voltage, (W).
P_{DCs} : Predicted DC-power input to inverter, equal to the PV array maximum power, (W).
V_{DCs} : Simulated DC-voltage input, equal to the PV array maximum power voltage, (V).
P_{ACo} : Maximum AC-power rating for inverter at reference operating condition (ROC), (W).
P_{DC0} : DC-power level at which the AC-power rating is achieved at the ROC, (W).
V_{DC0} : DC-voltage level at which the AC-power rating is achieved at the ROC, (V).
P_{S0} : DC power required to start the inversion process, (W).
C_0 : Parameter defining the curvature of the relationship between AC power and DC power (1/W).
C_1 , C_2 and C_3 are the empirical coefficient allowing respectively P_{DC0} , P_{S0} and C_0 to vary linearly with DC-voltage input, (1/V).

3.2.3 Validation of models and results.

Validation the PV module Temperature model
Here, the module temperature model is fitted with the experimental dataset of six days (Figure 3.2), and for best fit with measured data of PV module the NOCT coefficient of PV module temperature (c) was identified as 0.851.
The NOCT coefficient of PV module temperature, c, was identified to be 0.851. The model describes the data well, as shown in Figure 3.2 Precisely, the model was calibrated with PV module (ISOFOTON I-106/12) temperature measurement data of six days recorded using an SMA SensorBox with a 4-wire pt100 surface temperature sensor located in the back sheet of the PV module. Indeed, SMA sunny SensorBox measures the irradiance on the tilted plane, ambient temperature, PV module temperature, and wind velocity.
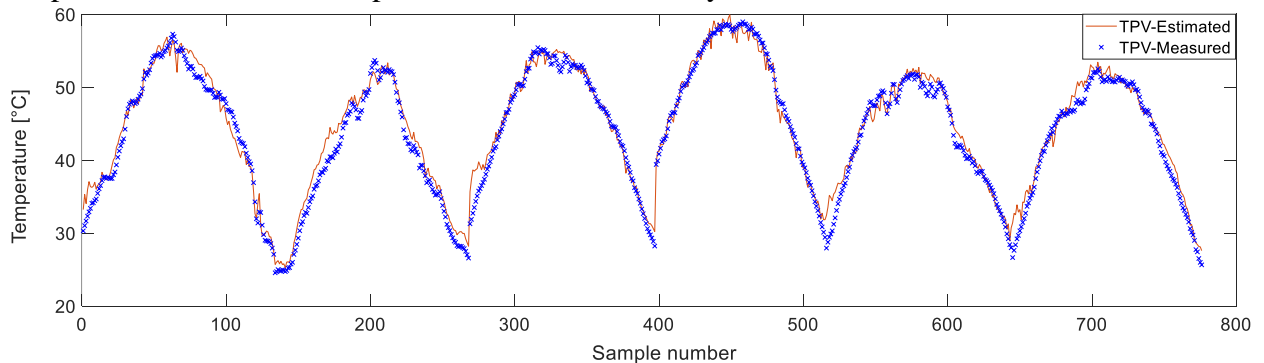
Figure 3.2 Evolution of the PV module temperature measured and estimated under MATLAB.

Three representative statistical indicators are considered to assess the prediction performance and accuracy of behavioral models: the coefficient of determination (R^2), root mean square error (RMSE), and mean absolute error (MAE). These metrics are computed as follows

$$MAE = \frac{1}{n}\sum_{i=1}^{n}|Y_i - \widehat{Y_i}| \tag{3.10}$$

$$RMSE = \sqrt{\frac{1}{n}\sum_{i=1}^{n}(Y_i - \widehat{Y_i})^2} \tag{3.11}$$

$$R^2 = 1 - \frac{\sum_{i=1}^{n}(Y_i - \widehat{Y_i})^2}{\sum_{i=1}^{n}(Y_i - \bar{Y})^2} \tag{3.12}$$

Where Y_i are the actual values, $\widehat{Y_i}$ are the corresponding estimated values, $\bar{Y}$ refers to the mean value of Y_i, and n is the number of measurements. The measurements of effectiveness for the used PV module temperature model listed in Table 3.1 confirm its good prediction performance.

Table 3.1 Regression metrics for the used PV module temperature model.

Indicator	MAE	RMSE	MAE (%)	RMSE (%)	R^2
Values	1.19 °C	1.53 °C	1.99	2.56	0.97

Validation of the electrical models

To verify the prediction accuracy of the abovementioned electrical empirical models, we used measurements collected under normal operating conditions without any faults and power losses. Figure 3.3 (a-b) show clear sky day profile of measured tilted irradiance, measured ambient temperature and predicted temperature of PV module, used as input to simulate DC current and DC voltage of the PV sub-array at MPP, and AC power at the inverter output.
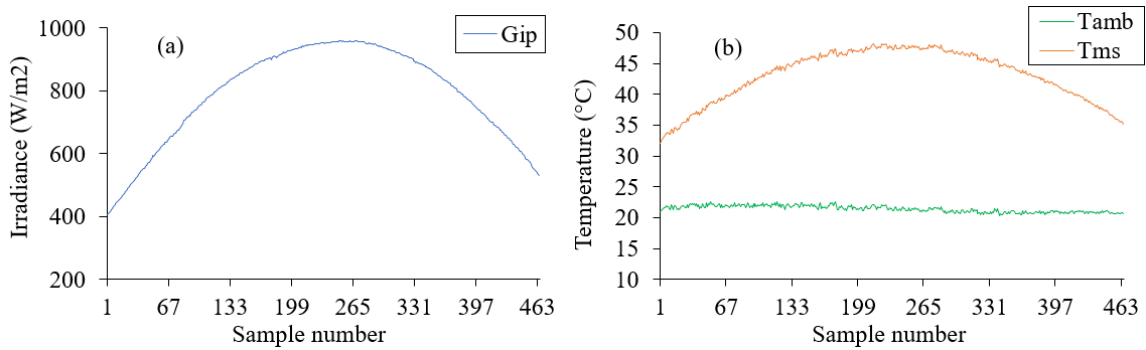
Figure 3.3 Clear sky day profile of (a) measured tilted irradiance, and (b) measured ambient temperature and predicted PV module temperature.

Here, the coefficients of the PV sub-array model and the inverter model were identified using a curve fitting toolbox under MATLAB software, where the fitting is based on nonlinear least squares method and trust-region algorithm (Figure 3.4).

103
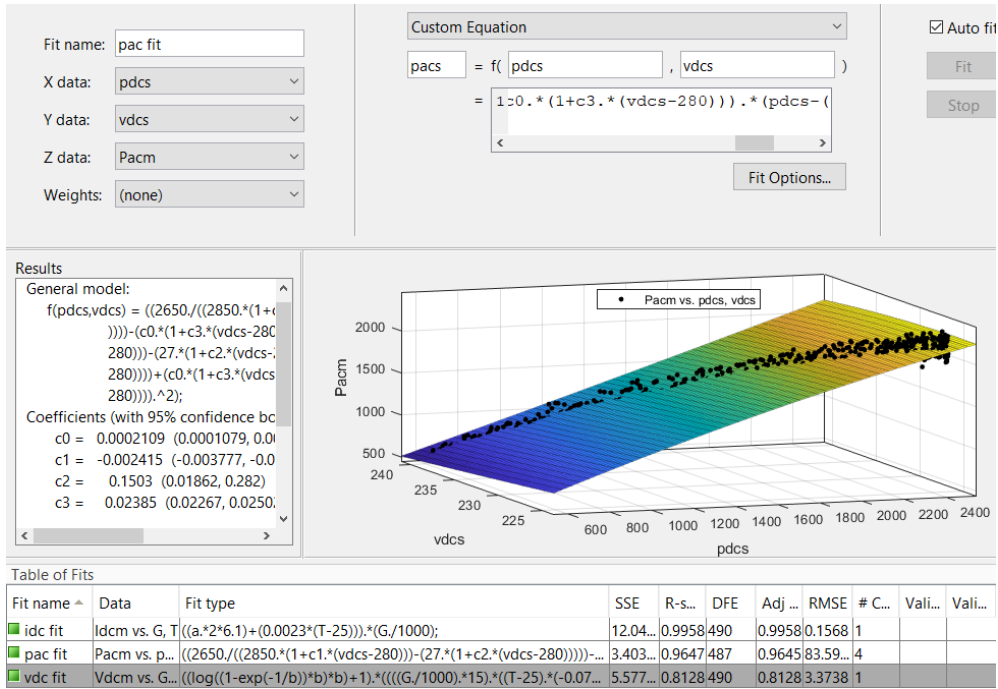
Figure 3.4 Coefficients identification under MATLAB using curve fitting tool.

Four parameters of the sandia inverter model were set in the following values based on datasheet specification of Fronius IG30 inverter: P_{AC0} = 2650W, P_{DC0} = 2850W, V_{DC0} = 280V and P_{S0} = 27W, in order, to facilitate the parameters extraction process. Table 3.2 gives the identified coefficients values for predicted DC current, DC voltage of PV sub-array, and AC power at the output of the inverter.

Table 3.2 Identified coefficients for predicted DC current, DC voltage and AC power.

Estimated parameter	I_{DCs}	V_{DCs}	P_{ACs}			
Identified coefficient	a	b	C_0	C_1	C_2	C_3
Band limits	0 to 1	0.01 to 0.18	-1 to 1			
Identified values	0.9302	0.1203	2.11e-04	2.41e-03	0.15	0.0238

Figure 3.5 (a-d) show the simulation results using the identified parameters of DC current, DC voltage, DC power and AC power compared with measured data during one clear sky day.
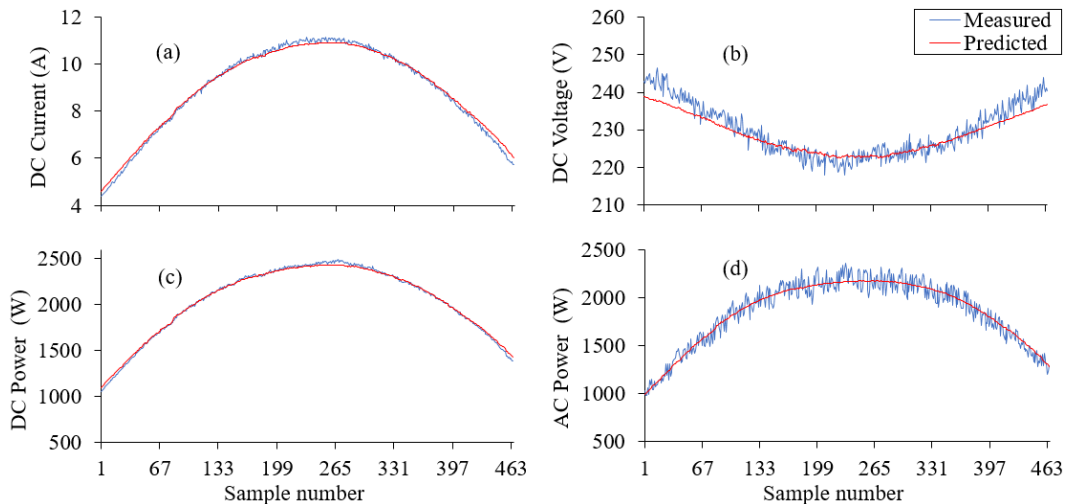
Figure 3.5 Measured and predicted plot of (a) DC current, (b) DC voltage, (c) DC power and (d) AC power for clear sky day.

Figure 3.6 (a-d) show the scatter plots of (a) DC current, (b) DC voltage, (c) DC power and (d) AC power for clear sky day case.
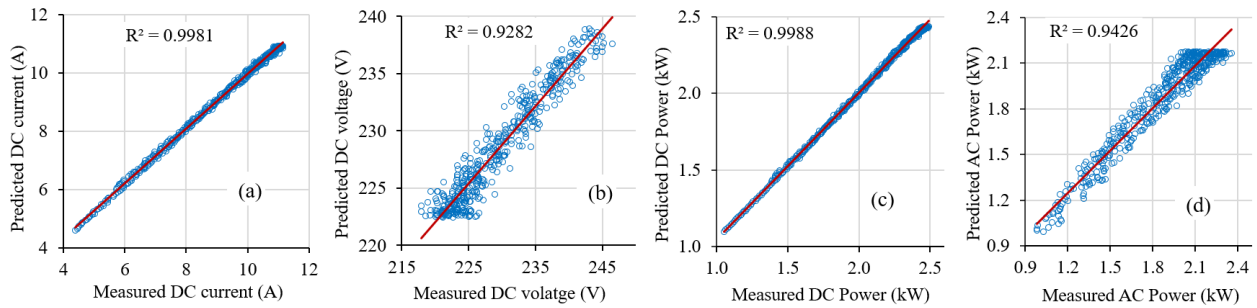
Figure 3.6 Scatter plot of (a) DC current, (b) DC voltage, (c) DC power and (d) AC power for clear sky day.

We observe from Figure 3.5 and 3.6 we see a good agreement of the measured and estimated DC current, DC voltage, AC power, and DC power.

In addition, a second validation of the model was carried out using two other days with clear and cloudy skies, in order to evaluate the prediction accuracy of the empirical electrical models. Figure 3.7 (a-b) illustrate the profiles of clear and cloudy days of (a) measured tilted irradiance and (b) measured ambient temperature with predicted temperature of PV module used as input to simulate DC current, DC voltage and DC power at MPP of the PV sub-array, and AC power at the output of the inverter using the identified coefficients mentioned in Table 3.2.
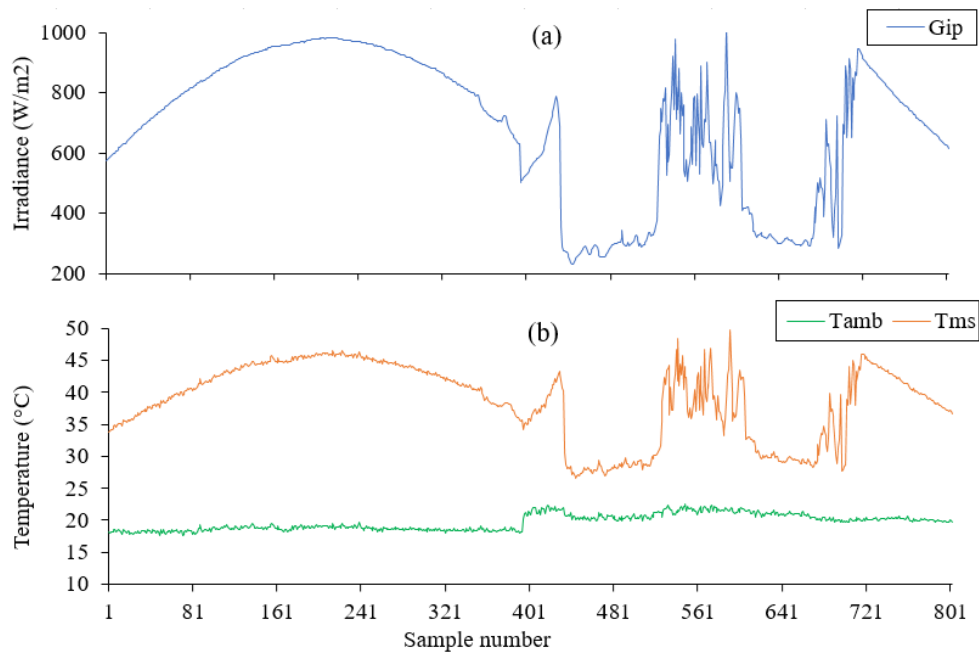
Figure 3.7 Profiles of clear and cloudy sky days of (a) measured tilted irradiance, (b) measured ambient temperature and predicted PV module temperature.

Figure 3.8 (a-d) display the simulation results of DC current, DC voltage, DC power and AC power from empirical models compared with the measured data during two days (i.e., clear and cloudy).

105
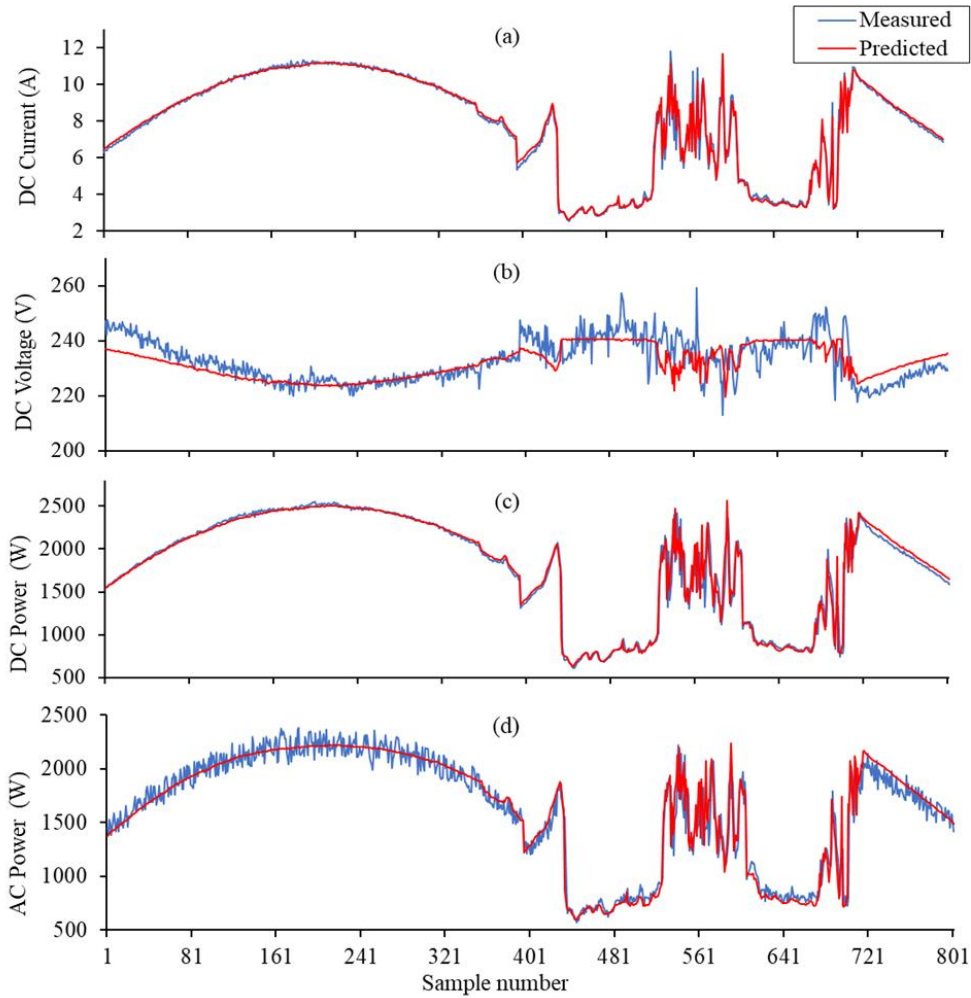
Figure 3.8 Measured and predicted plots of (a) DC current, (b) DC voltage, (c) DC power and (d) AC power for clear sky and cloudy sky day.

Figure 3.9 (a-d) show the scatter plots of (a) DC current, (b) DC voltage, (c) DC power and (d) AC power for two days (i.e., clear and cloudy).
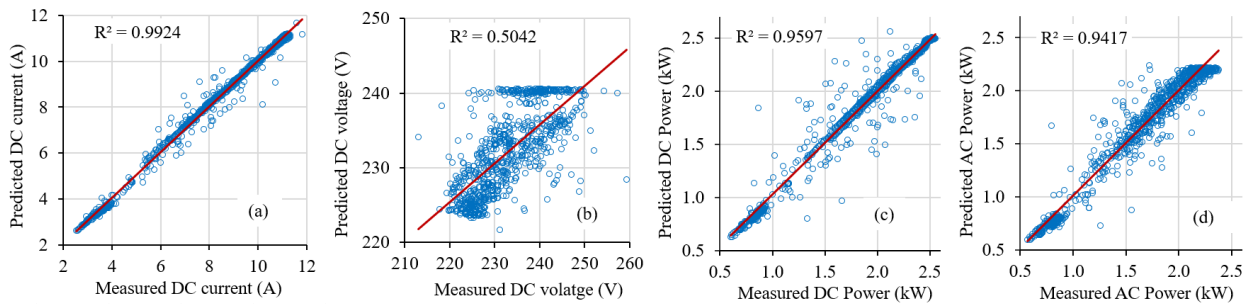
Figure 3.9 Scatter plots of (a) DC current, (b) DC voltage, (c) DC power and (d) AC power for clear and cloudy sky days.

The statistical prediction metrics for the electrical models to estimate DC current, DC voltage, DC power, and AC power calculated for the reference day and two other days are listed in Table 3.3

Table 3.3 Regression metrics for used models to predicte DC current, DC voltage, DC power and AC power.

Estimated parameter	Reference day (clear sky)				Validation days (clear and cloudy sky)			
	I_{DCs} (A)	V_{DCs} (V)	P_{DCs} (W)	P_{ACs} (W)	I_{DCs} (A)	V_{DCs} (V)	P_{DCs} (W)	P_{ACs} (W)
MAE	0.12	2.24	16.69	68.66	0.15	4.33	58.4	88
RMSE	0.14	2.81	21.07	80.60	0.25	5.7	119.7	126.7
MAE (%)	1.06	0.90	0.67	2.91	1.28	1.67	2.29	3.70
RMSE (%)	1.29	1.12	0.84	3.42	2.09	2.19	4.70	5.32
R^2	0.998	0.83	0.998	0.94	0.99	0.49	0.96	0.94

106

Results in Table 3.3 indicate a satisfying agreement between the measured data and the predicted value of DC current, and DC power in both cases: clear day and clear and cloudy days (i.e., R2 greater than 0.95). We observe also that the prediction of AC power using the Sandia inverter model, based on predicted DC voltage and DC power, is in agreement with measured values (i.e., R2=0.94). The filtering of AC power measurement noise leads to a decrease of MAE and RMSE errors values. On the other hand, we observed that for the estimated DC voltage, the R2 is low, due to the dynamic DC voltage variation, especially on a cloudy day. A reasonable prediction of the DC voltage is achieved under clear sky day with an R2 of 0.83. It is also recommended to use the measured data of the PV modules temperature directly instead of the simulation in order to better predict the DC voltage. It should be noted that as fault detection is based on DC power residuals, the relatively moderate prediction of DC voltage will not have any impact on the performance of the proposed detection procedure. In summary, the above-described empirical models fit relatively well with the measured data. These models are constructed using fault-free data and will generate residuals of new arrival data for fault detection purposes.

3.3 PCA-based non-parametric model.

This modeling section was developed in collaboration with researchers affiliated with King Abdullah University of Science and Technology (KAUST) University.

Principal Component Analysis (PCA), a dimensionality reduction approach, is becoming increasingly popular for learning relevant and important features from multivariate data [250]. PCA projects multivariate data into a lower-dimensional subspace to revealing the cross-correlation inherent between process variables [251] [252].

This section consists in constructing a reference PCA model using data gathered from the PV system under normal conditions. First, the raw data collected from the monitored PV system (fault free data) is preprocessed by scaling every variable to have zero mean and unit variance. Then, to select the appropriate number of Principal Components (PCs) to maintain in the PCA model, the covariance matrix of the scaled data is computed and the eigenvalues and eigenvectors for the covariance matrix C are computed and sorted in decreasing order. Finally, the cumulative percentage variance (CPV) technique is utilized here due to its simplicity and efficiency. Thus, the number of maintained PCs, l, describing over that 90% of the variability in the data can be used to construct the reference PCA model (Figure 3.10). For more detail see [253].
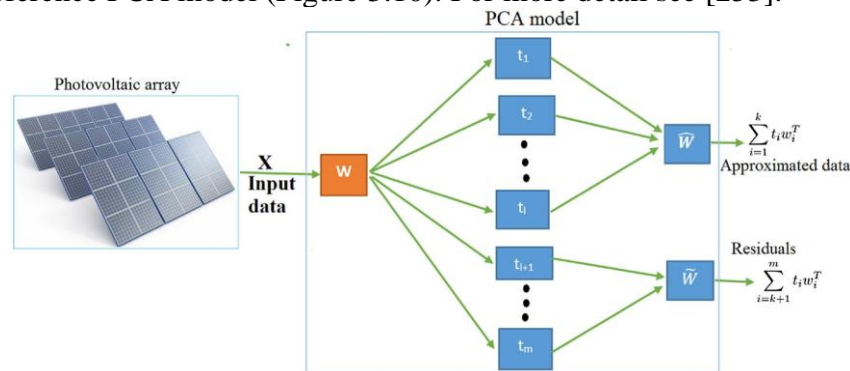
Figure 3.10 Conceptual representation of PCA.

To construct the PCA model, two days of data are gathered from the monitored PV system when running under nominal conditions. Nine collected variables are used to construct the reference PCA model: 1) irradiance, 2) ambient temperature, 3) cell temperature, 4) DC current, 5) DC voltage, 6) maximum DC power, 7) AC current, 8) AC voltage, and 9) AC power. To show relationships among measured variables and temporal records a Pearson correlation heatmap is delineated in Figure 3.11. The correlation heatmap indicates the strong correlation between solar irradiance and cell temperature with the electrical variables (Figure 3.11).
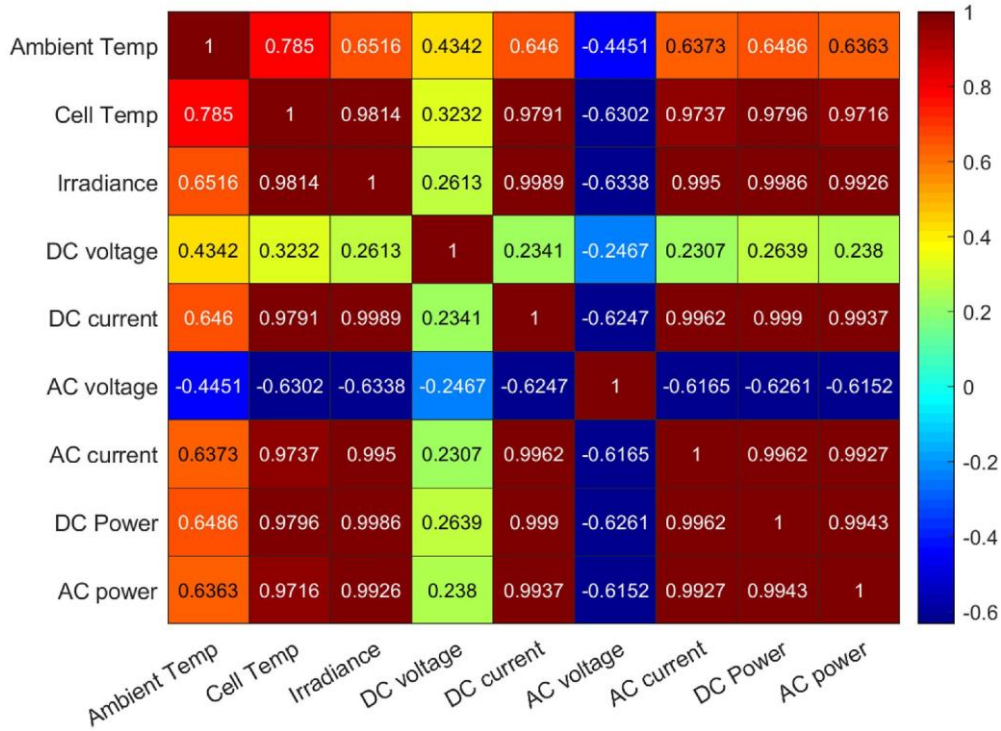
Figure 3.11 Heatmap of the correlation matrix of data.

From Figure 3.11, it can be noticed that there a high correlation between the following parameters: Irradiance, cell temperature, DC current, AC current, DC power and AC power. There is a positive correlation between cell temperature, DC current, AC current, DC power and AC power. It should be noted that DC voltage has a low correlation with the parameters (ambient and cell temperature, DC current, AC current, DC power, and AC power). AC voltage has no negative week relation with other parameters.

The cumulative person variance procedure is used to determine the optimum number of PCs in the PCA model. Three PCs describing 95.21% of the variability in the data are maintained to construct the PCA model (i.e., 77.45%, 11.40%, and 6.35%, respectively), see Figure 3.12.
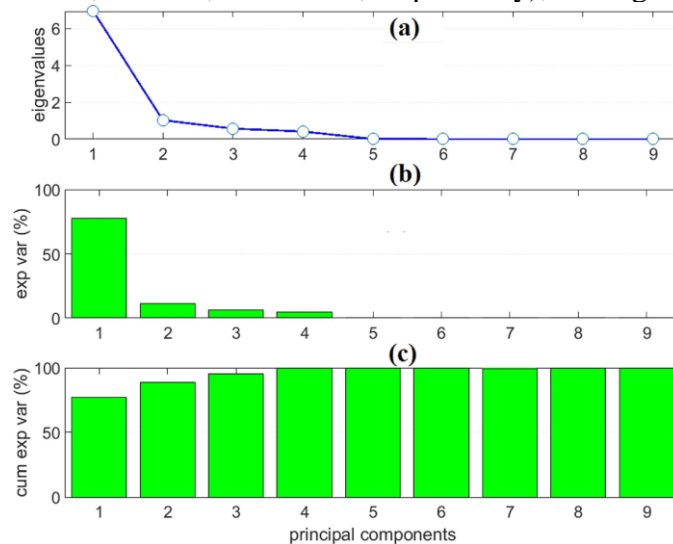
Figure 3.12 (a) Eigenvalues, (b) Explained variance and (c) Cumulative variance versus the number of PCs.

The constructed PCA model is verified under three different conditions: data collected from the PV array in clear sky day, cloudy sky day and under low irradiance conditions. In the first scenario, the obtained PCA model is verified using a clear sky day (October 8). The measured and the predicted data via PCA model are illustrated in Figure 3.13 (a–f). We can see a good agreement between the measured and the predicted data from the PCA model.

108
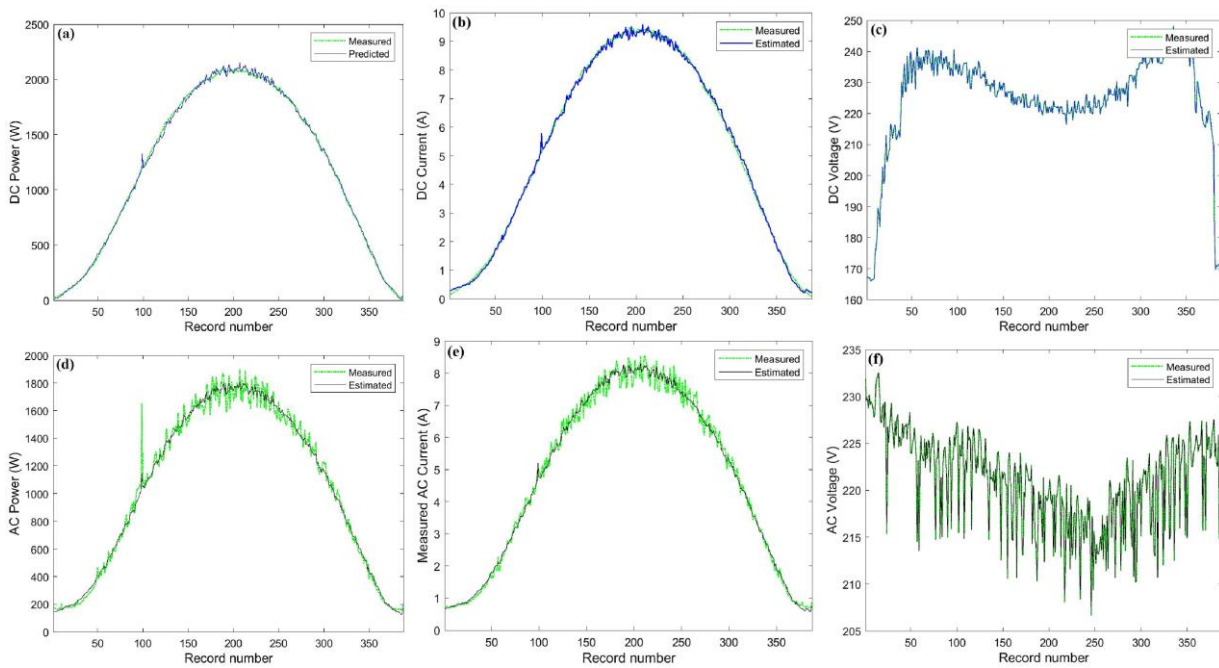
Figure 3.13 Collected and estimated using PCA of (a) maximum dynamic DC power, (b) DC current, (c) DC voltage, (d) AC power, (e) AC current and (f) AC voltage.

Furthermore, the PCA model has been tested with a cloudy day which has been collected in a different season Figure 3.14. Results illustrate the goodness of the PCA model in describing electrical measurements.
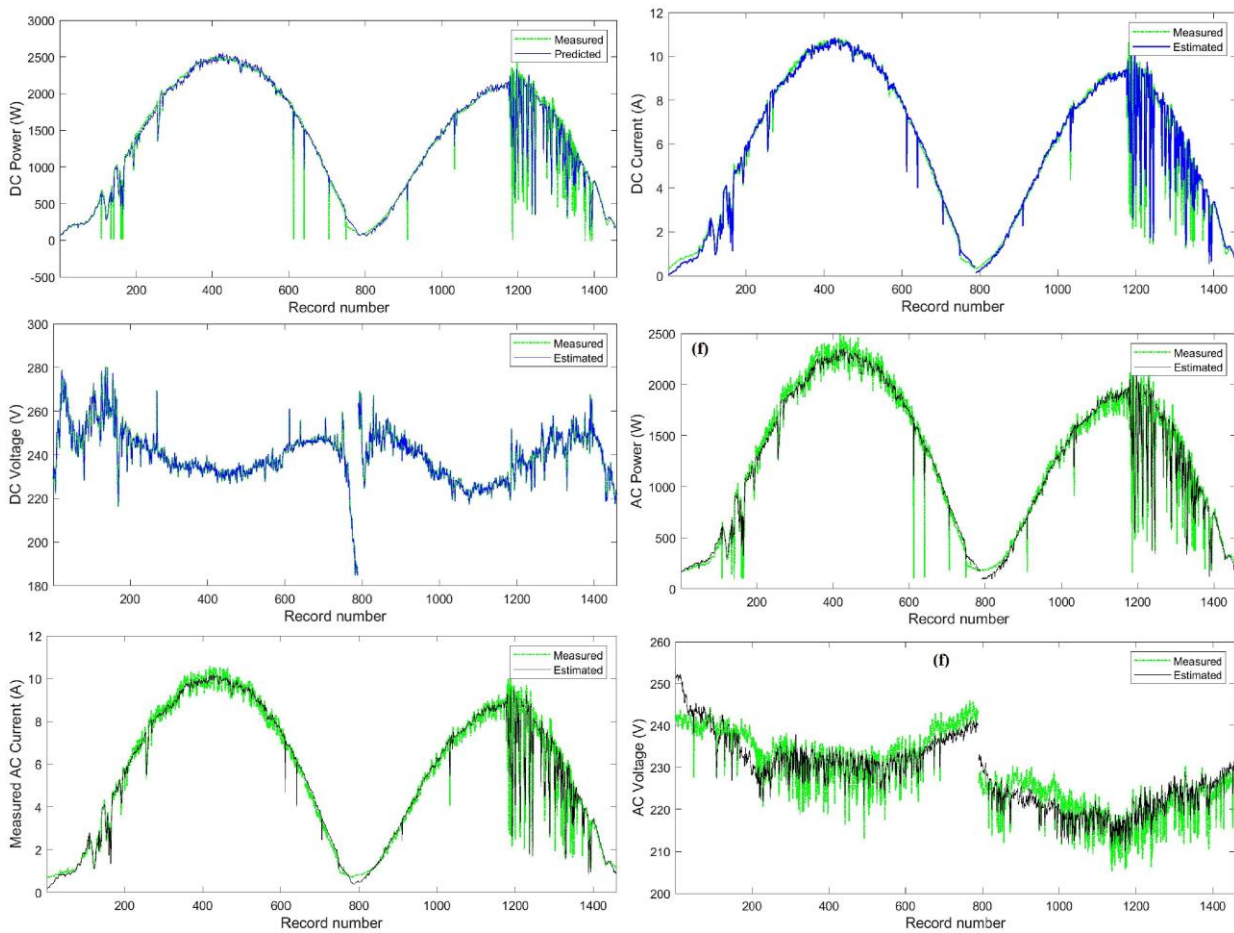
Figure 3.14 Collected and estimated using PCA of (a) maximum DC power, (b) DC current, (c) DC voltage, (d) AC power, (e) AC current and (f) AC voltage.

The non-parametric or Data-driven models, see the inspected PV system as a black box without parameterization, it estimates the electrical behavior of the PV system from a time series of input and output data. Still, it requires a lot of historical data to develop a behavioral model. Data-driven models have become appealing due to the availability of big data.

On the other hand, parametric models conceive the PV system as a white box, where each component can be modeled using a set of parameters related to empirical or electrical models. These models are specified in terms of power, type and size of the PV system. while model identification and calibration are mandatory for every PV installation. In addition, the accuracy and precision of the parametric model depend on 1) the performance of the model used, 2) the accuracy of the experimental data, and 3) the parameter estimation technique used. In our application, the three criteria mentioned above can be controlled and improved. Indeed, among the advantages of parametric models, are their simplicity and ease of implementation in any software and hardware environment. For this, the choice fell on parametric models.

3.4 Accuracy improvement of parametric models

The right choice of parametric models with a good calibration, are the key to minimize the error between measurement and simulation as much as possible in the normal operation of the PV system.

3.4.1 Effective Irradiance

Effective irradiance E_e is total plane of array (POA) irradiance adjusted for angle of incidence losses, soiling, and spectral mismatch. In a general sense it can be thought of as the irradiance that is "available" to the PV array for power conversion.

A simplified approach using a single irradiance sensor has been suggested, shown eq. (3.13).

$$E_e = \frac{E_{POA}}{E_0} . Sf \tag{3.13}$$

Where;

E_0 is a reference irradiance ($1000 \ W/m^2$)
Sf is the soiling factor (=1 when clean).
E_{POA} is the plane of array irradiance.

3.4.2 Cell/Module temperature model

Following the proportional relationship, between the voltage of the module and its temperature, an accurate estimation of the cell temperature allows a good prediction of the voltage behavior. For this, three other models taking in addition the effect of the wind speed on the PV cell/module temperature, consequently they depend on three parameters: the solar irradiance incident on module surface (G_i) in (W/m2), ambient air temperature *(Ta)* in (°C) and Wind velocity (W_v) in (m/s). These models were simulated and calibrated with the measured data, in order to choose the most accurate model.

NOCT model with wind velocity consideration.
The NOCT model assumes that wind velocity is always 1 m/s. However, the NOCT-2p model [138] takes into account the impact of the wind velocity on the cell temperature, this model is based on three variables (T_a , G_i , W_v) and two dimensionless parameters ($p1$, $p2$) as illustrated in eq. 3.14.

$$T_{cs} = T_a + p1 \left(\frac{G_i}{800} \cdot (T_{NOCT} - 20) \right) + p2 \cdot (W_v - 1) \tag{3.14}$$

Where:
$p1, p2$ take respectively into account the relationship between estimated cell temperature (T_c) with 1) incident irradiance (G_i) , and 2) wind velocity (W_v).

Faiman Module Temperature Model

Faiman model [254] is based on simple heat transfer concepts. The model is represented by equation (3.15).

$$T_{ms} = T_a + \frac{Gi}{f1 + f2 \cdot W_v} \tag{3.15}$$

Where:

T_{ms} = estimated temperature of PV module (°C)
T_a = ambient air temperature (°C)
G_i = the irradiance incident on the plane of the module or array (W/m^2)
$f1$ = the constant heat transfer component $(W/m^2 K)$
$f2$ = the convective heat transfer component $(W/m^2 K)$
W_v = wind velocity (m/s)

This model is validated with data experimental from seven different types of modules and fit the data to values of $f1$ and $f2$. All modules had front glass covers and Tedlar backs.

Sandia Module Temperature Model

To estimate back-surface module temperature (T_{ms}) in (°C), Sandia proposes an accurate model which depends on three parameters (Eq. 3.16): solar irradiance incident on module surface (G_i) in (W/m2), ambient air temperature (*Ta)* in (°C) *and* Wind velocity (W_v) in (m/s) [126].

$$T_{ms} = T_a + G_i \cdot e^{s1+s2 \cdot Wv} \tag{3.16}$$

Where:
s1 = Empirically-determined coefficient establishing the upper limit for module temperature at low wind speeds and high solar irradiance.
s2 = Empirically-determined coefficient establishing the rate at which module temperature drops as wind speed increases.

a and b are parameters that depend on the module construction and materials as well as on the mounting configuration of the module.

Sandia Cell Temperature Model

The Sandia cell temperature model estimates cell temperature from module temperature, T_m , plane of array irradiance, G_i, and a temperature difference parameter, ΔT. This difference parameter defines the temperature difference between the module and cell temperature.

The model form is represented by Eq. (3.17).

$$T_c = T_m + \frac{G_i}{E_0} . \Delta T \tag{3.17}$$

ΔT = parameter that depends on the module construction and materials as well as on the mounting configuration of the module [255]. In our PV array ΔT is fixed at 2°C.

To calculate the PV module temperature from cell temperature model we use the next relationship:

$$T_m = T_c - \frac{E_{POA}}{E_0} . \Delta T \tag{3.18}$$

3.4.3 Sandia PV Array Model

In order to improve the accuracy of the DC voltage estimation, we have used a behavioral model of the PV array developed by sandia national laboratory [126]. The Sandia PV Array Model are presented by the following equations below 3.19, 3.20 and 3.21.

DC Current model

$$I_{mp} = p \cdot (I_{mpp_{STC}} \cdot N_p(c_0 E_e + c_1 E_e^2) \cdot (1 + cti \cdot \alpha_{mp}(T_c - T_0))) \tag{3.19}$$

DC voltage model

$$V_{mp} = s \cdot (V_{mp\_STC} + c_2 N_s \cdot \delta(T_c) \cdot ln(E_e) + c_3 N_s(\delta(T_c) ln(E_e))^2 + ctv \cdot (T_c - T_0)) \tag{3.20}$$

With

$$\delta(T_c) = n \cdot k \cdot (T_c + 273.15)/q \tag{3.21}$$

Improved DC voltage model

A coefficient has been added to the DC voltage model in order to improve the accuracy, the model becomes (see Eq. 3.22 and 3.23).

$$V_{mp} = s \cdot (V_{mp_{STC}} + c_2 N_s \cdot \delta(T_e) \cdot ln(E_e) + c_3 N_s(\delta(T_e) ln(E_e))^2 + (ctv \cdot T_e . E_e) - (cve/E_e)) \tag{3.22}$$

With

$$\delta(T_e) = n \cdot k \cdot (T_e + 298.15)/q \tag{3.23}$$

The DC power at MPP is calculated by the following relationship

$$P_{mp} = V_{mp} \cdot I_{mp} \tag{3.24}$$

Where;

Imp = Current at the maximum-power point (A)
I_{mp_STC} = Current at the maximum-power point at STC (A)
$p = 2$ string in parallel
Vmp = Voltage at maximum-power point (V)
V_{mp_STC} = Voltage at maximum-power point at STC (V)
$s = 15$ modules in series
Pmp = Power at maximum-power point (W)
N_s = Number of cells in series in a module's cell-string
N_p = Number of cell-strings in parallel in module
k = Boltzmann's constant, 1.38066E-23 (J/K)
q = Elementary charge, 1.60218E-19 (coulomb)
T_c = Cell temperature inside module (°C)
T_0 = Reference cell temperature, typically 25°C
$T_e = T_c - T_0$
E_0 = Reference solar irradiance, typically 1000 W/m2
$\delta(T_c)$ = 'Thermal voltage' per cell at temperature Tc. For diode factor of unity (n=1) and a cell temperature of 25°C, the thermal voltage is about 26 mV per cell
$c0, c1$ = Empirically determined coefficients relating Imp to effective irradiance, Ee. equal to 1, (dimensionless)
$c2, c3$ = Empirically determined coefficients relating Vmp to effective irradiance (c2 is dimensionless, and c3 has units of 1/V)
cti = the normalized temperature coefficient for MPP current, equal to 2.3 mA/°C in datasheet.
ctv = the normalized temperature coefficient for MPP voltage, equal to -74 mV/°C in datasheet.
Cve = Empirically determined coefficients relating Vmp to effective irradiance.

3.4.4 Parameters identification.

For all used models, the parameters identification is done through curve fitting toolbox under MATLAB software, where the fitting is based on nonlinear least squares method and trust-region algorithm. In addition, the empirical models were validated and proved using experimental data collected from GCPV system.

The empirical models used to predict module back surface temperature as a function of tilted irradiance, ambient temperature, and wind speed, are a function of three variable. Therefore, we used the procedure given in [133] to decompose the temperature model equation into two equations in order to estimate the coefficients using curve fitting toolbox.

Table 3.4 gives the identified coefficients used to predict module back surface temperature.

The empirically identified coefficients used in order to predict DC current and DC voltage at MPP based on SAPM are given respectively in Table 3.5 and 3.6 for three Sub-arrays.

In last section, the sandia inverter model used to predict AC power was presented with four parameters for one inverter. In this section, eight coefficients were identified for three inverters based on sandia inverter model as shown in Table 3.7.

Table 3.4 Empirically identified coefficients used to predict module back surface temperature.

Module Temperature Model	NOCT$_{Wv}$for PV Cell			Faimam		Sandia	
Coefficient	p1	p2	T$_{NOCT}$	f1	f2	s1	s2
Values	0.7061	-0.9818	46.5	37.71	4.694	-3.691	-0.08396

Table 3.5 Empirically identified coefficients used to predict DC current using sandia model.

Coefficient	c_0	c_1	cti
Sub-array 1	0.961	-0.111	0.001
Sub-array 2	0.9828	-0.1338	0.001
Sub-array 3	0.9521	-0.1074	0.001

Table 3.6 Empirically identified coefficients used to predict DC voltage using sandia model.

Coefficient	c_2	c_3	n	cvt	cve
Sub-array 1	0.1239	4.292	2.442	-0.0731	0.3758
Sub-array 2	0.105	1.42	3.648	-0.07744	0.2891
Sub-array 3	0.1317	3.155	2.584	-0.07403	0.302

Table 3.7 Empirically identified coefficients used to predict AC power using sandia inverter model.

Coefficient	P_{S0}	V_{DC0}	P_{DC0}	P_{AC0}	C_0	C_1	C_2	C_3
Inverter 1	15	269.8	2715	2574	-2.011e-05	0.00168	0.4418	0.1339
Inverter 2	15.15	275.7	2770	2580	-4.172e-06	0.001387	0.3327	0.3249
Inverter 3	15	262	2743	2563	-1.11e-05	0.003248	0.7455	0.3097

3.4.5 Simulation result using sandia model for PV array

The simulation of all behavioral models listed in Table 3.8 was performed under MATLAB environment (see Appendix B.2). Before the simulation, all models were well calibrated using experimental data for a reference day with following condition.
o Clear sky day.
o Medium ambient temperature
o Without 1) measurement faults, 2) shading, 3) significant soiling, 4) electrical faults and other anomalies.

Table 3.8 Summary of selected models with thier references

Model types	Selected model with Reference
PV cell/module Temperature model	▪ Nominal Operating Cell Temperature (NOCT) model [247] ▪ NOCT model including the wind speed effect NOCTW [138] ▪ Faimen model for module temperature [254]. ▪ Sandia model to estimate module temperature [126].
DC Current model	▪ Bellini [248] ▪ Sandia PV Array Performance Model (SAPM) [126].
DC Voltage model	▪ Eduardo [249] ▪ Sandia PV Array Performance Model [126].
AC power model	▪ Sandia Inverter model [140]

Figure 3.15 illustrates the PV cell temperatures of measured and predicted from four models. The measurements of effectiveness for the used PV cell temperature models listed in Table 3.8 confirm its good prediction performance.
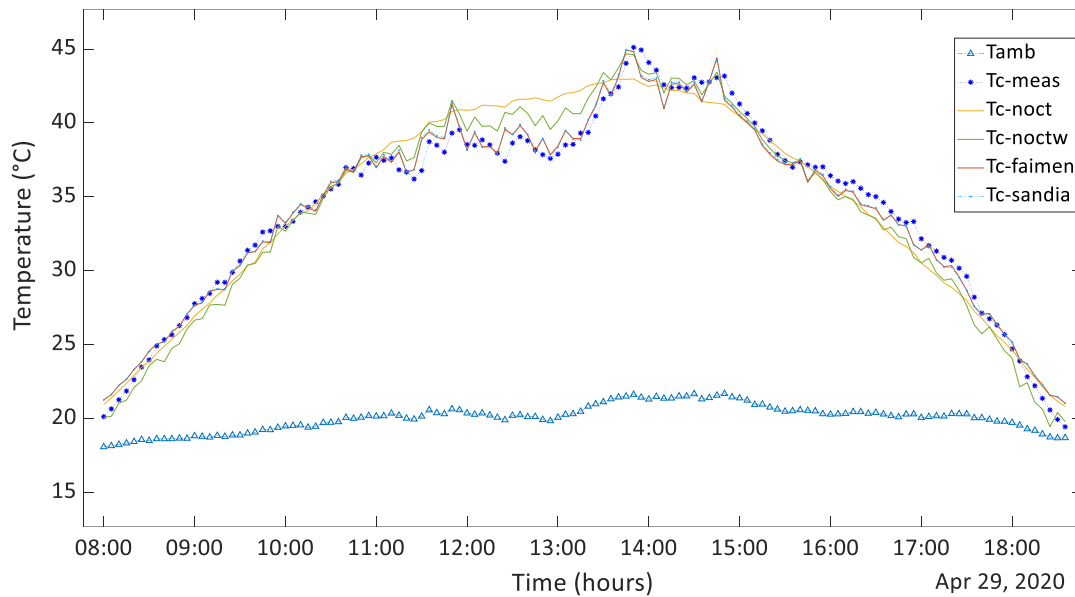
Figure 3.15 Measured PV cell temperature Vs. predicted from four model.

According to the regression metrics listed in Table 3.9, Sandia and Faimen models have almost the same performance, but sandia cell model is the best, in third position the NOCTW model with wind speed consideration.

Table 3.9 Regression metrics for the used PV cell temperature models.

Metrics/Param.	NOCT	NOCTw	Faimen	Sandia
MAE	1.2043	1.0368	0.62246	0.61698
RMSE	1.5523	1.2368	0.78094	0.77446
MAE (%)	2.6958	2.3209	1.3933	1.3811
RMSE (%)	3.4748	2.7685	1.7481	1.7336
R-squared	0.94333	0.96402	0.98566	0.98589

For the simulations results by way of example, we are satisfied to give just the graphs of sub system 2, because the plots of subsystem 1 and 3 look very similar to sub-system 2, the other sub system will be compared in the regression metrics tables.

Figure 3.16 shows the MPP current of the PV sub-array 2 measured and predicted from two models. Table 3.10 gives the regression metrics of two DC current models simulated for three sub-arrays. We can see a good agreement between the measured and the predicted data from models for all subarrays. For the Bellini model the **R2** is around **0.995,** while sandia model is more accurate with an **R2** of **0.999** for all PV subarrays.

114
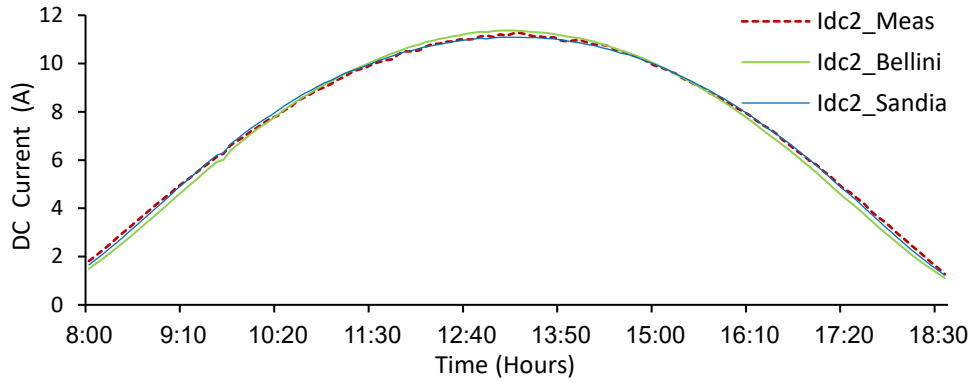
Figure 3.16 Measured Vs. predicted MPP current of the PV sub-array N°2.

Table 3.10 Regression metrics of DC current models simulated for three sub array.

Metrics/Param.	MAE (A)	RMSE (A)	MAE (%)	RMSE (%)	R-squared
Idc1-Bellini	0.18	0.22	1.58	1.96	0.995
Idc1-SNL	0.08	0.11	0.71	1.01	0.999
Idc2- Bellini	0.20	0.24	1.74	2.09	0.994
Idc2-SNL	0.09	0.10	0.76	0.92	0.999
Idc3- Bellini	0.16	0.20	1.48	1.82	0.995
Idc3-SNL	0.08	0.10	0.71	0.92	0.999

Figure 3.17 shows the MPP voltage of sub-array 2 measured and predicted from two behavioral models. Table 3.11 gives the regression metrics of two DC voltage models simulated for three PV subarrays. We can see a good fitting between the measured and the predicted data from two models for all subarrays. For the Eduardo model the **R2** is greater than **0.75,** sandia model is more accurate with an **R2** greater than **0.89** for three sub-arrays. We observe that for the predicted DC voltage, the **R2** is low, due to the dynamic DC voltage variation, while the **RMSE** is less than **0.98%** for Eduardo model and less than **0.66%** for Sandia model as shown in Table 3.11.
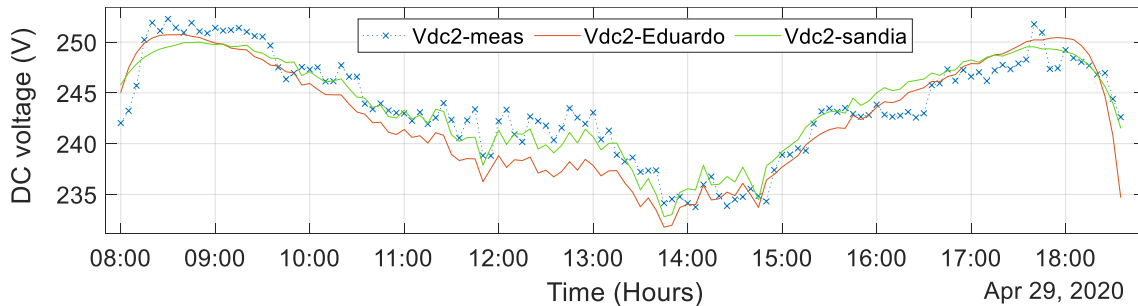
Figure 3.17 Measured and Simulated MPP voltage of the PV subarray N°2 .

Table 3.11 Regression metrics of DC Volatge models simulated for three sub-array.

Metrics/param.	MAE (V)	RMSE (V)	MAE (%)	RMSE (%)	R-squared
Vdc1-Ed	1.92	2.43	0.76	0.97	0.773
Vdc1-SNL	1.33	1.63	0.53	0.65	0.899
Vdc2-Ed	1.96	2.41	0.78	0.96	0.756
Vdc2-SNL	1.34	1.62	0.53	0.64	0.891
Vdc3-Ed	1.85	2.29	0.73	0.90	0.789
Vdc3-SNL	1.16	1.38	0.46	0.54	0.924

As we saw in the state-of-the-art section, that models of DC power based on direct estimation (i.e., one equation) are less accurate than models which are based on the product of DC current and DC voltage models. So, the DC power simulation results shown in the Figure 3.13 are based on the product of the estimated DC current and DC voltage.

115

Figure 3.18 displays the maximum DC power of sub-array 2 measured and predicted. Table 3.12 indicates a satisfying agreement between the measured data and the predicted value of DC power using both models (i.e., **R2** greater than **0.994**). We notice that the simulation results of DC power are very close to those of DC current.
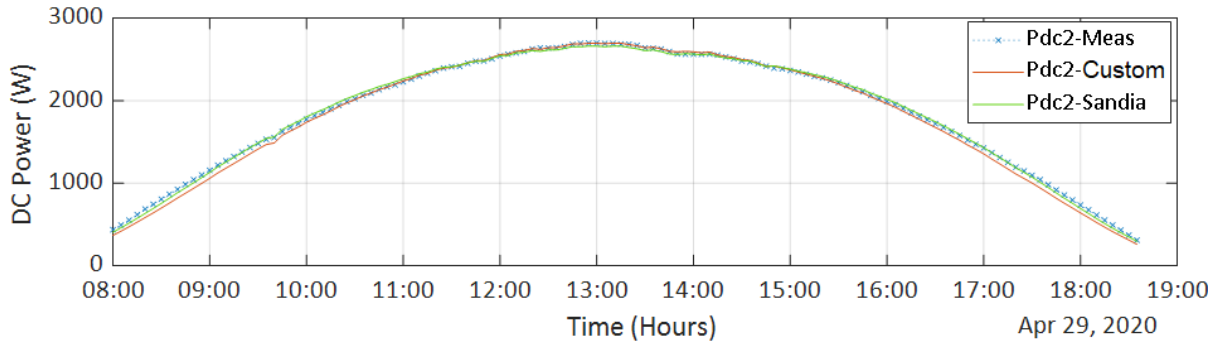
Figure 3.18 Measured and Simulated Maximum power of the PV sub-array N°2.

Table 3.12 Regression metrics of DC Power simulated for three sub-array.

metrics/param.	MAE (W)	RMSE (W)	MAE (%)	RMSE (%)	R-squared
Pdc1-Cstm	37.4	52.8	1.38	1.95	0.994
Pdc1-SNL	25.7	32.8	0.95	1.21	0.998
Pdc2-Cstm	39.3	53.4	1.45	1.98	0.994
Pdc2-SNL	23.4	27.0	0.87	1.00	0.999
Pdc3-Cstm	33.9	48.5	1.26	1.81	0.995
Pdc3-SNL	23.3	29.3	0.87	1.09	0.998

We also observe that the prediction of AC power using the Sandia inverter model, based on the predicted DC voltage and DC power, agrees very well with the measurement data as shown in Figure 3.19, with an **R2** greater than **0.999** and an RMSE that does not exceed **0.93%** for the three simulated inverters (Table 3.13).
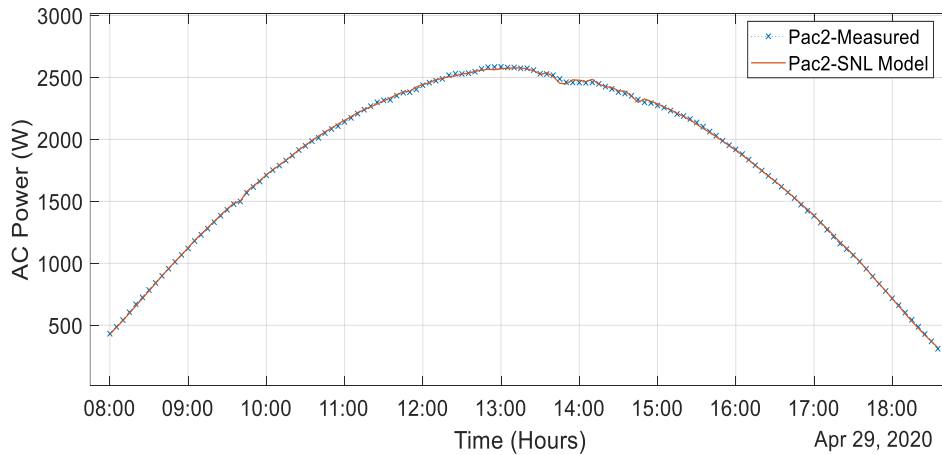
Figure 3.19 Measured and Simulated AC power at the inverter output.

Table 3.13 Regression metrics of AC Power model simulated for the three inverters of the GCPVS.

Parameters	MAE (W)	RMSE (W)	MAE (%)	RMSE (%)	R-squared
Pac1-SNL	18.9	24.1	0.73	0.93	0.999
Pac2-SNL	7.8	9.86	0.30	0.38	1.000
Pac3-SNL	17.2	24.0	0.66	0.92	0.999

In summary, the above described empirical models fit well with the measured data. Note that the calibration of representative models is very important, in order to try to approximate the experimental reference data as much as possible and to accurately emulate the electrical behavior of all components of the PV system. These models are constructed using fault-free data and will generate residuals of new arrival data for fault detection purposes.

3.5 Model implementation under LabVIEW

Figure 3.20 illustrates the process of integrating models calibrated in MATLAB into the LabVIEW environment. All behavioral models are implemented under LabVIEW code diagram using a graphical program combined with textual program (Figure 3.21), this is called a virtual instrument (VI). The detailed textual program of sandia models and performance metrics was given in Appendix B.2.

The layout of the developed VI can be viewed in front panel for an interactive user-interface, including different tabs shown in Figures 3.22 to 3.26.
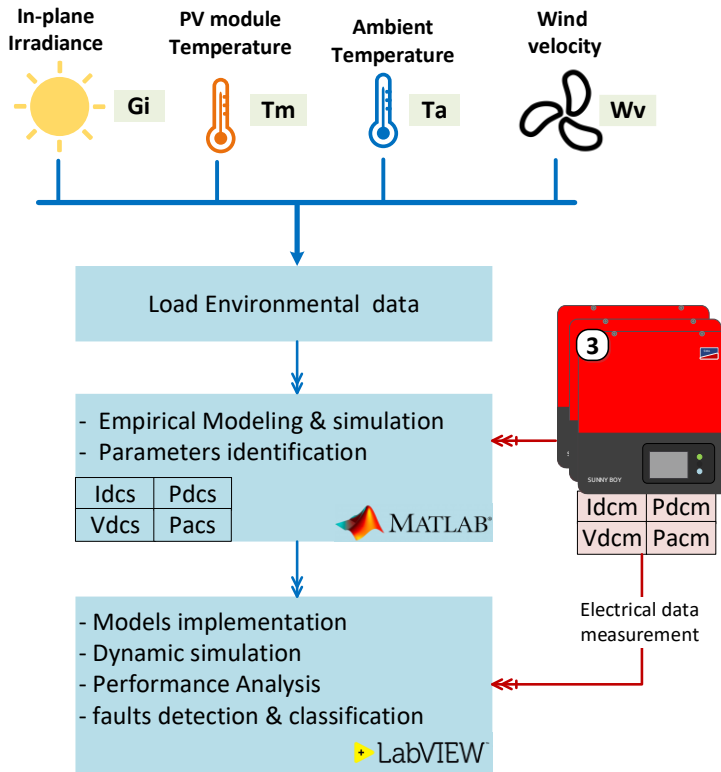
Figure 3.20 Flowchart of modeling and validation using MATLAB and dynamic modeling under LabVIEW.
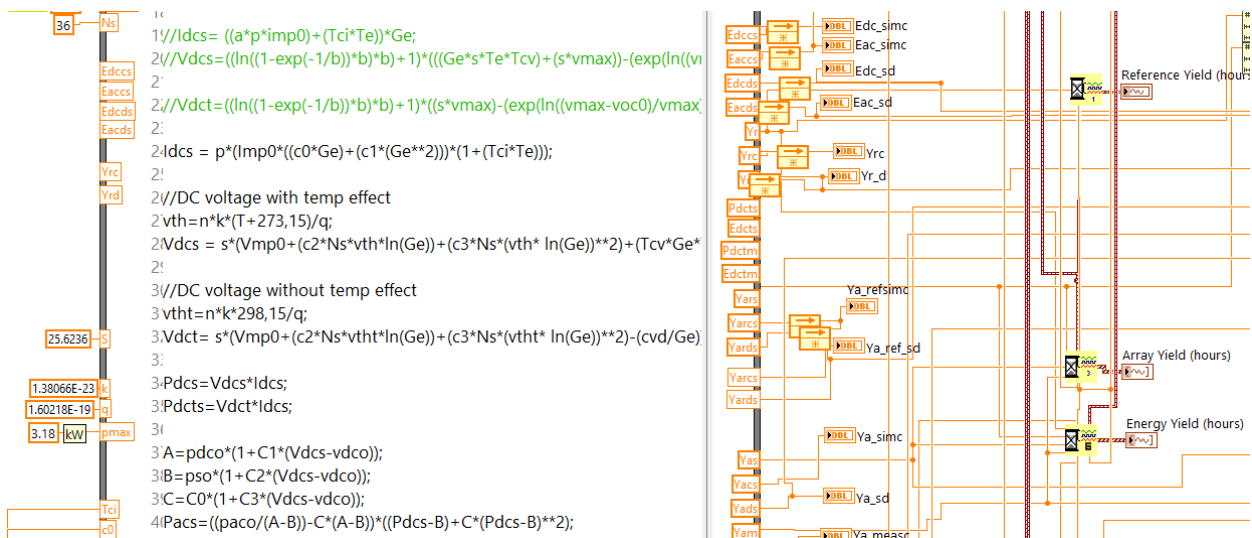
Figure 3.21 sample of modelization code under LabVIEW block diagram.
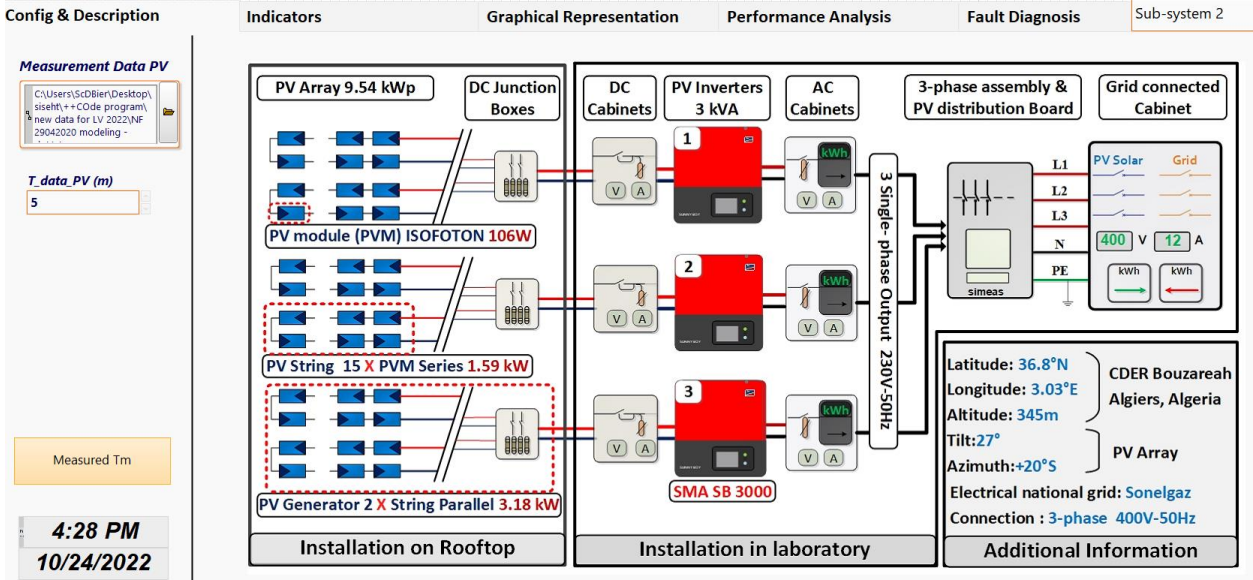
Figure 3.22 Designed interface for dynamic modeling and performance analysis.
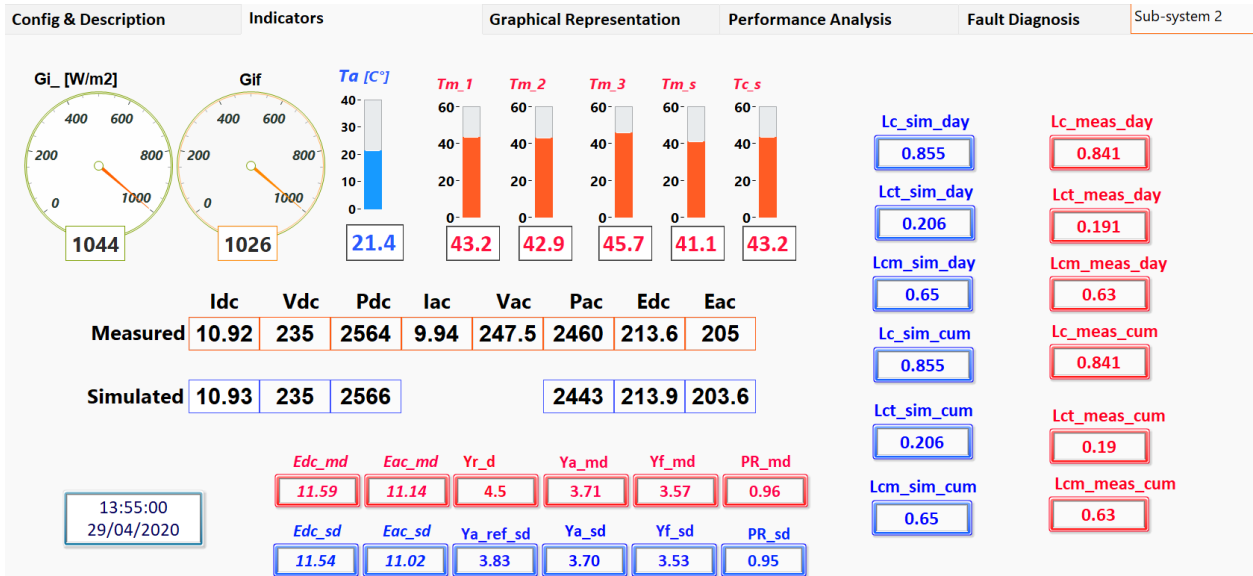
Figure 3.23 Modeling interface -Tab for instantaneous indicators.
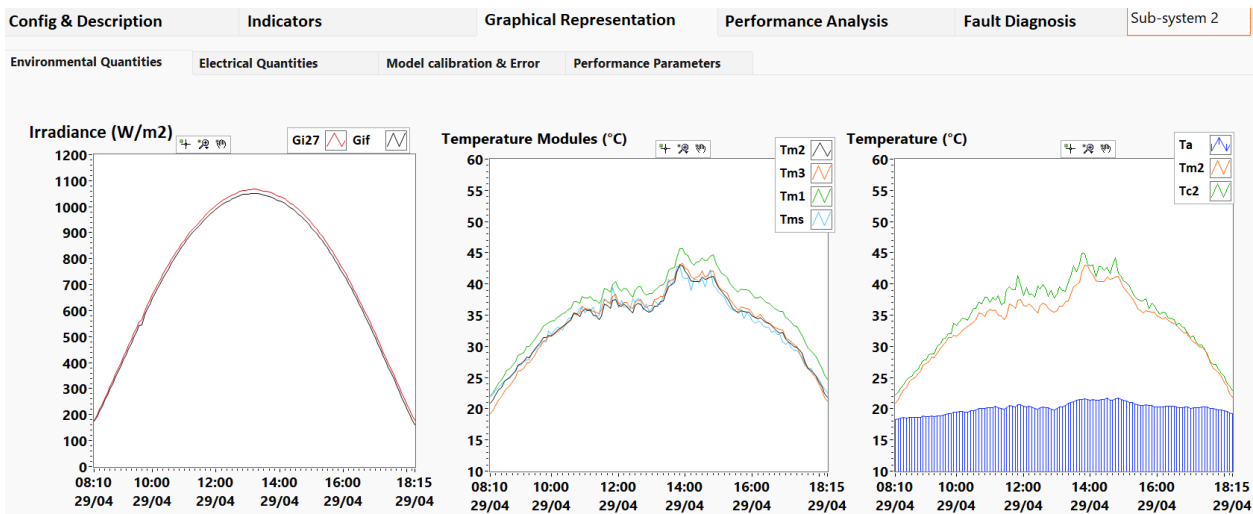
Figure 3.24 measurement graphs of tilted irradiances , ambient temperature and modules temperatures.
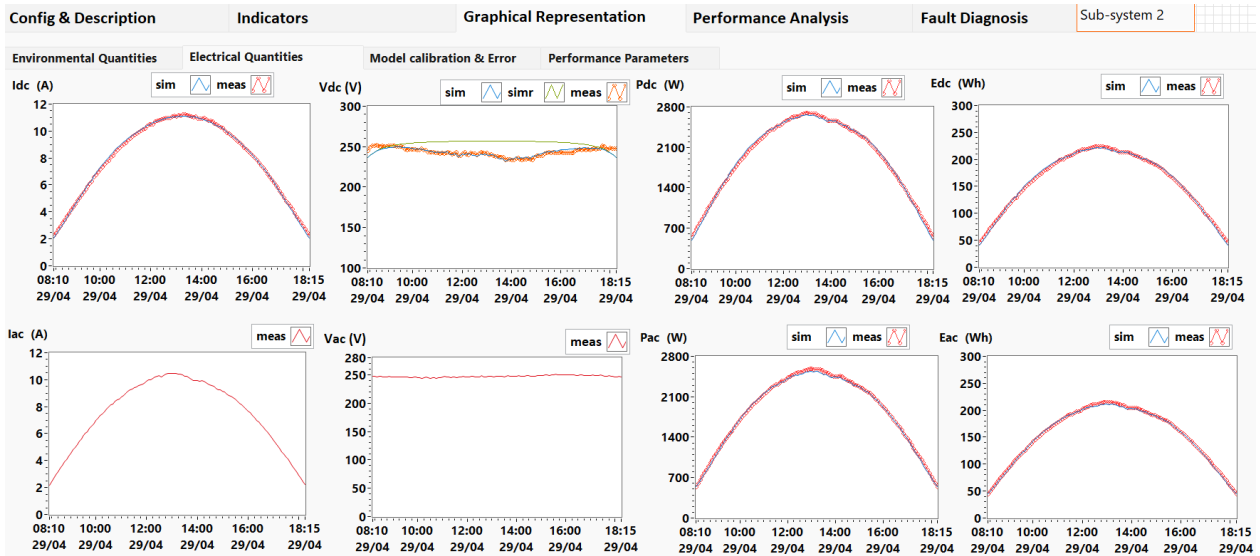
Figure 3.25 Measurement graphs of both measured and predicted DC& AC Electrical quantities.
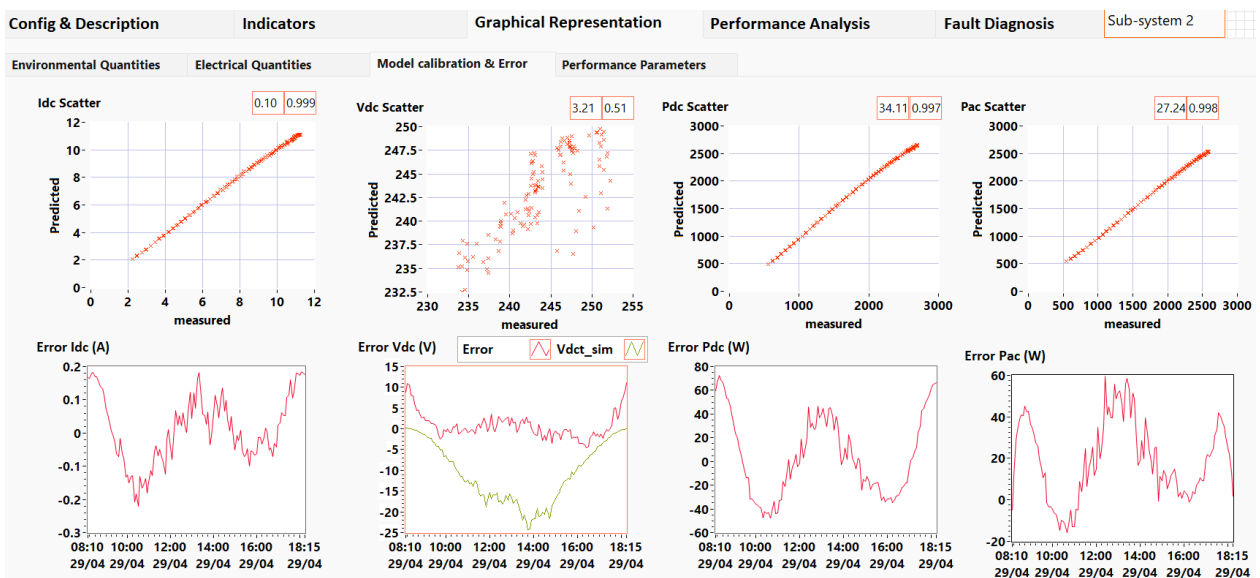
Figure 3.26 Modeling interface -Tab for Models calibration.

As shown in Figures 3.22 to 3.26, the designed interface was very user-friendly, using modern indicators and waveform graphics. The modeling results were very satisfactory, with a better fit to the reference electrical measurements for all PV subsystems.

3.6 PV System Performance

The objective in this section is to evaluate and analyze the performances of a PV system connected to low voltage grid using LabVIEW platform. The main task is to model and evaluate different yields and other parameters for a PV system.

In the modeling interface, we have developed a new tab dedicated for performance analysis that contains 4 sub-tabs (Figure 3.22).

The Performance analysis is applied for a period of seven (7) days selected from April to august, this analysis consists to calculating several indicators and performance metrics [148] [149].

The daily irradiation received E_r in (kWh/m2/day) measured on the horizontal and tilted planes as indicated by the equation 3.25.

$$E_r = ((G_r . \Delta_t) + E_{r-1} . b_{id})/1000 \qquad (3.25)$$

119

The average temperature T_{av} for ambient and PV cell each day according to the following equation 3.26.

$$T_{av} = ((T.\Delta_t) + T_{av-1}.b_{id})/N_{sp} \qquad (3.26)$$

The DC and AC daily electrical energy E_e in (kWh /day) measured and simulated were represented by eq. 3.27.

$$E_e = ((P.\Delta_t) + E_{e-1}.b_{id})/1000 \qquad (3.27)$$

where:

Δ_t : sampling time in hours

b_{id} : Daily Initialization Bit

N_{sp} : Number of samples during the day

The yields of the PV system are expressed as: reference yield (Y_r), array yield (Y_a) and final yield (Y_f) given in [hr], as well as the performance ratio (*PR*) expressed in [%], they can be obtained from the simulation results using the formulas (3.28 to 3.31) which are used in accordance the IEC 61724 standard [77] to evaluate the performance of a GCPV installation. [151] [149].

$$Y_r = \frac{\int_0^{\Delta t} G_h}{G_0} \qquad (3.28)$$

$$Y_a = \frac{\int_0^{\Delta t} E_{dc}}{P_0} \qquad (3.29)$$

$$Y_f = \frac{\int_0^{\Delta t} E_{ac}}{P_0} \qquad (3.30)$$

$$PR = \frac{Y_f}{Y_r} = \frac{E_{ac}}{E_{dc}} \qquad (3.31)$$
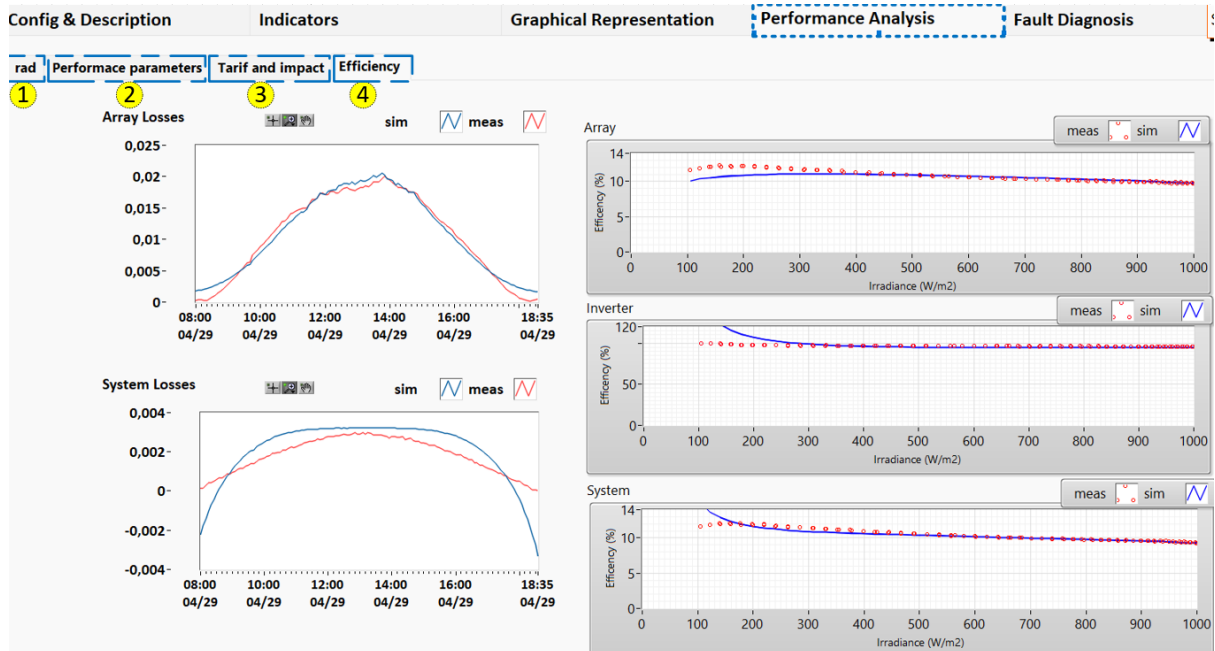
Figure 3.27 Designed performance analysis Tab.

The performance parameters and other indicators are plotted in graphics under LabVIEW interface with different representation, as shown in the Figures (3.28 to 3.32).

Figure 3.28 illustrates Graphical representation of performance parameters for 7 days. Figure 3.29 shows the histograms for daily analysis and indicators for the cumulated values of 1) received irradiation energy in (kWh/m^2/day), 2) average of ambient temperature and PV cell temperature in (°C), 3) measured and predicted energy of DC & AC in (kWh/day), and 4) performance ratio.
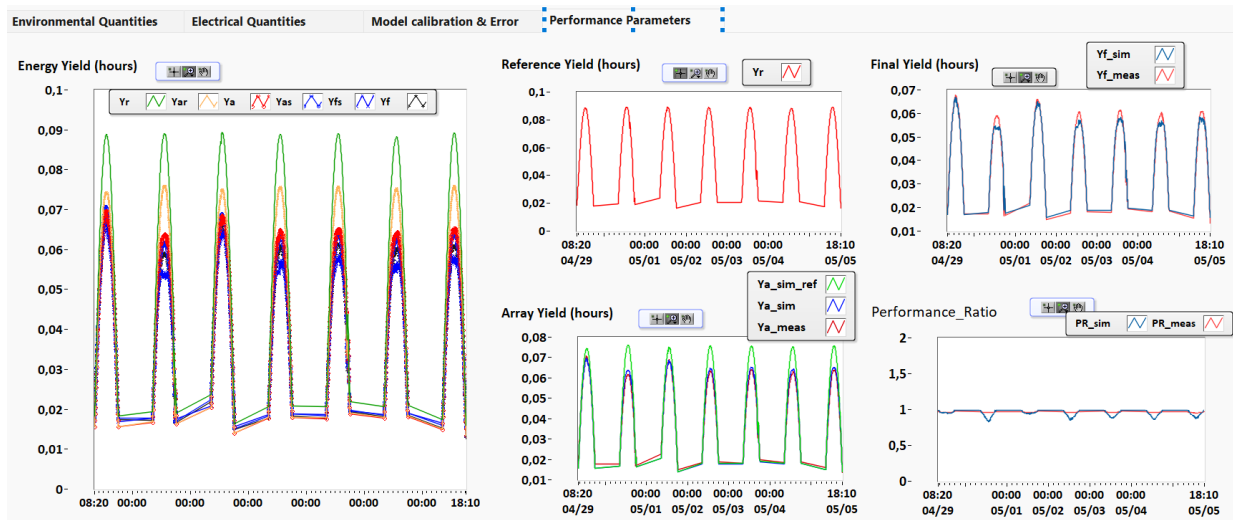
Figure 3.28 Graphical representation of performance parameters for 7 days.
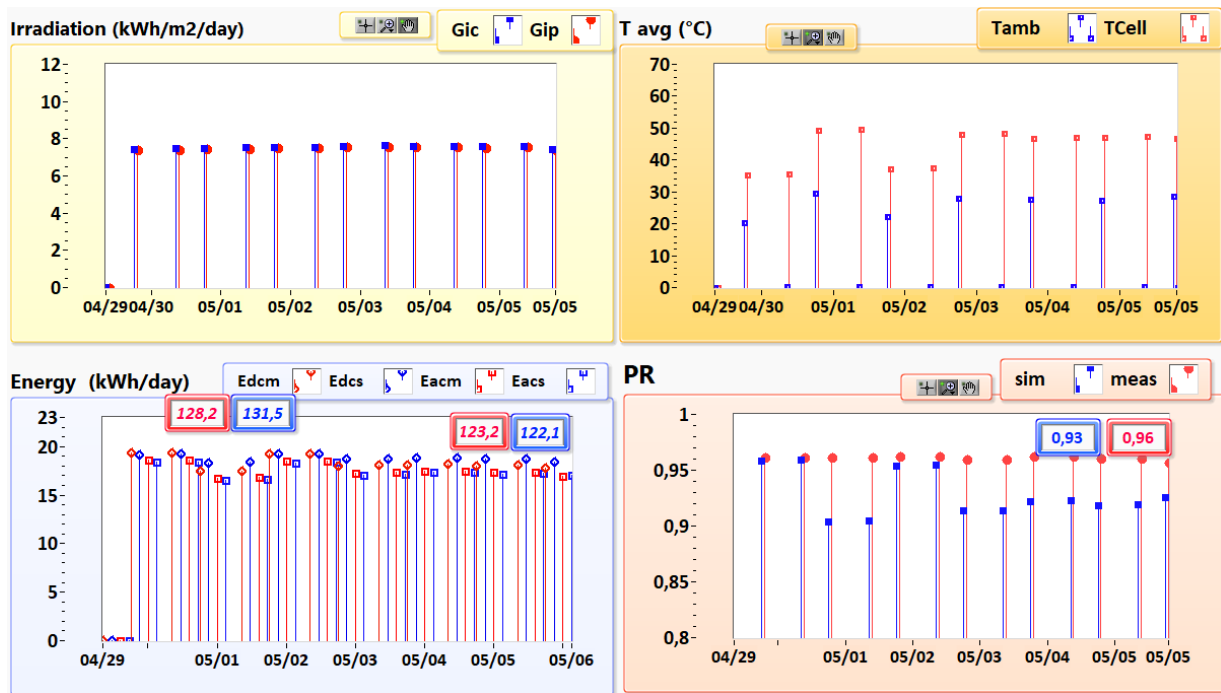
Figure 3.29 Histogram of irradiation energy, temperatures average, DC / AC Energy and performance ratio.

Figure 3.30 shows the histograms representation of 1) reference yield (Y_r), 2) array yield (Y_a) and 3) final yield (Y_f) given in [hr], as well as the 4) performance ratio (*PR*) expressed in [%] according to the IEC 61724-1.
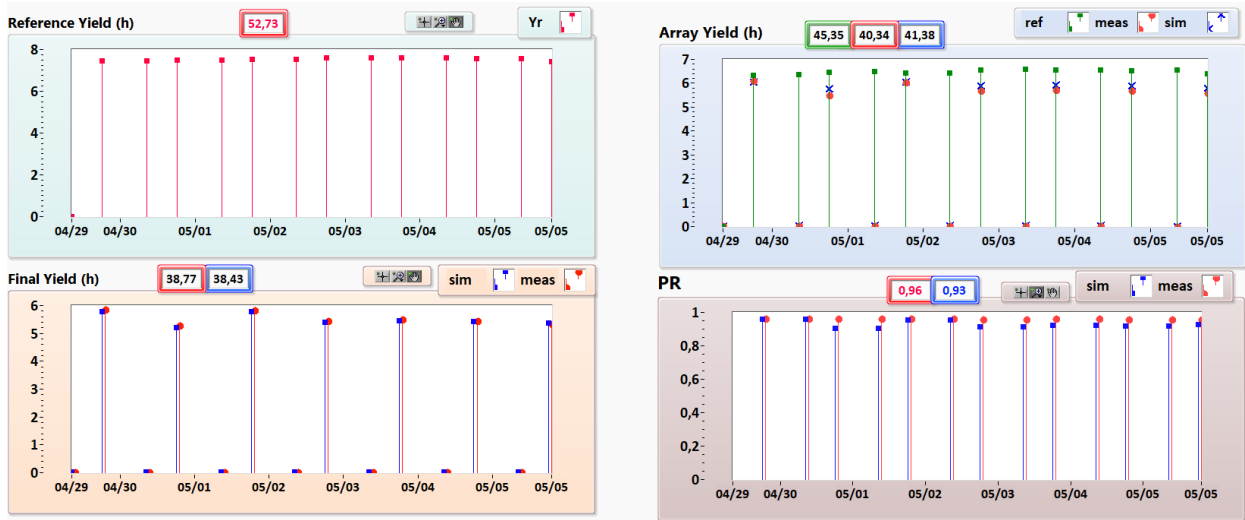
Figure 3.30 Histogram of all Performance parameters according to the IEC 61724-1.

Figure 3.31 displays the histograms for daily analysis and indicators for the cumulated values of 1) AC energy produced by PV system for one sub system in (kWh/day), 2) energy price analysis using Sonelgaz medium tariff (i.e., 4.179 DZD/kWh), 3) energy price analysis using feed-in tariff made for 1 to 5MWp PV power plant in Algeria (i.e., 15.94 DZD/kWh) and 4) avoided CO_2 emission using a PV power plant, Knowing that for 1 kWh produced by a gas-fired power plant we have 0.38 kg of CO_2 emitted.
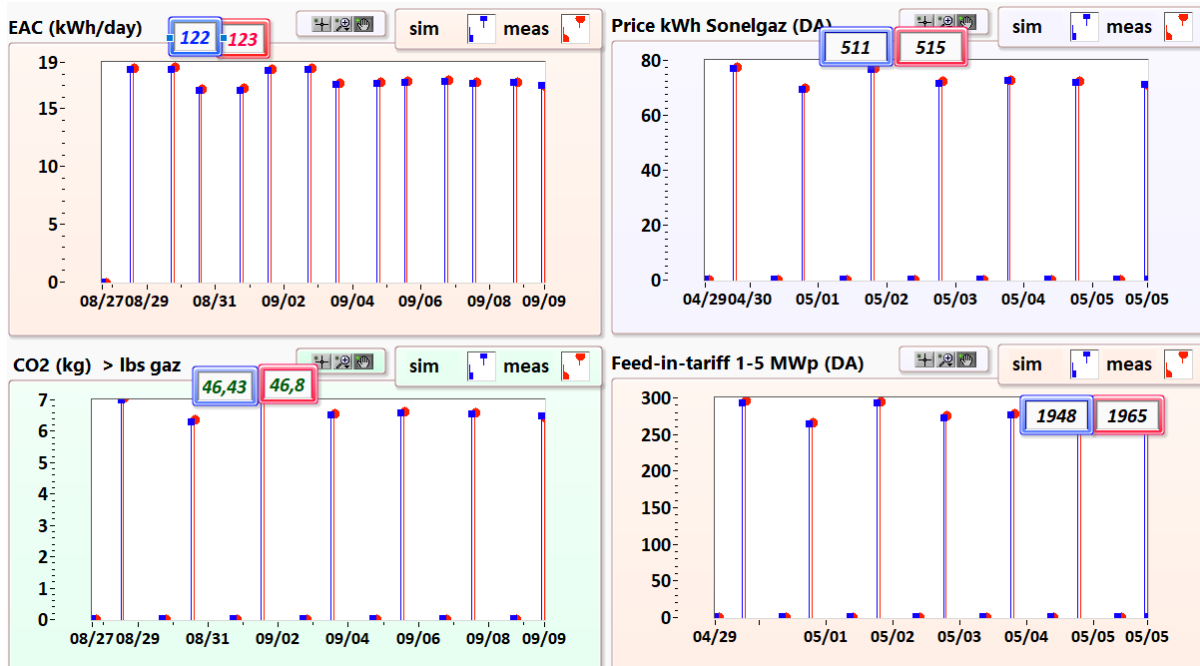
Figure 3.31 Histogram of AC energy, sonelgaz KWh price, feed-in tariff price and avoided CO_2.

122

The measured efficiency of the PV sub-system versus simulated are represented in Figure 3.32 for seven days.
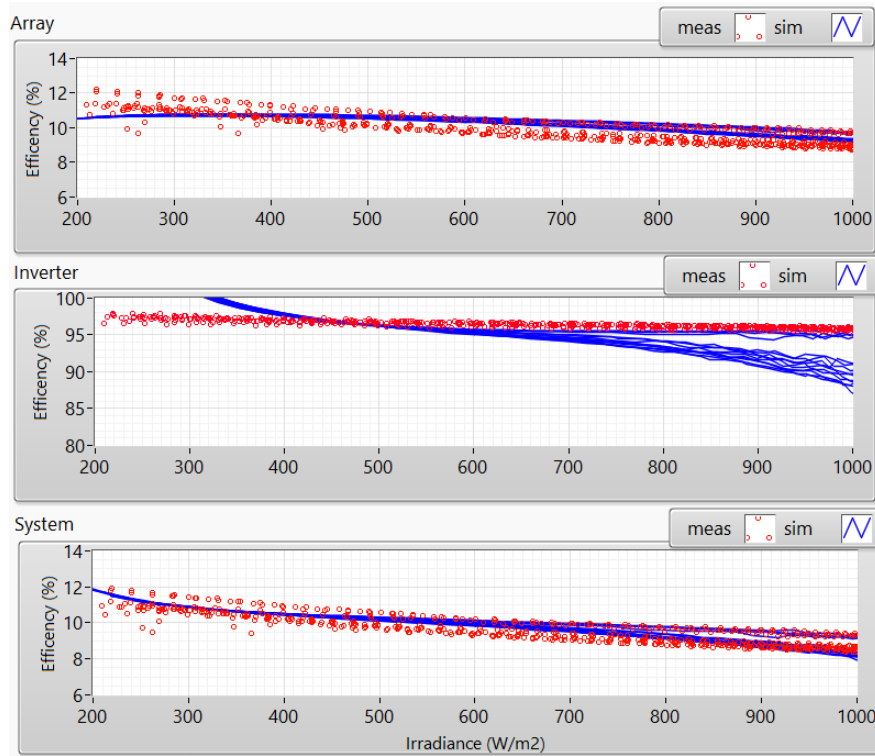
Figure 3.32 Measured and predicted efficiency of PV array, inverter and system.

According to results, we can tell that the performance ratio of the GCPV system is above 93 %, The PV system efficiency varies between 8% and 12% from 200 W/m^2 up to 1000 W/m^2, and the comparison of efficiency between the experimental and the simulation, showed a good agreement especially for irradiance higher than 400 W/m^2.

3.7 Conclusion

In this chapter, several models were selected and tested in order to choose the best for each modeling part. The results obtained by simulation were validated using reference data measurements of the 9.54 kWp GCPVS in MATLAB, the comparison showed good agreement, and that the models developed by SNL are the best (i.e., cell/module temperature model, SAPM to predict DC current and DC voltage and sandia inverter model to estimate AC power).

For the non-parametric model based on PCA, we saw a good agreement between the measured and the predicted data, results illustrate the goodness of the PCA model, the generated residuals based on the developed PCA reference model will be evaluated by multivariate monitoring charts to detect fault.

The user-interface developed under LabVIEW makes it possible to model the electrical behavior of GCPVS and to analyze the performance of meteorological and electrical data by calculating the performance ratio and the energy yields of the PV system, the interface also allows a dynamic visualization of all data and information with different scenarios.

Note that the user-interface created is extensible to integrate multiple performance model and to analyze data using advanced techniques (e.g., Machine Learning, statistical methods and hybrid methods) for modeling, performances analysis and faults detection in a PV system. The deviations between the simulated and measured values represents a detection of the operation anomaly of PV system.

Chapter 4

Fault Detection and Diagnosis of Grid Connected PV System

Chapter 4 : Fault Detection and Diagnosis of Grid Connected PV System

4.1 Introduction

Faults diagnostic in PV system is crucial for improving their resilience and ensuring the continuous delivery of electricity. In general, the fault diagnosis process is determined by comparison between both normal (i.e., predicted behavior by simulation) and faulty data for each type of failure (i.e., observed behavior by measurement) see (Figure 4.1). While, the identification or classification of faults is the most important step of the failure routine process. In another way, this method consists of comparing the amount of energy that a PV system is supposed to produce with the actual performance.

As we saw in **Chapter 3**, that the performance simulation of a PV system is based on either parametric or nonparametric models. The two approaches can share the same inputs (e.g., irradiance, temperature, wind speed, etc.) and the same output which is the power produced by PV system. In most cases, meteorological data is measured by sensors installed on the site or retrieved from satellite measurements. Indeed, the prediction system consists of a behavioral model. The meteorological data are entered into the PV model, which then generates predicted behavior of PV installation. When the system performance is significantly lower than simulated, the fault detection system classifies the PV system as faulty.

An inherent challenge of this method is knowing the accuracy of predictions by parametric models. Since the performance of the PV system is influenced by many parameters, it is highly essential to estimate the parameters of behavioral models in order to have a good calibration to experimental measurements under normal operating conditions without faults or any loss in performance. It is also recommended to auto-calibrate the predictions due to the gradual evolution of the parameters over time. In summary, prediction systems that monitor PV performance examine and compare current PV performance to predictions over time before concluding that the PV system is underperforming. The prediction method for identifying faults provides a variety of additional advantages for the PV market by expanding the possible applications of the fault detection system [6]. Figure 4.1 shows a block diagram of the general method used to identify faults using the prediction method.
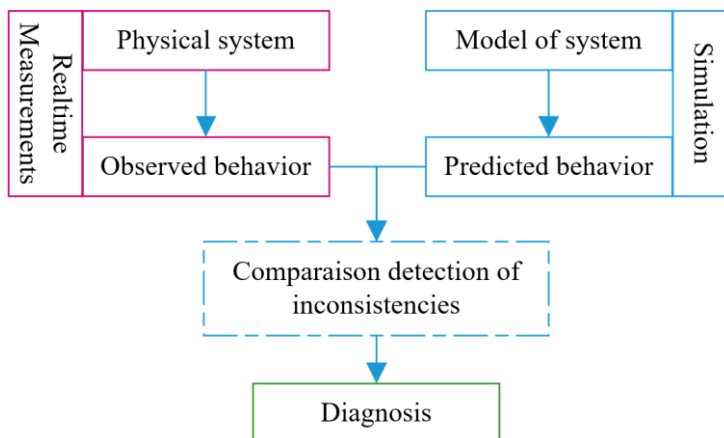
Figure 4.1 Block diagram of a PV fault detection system using the prediction method.

Generally, Fault Detection and Identification (FDI) techniques that exploit the analytical monitoring data are based on one of the following methods: 1) Real-time difference measurement, 2) Signal processing, 3) Statistical analysis or 4) Machine learning and deep learning, while the combination of these methods offers fast and accurate diagnosis. Indeed, each data analytic technique used for the FDI in monitored PV systems, has its own advantages and limitations. Hence, the decision for the most cost-effective and more appropriate FDI solution depends on numerous factors [16], [193].After carrying out the monitoring, calibration of models and performance analysis, the last step will be the detection and identification of faults occurring in a PV system connected to the grid.

In this chapter we present two fault diagnostic techniques. The first technique is based on accurate parametric behavioral model for calculate the residuals, the residue examination is performed using performance loss analysis of forth indicators that allowing the detection and the recognition of faults type occurring in the PV system. Six types of faults and nine cases were considered in this section: 1) Open circuit Fault 2) PV string Fault, 3) partial shading of pylons, 4) soiling on the PV array, 5) short circuit fault with four (4) cases (i.e., 2, 3, 4 and 6 PV Modules short-circuited) and 6) DC -AC efficiency faults. Finally, these faults were detected and identified using a convivial user interface with other additional features. The second techniques consist in developing a simple and efficient diagnostic method based on parametric models and the Double Exponentially Weighted Moving Average (DEWMA) scheme. The residuals were calculated with parametric and nonparametric models. While residue quantification is performed using DEWMA technique in order to detect and identify faults occurring in the PV system. Six environmental and electrical faults from a 9.54 kWp grid-connected PV system were considered to evaluate the feasibility of the designed detection methods. these faults were successfully located.

4.2 Detection and identification of fault based on Real-time Difference Measurement

In this section, we have interested in the Real-time Difference Measurement (RDM) method. As we have seen in **chapter 2**, a PV system during operation, it can be subjected to several large power losses caused by different failures that can appear on the DC and AC sides of a PV system. Detecting faults and anomalies in a PV system is very important in order to 1) achieve the desired electrical power production, 2) avoid downtime and 3) minimize maintenance costs. In the last ten years, numerous works based on RDM method have been published. In [195] an automatic supervision and PV array fault detection procedure was proposed under MATLAB environment, this method are based on power losses analysis and deviation examination of DC current and DC voltage. In [196] an evaluation of both Current and Voltage indicators for automatic detection of main faults occurring in the PV systems was achieved, for real-time supervision this method can be easily integrated into inverter. In [200] two indicators named power and voltage ratio were used to identify faults in PV array. In [197], a level online Fault detection and diagnosis technique based on Power losses Analysis for PV systems was proposed. In [201] An overview of the main strategies for analytic fault detection and diagnosis methods based on power losses analysis, and Current-voltage (I-V) indicators are reported. Recently a simple and efficient approach was proposed in [202] to detect and to identify most common faults in PV systems using three indicators of current voltage and power.

4.2.1 Used faults for evaluation of the proposed method.

The proposed fault detection and identification technique based on four indicators was evaluated using experimental data collected from a GCPVS at CDER, Algiers. Six types of faults have been considered in this section: F1) Open circuit Fault F2) PV string Fault, F3) temporary partial shading, F4) dust on the PV array, F5) short circuit Fault with four (4) cases (i.e., 2, 3, 4 and 6 PV Modules short-circuited) and F6) DC -AC conversion faults (Figure 4.2).
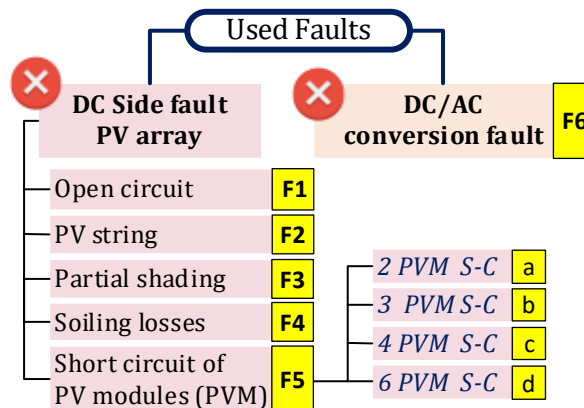
Figure 4.2 Used datasets faults for PLR method evaluation.

Open circuit fault

The purpose of this scenario is to investigate the ability of the proposed technique to identify an open circuit fault. An open circuit fault may appear if there is an instantaneous disconnection of the inverter or the switching off of the residual current circuit breaker (RCCB).

The PV inverter disconnects if 1) the electrical characteristics of the output of the PV generator are outside the operating limit of the inverter or if there is a 2) grid instability. This fault pushes the shutdown of the system until a new reconnection of the inverter. If the residual currents (earth leakage) exceed 30mA or if an electrical fault occurs in the PV system, the RCCB switches off, causing the PV installation to shut down until it is manually switched on.

Figure 4.3 illustrates the photos of the occurred open-circuit after the circuit breaker tripping or after inverter temporary disconnection.
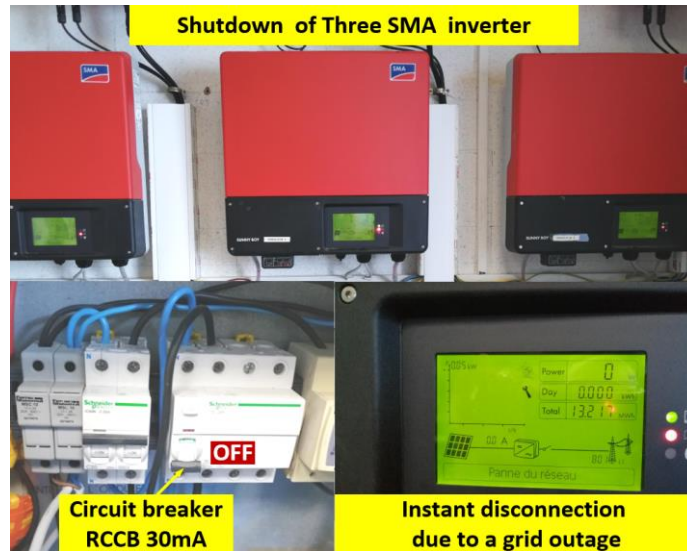
Figure 4.3 Photos of the occurred open circuit fault after the circuit breaker tripping or after inverter temporary disconnection.

String faults

The purpose of this case is to evaluate the ability of the proposed method to detect and locate PV string faults in a PV generator. Practically, string faults are one of the most common faults resulting in large loss of power produced on the DC side of the PV system.

Frequently, this fault can appear if 1) the DC protection (i.e., DC circuit breaker, fuses) is damaged, 2) there is a bad connection of the cables with the terminal blocks which generates arcs 3) or if a disconnection has produced between PV modules in series, (i.e., open circuit in the string).

Here, this fault was created on purpose by turning off the DC circuit breaker of our GCPVS (Figure 4.4-a) or by a real fault following an arc between the cable and the terminal block (Figure 4.4-b).
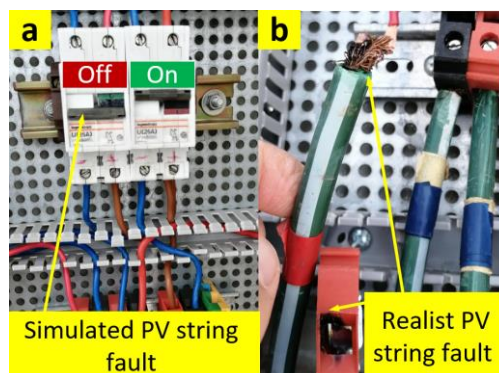
Figure 4.4 Photos of the a) simulated and b) realist PV string fault.

Partial shading

The purpose of this scenario is to analyze the ability of the proposed methods to distinguish partial shading from others anomalies. Partial shading is the uneven distribution of irradiation on the PV array. Shading losses occur due to several obstacles (e.g., pylons, tall building and trees…. etc.) [256]. The partial shading on the PV array at CDER is mainly due to the shading of two tall pylons (Figure 4.5-a) during a given period of the day, which depends on the sun height throughout the year. Figure 4.5-b illustrates the pylon shadow on the PV subarray 3. In this section, the shading is therefore not modeled, it is considered as an anomaly.
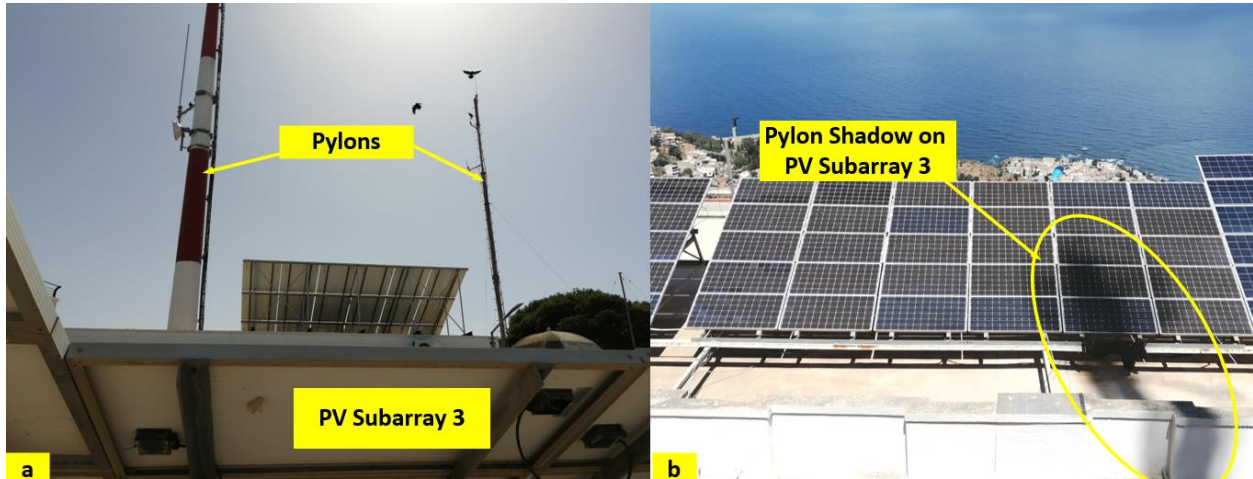
Figure 4.5 photos of a) pylons around PV array and b) shading on the PV subarray 3.

Soiling losses

Soiling power losses depend on 1) environmental conditions, 2) frequency of rainfall, 3) tilt of PV module, 4) cleaning schedule and others. Dust is one of the major problems with any solar PV system, especially in desert regions. Soiling can negatively impact the performances of PV systems by causing power losses up to 15% per year and conceivably higher in deserts [8]. The accumulation of dust on PV modules is linked to several factors, such as PV module inclination, module type, and humidity (Figure 4.6)
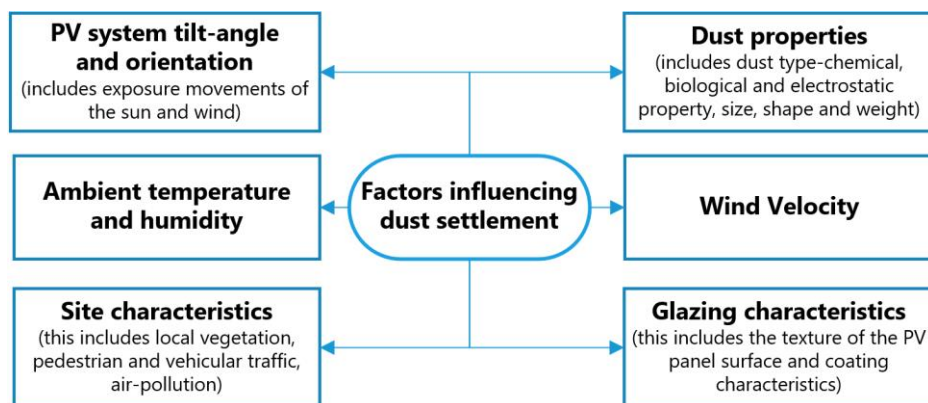
Figure 4.6 Factors influencing dust settlement.

In the CDER's PV system, the soiling losses are due to accumulated dust and bird droppings (Figure 4.7).

Figure 4.7 Dust accumulation and bird dropping on PV subarray 1.

Short-circuit fault.

Short-circuit faults can be caused by bad wiring within PV modules. Also, aging, vibration, and PV modules abrasion represent key sources of short-circuit faults [257]. This kind of fault can cause damage or performance degradation of the PV Modules. Here, four cases are considered (i.e., 2, 3, 4 and 6 short-circuited PV Modules) in order to evaluate the method based on electrical indicators rating. The faults are intentionally created by short-circuiting the modules in the same string according to the desired case. Figure 4.8 shows some cases of short circuit fault in the PV modules.
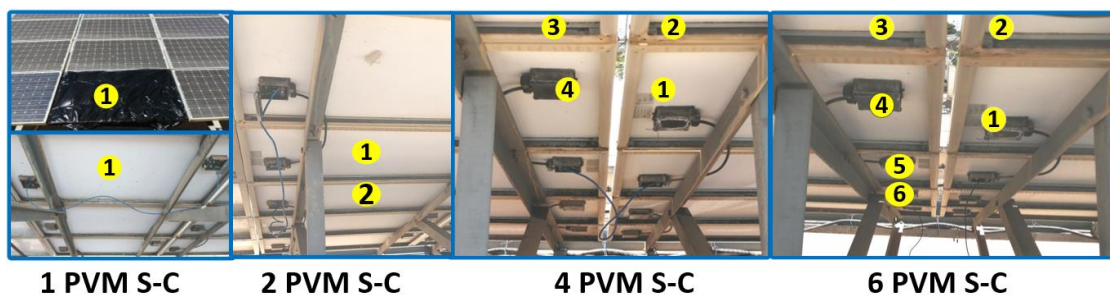
Figure 4.8 Photo of some scenarios of PV modules (PVM) in short circuit (S-C).

DC/AC conversion fault

Inverters convert energy from direct current to alternating current with an efficiency that varies according to the load of the inverter. Manufacturers are usually able to provide an inverter's efficiency profile for low, medium, and high voltages. The inverter may be affected by a drop in desired efficiency according to the profile indicated in the data sheet following electrical problems or degradation of the DC/AC conversion components. this last fault is simulated with conversion efficiency of 80% instead of 95%.

4.2.2 Performance loss rate method using four electrical indicators

In this section we propose a simple and reliable method for detection and localization of various faults in PV systems using four indicators (i.e., DC current, DC voltage, DC power and AC power), the upper and lower thresholds of four indicators are calculated using the simulation results of the parametric models already seen in chapter 3.

Eq 4.1 to Eq. 4.4 show the four used indicators depending on the following quantities DC current, DC voltage, DC power and AC power.

$$IdcR = \frac{Idc_{Sim}}{Idc_{Meas}} \quad (4.1) \qquad VdcR = \frac{Vdc_{Sim}}{Vdc_{Meas}} \quad (4.2)$$

$$PdcR = \frac{Pdc_{Sim}}{Pdc_{Meas}} \quad (4.3) \qquad PacR = \frac{Pac_{Sim}}{Pac_{Meas}} \quad (4.4)$$

For a first classification, the combination of the two indicators ($i.e., PdcR \& PacR$) makes it possible to locate the side of the fault either DC or AC, and while the majority of the malfunctions occur on the DC side, the refinement of the classification of the faults in the side DC is realized by two other indicators ($i.e., IdcR \& VdcR$). A reference threshold has been established for four indicators. Each fault in DC side has well-defined losses either in current or voltage or in both indicators at the same time. Based on this, the most probable fault can be determined. Figure 4.9 illustrate the Flowchart of the proposed fault detection and diagnosis strategy.
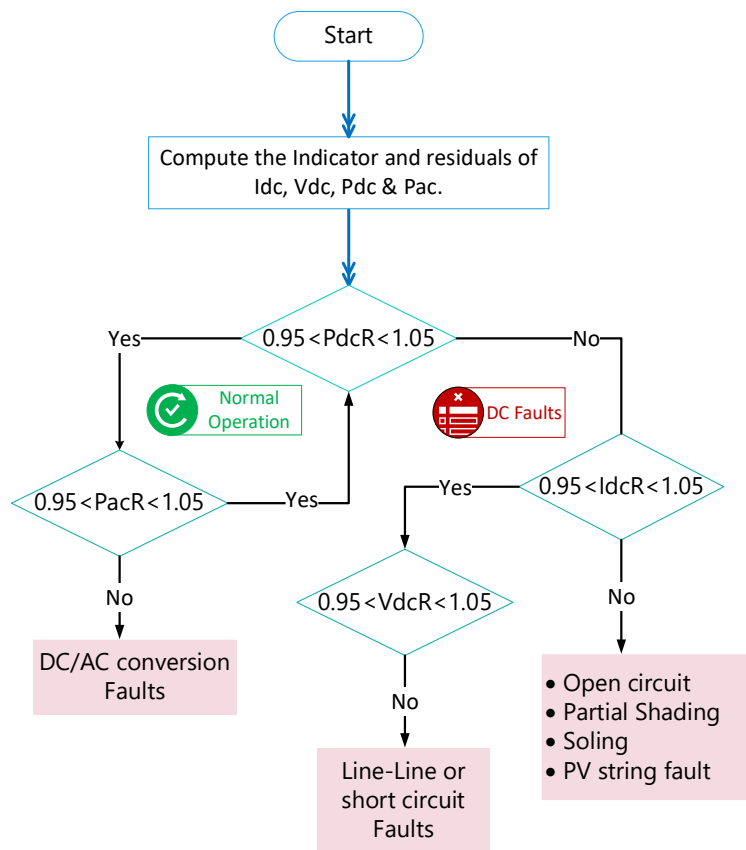
Figure 4.9 Flowchart of the proposed fault detection and diagnosis strategy.

The fourth indicators have been calculated under LabVIEW, several thresholds have been set for each fault in order to distinguish and identify each type. Figure 4.10 shows the fault localization program based on Boolean function using graphical code under LabVIEW environment.

130
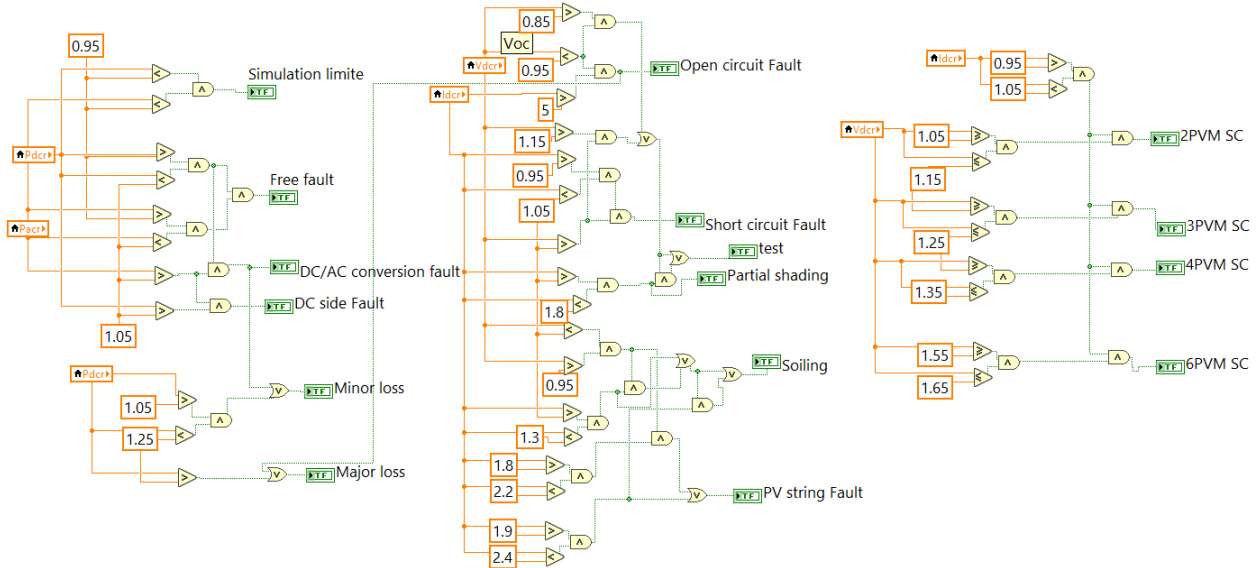
Figure 4.10 Fault classification program using graphical code under LabVIEW environment

After developing graphical code under LabVIEW environment for fault detection and identification, a new tab was added to our interface this tab contain the following features (Figure 4.11):

✓ DC& AC Energy loss indicators for 1 day and cumulated day
✓ Four visual chart indicators (i.e., IdcFi, VdcFi, PdcFi, PacFi) with threshold limits
✓ Boolean digital indicators (LED) for fault types classification and identification.
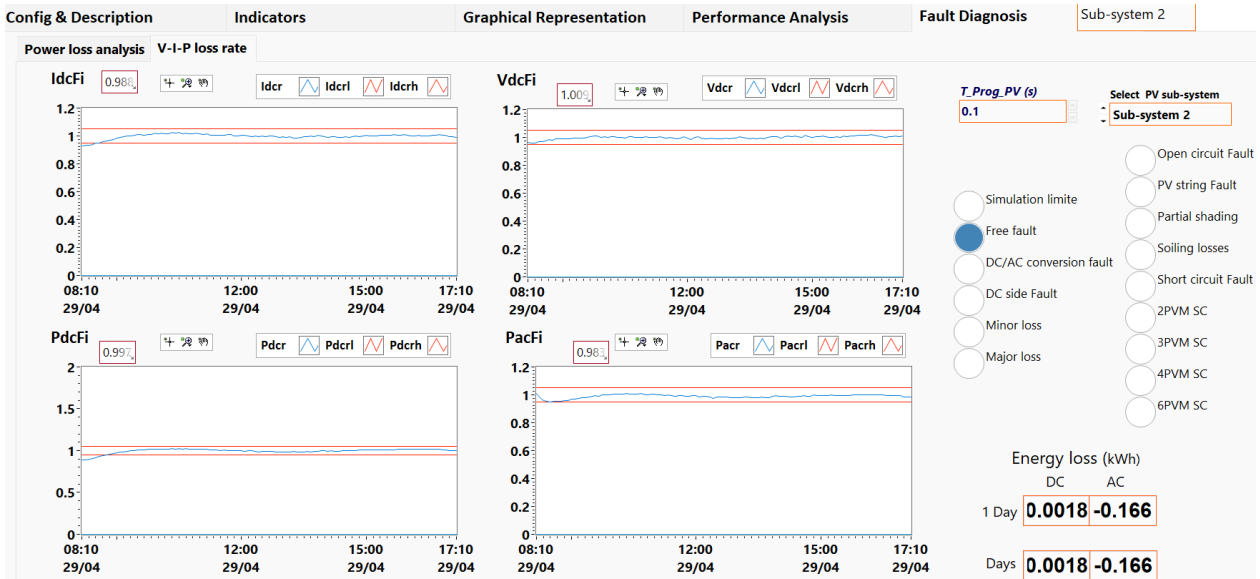
Figure 4.11 designed fault diagnosis interface _Free fault case 29042020 sub system 1.

4.2.3 Faults detection and identification results

Open-circuit fault detection

The used method can easily recognize this fault. because the current indicator is equal to zero (i.e., no production Idc = 0) and the voltage indicator is less than 0.95 (i.e., the voltage is in open circuit Vdc = Voc). The detection results with thresholds are illustrated in Figure 4.12.

131
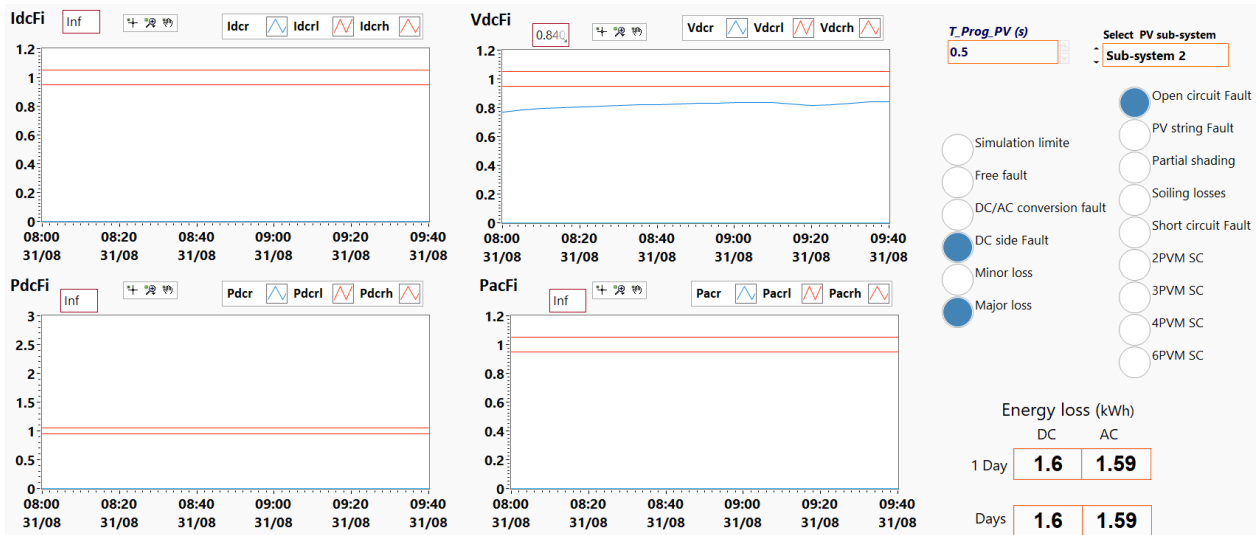
Figure 4.12 recognition of open circuit fault in PV subsystem 2.

PV string fault detection

In our PV system the PV string fault causes a decrease in relatively 50% of the rated power because of the disconnection of the two strings. The proposed method can easily discover this severe fault. To identify this type of fault, we check the DC current and voltage indicators in (Figure 4.13). We can see after the appearance of the string fault that the DC current is almost currency in two because we have two strings in parallel, while the DC voltage does not change significantly. From this analysis, we conclude that the occurred fault is due to string fault.
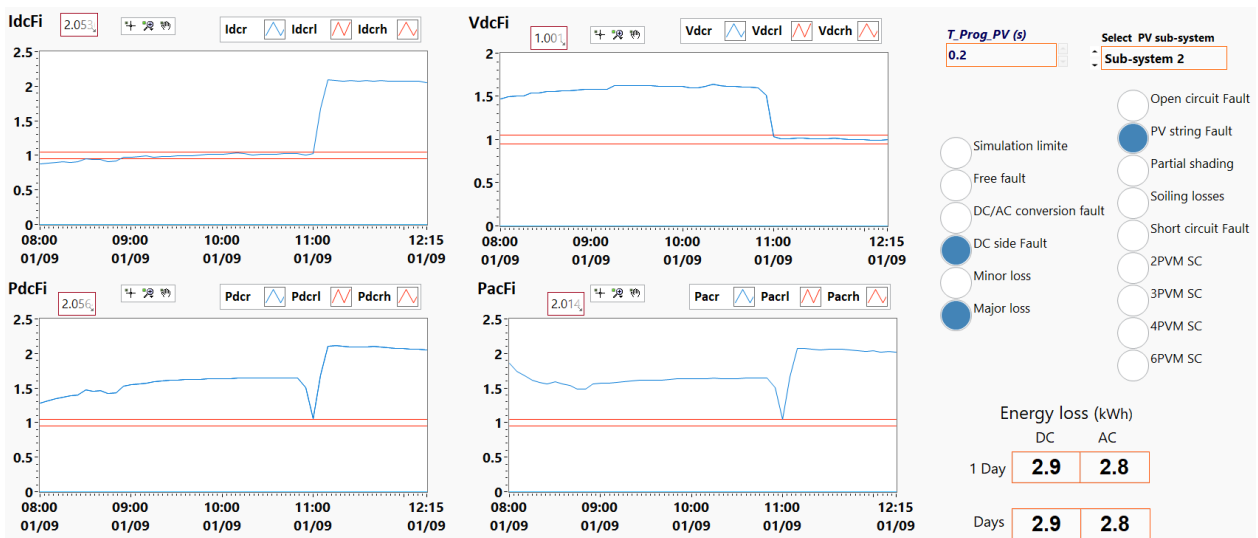
Figure 4.13 Identification of PV string fault in subarray 2.

Partial shading detection

This experiment is devoted to assess the capability of PLR monitoring technique to identify the temporary partial shading caused by pylons.

To detect this fault, analysis of the dynamic behavior of both DC current and DC voltage indicators at the same time is essential. When a partial shading fault has occurred on the PV array, the DC current decreases according to the shading intensity and its distributed surface over the PV array, while the DC current is also linked to the series/parallel arrangement depending shading, the second sign is instability of DC voltage. So, to identify this fault, we use the combination of its two signs that appear.

132

As we can see in Figure 4.14 the DC current indicator well above the upper threshold (i.e., IdcR=1.65), up to this point, there is a possibility of three malfunctions (i.e., PV string fault, soiling losses and partial shading), for the soiling losses the IdcR is less than *1.2* and for string the IdcR is around 2, then, there remains only one defect which is the partial shading. the parametric approach can identify the shading faults but there is a possibility of non-distinction with other faults in DC side, which leads to false identification. The hybridization with other methods such as statistical, signal processing and machines learning can give a better precision and accuracy.
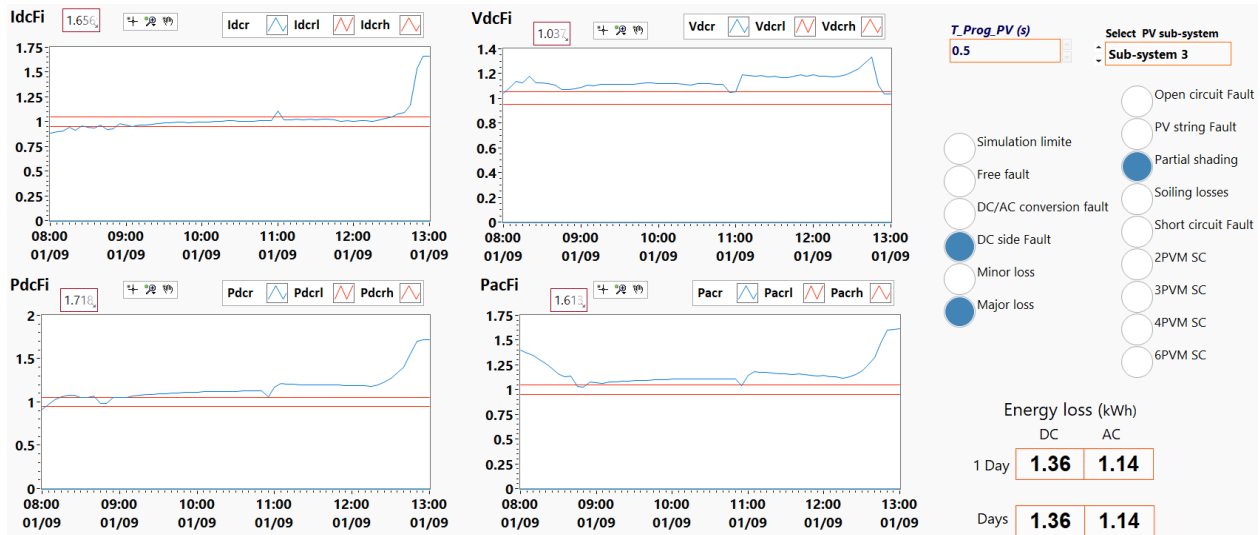
Figure 4.14 Localisation of the temporary partial shading fault caused by pylon.

Soiling losses detection

In this scenario, we assess the performance of the proposed techniques in uncovering power losses caused by soiling chased by accumulation of dust and bird droppings.

From Figure 4.15 we can see that the detection based on DC voltage indicator is in the confidence zone (i.e., 1.05 >VdcR > 0.95), while DC current and DC power indicators are slightly above the upper threshold (i.e., IdcR>1.053 and PdcR>1.07), which means the existence of a small accumulation of dust which generates a minor power loss of around 1 kWh per day.
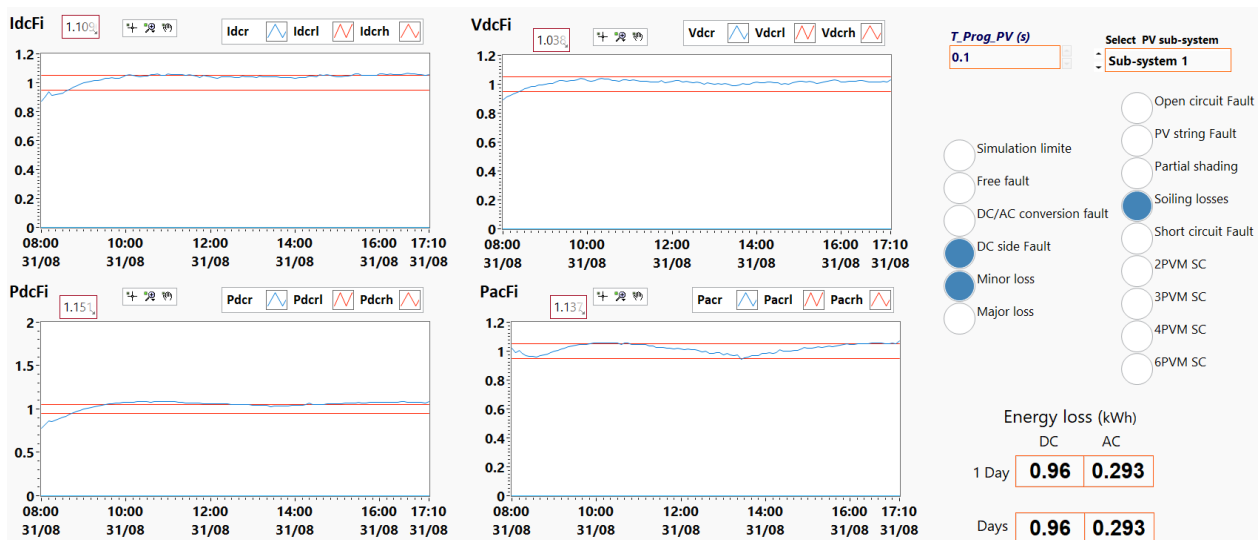
Figure 4.15 Identification of soiling losses caused by dust accumulation on the PV subarray 1.

133

Short-circuit fault detection.

This case study is devoted to the evaluation of the potentials of the proposed method to detect and classify the level of short-circuit faults. For this we present 2 cases: two and four short-circuited PV modules. The DC electrical parameters affected by this fault are mainly the DC voltage and the DC power. The DC current are not affected by this fault.

Figure 4.16 illustrates the detection results for two short-circuited PV modules, we can see that the DC indicator gives no sign of fault (i.e., IdcR=0.996), while the DC voltage and DC power indicators are above the upper limit of 1.05. (i.e., VdcR and PdcR >1.12), this situation corresponds for two short-circuited PV modules. this fault causes minor power losses. Note that recognizing a single module short circuit fault is a bit difficult.
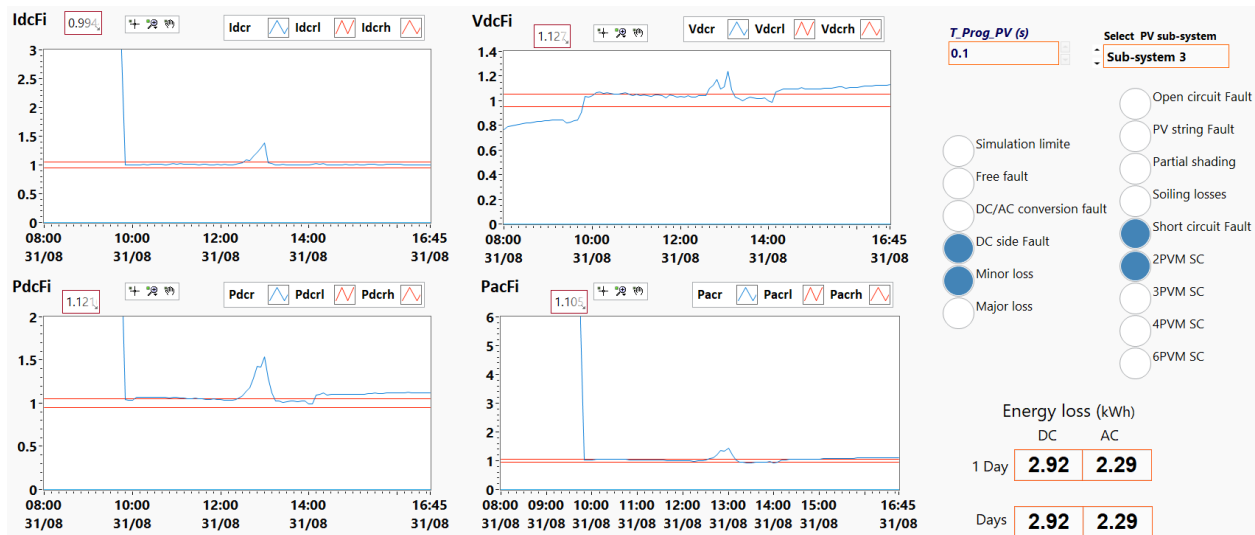
Figure 4.16 Identification of the 2 short-circuited PV modules.

Figure 4.17 illustrates the detection results of four short-circuited PV modules, we can see that the DC indicator gives no sign of fault (i.e., IdcR=1.01), while the DC voltage and DC power indicators are above the upper limit. (i.e., VdcR =1.29 and PdcR =1.31), this situation corresponds to a voltage loss of four PV modules in series. this fault causes an important power loss.
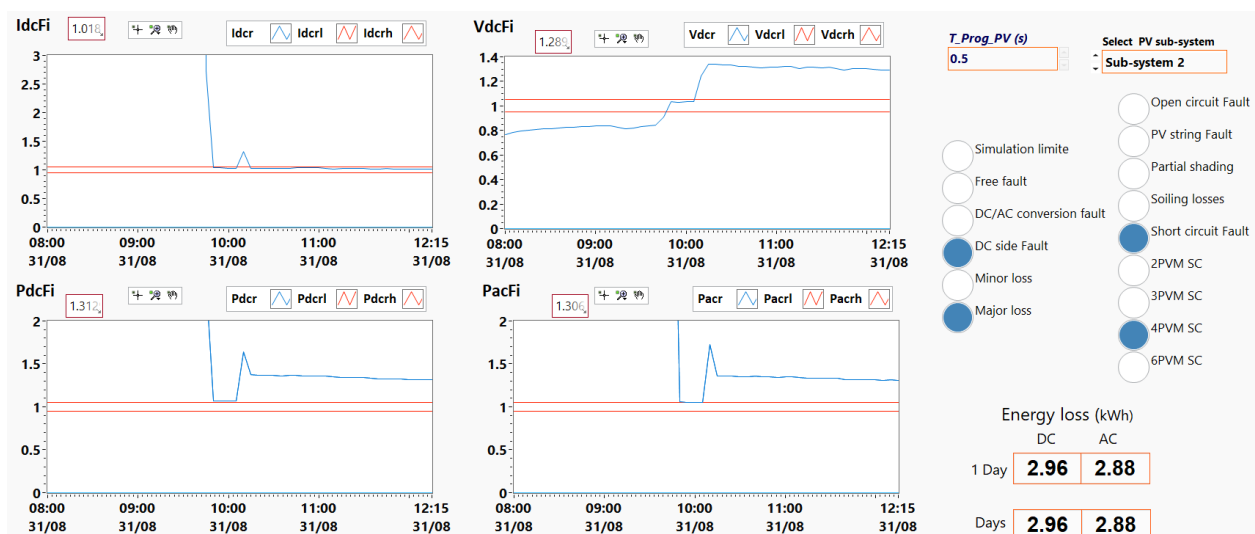
Figure 4.17 Identification of the 4 short-circuited PV modules.

134

DC/AC efficiency anomaly detection

The final test evaluation is devoted to assessing the potentials of the proposed technique to identify the fault in AC side. In Figure 4.18 all DC Indicators are located between lower and upper thresholds limits, which means there are no malfunctions in DC side, the AC power indicator is equal to *1.24*, it largely exceeds the high threshold, which strongly indicates the presence of an inverter performance anomaly.
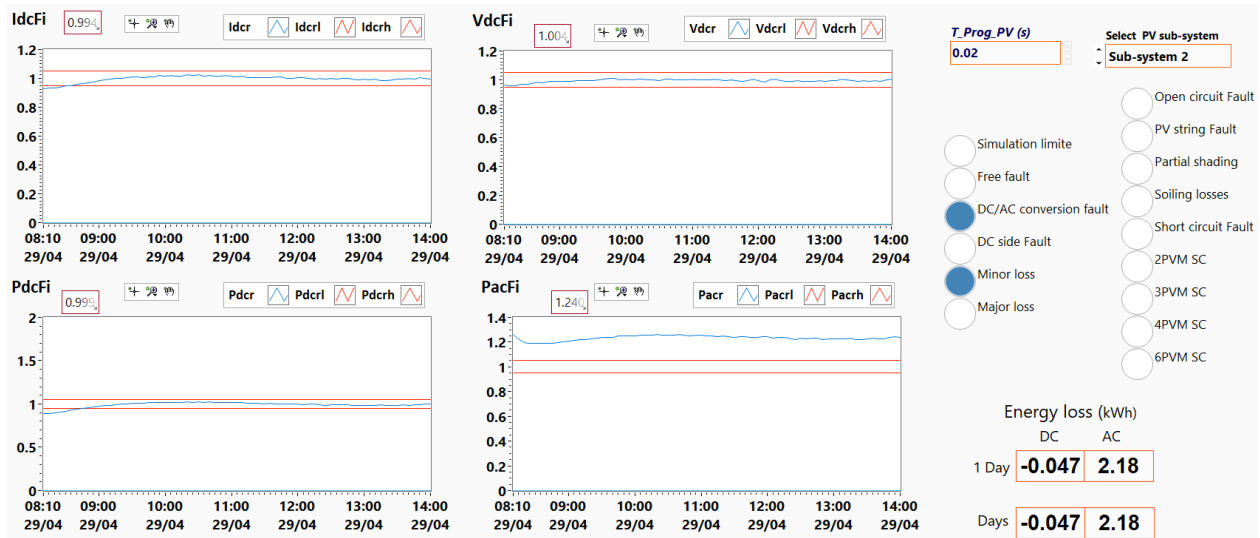
Figure 4.18 detection and classification of the DC/AC inverter efficiency fault.

Figures (4.19, 4.20 and 4.21) summarize some faults on DC side, detected and identified using I-V indicators, which were produced respectively in PV sub-system 2 during two days (i.e., 31 august and 01 September 2020) and in PV sub-system 3 during one day (01 September 2020).
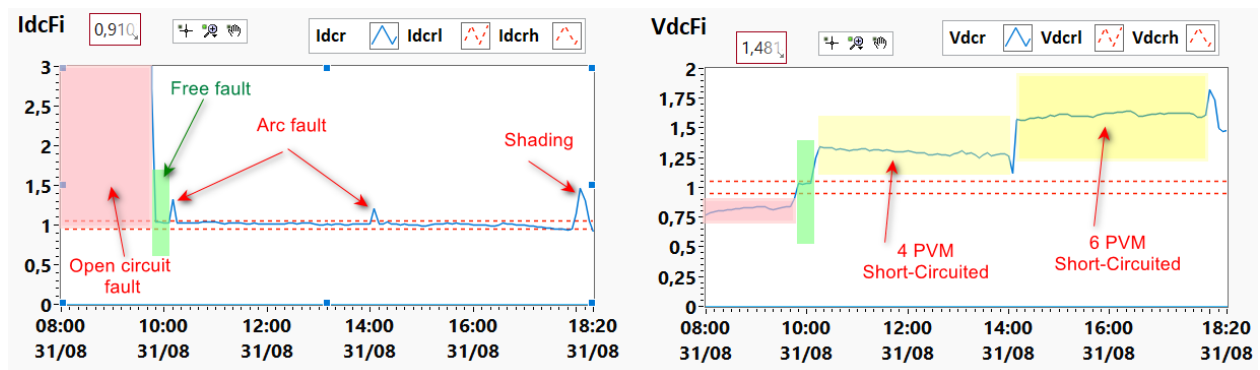
Figure 4.19 identified faults using I-V indicators occurring the PV sub-system 2 on 31/08/2020.
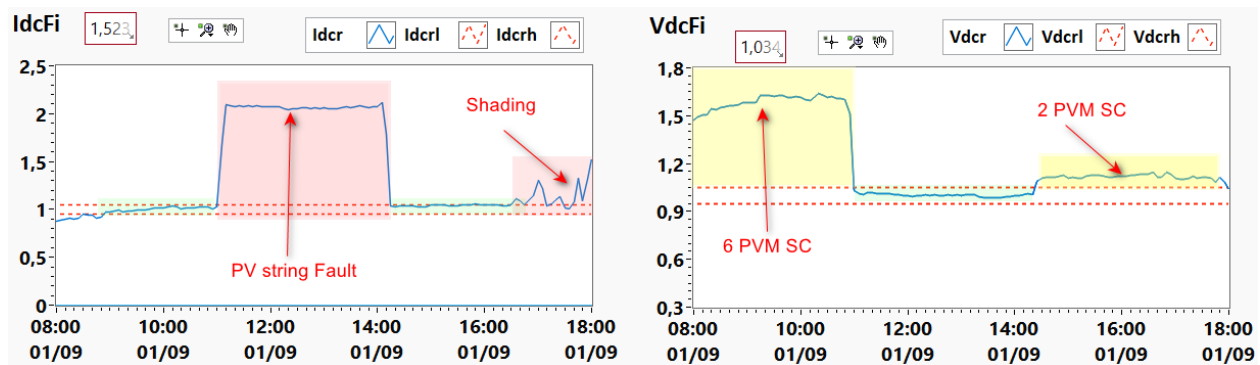
Figure 4.20 identified faults using I-V indicators occurring the PV sub-system 2 on 01/09/2020.
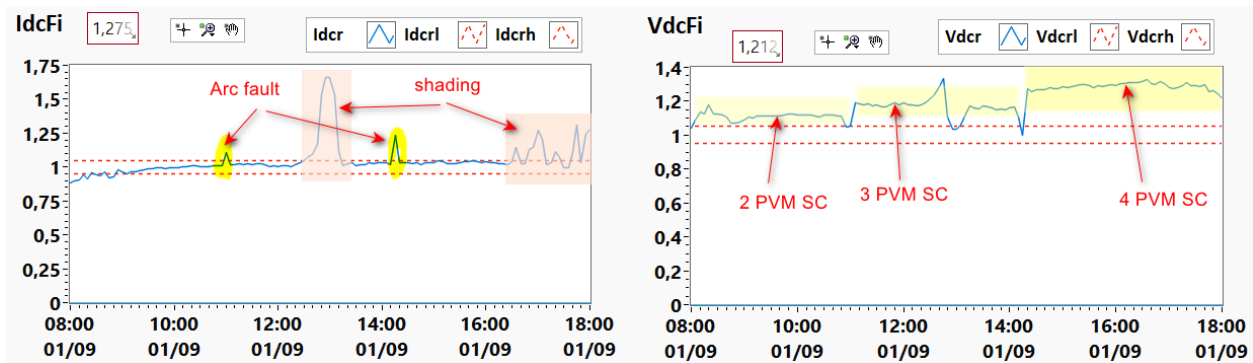
Figure 4.21 Identified faults using I-V indicators occurring the PV sub-system 3 on 01/09/2020.

In summary, in this section, the nine faults' cases were suitably identified and classified using a convivial user interface, along with other features that have been added to the interface. indeed, this method can identify only two modules in a short circuit, on the other hand, the losses of one PV module among fifteen in series are a little hard to quantify. The distinction of partial shading from other faults is difficult because it has large ranges of variation in losses over time, the use of time-series monitoring or other signal processing techniques can provide a solution to this problem.

4.3 Fault detection using Double Exponentially Weighted Moving Average scheme with empirical models

This section was developed in collaboration with researchers affiliated with King Abdullah University of Science and Technology (KAUST) University, it presents a monitoring method based on parametric models and the Double Exponentially Weighted Moving Average (DEWMA) scheme, this method combines simplicity and flexibility, where the residuals are calculated with parametric and non-parametric models, nonparametric control limits are computed using kernel density estimation (KDE) to enhance its sensitivity compared to the parametric control limits. The strategy for detecting the faults that have occurred is carried out with the DEWMA technique.

4.3.1 The proposed monitoring schemes

The single EWMA considers the current input and previously received inputs to uncover abnormalities in the process mean [258]. This design makes the EMWA scheme sensitive to a small or gradual drift. EWMA monitoring scheme is well used in practice because it is more accessible to establish [259].

In this study, the one-sided EWMA scheme, which uses the absolute value of EWMA statistic and only an upper control limit, will be used. For more details on the performance of the EWMA scheme, refer to [260]. To further enhance the capacity of the EWMA scheme to detect small changes in the process mean, the double EWMA (DEWMA) scheme is designed in [261] . The comparative study in [262] reveals that DEWMA outperforms the EWMA scheme in detecting small changes that are smaller than one half of the process standard deviation. For moderate and large faults, the two techniques showed comparable performance. Here we used DEWMA with equal smoothing constant as recommended in [262]. The anomaly detection can be achieved by plotting the DEWMA statistic with its upper and lower control limits, UCL, and LCL.

An anomaly is flagged out when the DEWMA statistic exceeds the control limits. It is worth noticing that the detection threshold in the DEWMA approach is calculated by assuming the Gaussianity of data [263]. When the Gaussian assumption is not verified, the monitoring results would be inappropriate. To alleviate this limitation, the distribution of the DEWMA statistic could be estimated by using KDE [264], which is a nonparametric probability density estimation approach. At first, the distribution of the DEWMA statistic in Eq. is estimated via univariate KDE using fault-free data. A nonparametric threshold of the DEWMA method is defined as the $(1 - \alpha)$-th quantile of the estimated distribution of DEWMA statistic obtained by KDE. A fault is flagged when the DEWMA statistic is above the decision threshold (Figure 4.22).

136

The DEWMA with nonparametric detection threshold is performed as follows:

- Step 1: Computing DEWMA charting statistic for each observation.
- Step 2: Estimating the probability density function for given DEWMA measurements via KDE.
- Step 3: Setting-up the detection threshold based on the previously estimated distribution of DEWMA in a nonparametric.
- Step 4: Flagging out a fault if the DEWMA statistic is above the detection threshold.
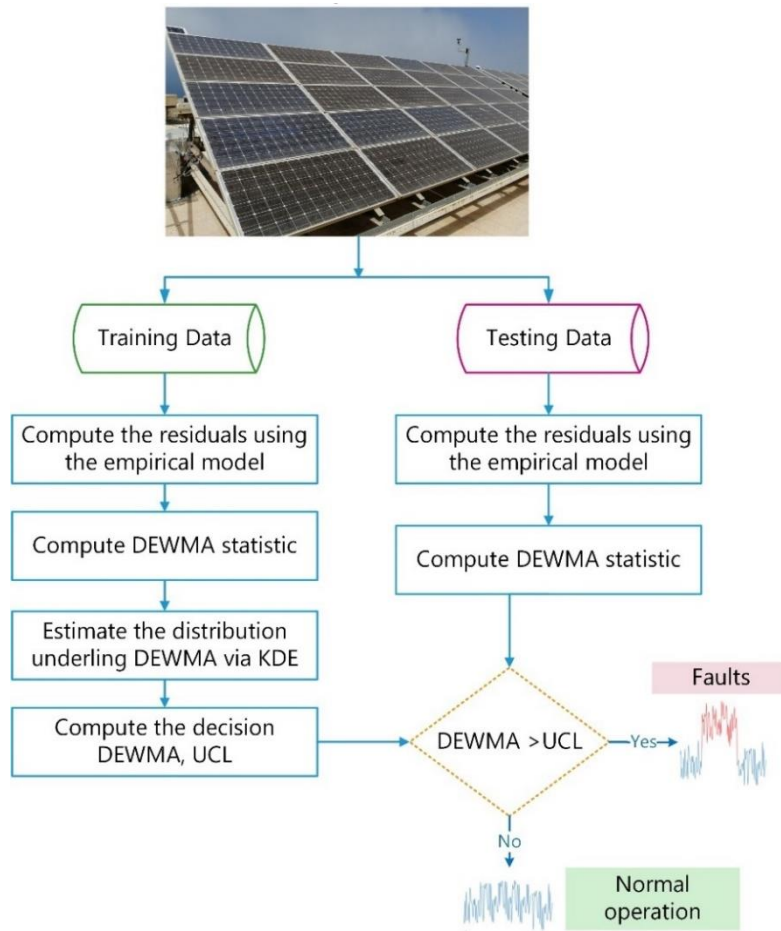
Figure 4.22 Flowchart of DEWMA-driven detection strategy.

4.3.2 Improved monitoring strategy using double exponential smoothing

This subsection is devoted to introducing the structure of the proposed fault detection methodology to detect anomalies. This approach is employed to detect faults occurring on the DC and AC outputs of a PV system. As described previously, the use of the empirical models is due to their simplicity and capability to predict DC and AC outputs of a PV system appropriately.

The empirical models are designed based on anomaly-free data and then adopted for monitoring new data. It is worth emphasizing that the models have been constructed based on standardized data. To this end, the raw data is standardized to have mean values is 0, and the standard deviation is 1. Specifically, each variable x_j from the raw measurements gathered from the inspected PV array is auto scaled as;

$$X_{j=}\frac{x_j - \mu_j^0}{\sigma_j^0}, j = 1, \dots, m \tag{4.5}$$

where m is the number of the collected variable (i.e., $m = 7$ in this case study).

μ_j^0 , σ_j^0 are the mean and standard deviation of the variable X_j under fault-free conditions, respectively.

Here, we merge these advantages of empirical models and the sensitivity of DEWMA schemes for detecting any abnormality in a PV array.

Indeed, empirical models are used to generate residuals for anomaly detection (Figure 4.23)
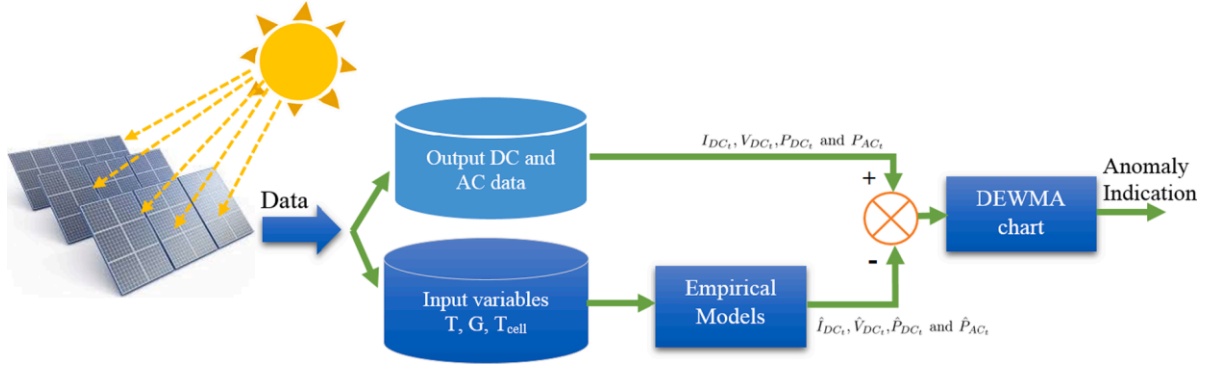
Figure 4.23 The framework of the proposed monitoring technique.

The residuals, $\mathbf{E} = [e_1, e_2, \ldots, e_n]$, are the difference between the DC and AC measurements outputs, (DC current I_{DCt}, DC voltage V_{DCt}, DC power P_{DCt} and AC power P_{ACt}) and their corresponding prediction from the empirical model (DC current, $\hat{I}_{DCt}$, DC voltage, $\hat{V}_{DCt}$, and DC power, $\hat{P}_{DCt}$ and AC power $\hat{P}_{ACt}$) from the PV array using measured tilted irradiance and ambient temperature.

The residuals represented in Eq. 4.6 to 4.9, offer pertinent information about the presence of abnormal conditions.

$$E_{I_{DCt}} = I_{DCt} - \hat{I}_{DCt} \tag{4.6}$$
$$E_{V_{DCt}} = V_{DCt} - \hat{V}_{DCt} \tag{4.7}$$
$$E_{P_{DCt}} = P_{DCt} - \hat{P}_{DCt} \tag{4.8}$$
$$E_{P_{ACt}} = P_{ACt} - \hat{P}_{ACt} \tag{4.9}$$

The detection thresholds of the DEWMA schemes are computed using residuals of fault-free data. The acquired new measurements from the inspected PV array are standardized by subtracting the mean of the training data, $\mu 0$, and dividing the standard deviations, $\sigma 0$. In the absence of anomalies, residuals fluctuate around zero, whereas in abnormal conditions, they diverge significantly from zero.

Here, the DEWMA scheme is first applied to the residuals of DC peak power and AC power to sense anomalies. Then, if DEWMA uncovers an anomaly, the residuals of DC voltage and current are checked to identify the type of the flagged anomaly.

Before assessing the effectiveness of DEWMA-based approaches, let us present the used evaluation indices in this study. Here, the commonly used metrics to verify the performance of anomaly detection, including true positive rate (TPR), false-positive rate (FPR), accuracy, and area under the curve (AUC), are used.

Figure 4.24 depicts a confusion matrix and recapitulate formulas of the used metrics. Also, the measure of EER (Equal Error Rate) is used to evaluate the performance of the proposed method. EER is calculated as the following:

$$EER = \frac{FPR + TPR}{2} \tag{4.10}$$

Figure 4.24 Performance indices used in fault detection.

4.3.3 Results and discussion

This section is consecrated in assessing the performance of DEWMA based detection procedures. Specifically, we investigate the capacity of these detection procedures to sense faults in the DC and AC sides of a PV system. Table 4.1 shows the considered faults with its discrimination based on DC current and DC voltage indicators.

Table 4.1 Faults discrimination based on DC current and DC voltage.

		Duration	DC Current Indicator (A)	DC Volatge Indicator (V)
F1	PV string fault (open circuit)	*Permanent*	50 %	✅
F2	Circuit Breaker Fault	*Permanent*	❌ Zero Energy	*Voc (280-300)*
F3	Inverter disconnection	*Temporary 1-5min*	❌ Zero Energy	*Voc (280-300)*
F4	Partial shading (pylons)	*Temporary 0.5-2 Hours*	15-35 %	260 220
F5	Soiling losses	*Permanent*	5-15 %	✅
F6-a	2 PV Modules short-circuited	*Permanent*	✅	10 %
F6-b	5 PV Modules short-circuited	*Permanent*	✅	22 %

String faults:

Here, we illustrate the performance of the fault detection approach applied to the PV system with open-circuit faults. This kind of fault occurred if DC protection has deteriorated or there is a disconnection between PV modules in series. To this end, we generate a string fault by intentionally switch off the circuit-breaker of the PV system. Essentially, one string is not connected to the PV array. For PV array performance monitoring, at first, the residuals are generated using the empirical models of DC current, voltage and power, and AC power. The parametric and nonparametric DEWMA approaches are applied to DC power and AC power to sense the presence of energy losses. The outputs of the DEWMA methods, when applied to the faulty dataset, are illustrated in Figure 4.25. Results point out the occurrence of significant energy losses in the PV system. This fault causes a decrease in relatively 50% of the rated power because of the disconnection of the two strings. The two approaches can easily discover this severe fault.

Figure 4.25 Illustration of the detection performance of the DEWMA charts applied to (a) DC power and (b) AC power dataset with a string fault.

139

To identify the type of fault, we check the DC current and voltage using the DEWMA scheme (Figure 4.26). We can see after the appearance of the string fault that the DC current is almost currency in two because we have two strings in parallel, while the DC voltage does not change significantly. From this analysis, we conclude that the occurred fault is due to string fault.
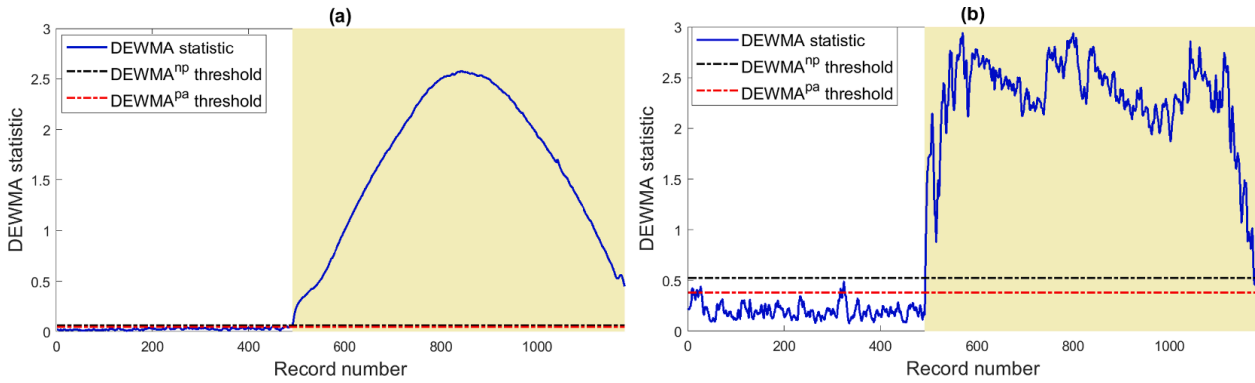
Figure 4.26 Results from DEWMA with parametric and nonparametric threshold for (a) DC current and (b) DC voltage.

The DEWMA scheme shows a slight superiority compared to the single EWMA (Table 4.2). The three schemes demonstrated a satisfying detection performance with lower FPR and the highest TPR, accuracy, and precision, because of the large magnitude of the string faults.

Table 4.2 Detection results by procedure when string fault occurred.

	TPR	FPR	Accuracy	Precision	F-Measure	AUC	EER
EWMA	1	0.039	0.984	0.973	0.986	0.981	0.016
DEWMA^{pa}	1	0.065	0.973	0.956	0.977	0.967	0.027
DEWMA^{np}	1	0	1	1	1	1	0

Inverter disconnections:

The focus of this case study is investigating the capacity of the DEWMA monitoring methods in sensing inverter disconnections. Essentially, inverter disconnections occurred when the electrical characteristics overpass the operating limits on the DC or AC part of the inverter. The operating limits are generally given in the datasheet. In the case of inverter disconnections, the PV system will shut down till reconnecting the inverter. Here, to show the detection performances of the considered methods, we choose one day of data that contains inverter disconnection faults. In this case study, the considered faults have resulted due to grid instability. The voltage and frequency of the grid have passed the operational limits of the inverter. Inverter disconnection faults are characterized by spike form and very short in time; this makes it quickly recognized from string faults and temporary shading.

The detection results of the monitoring methods are summarized in Figure 4.27, Figure 4.28 and Table 4.3. we can see that these anomalies are reflected in residuals of DC voltage and current. As this anomaly is easy to discriminate from the normal conditions, the DEMWA monitoring schemes showed good detection performance. The DEWMA scheme slightly improved the conventional EWMA scheme by achieving an AUC of 0.99 compared to 0.98 (Table 4.3).

This means that all inverter disconnections are appropriately detected. These results indicate that for anomaly with a large magnitude, double and single EWMA are comparable.

Figure 4.27 Illustration of the detection performance of the DEWMA charts applied to (a) DC power and (b) AC power dataset with inverter disconnections.

Figure 4.28 Illustration of the detection performance of the DEWMA charts applied to (a) DC current and (b) DC voltage dataset with inverter disconnections.

Table 4.3 Detection results by procedure when inverter disconnections occurred.

	TPR	FPR	Accuracy	Precision	F-Measure	AUC	EER
EWMA	0.98	0.01	0.98	0.99	0.98	0.98	0.017021
DEWMApa	0.99	0	0.99	1	0.99	0.99	0.005319
DEWMAnp	0.99	0.01	0.99	0.99	0.99	0.99	0.004255

Circuit breaker faults:

Performance assessment in PV systems is an essential aspect of guaranteeing the safe operation of these systems. To ensure reliable performances and protect PV installation against sudden shock or electrical faults, using residual current circuit breaker (RCCB) with a miniature circuit breaker (MCB) is undoubtedly essential. Notably, the RCCB aims to protect people from electric shock, while the MCB is exploited for protecting a PV installation against overloads or short circuits. The RCCB automatically shuts off power if an electrical fault happened in the PV system. Here, this type of fault is generated for one hour based on measured data. The performance of the parametric and nonparametric DEWMA methods applied to the faulty dataset over time are displayed in Figure 4.29 (a-b). The two charts can recognize this large fault. The results of the DEWMA with parametric and nonparametric detection thresholds applied to DC current and (b) DC voltage datasets are presented in Figure 4.30 (a-b).

Figure 4.29 Illustration of the detection performance of the DEWMA charts applied to (a) DC power and (b) AC power dataset with a circuit breaker fault.

Figure 4.30 Illustration of the detection performance of the DEWMA charts applied to (a) DC current and (b) DC voltage dataset with a circuit breaker fault.

The effectiveness metrics of the nonparametric DEWMA, the conventional single, and double EWMA schemes are tabulated in Table 4.4. As expected, the nonparametric DEWMA shows superior detection performance compared to the traditional DEWMA and single EWMA charts. Indeed, when the assumed parametric form of the data distribution (i.e., Gaussian in this case) is invalid, results from the nonparametric DEWMA is more appropriate because of it an assumption-free approach. In this case, detection results from the parametric DEWMA and EWMA schemes may not be effective as the detection threshold is fixed based on the normality assumption of the data.

Table 4.4 Detection results by procedure when a circuit breaker fault happened.

	TPR	FPR	Accuracy	Precision	F-Measure	AUC	EER
EWMA	0.939	0.066	0.934	0.5	0.653	0.937	0.066
DEWMApa	0.985	0.100	0.906	0.409	0.578	0.942	0.094
DEWMAnp	0.985	0.019	0.981	0.783	0.872	0.983	0.019

PV system with shaded modules

This experiment is devoted to an assessment of the capability of DEWMA-based monitoring approaches to detect partial shading. Partial shading can negatively impact the production of a PV system. As the power generated by a PV system is related to the received solar irradiance, when partial shading occurs, the power output will decrease proportionally as the shading heaviness increases. In general, shading losses can be caused by different elements, including pylons, building and trees. In this experiment, a partial shading is from two communication pylons on the inspected PV array (Figure 4.31), which can reduce the power yield of the PV array, are utilized for assessing the effectiveness of the DEWMA-based methods. This is done within the day. Here, the shading is treated as an abnormal event; then, it is not modeled.

142
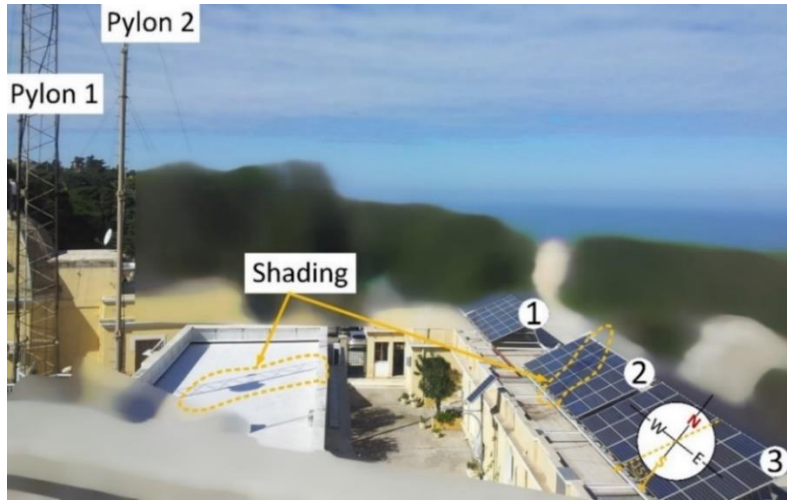
Figure 4.31 PV array with shaded modules due to two communication pylons installed in front of this PV array.

The DEWMA schemes with parametric and nonparametric detection thresholds have been applied to the residuals of DC and AC power to detect when partial shading occurred in the PV plant. Here the smoothing parameter ν is set to be 0.3. Results are depicted in Figure 4.32 (a-b). As can be noticed from Figure 4.33 (a), the nonparametric DEWMA scheme outperforms the parametric approach in terms of detection accuracy, and it gives precise detection of this shading without false alarms. Namely, the nonparametric threshold is computed more flexible without assumption on data distribution, while the parametric threshold is derived based on the assumption that data are Gaussian distributed. Using KDE to non-parametrically estimate the distribution of the residuals permits to get a more flexible and appropriate detection threshold, which leads to reduced false alarms and more accurate detection. As shown in Figure 4.33 (a-b), the partial shading of the two pylons causes a significant decrease in DC current and a small reduction in DC voltage with fluctuation. It is recommended to use DC current residues to diagnose this fault better. Furthermore, results indicate that the proposed algorithm can detect this anomaly and identify its type.
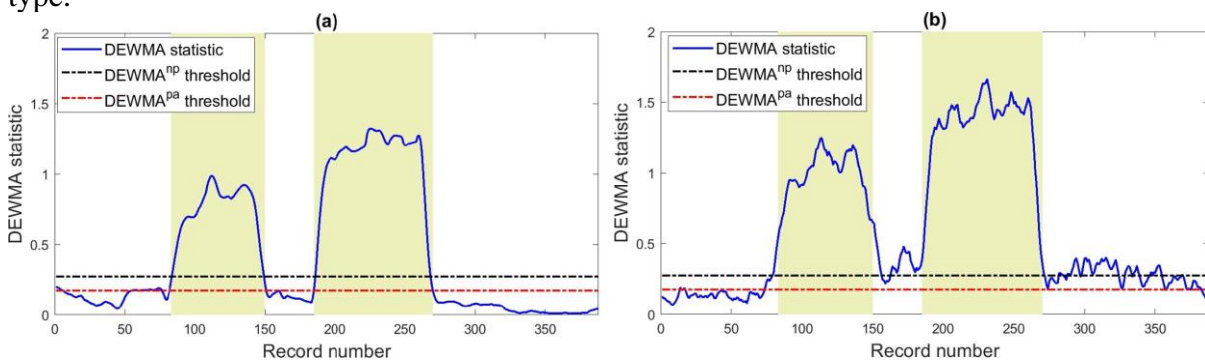
Figure 4.32 Illustration of the detection performance of the DEWMA charts applied to (a) DC power and (b) AC power dataset when shaded modules happened.
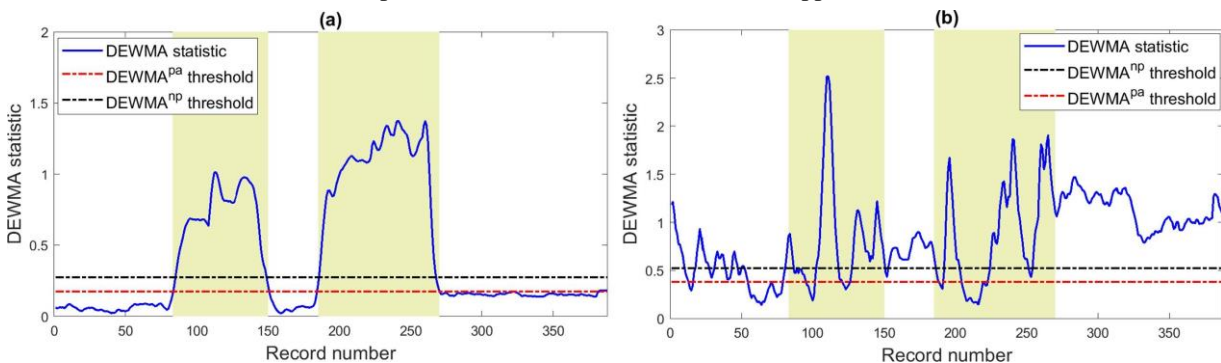
Figure 4.33 Illustration of the detection performance of the DEWMA charts applied to (a) DC current and (b) DC voltage dataset when shaded modules happened.

143

Results in Table 4.5 shows that the nonparametric DEWMA performed better than the conventional DEWMA and single EWMA schemes with lower FPR and the highest TPR, accuracy, and precision. The nonparametric DEWMA reaches an AUC of 0.984; the conventional DEWMA and EWMA schemes achieved an AUC of 0.932 and 0.65, respectively. The traditional methods flag this shading but with some false alarms and missed detection. Such results may suggest the nonparametric DEWMA rather than the conventional DEWMA, and EWMA charts for suitably uncover partial shading in a PV array.

Table 4.5 Detection results by procedure when shading has occurred.

	TPR	FPR	Accuracy	Precision	F-Measure	AUC	EER
EWMA	1	0.701	0.577	0.484	0.653	0.650	0.423
DEWMApa	0.987	0.124	0.920	0.840	0.907	0.932	0.080
DEWMAnp	0.968	0	0.987	1	0.983	0.984	0.013

Soiling losses

In this scenario, we assess the performance of the detection methods in uncovering power losses caused by soiling (accumulation of dust and bird droppings). The Layers of dust on the surface of the PV modules reduce the arrived sunlight to solar cells, which degrade the performance of PV modules and cause power losses. Figure 4.34 illustrates an example of PV modules with accumulating of dust caused by sand accumulation.

Figure 4.34 PV modules with dusty surface.

Figure 4.35 (a-b) shows the performance of the parametric and nonparametric DEWMA charts when applied to the residuals' DC power and AC power datasets collected from PV systems with dusty modules. The shaded area in Figure 4.35 (a-b) corresponds to the observation from the PV system with dusty modules, and the data corresponding to the non-shaded zone is from PV modules operating normally with cleaned PV modules. The two charts can recognize these large losses. The results show that the nonparametric DEWMA scheme offers better detection results without false alarms, and the parametric can detect these power losses but with few false alarms.
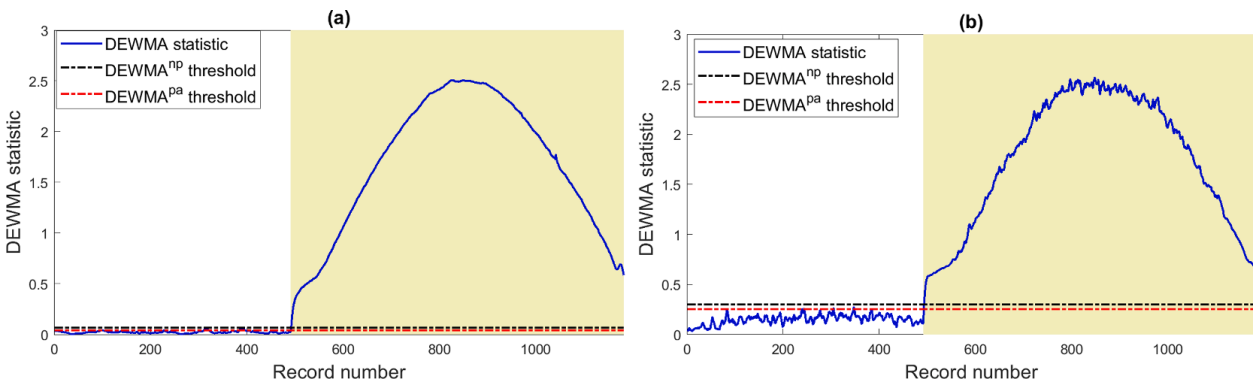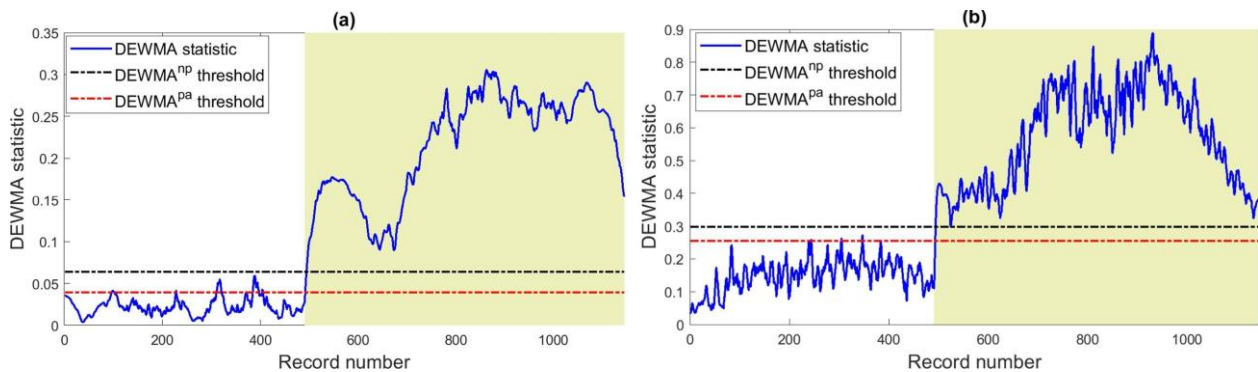

Figure 4.35 Illustration of the detection performance of the DEWMA charts applied to (a) DC power and (b) AC power dataset from dusty PV modules.

The two monitoring schemes based on the DC current and DC voltage residuals are given in Figure 4.36 (a-b). It can be seen that two charting statistics based DC current residuals are above the detection thresholds. The detection based on DC voltage residuals is not persistent over time.
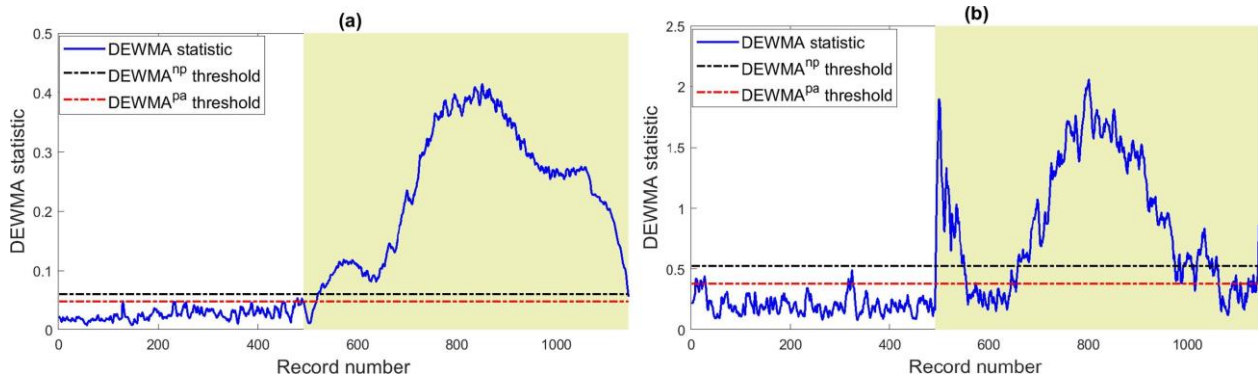
Figure 4.36 Illustration of the detection performance of the DEWMA charts applied to (a) DC current and (b) DC voltage dataset from dusty PV modules.

Short-circuit fault

The final experiment is devoted to assessing the potentials of the proposed techniques to detect short-circuit faults. Two cases are considered to assess the DEWMA-based methods; two PV modules short-circuited and five PV modules short-circuited. The electrical parameters affected by this fault are mainly DC voltage and DC power.

Figure 4.37 (a-b) illustrates the detection results of the parametric and nonparametric DEWMA charts when applied to residuals of DC and AC power. Here, the residuals are obtained using the empirical models constructed previously. As it can be observed from Figure 4.37 (a-b), the two charts recognize this short-circuit fault. The nonparametric DEMWA chart provides accurate detection compared to its parametric counterpart, resulting in several false alarms. To further diagnose such faults, the results of the DEWMA charts applied to residuals DC current and DC voltage datasets are illustrated in Figure 4.38 (a-b). The charting statistics based on residuals of DC current are below the detection thresholds, which means that DC current does not change by much (Figure 4.38-a). In comparison, the charting statistics based on residuals of DC voltage are above the detection thresholds (Figure 4.38-b). Thus, we conclude that the occurred fault is a short-circuit fault. The outputs of the three schemes: nonparametric DEWMA, and the conventional DEWMA and EWMA schemes are summarized in Table 4.6.
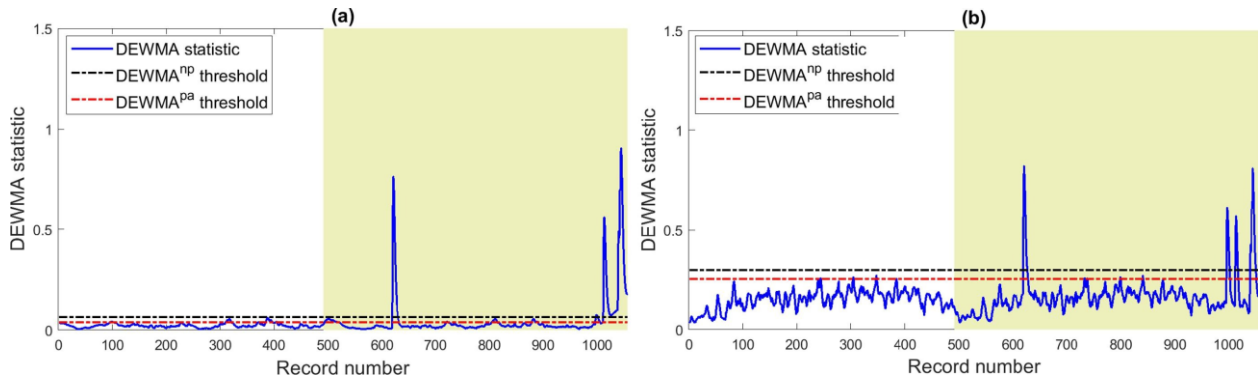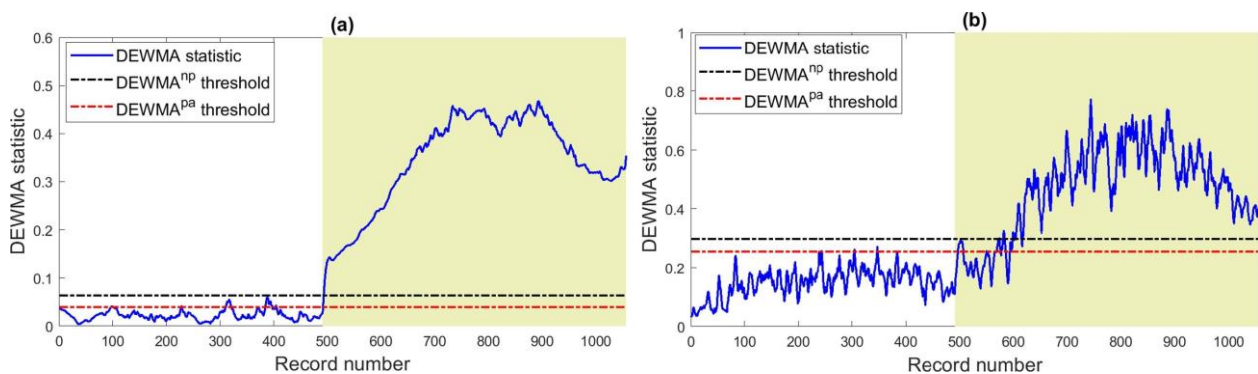

Figure 4.37 Illustration of the detection performance of the DEWMA charts applied to (a) DC power and (b) AC power datasets with two short-circuited modules.
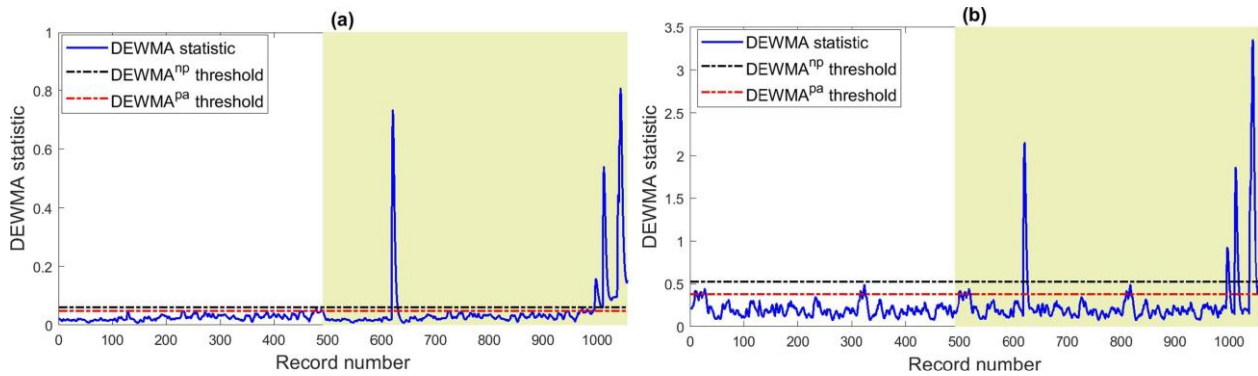
145
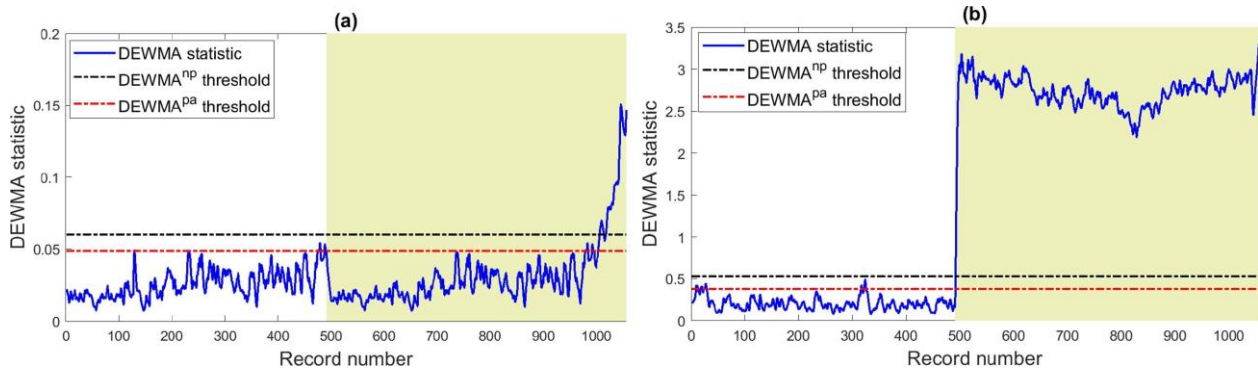
Figure 4.38 Illustration of the detection performance of the DEWMA charts applied to (a) DC current and (b) DC voltage datasets with two short-circuited modules.

Table 4.6 Detection results by procedure when two modules are short-circuited.

	TPR	FPR	Accuracy	Precision	F-Measure	AUC	EER
EWMA	1	0.039	0.983	0.972	0.986	0.981	0.017
DEWMApa	0.998	0.065	0.971	0.953	0.975	0.967	0.029
DEWMAnp	0.995	0	0.997	1	0.998	0.998	0.003

To further assess the fault detection and diagnosis performance of the DEWMA-based approaches, in the second scenario, five modules have been short-circuited from the inspected PV system. Monitoring results of DEWMA charts based on the residuals of output DC power and AC power, DC current, and DC voltage are presented in Figure 4.39 (a-b) and Figure 4.40 (a-b), respectively. It is worth noticing that the nonparametric DEWMA approach exhibits better detection performance and can easily detect short-circuit faults without false alarms. We concluded that the DEWMA chart with the nonparametric detection threshold is a very efficient method for short-circuit faults in PV systems. Also, the residuals generated by the empirical models provide capture useful information about abnormalities in the inspected PV system.
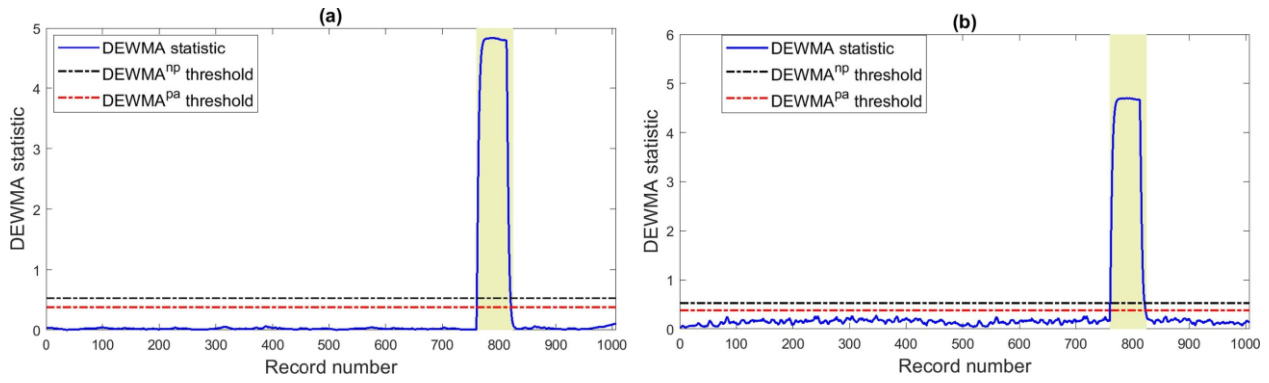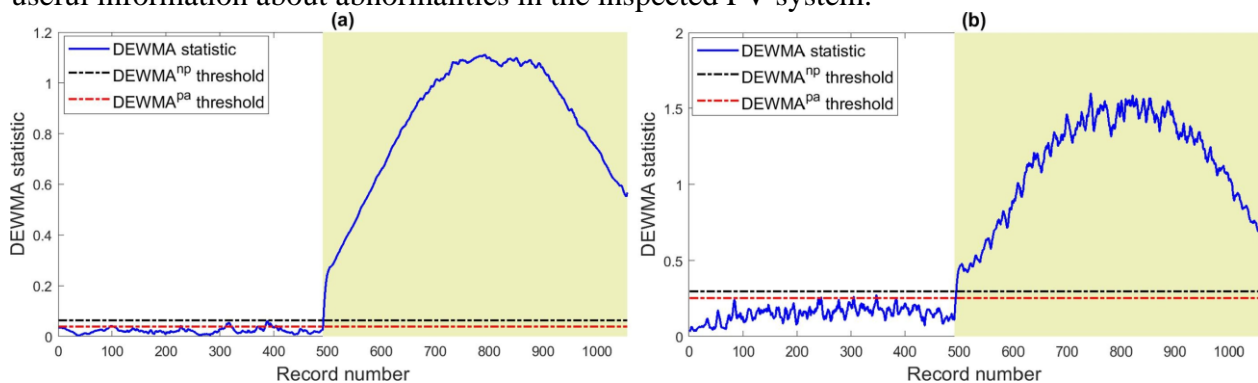

Figure 4.39 Illustration of the detection performance of the DEWMA charts applied to (a) DC power and (b) AC power datasets with five short-circuited modules.

The outputs of the three schemes: nonparametric DEWMA, and the conventional DEWMA and EWMA schemes are summarized in Table 4.7. The results underline the benefit of using the nonparametric DEWMA in terms of increasing the detection accuracy. It is worth pointing out that the DEWMA chart with a nonparametric threshold takes advantage of sensitivity DEWMA charting statistics and assumption-free in setting detection thresholds to improve fault detection and diagnosis performance in monitoring PV systems (see Figure 4.40).

Table 4.7 Detection results by procedure when five modules are short-circuited.

	TPR	FPR	Accuracy	Precision	F-Measure	AUC	EER
EWMA	1	0.039	0.982	0.967	0.983	0.981	0.018
DEWMApa	1	0.065	0.970	0.946	0.972	0.967	0.030
DEWMAnp	0.998	0	0.999	1	0.999	0.999	0.001

146
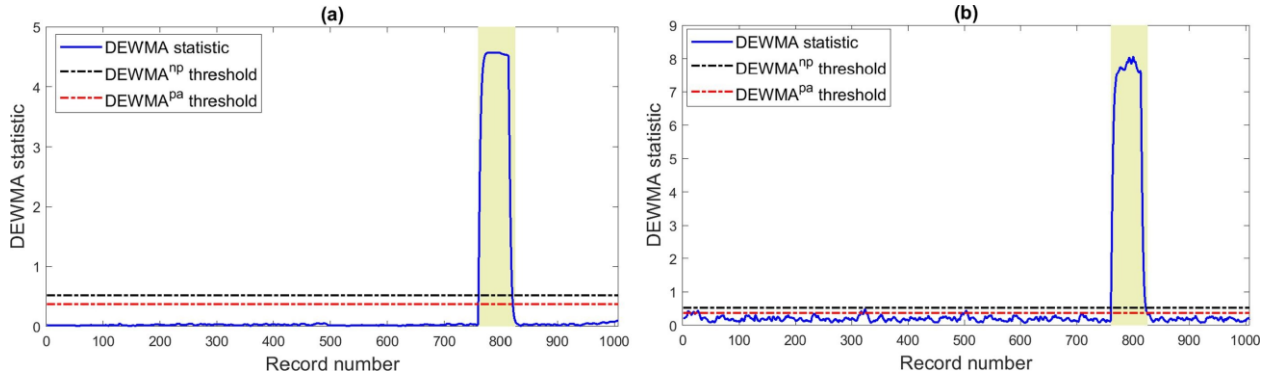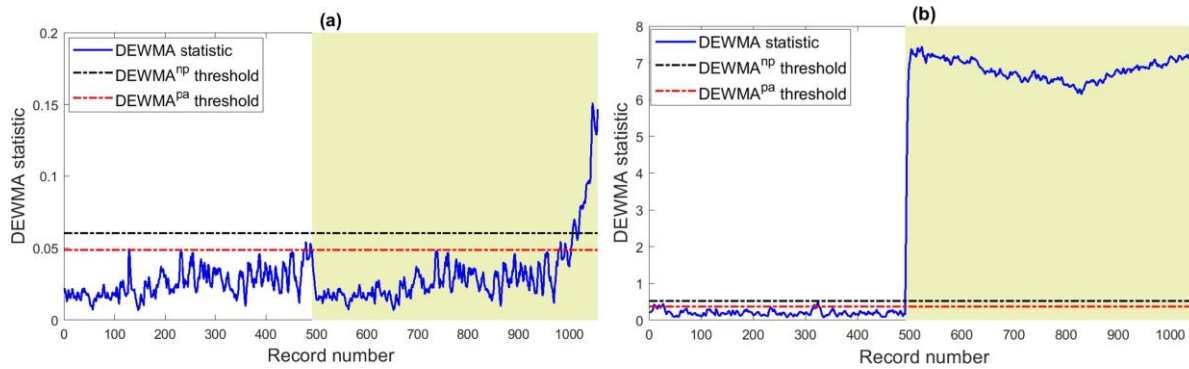
Figure 4.40 Illustration of the detection performance of the DEWMA charts applied to (a) DC current and (b) DC voltage datasets with five short-circuited modules.

In summary, this section shows that amalgamating empirical models to describe MPP DC current, voltage, power, and AC power with the good detection capability of DEWMA, enabling an efficient detection of anomalies in DC and AC sides of a PV system. Also, results proclaim the superior efficiency of the DEWMA scheme with a nonparametric threshold compared to the parametric counterpart and the single EWMA.

4.4 Conclusion.

faults can affect performance of PV system and cause their power production to decrease from their desired specification significantly. Since anomalies and failures are inevitable in a PV system, they must be suitably identified and corrected.

In this chapter, two techniques were investigated, In the first section, a simple technique for automatic diagnosis of the main faults in PV systems was proposed. This technique is based on the performance loss evaluation of four electrical indicators (i.e., DC current, DC voltage, DC power and AC power) based on sandia parametric models. The definition of both lower and upper threshold limits for each fault are established by faulty-dataset from 9.54 kWp experimental PV system. The nine faults' cases were properly detected and identified using a modest and convivial user interface, along with other features that have been added to this interface. The partial shading fault is well recognized, but there is a possibility of non-distinction with other faults in DC side, which leads to false identification, this problem can be solved by signal processing of a shading anomaly. The proposed technique is not complex and easy to integrate into the real-time monitoring program.

In the second section of this chapter, we have presented a simple and efficient diagnostic method based on parametric models and the double exponential moving average (DEWMA) scheme. The empirical models of PV array and PV inverter are employed to generate residuals, a second approach based on nonparametric models computed by KDE are applied. The residue examination is performed by DEWMA technique in order to detect and identify faults occurring in the PV system. The capacity of the designed detection schemes is verified using six types of electrical and environmental faults in order to assess the detection performance. The results claim that the DEWMA scheme with a non-parametric threshold gives more precision and accuracy than that based on the parametric models. These techniques can be applied to real-time monitoring of PV system operating conditions.

Despite the satisfying results achieved using the DEWMA-based procedure for fault detection purposes, this work can be further improved. Recently, deep learning-driven models have emerged as a promising line of research in modeling and forecasting time series data (Harrou et al., 2020, Harrou et al., 2020). In future work, we plan to develop advanced fault detection and diagnosis techniques by exploiting the extended capacity of deep learning models in modeling time dependencies in time-series data. In addition, the hybridization of techniques such as statistical, signal processing, machines learning and deep learning, can give a better precision and accuracy for fault diagnosis.

Conclusion and perspectives

Conclusion

Failures and anomalies in solar PV plants can affect their performance and cause their power production to decrease from their desired specification significantly, and since such faults are inevitable in a PV system, they must be properly detected, identified and well handled.

A comprehensive monitoring of all characteristic parameters adds a great value to the PV system leading to: extended system life, low maintenance requirements and low operating costs in order to have an optimum performance in a cost-effective and reliable way. Indeed, an advanced monitoring system makes it possible to acquire and analyze a number of performance parameters of the PV system and to compare them with calibrated models using intelligent techniques to detect drops in performance with classification of the various faults that can affect a PV system.

In **chapter 2**, we introduced the implementation of a real-time monitoring system for a 9.54 kWp grid-connected PV system (GCPVS), mainly composed of sensors, data acquisition instruments and LabVIEW graphical programming software. The external sensors mounted in the GCPVS were well calibrated with reference instruments and sensors and exhibit reliable and accurate measurements. The use of sophisticated and accurate PC-based DAQ hardware (i.e., Agilent 34970A, Keithley 2700 and Fluke 2638A) with LabVIEW software creates a virtual instrumentation (VI) system which is very useful for the acquisition, visualization, and analysis of measured data. PC-based DAQ can largely meet the requirements of IEC 61724 for PV system performance monitoring. A user-friendly interface under LabVIEW is designed, making it possible to retrieve, display and record the measured data of the environmental and electrical parameters which characterize the GCPVS. Several versions were developed in order to design the final interface. The proposed monitoring platform is customizable, and can be applied to any size and type of the PV system. The designed interface is also extensible for behavioral modeling, performance analysis and fault diagnosis using different methods and techniques.

In the last section of **chapter 2**, some case studies dealing with measurement and monitoring applied to different types of PV systems carried out at CDER, were presented. These case studies are:
1) Monitoring of an off-grid PV system using LabVIEW.
2) Monitoring & control of a PV water pumping test bench using LabVIEW.
3) I-V characterization and test of different PV modules using an I-V tracer PVPM 2540C.
4) Advanced electrical measurement of the grid connected PV system using three-phase electrical networks analyzer.

The obtained results so far are very encouraging and promising, as already presented.

Carrying out monitoring for different systems and PV test benches has enabled us to:

- Acquire knowledge on new electrical and physical phenomena.
- Become more familiar with new conditioning and measurement techniques.
- Handle multiple sensors, transducers, instruments, and software.

In **chapter 3**, several models were selected and tested in order to choose the best model for each modeling part. The results obtained by simulation were validated using reference data measurements of the 9.54 kWp GCPVS in MATLAB. The comparison showed good agreement, and that the models developed by SNL are the best (i.e., 1) cell/module temperature model, 2) SAPM to predict DC current, DC voltage and DC power and 3) SANDIA inverter model to estimate AC power).

For the non-parametric model based on PCA, we saw a good agreement between the measured and the predicted data. Simulation results illustrate the good accuracy of the PCA model.

The generated residuals based on the developed PCA reference model will be evaluated by multivariate monitoring charts to detect faults.

A user-friendly interface was designed and developed under LabVIEW in order to model the electrical behavior of GCPVS and to analyze the performance of environmental and electrical data by calculating the performance ratio and the energy yields of the PV system. The designed interface also allows a dynamic visualization of all data and information with different scenarios. Furthermore, the graphical program under LabVIEW is extensible to integrate multiple performance model and to analyze data using advanced techniques (e.g., Machine Learning, statistical methods and hybrid methods) for modeling, performance analysis and faults detection in a PV system. The difference between the simulated and measured values relates to a detection of the fault occurring in PV system.

In **chapter 4**, two techniques were investigated. In the first section, a simple technique for automatic diagnosis of the main faults in PV systems were proposed. This technique is based on the performance loss rate (PLR) evaluation of four electrical indicators (i.e., DC current, DC voltage, DC power and AC power) based on SANDIA parametric models. The definition of both lower and upper threshold limits for each fault are established by faulty-dataset from 9.54 kWp experimental PV system. The nine faults' cases were properly detected and identified using a simple and convivial user interface, along with other features that have been added to this interface. The partial shading fault is well recognized, but there is a possibility of non-distinction between other faults in DC side, which leads to false identification, this problem can be solved by signal processing of a shading anomaly. The proposed technique is not complex and easy to integrate into the real-time monitoring program.

In the second section of **chapter 4**, we presented a simple and efficient diagnostic method based on parametric models and the double exponential moving average (DEWMA) scheme. The empirical models of PV array and PV inverter are used to generate residuals. A second approach based on nonparametric models computed by KDE is applied. The residue examination is performed by DEWMA technique in order to detect and identify faults occurring in the PV system. The capacity of the designed detection schemes is verified using six types of electrical and environmental faults in order to assess the detection performance. The results show that the DEWMA scheme with a non-parametric threshold gives more precision and accuracy than that based on the parametric models. These techniques can be applied in real-time monitoring of PV system operating conditions.

Recommendations for further work

Despite the promising obtained results, this thesis could be improved with next features by:
- ✓ Increasing accuracy and precision of environmental measurements by adding other class A sensors (pyranometer; PT 100, wind sensor).
- ✓ Adding electrical sensors on the AC side of the PV system at the connection point to monitor the energy flow.
- ✓ Adding filters to the DC and AC electrical quantity measurement cards.
- ✓ Analysis of AC parameters (energies, frequencies, harmonics, etc.)
- ✓ Improving the precision of the models used. In addition, we plan to test other models to get a better electrical prediction.
- ✓ Using other fault detection techniques and making a comparative study of these methods.
- ✓ Adding of IoT functionalities to the monitoring system.
- ✓ Extending detection tests using other data from large-scale PV plants installed in Algeria.
- ✓ Developing advanced fault detection and diagnosis techniques by exploiting the extended capability of deep learning models.
- ✓ Integrating forecasting models

Bibliography

[1]   IRENA, "Renewable Capacity Statistics 2022," [Online]. Available: irena.org/publications.

[2]   BNEF, "Scale-up of Solar and Wind Puts Existing Coal, Gas at Risk | BloombergNEF," *Bloomberg New Energy Finance*, 2020. [Online]. Available: about.bnef.com.

[3]   IEA PVPS, "Trends in photovoltaic applications," 2021. [Online]. Available : iea-pvps.org/publications.

[4]   Gantner-instruments, "Effective plant monitoring promotes efficient PV," 2015. [Online]. Available :gantnerenvironment.com.

[5]   IEA-PVPS, Performance of New Photovoltaic System Designs. 2021. [Online]. Available : iea-pvps.org.

[6]   IEA-PVPS, "The use of advanced algorithms in PV failure monitoring," 2021. [Online]. Available : iea-pvps.org/publications.

[7]   IEA-PVPS, "Technical Assumptions Used in PV Financial Models Review of Current Practices and Recommendations," 2017. [Online]. Available : iea-pvps.org/publications.

[8]   IFC, "Utility-Scale Solar Photovoltaic Power Plants A Project Developer's Guide," International Finance Corporation, 2015. [Online]. Available: ifc.org.

[9]   IEC, Photovoltaic system performance – Part 1: Monitoring IEC 61724-1. 2021. [Online]. Available: https://webstore.iec.ch/publication/65561.

[10]   NREL, "Monitoring System Performance," in *PV Module Reliability Workshop*, 2011, p. 24. [Online]. Available: nrel.gov.

[11]   IEA-PVPS, "Analytical Monitoring of Grid-connected Photovoltaic Systems -Good practices for monitoring and performance analysis," 2014. [Online]. Available : iea-pvps.org/publications.

[12]   NREL, "Update on Edition 2 of IEC 61724 : PV System Performance Monitoring," 2014. [Online]. Available: nrel.gov.

[13]   NREL, Sandia, and Alliance Sunspec, "Best Practices in Photovoltaic System Operations and Maintenance," no. December, 2016, doi: NREL/TP-7A40-67553.

[14]   IEA-PVPS, "Performance, Operation and Reliability of Photovoltaic Systems," 2013. https://iea-pvps.org/research-tasks/performance-operation-and-reliability-of-photovoltaic-systems/# (accessed Feb. 08, 2022).

[15]   D. S. Pillai, F. Blaabjerg, and N. Rajasekar, "A Comparative Evaluation of Advanced Fault Detection Approaches for PV Systems," *IEEE J. Photovoltaics*, vol. 9, no. 2, pp. 513–527, 2019, doi: 10.1109/JPHOTOV.2019.2892189.

[16]   A. Livera, M. Theristis, G. Makrides, and G. E. Georghiou, "Recent advances in failure diagnosis techniques based on performance data analysis for grid-connected photovoltaic systems," *Renew. Energy*, vol. 133, pp. 126–143, 2019, doi: 10.1016/j.renene.2018.09.101.

[17]   I. U. Khalil *et al.*, "Comparative Analysis of Photovoltaic Faults and Performance Evaluation of its Detection Techniques," *IEEE Access*, vol. 8, pp. 26676–26700, 2020, doi: 10.1109/ACCESS.2020.2970531.

[18]   A. Mellit, "Recent Applications of Artificial Intelligence in Fault Diagnosis of Photovoltaic Systems," in *A Practical Guide for Advanced Methods in Solar Photovoltaic Systems*, vol. 128, Springer International Publishing, 2020, pp. 257–271.

[19]   Konrad Mertens, *Photovoltaics – Fundamentals, Technology, and Practice*, Second Edi. John Wiley & Sons Ltd, 2019.

[20]   Lazard, "Levelized Cost Of Energy, Levelized Cost Of Storage, and Levelized Cost Of Hydrogen," 2021. https://www.lazard.com/perspective/levelized-cost-of-energy-levelized-cost-of-storage-and-levelized-cost-of-hydrogen/ (accessed Feb. 16, 2022).

[21]   NREL, "2021 Electricity Annual Technology Baseline (ATB) Technologies and Data Overview," 2021. https://atb.nrel.gov/electricity/2021/index (accessed Feb. 19, 2022).

[22]   Solar Bankability, "PV Investment Technical Risk Management," 2017.

[23]   Ministère de l'Énergie | Algérie, "Programme de développement des énergies renouvelables 2015-2030." https://www.energy.gov.dz/?rubrique=energies-nouvelles-renouvelables-et-maitrise-de-lrenergie (accessed Dec. 10, 2019).

[24]   IRENA, "Statistiques de capacité renouvelable 2021," [Online]. Available : irena.org/publications.

[25]   IEA-PVPS, "Snapshot of Global PV Markets 2022," 2022. [Online]. Available: http://www.iea-pvps.org.

[26]   NREL, "Utility-Scale PV | Electricity," 2021. https://atb.nrel.gov/electricity/2021/utility-scale_pv (accessed Feb. 16, 2022).

[27]   M. Bolinger, J. Seel, C. Warner, and D. Robson, "Utility-Scale Solar , 2021 Edition," 2021.

[28]   BloombergNEF, "Solar - 10 Predictions for 2022," 2022. https://about.bnef.com/blog/solar-10-predictions-for-2022/ (accessed Feb. 16, 2022).

[29]   EnergyTrend, "Solar Price," 2022. https://www.energytrend.com/solar-price.html (accessed Feb. 19, 2022).

[30]   Clean Energy Reviews, "Most efficient solar panels 2022," 2022. https://www.cleanenergyreviews.info/blog/most-efficient-solar-panels (accessed Mar. 02, 2022).

[31]   Clean Energy Reviews, "Solar panel warranty explained," 2022. https://www.cleanenergyreviews.info/solar-panel-warranty (accessed Mar. 02, 2022).

[32]   A. Haque, F. Blaabjerg, and H. Wang, *Reliability of Power Electronics Converters for Solar Photovoltaic Applications*. 2021.

[33]   Y. Yang, K. A. Kim, F. Blaabjerg, and A. Sangwongwanich, *Advances in Grid-Connected Photovoltaic Power Conversion Systems*. Joe Hayton, 2019.

[34]   World Market Reports, "Global Solar Pv Inverters Market." https://www.marketreportsworld.com/global-solar-pv-inverters-market-20069556 (accessed Mar. 02, 2022).

[35]   HUAWEI, "Smart I-V Curve Diagnosis Technical White Paper," 2020. [Online].Available :solar.huawei.com.

[36]   SMA Solar Technology AG, "Technical Information SUNNY TRIPOWER CORE1 I-V Curve Diagnostic Function."

[37]   F. Obeidat, "A comprehensive review of future photovoltaic systems," *Sol. Energy*, vol. 163, no. October 2017, pp. 545–551, 2018, doi: 10.1016/j.solener.2018.01.050.

[38]   C.B.Honsberg and S.G.Bowden, "Photovoltaics Education Website," 2019. https://www.pveducation.org/ (accessed Feb. 14, 2022).

[39]   H. Haberlin, *PHOTOVOLTAICS SYSTEM DESIGN AND PRACTICE*. 2012.

[40]   A. Yaman and H. Eklas, *Photovoltaic systems : Fundamentals and Applications*. 2022.

[41]   D. Naghaviha, H. Nikkhajoei, and H. Karimi, *Step-by-Step Design of Large-Scale Photovoltaic Power Plants*, 1st editio. Wiley, 2022.

[42]   S. Rabindra and P. Venkateswarlu, *Solar PV Power Design, Manufacturing and Applications from Sand to Systems*. 2021.

[43]   Karl-Anders Weiß, *Photovoltaic Modules: Reliability and Sustainability*. 2021.

[44]   H. Wirth, *Photovoltaic Module Technology*. 2021.

[45]   G. T. Klise and J. S. Stein, "Models used to assess the performance of photovoltaic systems," *Sandia Natl. Lab.*, no. December, pp. 1–67, 2009.

[46]   PVPMC, "Plane of Array (POA) Irradiance." https://pvpmc.sandia.gov/modeling-steps/1-weather-design-inputs/plane-of-array-poa-irradiance/ (accessed Mar. 16, 2022).

[47]   Matt Perry, "New Product Support : Bifacial Plane of Array (BPOA)," 2018. https://www.campbellsci.com.cn/blog/albedo-resource-assessment (accessed Mar. 07, 2022).

[48]   J. S. Stein *et al.*, *Bifacial PV modules & systems Experience and Results from International Research and Pilot Applications*. 2021.

[49]   R. Kopecek and J. Libal, "Bifacial photovoltaics 2021: Status, opportunities and challenges," *Energies*, vol. 14, no. 8, 2021, doi: 10.3390/en14082076.

[50]   IEA-PVPS, *Climatic Rating of Photovoltaic Modules: Different Technologies for Various Operating Conditions*. 2020. [Online]. Available : iea-pvps.org/publications.

[51]   "Central Inverter vs String Inverter," 2019. https://www.renvu.com/Central-Inverter-vs-String-Inverter (accessed Mar. 06, 2022).

[52]   NREL, "Utility-Scale PV-Plus-Battery," 2021. https://atb.nrel.gov/electricity/2021/utility-scale_pv-plus-battery (accessed Feb. 16, 2022).

[53]   Clean Energy Reviews, "Best off-grid solar system," 2020. https://www.cleanenergyreviews.info/blog/best-off-grid-solar-system (accessed Mar. 03, 2022).

[54]   Clean Energy Reviews, "Lead-acid Vs lithium-ion batteries," 2020. https://www.cleanenergyreviews.info/blog/simpliphi-pylontech-narada-bae-lead-acid-battery (accessed Mar. 02, 2022).

[55]   Clean Energy Reviews, "MPPT Solar Charge Controllers Explained," 2020. https://www.cleanenergyreviews.info/blog/mppt-solar-charge-controllers (accessed Mar. 02, 2022).

[56]   Victron Energy, "Inverter/chargers." https://www.victronenergy.com/inverters-chargers (accessed Mar. 03, 2022).

[57]   Grundfos, "Solar water solutions." https://product-selection.grundfos.com/applications/municipal-water-supply/solar-water-solutions?tab=products (accessed Mar. 02, 2022).

[58]   LORENTZ, "Products - LORENTZ." https://www.lorentz.de/products-and-technology/products/ (accessed Mar. 02, 2022).

[59]   Clean Energy Reviews, "What is a hybrid inverter," 2021. https://www.cleanenergyreviews.info/blog/what-is-a-hybrid-inverter (accessed Mar. 02, 2022).

[60]   Yokogawa Electric Corporation, "Data Acquisition (DAQ)." https://www.yokogawa.com/solutions/products-platforms/data-acquisition/ (accessed Mar. 14, 2022).

[61]   A. Triki-lahiani, A. B. Abdelghani, and I. Slama-belkhodja, "Fault detection and monitoring systems for photovoltaic installations : A review," *Renew. Sustain. Energy Rev.*, no. July, pp. 0–1, 2017, doi: 10.1016/j.rser.2017.09.101.

[62]   F. P. Baumgartner, O. Maier, D. Schär, D. Sanchez, and P. Toggweiler, "SURVEY OF OPERATION AND MAINTENANCE COSTS OF PV PLANTS IN SWITZERLAND," 2015.

[63]   NREL;Sandia;Sunspec Alliance, "Best Practices in Photovoltaic System operations and Maintenance," 2016.

[64]   K. Keisang, T. Bader, and R. Samikannu, "Review of Operation and Maintenance Methodologies for Solar Photovoltaic Microgrids," *Front. Energy Res.*, vol. 9, no. November, pp. 1–15, 2021, doi: 10.3389/fenrg.2021.730230.

[65] S. R. Madeti and S. N. Singh, "Monitoring system for photovoltaic plants: A review," *Renew. Sustain. Energy Rev.*, vol. 67, pp. 1180–1207, Jan. 2017, doi: 10.1016/j.rser.2016.09.088.

[66] L. Cristaldi, M. Faifer, M. Lazzaroni, M. M. A. F. Khalil, M. Catelani, and L. Ciani, "Diagnostic architecture: A procedure based on the analysis of the failure causes applied to photovoltaic plants," *Meas. J. Int. Meas. Confed.*, vol. 67, pp. 99–107, 2015, doi: 10.1016/j.measurement.2015.02.023.

[67] S. Manzano, R. Peña, D. Guevara, and A. Ríos, "An Overview Of Remote Monitoring PV Systems: Acquisition, Storages, Processing And Publication Of Real-Time Data Based On Cloud Computing," *13Th Int. Work. Large-Scale Integr. Wind Power into Power Syst. as well as Transm. Networks Offshore Wind Power Plants 4th Sol. Integr. Work. which will be held*, 2014.

[68] M. M. Rahman, J. Selvaraj, N. A. Rahim, and M. Hasanuzzaman, "Global modern monitoring systems for PV based power generation: A review," *Renew. Sustain. Energy Rev.*, vol. 82, no. October, pp. 4142–4158, 2018, doi: 10.1016/j.rser.2017.10.111.

[69] M. M. Rahman, J. Selvaraj, N. A. Rahim, and M. Hasanuzzaman, "Global modern monitoring systems for PV based power generation: A review," *Renewable and Sustainable Energy Reviews*. 2018, doi: 10.1016/j.rser.2017.10.111.

[70] F. Shariff, N. A. Rahim, and W. P. Hew, "Zigbee-based data acquisition system for online monitoring of grid-connected photovoltaic system," *Expert Syst. Appl.*, 2015, doi: 10.1016/j.eswa.2014.10.007.

[71] I. M. Moreno-garcia *et al.*, "Real-Time Monitoring System for a Utility-Scale," pp. 1–25, 2016, doi: 10.3390/s16060770.

[72] E. L. Meyer, O. O. Apeh, and O. K. Overen, "Electrical and meteorological data acquisition system of a commercial and domestic microgrid for monitoring pv parameters," *Appl. Sci.*, vol. 10, no. 24, pp. 1–18, 2020, doi: 10.3390/app10249092.

[73] J. Medina-garcía, A. D. Martín, J. M. Cano, J. A. Gómez-galán, and A. Hermoso, "Efficient wireless monitoring and control of a grid-connected photovoltaic system," *Appl. Sci.*, vol. 11, no. 5, pp. 1–21, 2021, doi: 10.3390/app11052287.

[74] K. Xia, J. Ni, Y. Ye, P. Xu, and Y. Wang, "A real-time monitoring system based on ZigBee and 4g communications for photovoltaic generation," *CSEE J. Power Energy Syst.*, vol. 6, no. 1, pp. 52–63, 2020, doi: 10.17775/CSEEJPES.2019.01610.

[75] Solytic, "PV monitoring software comparison of costs & features 2021.," 2021. https://www.solytic.com/comparisons/pv-monitoring-software-comparison/ (accessed Dec. 09, 2021).

[76] K. A. Klise, J. S. Stein, and J. Cunningham, "Application of IEC 61724 Standards to Analyze PV System Performance in Different Climates (Presentation)," *44th IEEE Photovolt. Spec. Conf. Washington, DC. SAND2017-6464C*, no. 2011, pp. 1–6, 2017.

[77] IEC Webstore, "IEC 61724-1:2021 RLV Photovoltaic system performance - Part 1: Monitoring," 2021. https://webstore.iec.ch/publication/70170 (accessed Dec. 15, 2021).

[78] photovoltaic-software, "Solar Inverter monitoring." https://photovoltaic-software.com/pv-monitoring/monitoring-solar-inverter (accessed Mar. 13, 2022).

[79] Clean Energy Reviews, "Best Solar Inverters 2021," 2021. https://www.cleanenergyreviews.info/blog/best-grid-connect-solar-inverters-sma-fronius-solaredge-abb (accessed Dec. 25, 2021).

[80] SMA Solar, "Monitoring & Control SMA Solar." https://www.sma.de/en/products/monitoring-control.html (accessed Mar. 13, 2022).

[81] Solar-Log, "Products & Components Solar-Log™." https://www.solar-log.com/en/products-components/ (accessed Mar. 13, 2022).

[82] International Electrotechnical Commission (IEC), "Standard IEC 61724: Photovoltaic system performance monitoring – Guidelines for measurement, data exchange and analysis," *IEC 61724-1:2017*, 2017. .

[83] EKO Instruments, "PV Modules performance assesment." https://eko-eu.com/applications/pv-modules-performance-assesment (accessed Mar. 08, 2022).

[84] Campbell Scientific, "What is the difference between a thermopile pyranometer and a silicon photocell pyranometer?" https://www.campbellsci.com/faqs?v=2322 (accessed Mar. 08, 2022).

[85] E. Riley *et al.*, "Pyranometers and Reference Cells : Part 2 : What Makes the Most Sense for PV Power Plants," 2012. [Online]. Available: http://www.pvel.com/pdf/pyranometers_and_reference_cells_part2.pdf.

[86] Hukseflux, "Pyranometers versus PV reference cells in outdoor PV system performance monitoring," pp. 1–6, [Online]. Available: http://www.hukseflux.com.

[87] sensoray, "Comparison of Thermocouples, RTDs, and Thermistors." http://www.sensoray.com/support/appnotes/thermocouples_rtds_thermistors.htm (accessed Mar. 15, 2022).

[88] Omega Engineering, "What temperature probe is better for you?" https://www.omega.co.uk/temperature/z/thermocouple-rtd.html#faq (accessed Mar. 15, 2022).

[89] Kipp & Zonen, "DustIQ for PV soiling monitoring." https://www.kippzonen.com/Product/419/DustIQ-Soiling-Monitoring-System (accessed Mar. 15, 2022).

[90] Atonometrics, "Mars Optical Soiling Sensor." https://www.atonometrics.com/mars-optical-soiling-sensor-revolutionary-new-product/ (accessed Mar. 15, 2022).

[91] Apogee Instruments, "Solar Energy PV Monitoring." https://www.apogeeinstruments.com/solar-energy-pv-monitoring/ (accessed Mar. 15, 2022).

[92] NRG Systems, "Solar Met Sensors." https://www.nrgsystems.com/products/solar-met-sensors/ (accessed Mar. 16, 2022).

[93] Kipp & Zonen, "RT1 smart rooftop monitoring system for PV installations." https://www.kippzonen.com/Product/420/RT1-Smart-Rooftop-Monitoring-System#.YjBrBnrP1D8 (accessed Mar. 15, 2022).

[94] Campbell Scientific, "SOLAR200: Solar Monitoring Station." https://www.campbellsci.com/solar200 (accessed Mar. 15, 2022).

[95] EKO Instruments, "PV Site Solar monitoring." https://eko-eu.com/applications/pv-site-solar-monitoring (accessed Mar. 15, 2022).

[96] Campbell Scientific, "Class A Solar Resource Assessment System." https://www.campbellsci.com/sunscout (accessed Mar. 15, 2022).

[97] Campbell Scientific, "SOLAR1000: Solar Monitoring Station." https://www.campbellsci.com/solar1000 (accessed Mar. 15, 2022).

[98] M. Fuentes, M. Vivar, J. M. Burgos, J. Aguilera, and J. A. Vacas, "Design of an accurate, low-cost autonomous data logger for PV system monitoring using Arduino™ that complies with IEC standards," *Sol. Energy Mater. Sol. Cells*, vol. 130, pp. 529–543, 2014, doi: 10.1016/j.solmat.2014.08.008.

[99] S. R. Madeti and S. N. Singh, "Monitoring system for photovoltaic plants: A review," *Renew. Sustain. Energy Rev.*, vol. 67, pp. 1180–1207, 2017, doi: 10.1016/j.rser.2016.09.088.

[100] LEM, "Industry Current & Voltage Transducers," p. 101, 2014, [Online]. Available: http://www.lem.com.

[101] IEA-PVPS, "Qualification of PV Power Plants using Mobile Test Equipment," 2021. [Online]. Available: https://iea-pvps.org.

[102] P. Satish, J. Basant, J. Sandeep, and P. Preetha, "QUALITY CONTROL OF PV PLANTS WITH ON-SITE MOBILE PV MODULES TEST LABORATORY," 2019.

[103] T. Huld and A. M. Gracia Amillo, "Estimating PV module performance over large geographical regions: The role of irradiance, air temperature, wind speed and solar spectrum," *Energies*, vol. 8, no. 6, pp. 5159–5181, 2015, doi: 10.3390/en8065159.

[104] A. Gholami, M. Ameri, M. Zandi, and R. Gavagsaz Ghoachani, "Electrical, thermal and optical modeling of photovoltaic systems: Step-by-step guide and comparative review study," *Sustain. Energy Technol. Assessments*, vol. 49, no. June 2021, p. 101711, 2022, doi: 10.1016/j.seta.2021.101711.

[105] PVPMC, "Modeling Steps." https://pvpmc.sandia.gov/modeling-steps/ (accessed Dec. 20, 2021).

[106] C. W. Hansen, K. A. Klise, J. S. Stein, Y. Ueda, and K. Hakuta, "Calibration of Photovoltaic Module Performance Models," p. 85000, 2014.

[107] R. Rawat, S. C. Kaushik, and R. Lamba, "A review on modeling, design methodology and size optimization of photovoltaic based water pumping, standalone and grid connected system," *Renew. Sustain. Energy Rev.*, vol. 57, pp. 1506–1519, May 2016, doi: 10.1016/j.rser.2015.12.228.

[108] S. Bouchakour, "Estimation and monitoring of grid connected PV system generation," vol. 19, no. January 2017, pp. 277–290, 2016.

[109] J. S. Stein, "The photovoltaic Performance Modeling Collaborative (PVPMC)," *Conf. Rec. IEEE Photovolt. Spec. Conf.*, pp. 3048–3052, 2012, doi: 10.1109/PVSC.2012.6318225.

[110] IEA-PVPS, *PV Performance Modeling Methods and Practices Results*. IEA-PVPS, 2017. [Online]. Available : iea-pvps.org/publications.

[111] **B. Taghezouit**, A. Hadj Arab, C. Larbes, and S. Bouchakour, "Dynamic Modelling and Performance Analysis for a Grid-Connected PV System under LabVIEW," pp. 1–6, 2018.

[112] **B. Taghezouit**, F. Harrou, Y. Sun, A. H. Arab, and C. Larbes, "A simple and effective detection strategy using double exponential scheme for photovoltaic systems monitoring," *Sol. Energy*, vol. 214, pp. 337–354, 2021, doi: 10.1016/j.solener.2020.10.086.

[113] T. Huld *et al.*, "A power-rating model for crystalline silicon PV modules," *Sol. Energy Mater. Sol. Cells*, vol. 95, no. 12, pp. 3359–3369, 2011, doi: 10.1016/j.solmat.2011.07.026.

[114] **B. Taghezouit**, F. Harrou, Y. Sun, A. H. A. H. Arab, and C. Larbes, "Multivariate statistical monitoring of photovoltaic plant operation," *Energy Convers. Manag.*, vol. 205, no. November 2019, p. 112317, 2020, doi: 10.1016/j.enconman.2019.112317.

[115] S.-A. Blaifi, S. Moulahoum, R. Benkercha, **B. Taghezouit**, and A. Saim, "M5P model tree based fast fuzzy maximum power point tracker," *Sol. Energy*, vol. 163, pp. 405–424, 2018, doi: 10.1016/j.solener.2018.01.071.

[116] M. P. Almeida, O. Perpiñán, and L. Narvarte, "PV power forecast using a nonparametric PV model," *Sol. Energy*, vol. 115, pp. 354–368, 2015, doi: 10.1016/j.solener.2015.03.006.

[117] A. Bakdi, W. Bounoua, S. Mekhilef, and L. M. Halabi, "Nonparametric Kullback-divergence-PCA for intelligent mismatch detection and power quality monitoring in grid-connected rooftop PV," *Energy*, vol. 189, p. 116366, 2019, doi: 10.1016/j.energy.2019.116366.

[118] R. Fazai *et al.*, "Machine learning-based statistical testing hypothesis for fault detection in photovoltaic systems," *Sol. Energy*, vol. 190, no. April, pp. 405–413, 2019, doi: 10.1016/j.solener.2019.08.032.

[119] A. Al–bashir, M. Al-Dweri, A. Al–ghandoor, B. Hammad, and W. Al–kouz, "Analysis of effects of solar irradiance, cell temperature and wind speed on photovoltaic systems performance," *Int. J. Energy Econ. Policy*, vol. 10, no. 1, pp. 353–359, 2020, doi: 10.32479/ijeep.8591.

[120] S. Alsadi and T. Khatib, "Photovoltaic power systems optimization research status: A review of criteria, constrains, models, techniques, and software tools," *Appl. Sci.*, vol. 8, no. 10, 2018, doi: 10.3390/app8101761.

[121] Siliken, "Best PV System Design Software for Your Solar Business," 2021. https://siliken.com/best-solar-design-software/ (accessed Dec. 27, 2021).

[122] D. González-Peña, I. García-Ruiz, M. Díez-Mediavilla, M. I. Dieste-Velasco, and C. Alonso-Tristán, "Photovoltaic prediction software: Evaluation with real data from northern Spain," *Appl. Sci.*, vol. 11, no. 11, 2021, doi: 10.3390/app11115025.

[123] IEA-PVPS, "Analytical Monitoring of Grid-connected Photovoltaic Systems," 2014.

[124] Solar power world online, "Top Solar Software and Monitoring Products," 2021. https://www.solarpowerworldonline.com/2021-solar-software-monitoring-products/ (accessed Dec. 16, 2021).

[125] R. Ahmed, V. Sreeram, Y. Mishra, and M. D. Arif, "A review and evaluation of the state-of-the-art in PV solar power forecasting: Techniques and optimization," *Renew. Sustain. Energy Rev.*, vol. 124, no. June 2019, p. 109792, 2020, doi: 10.1016/j.rser.2020.109792.

[126] D. L. King, W. E. Boyson, and J. A. Kratochvil, "Photovoltaic array performance model," *Sandia Rep. No. 2004-3535*, vol. 8, no. December, pp. 1–19, 2004, doi: 10.2172/919131.

[127] W. De Soto, S. A. Klein, and W. A. Beckman, "Improvement and validation of a model for photovoltaic array performance," *Sol. Energy*, vol. 80, no. 1, pp. 78–88, 2006, doi: 10.1016/j.solener.2005.06.010.

[128] A. P. Dobos, "PVWatts Version 5 Manual," *Tech. Rep. NREL/TP-6A20-62641*, no. September, p. 20, 2014.

[129] A. Dolara, S. Leva, and G. Manzolini, "Comparison of different physical models for PV power output prediction," *Sol. Energy*, vol. 119, pp. 83–99, 2015, doi: 10.1016/j.solener.2015.06.017.

[130] S. K. Firth, K. J. Lomas, and S. J. Rees, "A simple model of PV system performance and its use in fault detection," *Sol. Energy*, vol. 84, no. 4, pp. 624–635, Apr. 2010, doi: 10.1016/j.solener.2009.08.004.

[131] S. Qijun, L. Fen, Q. Jialin, Z. Jinbin, and C. Zhenghong, "Photovoltaic power prediction based on principal component analysis and Support Vector Machine," *IEEE PES Innov. Smart Grid Technol. Conf. Eur.*, pp. 815–820, 2016, doi: 10.1109/ISGT-Asia.2016.7796490.

[132] A. M. Humada *et al.*, "Modeling of PV system and parameter extraction based on experimental data: Review and investigation," *Sol. Energy*, vol. 199, no. February 2019, pp. 742–760, 2020, doi: 10.1016/j.solener.2020.02.068.

[133] B. H. King, C. W. Hansen, D. Riley, C. D. Robinson, and L. Pratt, "Procedure to Determine Coefficients for the Sandia Array Performance Model (SAPM)," no. June, pp. 3051–3056, 2016.

[134] R. Benkercha, S. Moulahoum, and **B. Taghezouit**, "Extraction of the PV modules parameters with MPP estimation using the modified flower algorithm," *Renew. Energy*, vol. 143, pp. 1698–1709, 2019, doi: 10.1016/j.renene.2019.05.107.

[135] B. Lekouaghet, A. Boukabou, and C. Boubakir, "Estimation of the photovoltaic cells/modules parameters using an improved Rao-based chaotic optimization technique," *Energy Convers. Manag.*, vol. 229, no. August 2020, p. 113722, 2021, doi: 10.1016/j.enconman.2020.113722.

[136] G. W. H. G. B. B. H. Friesen and Ekistica, "Photovoltaic Module Energy Yield Measurements: Existing Approaches and Best Practice," 2018.

[137] IEC Webstore, "IEC 60904-5:2011 Photovoltaic devices – Part 5: Determination of the equivalent cell temperature (ECT) of photovoltaic (PV) devices by the open-circuit voltage method," *IEC Webstore*, 2011. https://webstore.iec.ch/publication/3877 (accessed Dec. 20, 2021).

[138] P. M. Segado, J. Carretero, and M. Sidrach-de-Cardona, "Models to predict the operating temperature of different photovoltaic modules in outdoor conditions," *Prog. PHOTOVOLTAICS Res. Appl.*, vol. 23, pp. 1267– 1282, 2014, doi: 10.1002/pip.2549.

[139] D. P. N. Nguyen, K. Neyts, and J. Lauwaert, "Proposed models to improve predicting the operating temperature of different photovoltaic module technologies under various climatic conditions," *Appl. Sci.*, vol. 11, no. 15, 2021, doi: 10.3390/app11157064.

[140] D. L. King, S. Gonzalez, G. M. Galbraith, and W. E. Boyson, "Performance Model for Grid-Connected Photovoltaic Inverters," *Sandia Natl. Lab.*, vol. 38, no. September, pp. 655–660, 2007, [Online]. Available: http://jsedres.sepmonline.org/content/38/2/655.abstract.

[141] A. Driesse, P. Jain, and S. Harrison, "Beyond the curves: Modeling the electrical efficiency of photovoltaic inverters," *Conf. Rec. IEEE Photovolt. Spec. Conf.*, 2008, doi: 10.1109/PVSC.2008.4922827.

[142] "PV Performance Modeling Collaborative." https://pvpmc.sandia.gov/ (accessed Jun. 14, 2021).

[143] A. Ellis, M. Behnke, and C. Barker, "PV system modeling for grid planning studies," 2011, doi: 10.1109/PVSC.2011.6186478.

[144] J. S. Stein and B. Farnung, *PV Performance Modeling Methods and Practices Results*. 2017.

[145] K. Attari, A. Elyaakoubi, and A. Asselman, "Performance analysis and investigation of a grid-connected photovoltaic installation in Morocco," *Energy Reports*, vol. 2, no. December 2015, pp. 261–266, 2016, doi: 10.1016/j.egyr.2016.10.004.

[146] J. D. Mondol, Y. Yohanis, M. Smyth, and B. Norton, "Long term performance analysis of a grid connected photovoltaic system in Northern Ireland," *Energy Convers. Manag.*, vol. 47, no. 18–19, pp. 2925–2947, 2006, doi: 10.1016/j.enconman.2006.03.026.

[147] K. Attari, A. El Yaakoubi, and A. Asselman, "Comparative Performance Investigation between Photovoltaic Systems from two Different Cities," *Procedia Eng.*, vol. 181, pp. 810–817, 2017, doi: 10.1016/j.proeng.2017.02.471.

[148] D. Trillo-Montero, I. Santiago, J. J. Luna-Rodriguez, and R. Real-Calvo, "Development of a software application to evaluate the performance and energy losses of grid-connected photovoltaic systems," *Energy Convers. Manag.*, vol. 81, pp. 144–159, 2014, doi: 10.1016/j.enconman.2014.02.026.

[149] M. S. Adaramola, "Techno-economic analysis of a 2.1 kW rooftop photovoltaic-grid-tied system based on actual performance," *Energy Convers. Manag.*, vol. 101, pp. 85–93, 2015, doi: 10.1016/j.enconman.2015.05.038.

[150] F. Cherfa, A. Hadj Arab, R. Oussaid, K. Abdeladim, and S. Bouchakour, "Performance analysis of the mini-grid connected photovoltaic system at Algiers," *Energy Procedia*, vol. 83, pp. 226–236, 2015, doi: 10.1016/j.egypro.2015.12.177.

[151] M. S. Adaramola and E. E. T. Vågnes, "Preliminary assessment of a small-scale rooftop PV-grid tied in Norwegian climatic conditions," *Energy Convers. Manag.*, vol. 90, no. 2015, pp. 458–465, 2015, doi: 10.1016/j.enconman.2014.11.028.

[152] B. Shiva Kumar and K. Sudhakar, "Performance evaluation of 10 MW grid connected solar photovoltaic power plant in India," *Energy Reports*, vol. 1, pp. 184–192, 2015, doi: 10.1016/j.egyr.2015.10.001.

[153] G. S. Sharma *et al.*, "Performance Evaluation of a MW-Size Grid-Connected Solar Photovoltaic Plant Considering the Impact of Tilt Angle," *Sustain. 2022, Vol. 14, Page 1444*, vol. 14, no. 3, p. 1444, Jan. 2022, doi: 10.3390/SU14031444.

[154] R. Chandel and S. S. Chandel, "Performance analysis outcome of a 19-MWp commercial solar photovoltaic plant with fixed-tilt, adjustable-tilt, and solar tracking configurations," *Prog. Photovoltaics Res. Appl.*, no. July, pp. 1–22, 2021, doi: 10.1002/pip.3458.

[155] N. Sahouane *et al.*, "Energy and economic efficiency performance assessment of a 28 kWp photovoltaic grid-connected system under desertic weather conditions in Algerian Sahara," *Renew. Energy*, vol. 143, pp. 1318–1330, 2019, doi: 10.1016/j.renene.2019.05.086.

[156] Y. Zhao, "PROTECTION IN SOLAR PHOTOVOLTAIC ARRAYS," 2015.

[157] D. S. Pillai and N. Rajasekar, "A comprehensive review on protection challenges and fault diagnosis in PV systems," *Renew. Sustain. Energy Rev.*, vol. 91, no. March, pp. 18–40, 2018, doi: 10.1016/j.rser.2018.03.082.

[158] S. R. Madeti and S. N. Singh, "A comprehensive study on different types of faults and detection techniques for solar photovoltaic system," *Sol. Energy*, vol. 158, no. June, pp. 161–185, 2017, doi: 10.1016/j.solener.2017.08.069.

[159] M. Halwachs *et al.*, "Statistical evaluation of PV system performance and failure data among different climate zones," *Renew. Energy*, vol. 139, pp. 1040–1060, 2019, doi: 10.1016/j.renene.2019.02.135.

[160] IEA PVPS, "Quantification of Techniocal Risks in PV Power Systems," 2021. [Online]. Available: https://iea-pvps.org.

[161] IEA-PVPS, "Review of Failures of Photovoltaic Modules," 2014. [Online]. Available : iea-pvps.org.

[162] A. Haque, K. V. S. Bharath, M. A. Khan, I. Khan, and Z. A. Jaffery, "Fault diagnosis of Photovoltaic Modules," *Energy Sci. Eng.*, vol. 7, no. 3, pp. 622–644, 2019, doi: 10.1002/ese3.255.

[163] IEA-PVPS, *Review on Infrared and Electroluminescence Imaging for PV Field Applications*. 2018. [Online]. Available : iea-pvps.org/publications.

[164] R. Ebner, B. Kubicek, and G. Ujvari, "Non-destructive techniques for quality control of PV modules: Infrared thermography, electro- and photoluminescence imaging," *IECON Proc. (Industrial Electron. Conf.*, pp. 8104–8109, 2013, doi: 10.1109/IECON.2013.6700488.

[165] X. Li, W. Li, Q. Yang, W. Yan, and A. Y. Zomaya, "An Unmanned Inspection System for Multiple Defects Detection in Photovoltaic Plants," *IEEE J. Photovoltaics*, vol. 10, no. 2, pp. 568–576, 2020, doi: 10.1109/JPHOTOV.2019.2955183.

[166] M. Alsafasfeh, I. Abdel-Qader, B. Bazuin, Q. Alsafasfeh, and W. Su, "Unsupervised fault detection and analysis for large photovoltaic systems using drones and machine vision," *Energies*, vol. 11, no. 9, pp. 1–18, 2018, doi: 10.3390/en11092252.

[167] G. Alves Dos Reis Benatto *et al.*, "Drone-Based Daylight Electroluminescence Imaging of PV Modules," *IEEE J. Photovoltaics*, vol. 10, no. 3, pp. 872–877, 2020, doi: 10.1109/JPHOTOV.2020.2978068.

[168] V. Carletti, A. Greco, A. Saggese, and M. Vento, "An intelligent flying system for automatic detection of faults in photovoltaic plants," *J. Ambient Intell. Humaniz. Comput.*, vol. 11, no. 5, pp. 2027–2040, 2020, doi: 10.1007/s12652-019-01212-6.

[169] A. Mellit, G. M. Tina, and S. A. Kalogirou, "Fault detection and diagnosis methods for photovoltaic systems : A review," *Renew. Sustain. Energy Rev.*, vol. 91, no. February, pp. 1–17, 2018, doi: 10.1016/j.rser.2018.03.062.

[170] D. Stellbogen, "Use of PV circuit simulation for fault detection in PV array fields," *Conf. Rec. IEEE Photovolt. Spec. Conf.*, pp. 1302–1307, 1993, doi: 10.1109/pvsc.1993.346931.

[171] R. Rawat, S. C. Kaushik, and R. Lamba, "A review on modeling, design methodology and size optimization of photovoltaic based water pumping, standalone and grid connected system," *Renew. Sustain. Energy Rev.*, vol. 57, pp. 1506–1519, 2016, doi: 10.1016/j.rser.2015.12.228.

[172] Z. Chen, Y. Chen, L. Wu, S. Cheng, P. Lin, and L. You, "Accurate modeling of photovoltaic modules using a 1-D deep residual network based on I-V characteristics," *Energy Convers. Manag.*, vol. 186, no. December 2018, pp. 168–187, 2019, doi: 10.1016/j.enconman.2019.02.032.

[173] D. Wei, M. Wei, H. Cai, X. Zhang, and L. Chen, "Parameters extraction method of PV model based on key points of I-V curve," *Energy Convers. Manag.*, vol. 209, no. February, p. 112656, 2020, doi: 10.1016/j.enconman.2020.112656.

[174] J. Zhang *et al.*, "A reinforcement learning based approach for on-line adaptive parameter extraction of photovoltaic array models," *Energy Convers. Manag.*, vol. 214, no. April, p. 112875, 2020, doi: 10.1016/j.enconman.2020.112875.

[175] S. Das, A. Hazra, and M. Basu, "Metaheuristic optimization based fault diagnosis strategy for solar photovoltaic systems under non-uniform irradiance," *Renew. Energy*, 2017, doi: 10.1016/j.renene.2017.10.053.

[176] Z. Chen, L. Wu, S. Cheng, P. Lin, Y. Wu, and W. Lin, "Intelligent fault diagnosis of photovoltaic arrays based on optimized kernel extreme learning machine and I-V characteristics," *Appl. Energy*, vol. 204, pp. 912–931, 2017, doi: 10.1016/j.apenergy.2017.05.034.

[177] Z. Chen, Y. Chen, L. Wu, S. Cheng, and P. Lin, "Deep residual network based fault detection and diagnosis of photovoltaic arrays using current-voltage curves and ambient conditions," *Energy Convers. Manag.*, vol. 198, no. May, p. 111793, 2019, doi: 10.1016/j.enconman.2019.111793.

[178] T. Tanaka, T. Hayashi, T. Nagayama, T. Yanagidaira, and Y. Inui, "Proposal of novel degradation diagnosis method for photovoltaic module employing xenon flash lighting system and detector capacitor," *Energy Convers. Manag.*, vol. 186, no. September 2018, pp. 450–461, 2019, doi: 10.1016/j.enconman.2019.02.059.

[179] W. Chine, A. Mellit, V. Lughi, A. Malek, G. Sulligoi, and A. Massi Pavan, "A novel fault diagnosis technique for photovoltaic systems based on artificial neural networks," *Renew. Energy*, vol. 90, pp. 501–512, 2016, doi: 10.1016/j.renene.2016.01.036.

[180] Z. Yi and A. H. Etemadi, "Line-to-line fault detection for photovoltaic arrays based on multi-resolution signal decomposition and two-stage support vector machine," *IEEE Trans. Ind. Electron.*, vol. 64, no. 11, 2017, doi: 10.1109/TIE.2017.2703681.

[181] S. Fadhel *et al.*, "PV shading fault detection and classi fi cation based on I-V curve using principal component analysis : Application to isolated PV system," *Sol. Energy*, vol. 179, no. December 2018, pp. 1–10, 2019, doi: 10.1016/j.solener.2018.12.048.

[182] S. Spataru, D. Sera, T. Kerekes, and R. Teodorescu, "Monitoring and Fault Detection in Photovoltaic Systems Based On Inverter Measured String I-V Curves," in *31st European Photovoltaic Solar Energy Conference and Exhibition- EU PVSEC*, 2015, pp. 1667–1674, doi: 10.4229/EUPVSEC20152015-5BO.12.2.

[183] S. Sarikh, M. Raoufi, A. Bennouna, A. Benlarabi, and B. Ikken, "Implementation of a plug and play I-V curve tracer dedicated to characterization and diagnosis of PV modules under real operating conditions," *Energy Convers. Manag.*, vol. 209, no. February, p. 112613, 2020, doi: 10.1016/j.enconman.2020.112613.

[184] Huawei, "Smart I-V Curve Diagnosis," no. 03, 2020, [Online]. Available: https://solar.huawei.com/en-GB/download?p=%2F-%2Fmedia%2FSolar%2Fattachment%2Fpdf%2Feu%2Fdatasheet%2FIV-Curve.pdf.

[185] T. Takashima, J. Yamaguchi, and M. Ishida, "Disconnection Detection Using Earth Capacitance Measurement in Photovoltaic Module String," *Prog. PHOTOVOLTAICS Res. Appl.*, vol. 16, pp. 669–677, 2008, doi: 10.1002/pip.

[186] S. Roy, M. K. Alam, F. Khan, J. Johnson, and J. Flicker, "An Irradiance Independent, Robust Ground Fault Detection Scheme for PV Arrays Based on Spread Spectrum Time Domain Reflectometry (SSTDR)," *IEEE Trans. Power Electron.*, vol. 8993, no. c, pp. 1–1, 2017, doi: 10.1109/TPEL.2017.2755592.

[187] Q. Xiong *et al.*, "Detecting and localizing series arc fault in photovoltaic systems based on time and frequency characteristics of capacitor current," *Sol. Energy*, vol. 170, no. May, pp. 788–799, 2018, doi: 10.1016/j.solener.2018.06.004.

[188] Z. Wang, S. McConnell, R. S. Balog, and J. Johnson, "Arc fault signal detection - Fourier transformation vs. wavelet decomposition techniques using synthesized data," *2014 IEEE 40th Photovolt. Spec. Conf. PVSC 2014*, pp. 3239–3244, 2014, doi: 10.1109/PVSC.2014.6925625.

[189] J. Flicker and J. Johnson, "Photovoltaic ground fault detection recommendations for array safety and operation," *Sol. Energy*, vol. 140, pp. 34–50, 2016, doi: 10.1016/j.solener.2016.10.017.

[190] I. M. Dupont, P. C. M. Carvalho, S. C. S. Jucá, and J. S. P. Neto, "Novel methodology for detecting non-ideal operating conditions for grid-connected photovoltaic plants using Internet of Things architecture," *Energy Convers. Manag.*, vol. 200, no. May, p. 112078, 2019, doi: 10.1016/j.enconman.2019.112078.

[191] S. ali Blaifi, S. Moulahoum, **B. Taghezouit**, and A. Saim, "An enhanced dynamic modeling of PV module using Levenberg-Marquardt algorithm," *Renew. Energy*, vol. 135, pp. 745–760, 2019, doi: 10.1016/j.renene.2018.12.054.

[192] P. Pernot and F. Cailliez, "A critical review of statistical calibration/prediction models handling data inconsistency and model inadequacy," *AIChE J.*, vol. 63, no. 10, pp. 4642–4665, 2017, doi: 10.1002/aic.15781.

[193] D. S. Pillai and N. Rajasekar, "A comprehensive review on protection challenges and fault diagnosis in PV systems," *Renew. Sustain. Energy Rev.*, vol. 91, no. July 2017, pp. 18–40, 2018, doi: 10.1016/j.rser.2018.03.082.

[194]   IEA-PVPS, *Assessment of Performance Loss Rate of PV Power Systems*. 2021.

[195]   A. Chouder and S. Silvestre, "Automatic supervision and fault detection of PV systems based on power losses analysis," *Energy Convers. Manag.*, vol. 51, no. 10, pp. 1929–1937, 2010, doi: 10.1016/j.enconman.2010.02.025.

[196]   S. Silvestre, M. A. Da Silva, A. Chouder, D. Guasch, and E. Karatepe, "New procedure for fault detection in grid connected PV systems based on the evaluation of current and voltage indicators," *Energy Convers. Manag.*, vol. 86, pp. 241–249, 2014, doi: 10.1016/j.enconman.2014.05.008.

[197]   S. R. Madeti and S. N. Singh, "Online modular level fault detection algorithm for grid-tied and off-grid PV systems," *Sol. Energy*, vol. 157, no. May, pp. 349–364, 2017, doi: 10.1016/j.solener.2017.08.047.

[198]   S. Silvestre, L. Mora-Lopez, S. Kichou, F. Sanchez-Pacheco, and M. Dominguez-Pumar, "Remote supervision and fault detection on OPC monitored PV systems," *Sol. Energy*, vol. 137, pp. 424–433, 2016, doi: 10.1016/j.solener.2016.08.030.

[199]   S. R. Madeti and S. N. Singh, "Online fault detection and the economic analysis of grid-connected photovoltaic systems," *Energy*, vol. 134, pp. 121–135, Sep. 2017, doi: 10.1016/j.energy.2017.06.005.

[200]   M. Dhimish and V. Holmes, "Fault detection algorithm for grid-connected photovoltaic plants," *Sol. Energy*, vol. 137, pp. 236–245, 2016, doi: 10.1016/j.solener.2016.08.021.

[201]   S. Silvestre, *Chapter 7 - Strategies for Fault Detection and Diagnosis of PV Systems*. Elsevier Inc., 2018.

[202]   Y. Chaibi, M. Malvoni, A. Chouder, M. Boussetta, and M. Salhi, "Simple and efficient approach to detect and diagnose electrical faults and partial shading in photovoltaic systems," *Energy Convers. Manag.*, vol. 196, pp. 330–343, Sep. 2019, doi: 10.1016/J.ENCONMAN.2019.05.086.

[203]   A. Drews *et al.*, "Monitoring and remote failure detection of grid-connected PV systems based on satellite observations," *Sol. Energy*, vol. 81, no. 4, pp. 548–564, 2007, doi: 10.1016/j.solener.2006.06.019.

[204]   IEA-PVPS, "Improving Efficiency of PV Systems Using Statistical Performance Monitoring," 2017. [Online]. Available : iea-pvps.org/publications.

[205]   E. Garoudja, F. Harrou, Y. Sun, K. Kara, A. Chouder, and S. Silvestre, "Statistical fault detection in photovoltaic systems," *Sol. Energy*, vol. 150, pp. 485–499, 2017, doi: 10.1016/j.solener.2017.04.043.

[206]   F. Harrou, Y. Sun, **B. Taghezouit**, A. Saidi, and M.-E. Hamlati, "Reliable fault detection and diagnosis of photovoltaic systems based on statistical monitoring approaches," *Renew. Energy*, vol. 116, pp. 22–37, Feb. 2018, doi: 10.1016/J.RENENE.2017.09.048.

[207]   F. Harrou, **B. Taghezouit**, and Y. Sun, "Robust and fl exible strategy for fault detection in grid-connected photovoltaic systems," *Energy Convers. Manag.*, vol. 180, no. June 2018, pp. 1153–1166, 2019, doi: 10.1016/j.enconman.2018.11.022.

[208]   M. Dhimish, V. Holmes, B. Mehrdadi, and M. Dales, "Simultaneous fault detection algorithm for grid-connected photovoltaic plants," *IET Renew. Power Gener.*, vol. 11, no. 12, pp. 1565–1575, 2017, doi: 10.1049/iet-rpg.2017.0129.

[209]   **B. Taghezouit**, F. Harrou, Y. Sun, A. H. Arab, and C. Larbes, "Multivariate statistical monitoring of photovoltaic plant operation," *Energy Convers. Manag.*, vol. 205, no. August 2019, p. 112317, 2020, doi: 10.1016/j.enconman.2019.112317.

[210]   H. Ding *et al.*, "Local outlier factor-based fault detection and evaluation of photovoltaic system," *Sol. Energy*, vol. 164, no. November 2017, pp. 139–148, 2018, doi: 10.1016/j.solener.2018.01.049.

[211]   M. Mansouri, A. Al-khazraji, M. Hajji, and M. Faouzi, "Wavelet optimized EWMA for fault detection and application to photovoltaic systems," *Sol. Energy*, vol. 167, no. November 2017, pp. 125–136, 2018, doi: 10.1016/j.solener.2018.03.073.

[212]   F. Mallor, T. León, L. De Boeck, S. Van Gulck, M. Meulders, and B. Van Der Meerssche, "A method for detecting malfunctions in PV solar panels based on electricity production monitoring," *Sol. Energy*, vol. 153, pp. 51–63, 2017, doi: 10.1016/j.solener.2017.05.014.

[213]   I. S. Kim, "On-line fault detection algorithm of a photovoltaic system using wavelet transform," *Sol. Energy*, vol. 126, pp. 137–145, 2016, doi: 10.1016/j.solener.2016.01.005.

[214]   B. P. Kumar, G. S. Ilango, M. J. B. Reddy, and N. Chilakapati, "Online Fault Detection and Diagnosis in Photovoltaic Systems Using Wavelet Packets," *IEEE J. Photovoltaics*, vol. 8, no. 1, pp. 257–265, 2018.

[215]   E. Garoudja, A. Chouder, K. Kara, and S. Silvestre, "An enhanced machine learning based approach for failures detection and diagnosis of PV systems," *Energy Convers. Manag.*, vol. 151, no. June, pp. 496–513, 2017, doi: 10.1016/j.enconman.2017.09.019.

[216]   C. B. Jones, J. S. Stein, S. Gonzalez, and B. H. King, "Photovoltaic system fault detection and diagnostics using Laterally Primed Adaptive Resonance Theory neural network," *2015 IEEE 42nd Photovolt. Spec. Conf.*, no. 1, pp. 1–6, 2015, doi: 10.1109/PVSC.2015.7355834.

[217]   F. Harrou, **B. Taghezouit**, and Y. Sun, "Improved kNN-Based Monitoring Schemes for Detecting Faults in PV Systems," *IEEE J. Photovoltaics*, pp. 1–11, 2019, doi: 10.1109/JPHOTOV.2019.2896652.

[218]   S. R. Madeti and S. N. Singh, "Modeling of PV system based on experimental data for fault detection using kNN method," *Sol. Energy*, vol. 173, no. March, pp. 139–151, 2018, doi: 10.1016/j.solener.2018.07.038.

[219]   R. Benkercha and S. Moulahoum, "Fault detection and diagnosis based on C4.5 decision tree algorithm for grid connected PV system," *Sol. Energy*, vol. 173, no. April, pp. 610–634, 2018, doi: 10.1016/j.solener.2018.07.089.

[220] E. Jean, R. Sambatra, and N. Heraud, "PV Fault Detection Using the Least Squares Method," in *International Conference and Exposition on Electrical and Power Engineering (EPE 2016)*, 2016, no. Epe, pp. 20–22.

[221] M. Tadj, K. Benmouiza, A. Cheknane, and S. Silvestre, "Improving the performance of PV systems by faults detection using GISTEL approach," *Energy Convers. Manag.*, vol. 80, pp. 298–304, 2014, doi: 10.1016/j.enconman.2014.01.030.

[222] M. Dhimish, V. Holmes, B. Mehrdadi, and M. Dales, "Comparing Mamdani Sugeno fuzzy logic and RBF ANN network for PV fault detection," *Renew. Energy*, vol. 117, pp. 257–274, 2018, doi: 10.1016/j.renene.2017.10.066.

[223] H. Zhu *et al.*, "Study of joint temporal-spatial distribution of array output for large-scale photovoltaic plant and its fault diagnosis application," *Sol. Energy*, vol. 181, no. August 2018, pp. 137–147, 2019, doi: 10.1016/j.solener.2019.01.083.

[224] X. Lu *et al.*, "Fault diagnosis for photovoltaic array based on convolutional neural network and electrical time series graph," *Energy Convers. Manag.*, vol. 196, no. February, pp. 950–965, 2019, doi: 10.1016/j.enconman.2019.06.062.

[225] Y. Zhao, R. Ball, J. Mosesian, J.-F. de Palma, and B. Lehman, "Graph-Based Semi-supervised Learning for Fault Detection and Classification in Solar Photovoltaic Arrays," *IEEE Trans. Power Electron.*, vol. 30, no. 5, pp. 2848–2858, 2015, doi: 10.1109/TPEL.2014.2364203.

[226] F. Harrou, A. Dairi, **B. Taghezouit**, and Y. Sun, "An unsupervised monitoring procedure for detecting anomalies in photovoltaic systems using a one-class Support Vector Machine," *Sol. Energy*, vol. 179, no. December 2018, pp. 48–58, 2019, doi: 10.1016/j.solener.2018.12.045.

[227] T. Pei, L. Li, J. Zhang, and X. Hao, "Module block fault locating strategy for large-scale photovoltaic arrays," *Energy Convers. Manag.*, vol. 214, no. May, p. 112898, 2020, doi: 10.1016/j.enconman.2020.112898.

[228] H. Koga and N. Kawabata, "A Study Regarding Failure Detection for String Monitoring Systems in Photovoltaics. Field Trial at the F Onomichi Photovoltaic Power Plant," *Electr. Eng. Japan (English Transl. Denki Gakkai Ronbunshi)*, vol. 196, no. 1, pp. 3–10, 2016, doi: 10.1002/eej.22833.

[229] P. R. Satpathy and R. Sharma, "Power and mismatch losses mitigation by a fixed electrical reconfiguration technique for partially shaded photovoltaic arrays," *Energy Convers. Manag.*, vol. 192, no. April, pp. 52–70, 2019, doi: 10.1016/j.enconman.2019.04.039.

[230] A. Chouder, S. Silvestre, B. Taghezouit, and E. Karatepe, "Monitoring, modelling and simulation of PV systems using LabVIEW," *Sol. Energy*, vol. 91, pp. 337–349, 2013, doi: 10.1016/j.solener.2012.09.016.

[231] P. T. Le, H. L. Tsai, and T. H. Lam, "A wireless visualization monitoring, evaluation system for commercial photovoltaic modules solely in MATLAB/Simulink environment," *Sol. Energy*, vol. 140, pp. 1–11, 2016, doi: 10.1016/j.solener.2016.10.043.

[232] C. Ventura and G. M. Tina, "Utility scale photovoltaic plant indices and models for on-line monitoring and fault detection purposes," *Electr. Power Syst. Res.*, vol. 136, pp. 43–56, 2016, doi: 10.1016/j.epsr.2016.02.006.

[233] I. González, A. J. Calderón, and J. M. Andújar, "Novel remote monitoring platform for RES-hydrogen based smart microgrid," *Energy Convers. Manag.*, vol. 148, pp. 489–505, 2017, doi: 10.1016/j.enconman.2017.06.031.

[234] **B. Taghezouit,** A. H. Arab, C. Larbes, S. Smail, and A. Kamel, "Design of an accurate monitoring system for a grid-connected PV system based on LabVIEW," *Int. Symp. Mechatronics Renew. Energies*, p. 6, 2018.

[235] M. Khan, J. Iqbal, M. Ali, A. Muhmmad, A. Zahir, and N. Ali, "Designing and implementation of energy-efficient wireless photovoltaic monitoring system," *Trans. Emerg. Telecommun. Technol.*, no. April, pp. 1–11, 2019, doi: 10.1002/ett.3685.

[236] J. Montes-Romero, M. Piliougine, J. V. Muñoz, E. F. Fernández, and J. De La Casa, "Photovoltaic device performance evaluation using an open-hardware system and standard calibrated laboratory instruments," *Energies*, vol. 10, no. 11, 2017, doi: 10.3390/en10111869.

[237] A. Hadj Arab *et al.*, "Connection of the CDER-Algiers photovoltaic system to low-voltage distribution grid," *Energy Procedia*, vol. 136, pp. 145–150, 2017, doi: 10.1016/j.egypro.2017.10.311.

[238] SMA Solar Technology, "SUNNY WEBBOX data sheet." [Online]. Available: files.sma.de/downloads/BEWEBBOXBT-DFR114912.pdf.

[239] SMA Solar Technology, "Sunny Portal data sheet." [Online]. Available: https://www.sunnyportal.com/Templates/PublicPagesPlantList.aspx.

[240] Agilent, "Agilent 32970A/34972A Data Acquisition / Switch : Service Guide," 2012.

[241] NI, "What is LabVIEW?," 2021. https://www.ni.com/en-lb/shop/labview.html (accessed Dec. 20, 2021).

[242] Keithley, "Model 2700 Multimeter / Switch System, User ' s Manual," p. 462, 2016. [Online]. Available: https://download.tek.com › 2700-900-01K_Feb_2016.

[243] Fluke, "2638A Hydra Series III Data Acquisition System/Digital Multimeter." https://eu.flukecal.com/products/data-acquisition-and-test-equipment/data-acquisition/2638a-hydra-series-iii-data-acquisitio?quicktabs_product_details=1 (accessed Dec. 25, 2021).

[244] S. Bouchakour *et al.*, "Investigation of the voltage quality at PCC of grid connected PV system," *Energy Procedia*, vol. 141, pp. 66–70, 2017, doi: 10.1016/j.egypro.2017.11.013.

[245] L. D. O. Santos, P. C. M. de Carvalho, and C. de Oliveira Carvalho Filho, "Photovoltaic Cell Operating Temperature Models: A Review of Correlations and Parameters," *IEEE J. Photovoltaics*, vol. PP, pp. 1–12, 2021, [Online]. Available: https://ieeexplore.ieee.org/document/9585073/.

158

[246] T. A. Olukan and M. Emziane, "A comparative analysis of PV module temperature models," *Energy Procedia*, vol. 62, pp. 694–703, 2014, doi: 10.1016/j.egypro.2014.12.433.

[247] M. C. Alonso García and J. L. Balenzategui, "Estimation of photovoltaic module yearly temperature and performance based on Nominal Operation Cell Temperature calculations," *Renew. Energy*, 2004, doi: 10.1016/j.renene.2004.03.010.

[248] a. Bellini, S. Bifaretti, V. Iacovone, and C. Cornaro, "Simplified model of a photovoltaic module," *2009 Appl. Electron.*, no. 3, pp. 3–7, 2009.

[249] O. Gil-Arias and E. I. Ortiz-Rivera, "A general purpose tool for simulating the behavior of PV solar cells, modules and arrays," *11th IEEE Work. Control Model. Power Electron. COMPEL 2008*, 2008, doi: 10.1109/COMPEL.2008.4634686.

[250] S. Yin, S. X. Ding, X. Xie, and H. Luo, "A review on basic data-driven approaches for industrial process monitoring," *IEEE Transactions on Industrial Electronics*. 2014, doi: 10.1109/TIE.2014.2301773.

[251] T. Cheng, F. Harrou, Y. Sun, and T. Leiknes, "Monitoring Influent Measurements at Water Resource Recovery Facility Using Data-Driven Soft Sensor Approach," *IEEE Sens. J.*, 2019, doi: 10.1109/JSEN.2018.2875954.

[252] S. J. Qin, "Survey on data-driven industrial process monitoring and diagnosis," *Annu. Rev. Control*, 2012, doi: 10.1016/j.arcontrol.2012.09.004.

[253] **B. Taghezouit**, F. Harrou, Y. Sun, A. H. Arab, and C. Larbes, "Multivariate statistical monitoring of photovoltaic plant operation," *Energy Convers. Manag.*, vol. 205, 2020, doi: 10.1016/j.enconman.2019.112317.

[254] D. Faiman, "Assessing the Outdoor Operating Temperature of Photovoltaic Modules," *Prog. PHOTOVOLTAICS Res. Appl.*, vol. 16, pp. 307–315, 2008, doi: 10.1002/pip.813.

[255] P. Gilman, A. Dobos, N. DiOrio, J. Freeman, S. Janzou, and D. Ryberg, "System Advisor Model (SAM) Photovoltaic Model Technical Reference Update," *Natl. Renew. Energy Lab.*, no. March, p. 93, 2018, [Online]. Available: https://sam.nrel.gov/%0Ahttps://sam.nrel.gov/images/web_page_files/sam-help-2018-11-11-r4.pdf%0Asam.nrel.gov/content/downloads.

[256] D. S. Pillai and N. Rajasekar, "A comprehensive review on protection challenges and fault diagnosis in PV systems," *Renewable and Sustainable Energy Reviews*, vol. 91. Elsevier Ltd, pp. 18–40, Aug. 01, 2018, doi: 10.1016/j.rser.2018.03.082.

[257] Z. Chen, Y. Chen, L. Wu, S. Cheng, and P. Lin, "Deep residual network based fault detection and diagnosis of photovoltaic arrays using current-voltage curves and ambient conditions," *Energy Convers. Manag.*, vol. 198, no. July, p. 111793, 2019, doi: 10.1016/j.enconman.2019.111793.

[258] J. S. Hunter, "The Exponentially Weighted Moving Average," *J. Qual. Technol.*, vol. 18, no. 4, pp. 203–210, Oct. 1986, doi: 10.1080/00224065.1986.11979014.

[259] F. Harrou, M. Nounou, and H. Nounou, "A statistical fault detection strategy using PCA based EWMA control schemes," 2013, doi: 10.1109/ASCC.2013.6606311.

[260] J. M. Lucas and M. S. Saccucci, "Exponentially weighted moving average control schemes: Properties and enhancements," *Technometrics*, 1990, doi: 10.1080/00401706.1990.10484583.

[261] S. E. Shamma and A. K. Shamma, "Development and Evaluation of Control Charts Using Double Exponentially Weighted Moving Averages," *Int. J. Qual. Reliab. Manag.*, 1992, doi: 10.1108/02656719210018570.

[262] L. Zhang and G. Chen, "An Extended EWMA Mean Chart," *Qual. Technol. Quant. Manag.*, vol. 2, no. 1, pp. 39–52, Jan. 2005, doi: 10.1080/16843703.2005.11673088.

[263] F. Harrou, M. M. Hittawe, Y. Sun, and O. Beya, "Malicious attacks detection in crowded areas using deep learning-based approach," *IEEE Instrum. Meas. Mag.*, vol. 23, no. 5, pp. 57–62, Aug. 2020, doi: 10.1109/mim.2020.9153576.

[264] E. B. Martin and A. J. Morris, "Non-parametric confidence bounds for process performance monitoring charts," *J. Process Control*, 1996, doi: 10.1016/0959-1524(96)00010-8.

Appendix

Appendix A
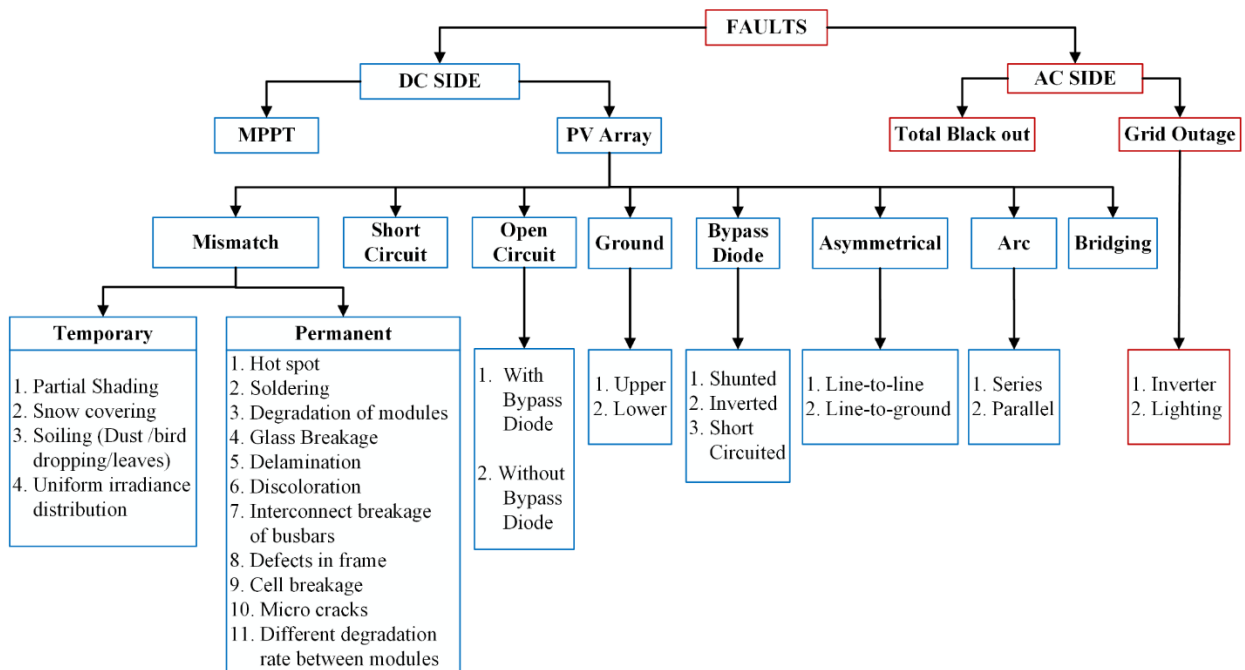
Figure 0.1 Classification of various fault occurring in DC & AC side of the PV system

Table 0.1 Description of losses occurring in a PV Power Plant.

Loss	Description
Air pollution	The solar resource can be reduced significantly in some locations due to air pollution from industry and agriculture. Air pollution reduces solar irradiance incident on the module and thereby reduces power output. This is more significant in urban and peri-urban locations, particularly in more recently industrialized nations.
Soiling	Losses due to soiling (dust and bird droppings) depend on the environmental conditions, rainfall frequency, and cleaning strategy as defined in the O&M contract. This loss can be relatively large compared to other loss factors. It has the potential to reach up to 15 percent annually and potentially higher in deserts, but is usually less than 4 percent unless there is unusually high soiling or problems from snow settling on the modules for long periods of time. The soiling loss may be expected to be lower for modules at a high tilt angle as inclined modules will benefit more from the natural cleaning effect of rainwater. Tracking systems typically record similar soiling losses as fixed systems. As this loss can have an important impact on the PR, it is recommended that an expert is consulted to quantify the soiling loss.
Shading	Shading losses occur due to mountains or buildings on the far horizon, mutual shading between rows of modules and near shading due to trees, buildings, pylons or overhead cabling. To model near-shading losses accurately, it is recommended that a 3D representation of the plant and shading obstacles are generated within the modelling software. This loss can potentially be quite large; thus, it is important that the plant is modelled accurately.
Electrical shading	The effect of partial shadings on electrical production of the PV plant is non-linear and is modelled through partitioning of the strings of modules. Modules installed in landscape configuration for an orientation towards the equator will typically experience less electrical shading losses than modules installed in portrait configuration due to the connection of diodes. Similarly, some types of thin-film technology are less impacted than crystalline PV modules. Electrical shading effects can typically be set within the modelling software. This will be quantified differently depending on module configuration, chosen technology and the system type (i.e., tracking or fixed).
Incident angle	The incidence angle loss accounts for radiation reflected from the front glass when the light striking it is not perpendicular. For tilted PV modules, these losses may be expected to be larger than the losses experienced with dual axis tracking systems, for example.
Low irradiance	The conversion efficiency of a PV module generally reduces at low light intensities. This causes a loss in the output of a module compared with the Standard Test Conditions (STC) (1,000W/m2). This "low irradiance loss" depends on the characteristics of the module and the intensity of the incident radiation. Most module manufacturers will be able to provide information on their module low irradiance losses. However, where possible, it is preferable to obtain such data from independent testing institutes.

Module temperature	The characteristics of a PV module are determined at standard temperature conditions of 25˚C. For every degree rise in Celsius temperature above this standard, crystalline silicon modules reduce in efficiency, generally by around 0.5 percent. In high ambient temperatures under strong irradiance, module temperatures can rise appreciably. Wind can provide some cooling effect, which can also be modelled.
Module quality	Most PV modules do not exactly match the manufacturer's nominal specifications. Modules are sold with a nominal peak power and a guarantee of actual power within a given tolerance range. The module quality loss quantifies the impact on the energy yield due to divergences in actual module characteristics from the specifications. Typically, the module output power at STC is greater than the nominal power specified in the datasheets. As such, a positive quality factor can be applied to the energy yield.
Module mismatch	Losses due to "mismatch" are related to the fact that the real modules in a string do not all rigorously present the same current/voltage profiles; there is a statistical variation between them which gives rise to a power loss. This loss is directly related to the modules' power tolerance.
Degradation	The performance of a PV module decreases with time (see Section 3.3.5). If no independent testing has been conducted on the modules being used, then a generic degradation rate depending on the module technology may be assumed. Alternatively, a maximum degradation rate that conforms to the module performance warranty may be considered as a conservative estimate.
Inverter performance	Inverters convert current from DC into AC with an efficiency that varies with inverter load. Manufacturers are usually able to provide an inverter's efficiency profile for low, medium and high voltages; entering these into the modelling software will provide more accurate inverter losses.
MPP tracking	The inverters are constantly seeking the maximum power point (MPP) of the array by shifting inverter voltage to the MPP voltage. Different inverters do this with varying efficiency.
Curtailment of tracking	Yield losses can occur due to high winds enforcing the stow mode of tracking systems so that the PV modules are not optimally orientated.
Transformer performance	Transformer losses are usually quantified in terms of iron and resistive/inductive losses, which can be calculated based on the transformer's no-load and full-load losses.
DC cable losses	Electrical resistance in the cable between the modules and the input terminals of the inverter give rise to ohmic losses ($I^2.R$). * These losses increase with temperature. If the cable is correctly sized, this loss should be less than 3 % percent annually.
Ohmic Loss	is the voltage drop across the cell during passage of current due to the internal resistance of the cell
AC cable losses	AC cable losses are the ohmic losses in the AC cabling. This includes all cables post inverter up to the metering point. These losses are typically smaller than DC cable losses and are usually smaller for systems that use central inverters.
Auxiliary power	Power may be required for electrical equipment within the plant. This may include security systems, tracking motors, monitoring equipment and lighting. Plants with string inverter configurations will typically experience smaller auxiliary losses than central inverter configurations. It is usually recommended to meter this auxiliary power requirement separately. Furthermore, care should be taken as to how to quantify both daytime and nighttime auxiliary losses.
Downtime	Downtime is a period when the plant does not generate due to failure. The downtime periods will depend on the quality of the plant components, design, environmental conditions, diagnostic response time, and repair response time.
Grid availability and disruption	The ability of a PV power plant to export power is dependent on the availability of the distribution or transmission network. The owner of the PV plant relies on the distribution network operator to maintain service at high levels of availability. Unless detailed information is available, this loss is typically based on an assumption that the local grid will not be operational for a given number of hours/days in any one year, and that it will occur during periods of average production.
Grid compliance loss	Excessive loading of local transmission or distribution network equipment such as overhead lines or power transformers may lead to grid instability. In this case, the voltage and frequency of the grid may fall outside the operational limits of the inverters and plant downtime may result. In less developed regional networks, the risk of downtime caused by grid instability can have serious impacts on project economics.

Appendix B

1) Modeling program under MATLAB for three sub-system of GCPVS

```matlab
%data calibration
%variables
Ge =(G./1000);
T0=25;
Wv=WindVel;
sz= size(G);
z=sz(1,1);

% 29042020 day faults free
%Temperature module Simulation----
TPV1=1.14.*(Ta-25)+0.0175.*(G-300)+30; %Based onenvironmentalparameters
TPV3=30+0.0175.*(G-150)+1.14.*(Ta-25);%based on ross
TPV4=Ta+(0.028.*G)-1;%based on ross
TPV7=Ta+(G./800).*(44-25);%Model Noct Tnoct=47°C
TPV6=Ta+(0.0155.*G)+0.7;%based on ross
TPV8=(0.03.*G)+Ta;
TPV2=Ta+(0.031.*G)-0.058; %based on ross
TPV5=Ta+(0.031.*G);%based on ross

%choosen model temp for noct
  %NOCT modell-------------------------------------------

%       f(Tamb,G) = Tamb+p0.*((G./800).*(Tnoct-20))

  Tnoct =  46.5 ;% (-3.86e+07, 3.86e+07)
  p0 =      0.6149 ; %(-8.958e+05, 8.958e+05)
  dTcm=2;%difference btw module and cell 1-3
  Tc2=Tm2+(Ge.*dTcm);
  Tc_noct=Tamb+p0.*((G./800).*(Tnoct-20)); %Model Noct Tnoct=47°C

%Other Tempearature cell models
%Model Based on NOCT model; Includes the impact of wind speed.with 2 parameters [98]
% General model:  f(G,Wv) = p1.*((G./800).*(Tnoctw-20))+p2.*(Wv-1)

      Tnoctw =        46.5; %(-5.967e+07, 5.967e+07)
      p1 =       0.7061;  %(-1.59e+06, 1.59e+06)
      p2 =      -0.9818;   % (-1.25, -0.7137)

Xn=Tc2-Tamb;
Tc_noctw=Tamb+p1.*((G./800).*(Tnoctw-20))+p2.*(Wv-1);%Based on NOCT model; Includes the impact of wind
speed.with 2 parameters [98]
%---------------------------------------------
%PV temperature SIMULATION   //Faimen
% typical value U0=25; U1=6.84;
%General model: f(Wv) = U0+(U1.*Wv)
  U0 =       37.71  ;%(36.09, 39.33)
  U1 =       4.694 ;% (4.25, 5.138)

% Tm_faimen=Tamb+(Gi./(U0+(U1.*Wv))); % Tm_faimen=Tamb+(Gi./Xf);

Xf=G./(Tm2-Tamb);
Tm_faimen=Tamb+(G./(U0+(U1.*Wv)));
Tc_faimen=Tm_faimen+(Ge.*dTcm);

%-------------------------------------------
%sandia model module and cell
% COEFFICIENTS FOR Glass/cell/glass AND Open rack/ a=-3.47; % b=-0.0594;
% General model: f(Wv) = a+b*Wv
      a =      -3.691 ;% (-3.71, -3.673)
      b =     -0.08396 ; %(-0.08903, -0.0789)
% Xs=a+bWv;
% Tm_sandia=G.*(exp(Xs))+Tamb
Xs=log((Tm2-Tamb)./G);
Tm_sandia=G.*(exp(a+(b.*Wv)))+Tamb; % sandia Model

%ΔT temperature between Module and cell °C
Tc_sandia=Tm_sandia+(Ge.*dTcm);
T1=Tc_noct;
T2=Tc_noctw;
T3=Tc_faimen;
T4=Tc_sandia;

Tm_meas=Tm2;%Select temp of module Tm1 Tm2 or Tm3
```

```matlab
Tc_meas=Tm_meas+(Ge.*dTcm);%convert data module to cell
T5=Tc_meas;

%Select temp for model T1, T2 , T3 , T4, T5
T=T3;%T2=Tc_sandia;

Te=(T-T0);
%------------------------------------------------------------------------
%PVWATT MODEL
Ctp1 =        -0.05;   % (-4.758, 4.658)
cp1 =        0.8061 ; %(0.7856, 0.8267)
Ctp2 =        -0.05 ;% (-4.809, 4.709)
cp2  =        0.8076 ; %(0.7869, 0.8284)
Ctp3 =        -0.05 ; %(-2.265, 2.165)
cp3 =        0.8016 ;% (0.7834, 0.8199)
pdcspw1=((cp1.*3180)+(Ctp1.*Te)).*Ge;
pdcspw2=((cp2.*3180)+(Ctp2.*Te)).*Ge;
pdcspw3=((cp3.*3180)+(Ctp3.*Te)).*Ge;
%------------------------------------------------------------
%Edouardo Model
    %SUB ARRAY 1
        ai1 =        0.8716;  %(0.8675, 0.8757)
        cti1 =        0.001;  %(fixed at  bound)
        bv1 =        0.09667 ; %(0.09538, 0.09796)
        ctv1 =        -0.08037; % (-0.08549, -0.07525)
    %SUB ARRAY 2
        ai2 =        0.872  ; %(0.8676, 0.8764)
        cti2 =        0.001 ; %(fixed at bound)
        bv2 =        0.09652; % (0.09525, 0.0978)
        ctv2 =        -0.0784 ; %(-0.08348, -0.07333)
        %SUB ARRAY 3
        ai3 =        0.8638  ;%(0.8601, 0.8676)
        cti3 =        0.001 ; %(fixed at bound)
        bv3 =        0.09485 ;     %(0.09464, 0.09506)
        ctv3 =        -0.07909 ;% (-0.07992, -0.07826)

%DC current & voltage modelisation
idcs1=((ai1.*2.*6.1)+(cti1.*Te)).*Ge;
vdcs1=((log((1-exp(-1./bv1)).*bv1).*bv1)+1).*((Ge.*15.*Te.*ctv1)+(15.*21.6000000001)-
(exp(log((21.6000000001-21.6)./21.6000000001).*Ge).*(15.*21.6000000001)));
pdcs1=idcs1.*vdcs1;

idcs2=((ai2.*2.*6.1)+(cti2.*Te)).*Ge;
vdcs2=((log((1-exp(-1./bv2)).*bv2).*bv2)+1).*((Ge.*15.*Te.*ctv2)+(15.*21.6000000001)-
(exp(log((21.6000000001-21.6)./21.6000000001).*Ge).*(15.*21.6000000001)));
pdcs2=idcs2.*vdcs2;

idcs3=((ai3.*2.*6.1)+(cti3.*Te)).*Ge;
vdcs3=((log((1-exp(-1./bv3)).*bv3).*bv3)+1).*((Ge.*15.*Te.*ctv3)+(15.*21.6000000001)-
(exp(log((21.6000000001-21.6)./21.6000000001).*Ge).*(15.*21.6000000001)));
pdcs3=idcs3.*vdcs3;

%SANDIA PV ARRAY MODEL

% Finding simulated values of Vmp and Imp using Sandia Model:
s=15; %number of modules in series
p=2;   %number of parallel string
T0 = 25;      % reference temperature
q = 1.60218E-19;  % elementary charge
k = 1.38066E-23; %Boltzmann constant
Imp0 = 6.1 ;   %STC value from data sheet
Vmp0 = 17.4 ;   %STC value from data sheet
Ns = 36;        %number of cell in PV module

% parameter identification IDC AND  VDC for 29042020 day
% Tci = 0.0023;  % temperature coefficient of Impp from data sheet
%Tcv = -0.074;  % temperature coefficient of Vmpp from data sheet

%subarray 1
        Tci1 =        0.001; % (fixed at bound)
        c01 =        0.961 ; %(0.952, 0.97)
        c11 =        -0.1111 ; %(-0.1209, -0.1014)
        Tcv1 =        -0.09755 ; %(-0.09867, -0.09642)
        c21 =        0.116 ; %(-6149, 6149)
        c31 =        -3.195 ; %(-3.386e+05, 3.386e+05)
        n1 =        1.854 ; %(-9.825e+04, 9.826e+04)
%subarray 2
        Tci2 =        0.001; % (fixed at bound)
```

```
        c02 =       0.9828 ; %(0.9721, 0.9934)
        c12 =      -0.1338 ; %(-0.1453, -0.1222)
        Tcv2 =     -0.09567; % (-0.0961, -0.09524)
        c22 =       0.0674 ; %(-1106, 1106)
        c32 =       -2.184; % (-7.167e+04, 7.167e+04)
        n2 =        2.418 ;% (-3.966e+04, 3.967e+04)
%subarray 3
        Tci3 =      0.001; % (fixed at bound)
        c03 =       0.9521 ; %(0.9432, 0.9611)
        c13 =      -0.1074 ; %(-0.1171, -0.09779)
        Tcv3 =     -0.09343 ;% (-0.09447, -0.09238)
        c23 =      0.06389 ; %(-3211, 3211)
        c33 =       -2.103 ;% (-2.114e+05, 2.114e+05)
        n3 =        2.34 ; %(-1.176e+05, 1.176e+05)

%improved sandia voltage model
        Tcv1c =     -0.0731 ;% (-0.07878, -0.06741)
        c21c =       0.1239 ; %(-7090, 7090)
        c31c =        4.292 ; %(-4.91e+05, 4.91e+05)
        cvd1 =       0.3758 ; %(0.2948, 0.4568)
        n1c =         2.442 ;%(-1.397e+05, 1.397e+05)
        Tcv2c =    -0.07744 ;% (-0.08335, -0.07152)
        c22c =        0.105 ; %(-7267, 7267)
        c32c =         1.42 ;% (-1.966e+05, 1.966e+05)
        cvd2 =       0.2891 ; %(0.2048, 0.3733)
        n2c =         3.648 ;%(-2.524e+05, 2.525e+05)
        Tcv3c =     -0.07403 ; %(-0.07913, -0.06893)
        c23c =       0.1317 ; %(-8100, 8101)
        c33c =        3.155 ; %(-3.882e+05, 3.882e+05)
        cvd3 =        0.302 ;% (0.2295, 0.3746)
        n3c =        2.584;%  (-1.59e+05, 1.59e+05)

% Create variables, set them to 0
Imp = 0 ; Vmp = 0; Vmt=0;
%  Perform the calculations for the outputs
Imp1 = p.*(Imp0.*((c01.*Ge)+(c11.*(Ge.^2)))).*(1+(Tci1.*Te)));%sandia current model
Vmp1 = s.*((Vmp0)+(c21.*Ns.*(n1.*k.*(Te+298.15)./q).*log(Ge))+(c31.*Ns.*((n1.* k.*(Te+298.15)/q).*
log(Ge)).^2)+(Tcv1.*Ge.*Te)); %DC voltage with temp effect
Vmp1C = s.*((Vmp0)+(c21c.*Ns.*(n1c.*k.*(Te+298.15)./q).*log(Ge))+(c31c.*Ns.*((n1c.* k.*(Te+298.15)/q).*
log(Ge)).^2)+(Tcv1c.*Ge.*Te)-(cvd1./Ge));%DC voltage with temp effect and correction
Vmt1 = s.*((Vmp0)+(c21c.*Ns.*(n1c.*k.*(298.15)/q).*log(Ge))+(c31c.*Ns.*((n1c.*k.*(298.15)/q).*
log(Ge)).^2)); %DC voltage without temp effect

Imp2 = p.*(Imp0.*((c02.*Ge)+(c12.*(Ge.^2)))).*(1+(Tci2.*Te)));
Vmp2 = s.*((Vmp0)+(c22.*Ns.*(n2.*k.*(Te+298.15)./q).*log(Ge))+(c32.*Ns.*((n2.* k.*(Te+298.15)/q).*
log(Ge)).^2)+(Tcv2.*Ge.*Te)); %DC voltage with temp effect
Vmp2C = s.*((Vmp0)+(c22c.*Ns.*(n2c.*k.*(Te+298.15)./q).*log(Ge))+(c32c.*Ns.*((n2c.* k.*(Te+298.15)/q).*
log(Ge)).^2)+(Tcv2c.*Ge.*Te)-(cvd2./Ge));
Vmt2 = s.*((Vmp0)+(c22c.*Ns.*(n2c.*k.*(298.15)/q).*log(Ge))+(c32c.*Ns.*((n2c.*k.*(298.15)/q).*
log(Ge)).^2)); %DC voltage without temp effect

Imp3 = p.*(Imp0.*((c03.*Ge)+(c13.*(Ge.^2)))).*(1+(Tci3.*Te)));
Vmp3 = s.*((Vmp0)+(c23.*Ns.*(n3.*k.*(Te+298.15)./q).*log(Ge))+(c33.*Ns.*((n3.* k.*(Te+298.15)/q).*
log(Ge)).^2)+(Tcv3.*(Ge).*Te)); %DC voltage with temp effect
Vmp3C = s.*((Vmp0)+(c23c.*Ns.*(n3c.*k.*(Te+298.15)./q).*log(Ge))+(c33c.*Ns.*((n3c.* k.*(Te+298.15)/q).*
log(Ge)).^2)+(Tcv3c.*Ge.*Te)-(cvd3./Ge));
Vmt3 = s.*((Vmp0)+(c23c.*Ns.*(n3c.*k.*(298.15)/q).*log(Ge))+(c33c.*Ns.*((n3c.*k.*(298.15)/q).*
log(Ge)).^2)); %DC voltage without temp effect

Vdcs1 = Vmp1C;%SELECT Vmp1 or Vmp1C
Vdcst1=Vmt1;
Idcs1 = Imp1;
Pdcs1=Vdcs1.*Idcs1;

Vdcs2 = Vmp2C;%SELECT Vmp2 or Vmp2C
Vdcst2=Vmt2;
Idcs2 = Imp2;
Pdcs2=Vdcs2.*Idcs2;

Vdcs3 = Vmp3C;%SELECT Vmp3 or Vmp3C
Vdcst3=Vmt3;
Idcs3 = Imp3;
Pdcs3=Vdcs3.*Idcs3;

%Pac SNL inverter model  based on PVAM sandia
% General model:f(Vdcs,Pdcs) = ((pac0./((pdc0.*(1+C1.*(Vdcs-vdc0)))-(ps0.*(1+C2.*(Vdcs-vdc0)))))-
(C0.*(1+C3.*(Vdcs-vdc0))).*((pac0.*(1+C1.*(Vdcs-vdc0)))-(ps0.*(1+C2.*(Vdcs-vdc0))))).*((Pdcs-
(ps0.*(1+C2.*(Vdcs-vdc0))))+(C0.*(1+C3.*(Vdcs-vdc0))).*(Pdcs-(ps0.*(1+C2.*(Vdcs-vdc0)))).^2);
```

164

```matlab
% identification after improve dc voltage model
    C01  =  -2.011e-05 ;%  (-1.208, 1.208)
    C11  =     0.00168 ; %(-1.367, 1.37)
    C21  =      0.4418 ; %(-8.753e+04, 8.754e+04)
    C31  =      0.1339 ; %(-8045, 8045)
    pac01 =        2574 ;% (-2.877e+06, 2.882e+06)
    pdc01 =        2715 ;% (-5.116e+06, 5.122e+06)
    ps01  =          15 ; %(-2.972e+06, 2.972e+06)
    vdc01 =       269.8 ;% (-4.482e+05, 4.487e+05)

    C02  =  -4.172e-06 ; %(-0.08124, 0.08123)
    C12  =    0.001387; %(-0.1023, 0.105)
    C22  =      0.3327; %(-6602, 6602)
    C32  =      0.3249 ; %(-6320, 6321)
    pac02 =        2580 ;% (-7.153e+05, 7.205e+05)
    pdc02 =        2770 ; %(-9.985e+05, 1.004e+06)
    ps02  =       15.15 ; %(-3.007e+05, 3.007e+05)
    vdc02 =       275.7 ;% (-5.936e+04, 5.991e+04)

    C03  =   -1.11e-05 ;% (-0.8359, 0.8359)
    C13  =    0.003248 ; %(-3.352, 3.358)
    C23  =      0.7455 ; %(-1.351e+05, 1.351e+05)
    C33  =      0.3097 ;% (-2.333e+04, 2.333e+04)
    pac03 =        2563; % (-3.216e+06, 3.221e+06)
    pdc03 =        2743 ;% (-5.629e+06, 5.634e+06)
    ps03  =          15 ; %(-2.719e+06, 2.719e+06)
    vdc03 =         262 ; %(-2.429e+05, 2.434e+05)

Pacs1=((pac01./((pdc01.*(1+C11.*(Vdcs1-vdc01)))-(ps01.*(1+C21.*(Vdcs1-vdc01)))))-(C01.*(1+C31.*(Vdcs1-vdc01)))).*((pac01.*(1+C11.*(Vdcs1-vdc01)))-(ps01.*(1+C21.*(Vdcs1-vdc01)))))).*((Pdcs1-(ps01.*(1+C21.*(Vdcs1-vdc01))))+(C01.*(1+C31.*(Vdcs1-vdc01))).*(Pdcs1-(ps01.*(1+C21.*(Vdcs1-vdc01)))).^2);
Pacs2=((pac02./((pdc02.*(1+C12.*(Vdcs2-vdc02)))-(ps02.*(1+C22.*(Vdcs2-vdc02)))))-(C02.*(1+C32.*(Vdcs2-vdc02)))).*((pac02.*(1+C12.*(Vdcs2-vdc02)))-(ps02.*(1+C22.*(Vdcs2-vdc02)))))).*((Pdcs2-(ps02.*(1+C22.*(Vdcs2-vdc02))))+(C02.*(1+C32.*(Vdcs2-vdc02))).*(Pdcs2-(ps02.*(1+C22.*(Vdcs2-vdc02)))).^2);
Pacs3=((pac03./((pdc03.*(1+C13.*(Vdcs3-vdc03)))-(ps03.*(1+C23.*(Vdcs3-vdc03)))))-(C03.*(1+C33.*(Vdcs3-vdc03)))).*((pac03.*(1+C13.*(Vdcs3-vdc03)))-(ps03.*(1+C23.*(Vdcs3-vdc03)))))).*((Pdcs3-(ps03.*(1+C23.*(Vdcs3-vdc03))))+(C03.*(1+C33.*(Vdcs3-vdc03))).*(Pdcs3-(ps03.*(1+C23.*(Vdcs3-vdc03)))).^2);

%Calculate modeling metrics for all models

e1=T5-T1;e2=T5-T2;e3=T5-T3;e4=T5-T4;
S=T5-mean(T5);

rs1 = 1 -((norm(e1).^2)./(norm(S).^2));
rs2 = 1 -((norm(e2).^2)./(norm(S).^2));
rs3 = 1 -((norm(e3).^2)./(norm(S).^2));
rs4 = 1 -((norm(e4).^2)./(norm(S).^2));

rs=[rs1 rs2 rs3 rs4];

namet=["Tcnoct" "Tcnoctw" "Tcfaimen" "Tcsandia"];

maxt=max(T2);
ei=[e1 e2 e3 e4];
MAe =(sum(abs(ei))./z);
RMSe =sqrt(sum((ei).^2)./z);
MAep=MAe.*100./maxt;
RMSep=RMSe.*100./maxt;
%Maxtemp=45;
vecnamet=["param"; "MAE" ;"RMSe"; "MAEp"; "RMSEp";"R-squared"];
errort= [namet; MAe ;RMSe; MAep; RMSep;rs];
Ert = cat(2,vecnamet,errort);

%calculate error electrical value

E1=Idc1-idcs1;E2=Vdc1-vdcs1;E3=Pdc1-pdcs1;
E4=Idc2-idcs2;E5=Vdc2-vdcs2;E6=Pdc2-pdcs2;
E7=Idc3-idcs3;E8=Vdc3-vdcs3;E9=Pdc3-pdcs3;

S1=Idc1-mean(Idc1);S2=Vdc1-mean(Vdc1);S3=Pdc1-mean(Pdc1);
S4=Idc2-mean(Idc2);S5=Vdc2-mean(Vdc2);S6=Pdc2-mean(Pdc2);
S7=Idc3-mean(Idc3);S8=Vdc3-mean(Vdc3);S9=Pdc3-mean(Pdc3);

Rs1 = 1 -((norm(E1).^2)./(norm(S1).^2));
Rs2 = 1 -((norm(E2).^2)./(norm(S2).^2));
Rs3 = 1 -((norm(E3).^2)./(norm(S3).^2));
Rs4 = 1 -((norm(E4).^2)./(norm(S4).^2));
```

165

```
Rs5 = 1 -((norm(E5).^2)./(norm(S5).^2));
Rs6 = 1 -((norm(E6).^2)./(norm(S6).^2));
Rs7 = 1 -((norm(E7).^2)./(norm(S7).^2));
Rs8 = 1 -((norm(E8).^2)./(norm(S8).^2));
Rs9 = 1 -((norm(E9).^2)./(norm(S9).^2));

Rs=[Rs1 Rs2 Rs3 Rs4 Rs5 Rs6 Rs7 Rs8 Rs9 ];
name=["idc1" "vdc1" "pdc1" "idc2" "vdc2" "pdc2" "idc3" "vdc3" "pdc3" ];
maxmeas=[max(Idc1) max(Vdc1) max(Pdc1) max(Idc2) max(Vdc2) max(Pdc2) max(Idc3) max(Vdc3) max(Pdc3)];
Ei=[E1 E2 E3 E4 E5 E6 E7 E8 E9 ];
MAE =(sum(abs(Ei))./z);
RMSE =sqrt(sum((Ei).^2)./z);
MAEp=MAE.*100./maxmeas;
RMSEp=RMSE.*100./maxmeas;
error= [name; MAE ;RMSE;maxmeas; MAEp; RMSEp;Rs];

vecname=["param"; "MAE" ;"RMSe";"maxmeas" ;"MAEp"; "RMSEp";"R-squared"];
Er = cat(2,vecname,error);

save data
DB29042020=[time2,Tamb,T1,T2,T3,T4,T5,Te,G,Ge,Wv,Idc1,idcs1,Idcs1,Vdc1,vdcs1,Vdcs1,Pdc1,pdcspw1,pdcs1,Pdcs
1,Pac1,Pacs1,Idc2,idcs2,Idcs2,Vdc2,vdcs2,Vdcs2,Pdc2,pdcspw2,pdcs2,Pdcs2,Pac2,Pacs2,Idc3,idcs3,Idcs3,Vdc3,v
dcs3,Vdcs3,Pdc3,pdcspw3,pdcs3,Pdcs3,Pac3,Pacs3];
```

2. Integration of sandia models and performance formula under LabVIEW using Formula node

```
//PV Array simulation
Ge=G/1000; Te=T-25;
Idcs = p*(Imp0*((c0*Ge)+(c1*(Ge**2)))*(1+(Tci*Te)));

//DC voltage with temp. effect
vth=n*k*(T+273,15)/q;
Vdcs = s*(Vmp0+(c2*Ns*vth*ln(Ge))+(c3*Ns*(vth* ln(Ge))**2)+(Tcv*Ge*Te)-(cvd/Ge));

//DC voltage without temp. effect
vtht=n*k*298,15/q;
Vdct= s*(Vmp0+(c2*Ns*vtht*ln(Ge))+(c3*Ns*(vtht* ln(Ge))**2)-(cvd/Ge));

Pdcs=Vdcs*Idcs;
Pdcts=Vdct*Idcs;
// PV inverter sandia model
A=pdco*(1+C1*(Vdcs-vdco));B=pso*(1+C2*(Vdcs-vdco));C=C0*(1+C3*(Vdcs-vdco));
Pacs=((paco/(A-B))-C*(A-B))*((Pdcs-B)+C*(Pdcs-B)**2);

//Measured power
Pdcm=Vdcm*Idcm;
if (Idcm<1)
{Pacm=Pdcm*pr;}
else
Pacm=Vacm*Iacm;

//Perforamnce Analysis

//Simulated Energy
Edcs=dt*Pdcs; Eacs=dt*Pacs;
Edccs=(Edcs/1000)+Edccs;
Eaccs=(Eacs/1000)+Eaccs;
Edcds=(Edcs/1000)+(Edcds*select);
Eacds=(Eacs/1000)+(Eacds*select);

//Measured Energy
Edcm=dt*Pdcm;Eacm=dt*Pacm;
Edccm=(Edcm/1000)+Edccm;
Eaccm=(Eacm/1000)+Eaccm;
Edcdm=(Edcm/1000)+(Edcdm*select);
Eacdm=(Eacm/1000)+(Eacdm*select);

// Energy loss
Edcce=Edccs-Edccm;
Edcde=Edcds-Edcdm;
Eacce=Eaccs-Eaccm;
Eacde=Eacds-Eacdm;


// PERFORMANCE PARAMETERs
// REFERENCE YIELD
Yr=G*dt/1000; Yrc=Yr+Yrc; Yrd=Yr+(Yrd*select);
//simulated reference ARRAY YIELD
```

166

```
Pdcts=Idcs*Vdct; Edcts=Pdcts*dt;
Yars=Edcts/pmax/1000; Yarcs=Yars+Yarcs; Yards=Yars+(Yards*select);
//ARRAY YIELD
Yas=Edcs/pmax/1000; Yacs=Edccs/pmax; Yads=Edcds/pmax;//Simulated
Yam=Edcm/pmax/1000; Yacm=Edccm/pmax; Yadm=Edcdm/pmax;//Measured
//FINAL YIELD
Yfs=Eacs/pmax/1000; Yfcs=Eaccs/pmax; Yfds=Eacds/pmax;//Simulated
Yfm=Eacm/pmax/1000; Yfcm=Eaccm/pmax; Yfdm=Eacdm/pmax;//Measured
//PERFORAMCE RATIO
PRs=Yfs/Yas; PRcs=Yfcs/Yacs; PRds=Yfds/Yads;//simulated
PRm=Yfm/Yam; PRcm=Yfcm/Yacm; PRdm=Yfdm/Yadm;//measured


//measured Efficiency
Eam=(100*Pdcm)/(S*G);//PV Array ,surface of PV array S=25,6236
Esm=(100*Pacm)/(S*G);//System
Eim=(100*Eacm)/(Edcm);//Inverter efficiency


//simulated Efficiency
Eas=(100*Pdcs)/(S*G);//PV Array
Ess=(100*Pacs)/(S*G);//System
Eis=(100*Eacs)/(Edcs);//Inverter


//losses inst
Lam=Yr-Yam; Las=Yr-Yas; Lsm=Yam-Yfm; Lss=Yas-Yfs;


//Co2 Emission
Co2sc=Eaccs*C2c; Co2mc=Eaccm*C2c; Co2sd=Eacds*C2c; Co2md=Eacdm*C2c;
//cost gained
cgssd=Eacds*pg; cgsmd=Eacdm*pg;cgisd=Eacds*ps; cgimd=Eacdm*ps;//Daily
cgss=Eaccs*pg; cgsm=Eaccm*pg; cgis=Eaccs*ps; cgim=Eaccm*ps;//cumulated


//CAPTURE LOSSES
Lcs=abs(Yr-Yas); Lccs=abs(Yrc-Yacs); Lcds=abs(Yrd-Yads);//Simulated
Lcm=abs(Yr-Yam); Lccm=abs(Yrc-Yacm); Lcdm=abs(Yrd-Yadm);//Measured
ELc=abs(Lcs-Lcm);//ERROR
//THERMAL CAPTURE LOSSES
Lcts=abs(Yars-Yas); Lctcs=abs(Yarcs-Yacs); Lctds=abs(Yards-Yads);//Simulated
Lctm=abs(Yars-Yam); Lctcm=abs(Yarcs-Yacm); Lctdm=abs(Yards-Yadm);//Measured
ELct=abs(Lcts-Lctm);//ERROR
// MISCELLANEOUS CAPTURE LOSSES
Lcms=abs(Lcs-Lcts); Lcmcs=abs(Lccs-Lctcs); Lcmds=abs(Lcds-Lctds);// Simulated
Lcmm=abs(Lcm-Lcts); Lcmcm=abs(Lccm-Lctcs); Lcmdm=abs(Lcdm-Lctds);// Measured
ELcm=abs(Lcms-Lcmm);//Error
```